

Coventry University
Institute for Future Transport and Cities

Towards a Wildfire Propagation Forecasting System Enhanced by UAV Swarms



Mohammad Tavakol Sadrabadi

Director of studies: Mauro S. Innocente (PhD)

Co-Supervisor: Jesper Christensen (PhD)

A Thesis Submitted in Partial Fulfilment of the University's
Requirements for the Degree of Doctor of Philosophy

April 22, 2025



Certificate of Ethical Approval

Applicant: Mohammad Tavakol Sadrabadi
Project Title: Swarm based Wildfire propagation monitoring and forecasting system

This is to certify that the above named applicant has completed the Coventry University Ethical Approval process and their project has been confirmed and approved as Low Risk

Date of approval: 05 Mar 2024
Project Reference Number: P133024

Declaration

All sentences or passages quoted in this document from other people's work have been specifically acknowledged by clear cross-referencing to the author, work, chapters, and publication links. Any illustrations that are not the work of the author of this report have been used with the explicit permission of the originator and are specifically acknowledged and cited. I understand that failure to do this amounts to plagiarism and will be considered grounds for failure. I hereby state that all figures from publications I co-authored presented in this thesis are derived from my own creations except for figures 2.8, 8.2, 8.1.

Name: Mohammad Tavakol Sadrabadi

Signature: Mohammad Tavakol Sadrabadi

Date: April 22, 2025

Acknowledgement

And finally, here I am, at the end of a long and instructive journey, concluding my PhD, for which I owe appreciation to many who helped me along the way.

First and foremost, I want to thank my partner in love and life for her endless support, love, and patience. Without her, this would not have been possible.

Above all, I am deeply grateful to my supervisors, particularly my director of studies, Dr Mauro S. Innocente, for their guidance, advice, and encouragement. They helped me grow as a researcher and always believed in me. I would also like to thank Professor Guillermo Rein and Professor Joaquim Peiro from Imperial College London for their valuable support and collaboration.

I also thank my reviewers, Dr. Jonathan Eden and Dr. Humberto Medina, for their valuable feedback and suggestions, which helped me improve my work.

I am thankful to my friends and colleagues for their support and for making this journey easier and more enjoyable.

Last but not least, I thank Coventry University and the Centre for Future Transport and Cities (CFTC) for providing the resources and environment I needed to complete my research.

Abstract

Wildfires have increased in frequency, duration and intensity during the past few decades primarily due to global changes in climate patterns. Wildfires are highly disastrous and impose significant negative economic, environmental, and societal impacts. Hence, even though their risk cannot be fully eliminated, developing reliable management and mitigation strategies is essential. Yet, accurate predictions of wildfire propagation dynamics are critical to enable reliable management, mitigate fire propagation and make timely decisions. Nevertheless, even at small scales, a thorough physics-based simulation of this dynamic behaviour can be costly and time-consuming, especially when fire-wind interactions are considered. A different group of models are developed to bypass this restriction by reducing or ignoring some physical rules, often at the expense of accuracy, to produce faster-than-real-time estimates of fire behaviour. However, predictions from these models are more questionable since they are decoupled from the atmosphere.

This research proposes a shift towards exploring the applications of unmanned aerial vehicle (UAV) swarms in enhancing existing wildfire emergency response systems, focusing on their capabilities in improving the accuracy of faster-than-real-time wildfire predictions. While UAVs have been utilized and proven successful in performing wildfire detection and monitoring tasks, their integration into existing wildfire emergency response systems has not been clearly explored, nor have their applications in aiding operational wildfire propagation forecasting models by providing real-time wind measurements.

This research primarily aims to develop solutions enabled by UAV swarms and artificial intelligence (AI) to improve the performance of existing decoupled wildfire propagation prediction models to assist emergency response management and decision-making. As a secondary contribution, it also identifies opportunities for better integration of UAVs into wildfire emergency response systems. Leveraging technologies such as UAV-based wind measurement, deep learning (DL), and computational fluid dynamics (CFD), this project involves designing and developing a framework to improve the accuracy of operational wildfire predictions. The framework is designed to estimate the high-resolution near-surface fire-driven wind field from the sparse UAV swarm-based wind measurements taken at the flight altitude. The estimated wind field would serve as input to decoupled operational models to improve their estimation accuracy and reduce uncertainty by mimicking the effect of fire-wind interaction on

wildfire propagation.

Consequently, the contributions of this research include: *(i)* developing a conceptual framework for the integration of UAVs within the existing wildfire emergency response systems, highlighting opportunities for maximizing the benefits of leveraging UAVs, *(ii)* designing and developing a framework to improve the accuracy of decoupled wildfire prediction models through continuously feeding model with wind fields constructed from UAV swarm measurements, *(iii)* design and develop an AI-driven framework for estimating the near-surface wind field from sparse UAV-based wind measurements, *(iv)* a machine learning framework based on combining data engineering, automated model fine-tuning, and utilizing advanced ML models for improving the accuracy of vegetation classification from cartographic data with the overall aim of improving wildfire prediction models reconciling the importance of vegetation type as input into the wildfire model, and finally *(v)* a detailed study of the effect of vegetation characteristics on wildfire propagation dynamics in grasslands, highlighting the importance of developing comprehensive understanding of fire dynamics to enable accurate predictions. The developed frameworks are expected to impact society and wildfire response systems positively by providing more accurate estimations of wildfire propagation as well as extracting the full potential of UAVs in wildfire fighting operations.

Contents

1	Introduction	1
1.1	What is a wildfire?	1
1.2	The need to manage wildfires	1
1.3	Motivation	2
1.4	Aims and Objectives	3
1.5	Research Methodology	4
1.6	Thesis Structure	5
1.7	Derived Publications	7
2	Background and Literature Review	10
2.1	Wildfire Combustion Process	10
2.1.1	Fuel characteristics	10
2.1.2	Premixed and non-premixed flame	11
2.1.3	Laminar and turbulent flames	12
2.1.4	Flame characteristics in wildfires	14
2.1.5	Temperature and velocity profiles of the flame	15
2.1.6	Ignition	16
2.1.7	Burning and heat release rate	20
2.1.8	Smouldering and glowing	21
2.2	Wildfire Propagation Mechanisms	22
2.2.1	Weather	22
2.2.2	Terrain slope	24
2.2.3	Fuel properties	25
2.3	Wildfire Propagation Modeling	26
2.4	Wildfire Emergency Response	28
2.4.1	Pre-fire stage	28
2.4.2	Amidst fire stage: response	33
2.4.3	Post-fire stage: loss evaluation and recovery	36
2.5	Unmanned Aerial Vehicles in Wildfire Emergency Response	39
2.5.1	Terminology and classifications	39
2.5.2	UAVs in pre-fire stage	41
2.5.3	UAVs in amidst-fire phase	41
2.5.4	UAVs in post-fire phase	43

2.6	Wind Measurements and Downscaling	45
2.7	Artificial Intelligence and Wildfire Science	48
2.8	Uncertainty estimation for flow field reconstruction	51
2.9	Highlighting Research Gaps	52
3	Materials and Methods	54
3.1	Fire Dynamics Simulator	54
3.1.1	Level-set model	55
3.1.2	Boundary fuel model	59
3.1.3	Lagrangian particle model	59
3.1.4	Reference cases and fuel modelling in FDS-LPM	59
3.1.5	Turbulent wind model and boundary conditions	61
3.1.6	Simulation domain and gridding	63
3.1.7	Model reliability and simulation scenarios	64
3.2	Fire Propagation Model for Fast Simulations	69
3.3	Utilised Machine-Learning Algorithms	72
3.3.1	Support vector machine	72
3.3.2	Decision trees	72
3.3.3	Random forest	73
3.3.4	Stacked models	73
3.3.5	Extreme gradient boosting	73
3.3.6	K-nearest neighbour	75
3.3.7	Adaptive boosting	75
3.3.8	Categorical boosting	75
3.3.9	Deep learning and convolutional neural networks	76
3.3.10	Attention mechanism and convolutional block attention module	79
4	Conceptual Design of a UAV-Swarm Based Wildfire Emergency Response System	83
4.1	Systems Engineering Overview	83
4.2	Stakeholder Requirements Identification	84
4.2.1	Stakeholders	85
4.2.2	Objectives and constraints	85
4.2.3	Operational scenarios	88
4.3	System Feasibility Analysis	89
4.4	System Requirements Analysis	90
4.4.1	Mechanical and operational requirements	90
4.4.2	Sensors and situational awareness	92
4.4.3	Autonomy and decision making	93
4.4.4	Swarm communication and coordination strategy	94
4.4.5	User interface and human-robot interaction	95
4.4.6	System digital twin	95
4.4.7	Performance requirements	96

4.5	System-Level Synthesis	97
4.5.1	Swarm composition	97
4.5.2	Potential UAV selection	98
4.5.3	Functional relationships	104
4.6	System Design Review	107
5	Effect of Vegetation, Terrain, and Wind Conditions on Wildfire Propagation Dynamics	109
5.1	Grasslands and Wildfires	109
5.1.1	RoS as a function of wind speed	110
5.1.2	RoS as a function of terrain slope	114
5.1.3	RoS as a function of vegetation characteristics	116
5.1.4	RoS as a function of propagation mode	119
5.2	Discussion	119
5.2.1	Are FDS results counter-intuitive?	119
5.2.2	To cut or not to cut?	122
6	Vegetation Cover Type Classification Using Cartographic Data	125
6.1	Dataset	125
6.1.1	Hyperparameter optimisation	128
6.2	Model Development and Accuracy Assessment	130
6.3	Results	131
6.3.1	Model feature importance	131
6.3.2	Recursive feature elimination	132
6.3.3	Accuracy measures	133
6.4	Discussion	134
7	Effect of Fire-Wind Coupling on Fire Propagation Estimations	138
7.1	Coupled or Decoupled?	138
7.2	Experimental Data and Model Calibration	139
7.2.1	Experimental data	139
7.2.2	Boundary conditions and grid Sensitivity	139
7.2.3	FDS-LS fuel definition and RoS_0 calibration	140
7.3	Effect of Coupling Strategies	140
8	Improving Wildfire Propagation Prediction Utilising Aerial Swarm-Based Real-Time Wind Measurements	145
8.1	The Conceptual Framework	145
8.2	Wind Field Downscaling and Uncertainty Quantification	148
8.2.1	System description	148
8.2.2	Simulations scenarios	149
8.2.3	Model architecture, dataset, and training procedure	149
8.2.4	High altitude flow field reconstruction	154

8.2.5	Near surface wind field estimation	164
8.3	Enhancing Wildfire Model Predictions	170
8.3.1	Effect of wind field update time	174
8.3.2	Effect of wind measurement uncertainty	177
9	Conclusions and Future Work	181
9.1	Conclusions	181
9.2	Research Contributions	182
9.3	Limitations	184
9.4	Future Work	184

List of Figures

1.1	Thesis Structure	6
2.1	Structure of a non-premixed flame, adopted from (Finney et al., 2021a)	12
2.2	The transition of laminar flame into turbulent flame with height of flame as a function of nozzle velocity, adopted from (Drysdale, 2011).	13
2.3	Schematic representation of the cross-section of a wind-driven flame characteristics.	15
2.4	Visual illustration of the flame diagram, adopted from (Finney et al., 2021a).	16
2.5	Relationship between the height (scaled) from the base of a small circular fire and the temperature along the flames' centreline, adopted from (Finney et al., 2021a).	17
2.6	Relationship between the height (scaled) from the base of a small circular fire and the fluid vertical velocity along the flames' centreline, adopted from (Finney et al., 2021a).	17
2.7	Comparison of flame length vs fire intensities estimated by different suggested equations.	21
2.8	Classification of fire propagation models. Modified from (Innocente & Grasso, 2019a) to make it specific to wildfires and to explicitly differentiate coupled from decoupled models (Tavakol Sadrabadi & Innocente, 2024).	27
2.9	Overview of wildfire management and emergency response phases, strategies, and actions (Tavakol Sadrabadi et al., 2024).	29
2.10	UAVs in different phases of wildfire emergency response(Tavakol Sadrabadi et al., 2024).	45
3.1	Model Domain, adopted from (Tavakol Sadrabadi & Innocente, 2025).	63
3.2	Model sensitivity and validation analysis, adopted from (Tavakol Sadrabadi & Innocente, 2025)	65
3.3	Comparison of simulated fire contours with the experimental results of CSIRO C064 experiment at different instants	66
3.4	Effect of grid size and Fire Intensity on Spectral Density of turbulence.	67

3.5	Effect of grid size on the measure of turbulence resolution $M(x)$ downstream of a 10 MW fire.	68
3.6	Structure used for the Stacked Classification models (Tavakol Sadrabadi & Innocente, 2023).	74
3.7	Schematic diagram of a CNN structure for regression or classification tasks.	77
3.8	Schematic diagram of a convolutional layer operation.	78
3.9	Schematic diagram of the CBAM module, adopted from (Woo et al., 2018).	79
3.10	Schematic diagram of the channel attention module, adopted from (Woo et al., 2018).	80
3.11	Schematic diagram of the spatial attention module, adopted from (Woo et al., 2018).	81
4.1	Life cycle of a system, which starts with the statement of a need and ends with the system's disposal. The focus here is on the <i>conceptual design</i> , which is aimed at defining the system in functional terms, adopted from (Faulconbridge & Ryan, 2002).	84
4.2	Overview of a UAV swarm system requirements (Tavakol Sadrabadi et al., 2024).	90
4.3	WER missions to which each of the three proposed UAV swarms could be assigned, adopted from (Tavakol Sadrabadi et al., 2024).	98
4.4	preference scores calculated for potential off-the-shelf alternatives for different types of UAVs in the swarm (Tavakol Sadrabadi et al., 2024).	105
4.5	Functional description of and relationships within the WER system, adopted from (Tavakol Sadrabadi et al., 2024).	106
5.1	quasi-steady RoS at different wind speeds and terrain slopes, adopted from (Tavakol Sadrabadi & Innocente, 2025)	111
5.2	Comparison of the simulated <i>RoS</i> with experimental model estimations over horizontal terrain, adopted from (Tavakol Sadrabadi & Innocente, 2025)	112
5.3	Variations of the <i>RoS</i> and RoS/RoS_h with terrain slopes at $u_{10}=6$ (m/s), and $u_{10}=12$ (m/s) for different vegetation heights, adopted from (Tavakol Sadrabadi & Innocente, 2025)	114
5.4	Comparison of the Simulated <i>RoS</i> with similar studies on different terrain slopes, adopted from (Tavakol Sadrabadi & Innocente, 2025)	115
5.5	Comparison of the distribution and trend of the Observed RoS of the head fire versus fuel height and bulk density for different datasets, adopted from (Tavakol Sadrabadi & Innocente, 2025)	118

5.6	Ratio of RoS/u_{10} as a function of Byram convective number (N_C) for the combined dataset of simulations and experimental results; dashed line represent the values $N_C=2$ and 10, implying two fire propagation regimes including wind-driven ($N_C<2$) and plume-dominated ($N_C >10$); solid orange line represents the best fit for the whole dataset, adopted from (Tavakol Sadrabadi & Innocente, 2025)	120
5.7	Variation of the RoS (a-c) and the corresponding Byram convective number N_c (d-f) against fuel height (H_g) for two different vegetations of Veg_1 and Veg_2 with bulk densities of $\rho_b = 1.313$ and $\rho_b = 0.616$ respectively, at different wind (u_{10}) velocities and varying terrain slopes; grey ; dashed line represent the values $N_C=2$ and 10, implying two fire propagation regimes including wind-driven ($N_C<2$) and plume-dominated ($N_C >10$), adopted from (Tavakol Sadrabadi & Innocente, 2025)	122
5.8	Variation of the RoS/u_{10} and the Byram convective number (N_c) against fuel height under different wind velocities, note that for each line the first point is extracted from Veg_1 with a bulk density equal to $\rho_b = 1.33$ and the second point from Veg_2 with bulk density $\rho_b = 0.616$, adopted from (Tavakol Sadrabadi & Innocente, 2025)	123
6.1	Study area location map: Roosevelt National Forest wilderness areas (Tavakol Sadrabadi & Innocente, 2023).	126
6.2	Feature correlation matrix (Pearson), with r below and p -value above the diagonal (Tavakol Sadrabadi & Innocente, 2023).	127
6.3	Pairwise distribution and relationship of features in the dataset, adopted from (Tavakol Sadrabadi & Innocente, 2023).	128
6.4	Visualisation of the hyperparameter optimisation procedure for the DT algorithm (Tavakol Sadrabadi & Innocente, 2023).	130
6.5	Visualisation of the hyperparameter optimisation procedure for the XGB algorithm. Note that the notation Ae-B is meant to represent $A \times 10^{-B}$ in scientific notation (Tavakol Sadrabadi & Innocente, 2023).	130
6.6	Relative importance of features.	132
6.7	Accuracy during recursive feature elimination test (Tavakol Sadrabadi & Innocente, 2023).	133
6.8	Accuracy of different classifiers for each cover class, adopted from (Tavakol Sadrabadi & Innocente, 2025).	134
6.9	Confusion matrix of the four best-performing classifiers for predicted cover type classes (Tavakol Sadrabadi & Innocente, 2023).	135
7.1	Evolution of simulated fire front location predicted by FDS-LS for CSIRO C064 and F19 experiments using Albini's fuel models, cell sizes of 1 m, 2 m, 3 m and 5 m, and both <i>coupled</i> (C) and <i>decoupled</i> (D) configurations. Results from field tests are also provided for reference (Tavakol Sadrabadi & Innocente, 2024).	140

7.2	(a) Evolution of simulated fire front location and (b) fire perimeter at three time instances since ignition, as predicted by coupled FDS-LS for CSIRO F19 experiment using custom fuel type defined by physical characteristics in Table 3.1, calibrated RoS_0 , and cell sizes of 2 m, 3 m and 5 m. Results from field test are also provided for reference (Tavakol Sadrabadi & Innocente, 2024).	141
7.3	(a) Headfire position for eight wind speeds in the range of 1–20 m/s and (b) their corresponding RoS for horizontal topography; and (c) headfire position for nine slope–wind combinations in the range of 1–10 m/s and 5–30% and (d) their corresponding RoS with fire propagating upslope. Both <i>coupled</i> (C) and <i>decoupled</i> (D) FDS-LS are used to model each scenario (Tavakol Sadrabadi & Innocente, 2024).	142
7.4	Fire perimeter as predicted by coupled (C) and decoupled (D) FDS-LS at three different times for three different slopes.	143
8.1	System-level description of the proposed methodology to enhance wild-fire model predictions using near-surface wind fields approximated from measurements at a high altitude (specifically, at flight height) (Tavakol Sadrabadi & Innocente, 2024).	146
8.2	Bird’s eye view of an envisioned wildfire emergency response system empowered by UAV swarms, which assimilates the proposed methodology shown in Figure 8.1 to enhance fire propagation model predictions. For the UAV swarm undertaking suppression activities, adopted from (Tavakol Sadrabadi & Innocente, 2024).	147
8.3	Architecture used for reconstructing the high-resolution wind field from low-resolution sensor data, showing: (a) high-altitude wind field sampled by UAVs in a structured formation, (b) generated low-resolution wind field as input to the super-resolution (SR) model, (c) terrain and fire data used as additional information for wind field reconstruction, (d) reconstructed high-altitude wind field, and (e) estimated near-surface wind field.	151
8.4	Wind sampling strategies	153
8.5	Results of the high-resolution wind and temperature field reconstruction for case 100(3) $u_{10} = 4$ m/s, $H_g = 0.2$ m and $S = 0\%$, depicting the high-resolution ground truth/target, mean prediction of the model, the reconstruction error, and comparison of the reconstructed value at the centre line of the field with model estimation and the model input.	158
8.6	Results of the high-altitude reconstruction of the U-component for case 49(3), $u_{10} = 4$ m/s, $H_g = 0.2$ m and $S = 0\%$ under different measurement noise levels, depicting the high-resolution ground truth/target, mean prediction of the model, the reconstruction error, and comparison of the reconstructed value at the centre line of the field with model estimation and the model input.	162

8.7	Results of the high-altitude reconstruction of the temperature (T) for case 49(3), $u_{10} = 4$ m/s, $H_g = 0.2$ m and $S = 0\%$ under different measurement noise levels, depicting the high-resolution ground truth/target, mean prediction of the model, the reconstruction error, and comparison of the reconstructed value at the centre line of the field with model estimation and the model input.	163
8.8	The near-surface velocity components (U, V, W) for case 49(3), $u_{10} = 4$ m/s, $H_g = 0.2$ m and $S = 0\%$, showing the high-resolution ground truth/target, the model's mean prediction, the reconstruction error, and a comparison of the estimated value along the centerline of the field with the ground truth (CFD)	165
8.9	The near-surface U-component of velocity for case 49(3), $u_{10} = 4$ m/s, $H_g = 0.2$ m and $S = 0\%$, under different measurement noise levels, showing the high-resolution ground truth/target, the model's mean prediction, the reconstruction error, and a comparison of the estimated value along the centerline of the field with the ground truth (CFD) . . .	167
8.10	The near-surface V-component of velocity for case 49(3), $u_{10} = 4$ m/s, $H_g = 0.2$ m and $S = 0\%$, under different measurement noise levels, showing the high-resolution ground truth/target, the model's mean prediction, the reconstruction error, and a comparison of the estimated value along the centerline of the field with the ground truth (CFD) . . .	169
8.11	The near-surface W-component of velocity for case 49(3), $u_{10} = 4$ m/s, $H_g = 0.2$ m and $S = 0\%$, under different measurement noise levels, showing the high-resolution ground truth/target, the model's mean prediction, the reconstruction error, and a comparison of the estimated value along the centerline of the field with the ground truth (CFD) . . .	169
8.12	The near-surface U-component of velocity for case 49(3), $u_{10} = 12$ m/s, $H_g = 0.5$ m and $S = +20\%$, under different measurement noise levels, showing the high-resolution ground truth/target, the model's mean prediction, the reconstruction error, and a comparison of the estimated value along the centerline of the field with the ground truth (CFD) . . .	171
8.13	The near-surface V-component of velocity for case 49(3), $u_{10} = 12$ m/s, $H_g = 0.5$ m and $S = +20\%$, under different measurement noise levels, showing the high-resolution ground truth/target, the model's mean prediction, the reconstruction error, and a comparison of the estimated value along the centerline of the field with the ground truth (CFD) . . .	171
8.14	The near-surface W-component of velocity for case 49(3), $u_{10} = 12$ m/s, $H_g = 0.5$ m and $S = +20\%$, under different measurement noise levels, showing the high-resolution ground truth/target, the model's mean prediction, the reconstruction error, and a comparison of the estimated value along the centerline of the field with the ground truth (CFD) . . .	172

8.15	The near-surface U-component of velocity for case 49(3), $u_{10} = 12$ m/s, $H_g = 1$ m and $S = -20\%$, under different measurement noise levels, showing the high-resolution ground truth/target, the model's mean prediction, the reconstruction error, and a comparison of the estimated value along the centerline of the field with the ground truth (CFD) . .	172
8.16	The near-surface V-component of velocity for case 49(3), $u_{10} = 12$ m/s, $H_g = 1$ m and $S = -20\%$, under different measurement noise levels, showing the high-resolution ground truth/target, the model's mean prediction, the reconstruction error, and a comparison of the estimated value along the centerline of the field with the ground truth (CFD) . .	173
8.17	The near-surface W-component of velocity for case 49(3), $u_{10} = 12$ m/s, $H_g = 1$ m and $S = -20\%$, under different measurement noise levels, showing the high-resolution ground truth/target, the model's mean prediction, the reconstruction error, and a comparison of the estimated value along the centerline of the field with the ground truth (CFD) . .	173
8.18	Simulated wildfire propagation at three points in time for the CSIRO C064 experiment using FDS-LPM (top) and FDS-BFM (bottom) models and $0.5 \times 0.5 \times 0.5$ m ³ cells.	174
8.19	Temperature profile at three points in time from a 120 s simulation of the CSIRO C064 experiment by FireProM-F (decoupled) enhanced by wind fields inputs derived from wind measurements with update intervals (Δt) as in Table 8.10. For the first 2 time steps, simulation results of FDS and experimental data from CSIRO are also included for visual comparison. Note that "X DW" stands for "X dynamic wind field inputs during the simulation".	176
8.20	Three time instances of the CSIRO C064 experiment, where actual measurements are shown by black markers whilst the fire perimeter predicted by FireProM-F enhanced by wind field inputs derived from wind measurements every $\Delta t = 5$ s are shown by red dotted lines.	177
8.21	Burned area of CSIRO C064 experiment at three time instances after ignition: experimentally measured, predicted by FDS-LPM (coupled), predicted by FireProM-F (decoupled) with frozen wind, and predicted by FireProM-F (decoupled) enhanced by wind field inputs derived from wind measurements with different update intervals (Δt). Note that "X DW" stands for "X dynamic wind field inputs during the simulation", whilst the percentage refers to Gaussian noise.	178
8.22	Temperature profile at three points in time from a 120 s simulation of the CSIRO C064 experiment by FireProM-F (decoupled) enhanced by wind fields inputs with 30 % (top) and 50 % (bottom) Gaussian noise with update interval $\Delta t = 30$ s. Note that "X DW" stands for "X dynamic wind field inputs during the simulation".	179

8.23	Temperature profile at three points in time from a 120 s simulation of the CSIRO C064 experiment by FireProM-F (decoupled) enhanced by wind fields inputs with 30 % (top) and 50 % (bottom) Gaussian noise with update interval $\Delta t = 10$ s. Note that "X DW" stands for "X dynamic wind field inputs during the simulation".	180
------	---	-----

List of Tables

2.1	UAV classification based on Airspace class of operation (Dalamagkidis, 2015a; Dalamagkidis et al., 2012)	40
3.1	Measured properties of CSIRO C064 and F19 experiments (Cheney et al., 1993; Mell et al., 2007) adopted from (Tavakol Sadrabadi & Innocente, 2025)	60
3.2	Summary of fuel physical properties and thermal decomposition coefficients, adopted from (Tavakol Sadrabadi & Innocente, 2025)	61
3.3	Overview of the simulated Geometric and physical properties of the vegetation, terrain, and wind	64
4.1	Overview of some important stakeholders of the WER system empowered by aerial UAV swarms and their requirements (Tavakol Sadrabadi et al., 2024).	86
4.2	Example of importance level of requirements for three different tasks or UAV types during a WER (Tavakol Sadrabadi et al., 2024)	99
4.3	Potential alternatives for long-range aerial imaging UAVs (Tavakol Sadrabadi et al., 2024).	100
4.4	Potential alternatives for small monitoring and response rotary wing UAVs (Tavakol Sadrabadi et al., 2024).	101
4.5	Currently available UAV platforms potentially suitable for amidst-fire response and post-fire recovery phase (Tavakol Sadrabadi et al., 2024).	101
4.6	Long range monitoring UAV HOQ (Tavakol Sadrabadi et al., 2024).	103
4.7	Small monitoring and response rotary-wing UAV HOQ (Tavakol Sadrabadi et al., 2024).	103
4.8	Heavy-load response rotary-wing UAV HOQ (Tavakol Sadrabadi et al., 2024).	104
4.9	Comparison of UAV hardware and operational requirements for wildfire operations at 40 m altitude.	104
5.1	Average and range of measured environmental and fire variables in the (Cruz et al. 2020) wheatland and (Cruz et al. 2018) grassland experiments, adopted from (Tavakol Sadrabadi & Innocente, 2025)	116

6.1	Hyperparameters for base learners and bagging ensembles (Tavakol Sadrabadi & Innocente, 2023).	129
6.2	Hyperparameters for boosting ensembles (Tavakol Sadrabadi & Innocente, 2023).	131
6.3	Accuracy metrics for the implemented models (Tavakol Sadrabadi & Innocente, 2023).	134
8.1	Effect of the number of model parameters on the SR performance for $n=100$, utilising first sampling strategy	153
8.2	Effect of the number of UAVs on the SR performance utilising first sampling strategy	155
8.3	effect of increasing the number of input randomly sampled low-resolution versions on SR model accuracy utilising random sampling strategy and $n=100$	156
8.4	performance evaluation metrics and uncertainty of the SR model against different testing subsets	156
8.5	Evaluation of performance metrics and uncertainty of the SR model against unseen UAV numbers	159
8.6	Evaluation of performance metrics and uncertainty of the SR model against different measurement noise	161
8.7	performance evaluation metrics and uncertainty of the near-surface wind estimations against different testing subsets	164
8.8	Evaluation of performance metrics and uncertainty of the near-surface wind estimations against unseen UAV numbers	166
8.9	Evaluation of performance metrics and uncertainty of the near-surface wind estimations against different measurement noise	168
8.10	Wind field inputs/updates during a 120 s simulation of wildfire propagation for different values of the time increment Δt .	174

Chapter 1

Introduction

1.1 What is a wildfire?

Unexpected and unwanted "Wildfires," "forest fires," "bushfires," or "wildland fires" are flames that start in rural and occasionally urban areas and spread via combustible vegetation (CIFFC, [2017](#)). These large and uncontrolled fires have increased frequently during the last decades on all continents, regardless of national firefighting capabilities or management strategies (Bowman et al., [2009](#); Westerling et al., [2006](#)). Yet, A lack of understanding of fire's basic function in Earth system processes, as well as a lack of comprehension of fire's involvement in global environmental change persists (Bowman et al., [2009](#)).

The intricate relationships among biological, meteorological, physical, and social elements influence the probability, spread, severity, duration, and span of a wildfire. Wildfire danger is changing globally due to population, land use, management practices, and climate changes. While areas that have never experienced a wildfire before are now in higher danger, those that have previously been affected by wildfires may see changes in risk, either increasing or decreasing (United Nations Environment Programme, [2022](#)). The rate of spread (RoS) of the fire is generally a function of the interplay of topographical, weather, and fuel factors. These include atmospheric conditions such as ambient wind speed, humidity, and temperature; topographic conditions such as slope, and fuel conditions such as vegetation type, height, density, and moisture content (Innocent et al., [2023](#); Moinuddin et al., [2021](#)).

1.2 The need to manage wildfires

In addition to disrupting natural processes like the water supply and possibly destroying roads and other infrastructure, wildfires can have both short-term and long-term negative impacts on public health. Road closures and company closures may also result from such situations interfering with supply chains and transportation. Furthermore, dangerous substances and fine particles created by combustion found in wildfire smoke

provide health risks, especially along the wildland-urban interface (WUI) (United Nations Environment Programme, 2022). Although eliminating wildfire risk is impossible, several strategies could be taken to mitigate their risks and impacts. These include controlling activities that may cause unintentional ignitions, managing vegetation and fuel to reduce wildfire probability and intensity before one occurs, and implementing management measures during a wildfire, such as firefighting and controlling efforts, and relocating threatened people (United Nations Environment Programme, 2022).

Grasslands cover up to 50 million square kilometres (37%) of the Earth's terrestrial surface (O'Mara, 2012) and comprise more than 80% of the world's burned land (Leys et al., 2018). In the United Kingdom, grasslands constitute almost 40% (Office for National Statistics, 2015), while in Australia, a substantial 70% of the land is covered by grasslands (Innocent et al., 2023), which highlights the importance of studying grassland fires. In several aspects, grass fires are not the same as forest fires. For example, because they are well-aerated, have a high surface-to-volume ratio of grass litter, and have no trees to block the wind, they may have a very high rate of spread (ROS), which puts people and buildings at high risk (Sjöström & Granström, 2023). Hence, predicting the pace of wildfire growth and spread particularly in the presence of high wind speeds and dry fuel moisture is essential for taking proactive warning measures that ultimately safeguard populations (Cruz & Alexander, 2019a). Gathered data from different wildfires highlight high mortality rates as well as significant economic impacts of these hazards. For instance, 482 deaths are reported in Australian wildfires from 1965 to 2017 accumulating both firefighters and civilians (Haynes et al., 2019). Additionally, economic studies indicate that for an average wildfire season, southern Europe experiences a production loss between 13 to 21 billion euros on top of direct firefighting costs (Meier et al., 2023). Hence, in the big picture, it could be inferred that estimating the spatiotemporal wildfire propagation is of inherent importance that enables informed and timely decisions to protect endangered communities, properties, and infrastructure and to minimise losses. For example, as seen in the 2018 Mati fire in Greece, an underestimation of the wildfire propagation led to road blockages, a lack of proper evacuation, and hence to the second most fatal wildfire of the century globally with more than 100 confirmed death cases (Kalogeropoulos et al., 2023).

1.3 Motivation

So far, a variety of models have been developed to serve the purpose of predicting wildfire behaviour. In a general view, and with respect to the model's integration with atmospheric dynamics, these models could be classified into two groups:

1. *Coupled*: models such as FDS (McGrattan et al., 2023), FIRETEC (Linn et al., 2002), etc., which accounts for fire-wind interaction
2. *Decoupled*: models such as FARSITE (Finney, 1998a), FireProM-F (Grasso & Innocente, 2020a), etc., which do not model fire-wind interaction. More precisely,

the effect of the fire on the wind field is not accounted for.

Both types have specific drawbacks. Coupled models, for instance, tend to have higher accuracy and lower uncertainty, but they are extremely computationally intensive and orders of magnitude slower than real-time as they solve a large set of complex governing equations for combustion and fluid flow. In contrast, decoupled models are fast, as they are mostly mechanistic surrogates –FireProM-F is physics-based– without atmospheric integration, but they have lower accuracy and higher uncertainty in the predictions. Hence, decoupled or operational models are used as a decision support tool during wildfire fighting and management campaigns to provide faster than real-time estimations on the spatio-temporal span of the wildfire incidence. However, since they are decoupled from the atmosphere, their estimations can significantly differ from the real wildfire behaviour.

On the other hand, given the advancements in UAV technology during the past years, the fire community has started paying attention to and employing them in many research projects and practical fire management initiatives, such as fire detection, monitoring, and even fire fighting activities (see Innocente & Grasso, 2019a). They often have some sensors on board, such as RGB or infrared cameras (Akhroufi et al., 2021), the Global Navigation Satellite System (GNSS), and the Inertial Navigation System (INS). Although the limitations that contribute to the limited flight time make UAVs less suitable for prolonged measurements, their three-dimensional mobility makes them flexible and cost-effective tools for providing spatiotemporal measurements of the desired variables, like the atmospheric wind (Thielicke et al., 2021).

Consequently, UAVs can provide low-cost solutions that assist data gathering and operational aids to any wildfire management system. Recalling the drawbacks of operational models, UAVs can also be used to provide real-time data into the operational models to enhance their predictions.

1.4 Aims and Objectives

This project aims to **develop a framework for enhancing the accuracy of faster-than-real-time wildfire propagation estimations of decoupled models through coupling high-resolution near-surface wind fields constructed from sparse UAV swarm-based wind measurements with reduced order CFD simulations and AI-driven vegetation classification.** It should be emphasised that, for such models to be used as a basis for UAV operation and to be able to reflect the effect of actions carried out by UAVs and other agents on wildfire dynamics and aid the UAV system for task planning and execution, the model should be physics-based and alternatives such as AI models have certain limitations and drawbacks despite their high inference speed.

Hence, the project intends to achieve this by incorporating CFD simulations, AI, and UAV swarms for real-time data measurements to support decision-making and

UAV swarm task planning and execution in wildfire incidents. Consequently, the objectives of this project could be enumerated as follows:

1. Design a wildfire emergency response system incorporating UAV swarm capabilities to empower existing wildfire management systems, as well as providing means for real-time atmospheric and fire measurements
2. Investigate how environmental factors, such as wind speed, terrain slope, vegetation heights and types, and vegetation management techniques, affect the spread of wildfires.
3. Develop an AI-driven model for vegetation (fuel) type classification utilising cartographic data for integration into the wildfire prediction model
4. Evaluate the impact of integrating the atmospheric dynamics with the decoupled fire propagation model on prediction accuracy and computational performance.
5. Design and implement a methodology for reconstructing wind fields from sparse UAV-based measurements, and incorporating the wind field into the physics-based decoupled wildfire prediction model to improve real-time forecasting.

1.5 Research Methodology

This section details the methodology utilised in this project.

Research Approach Wildfire experiments normally require access to specialised properties and staff such as dedicated farms and grasslands, firefighters, as well as expensive measurement facilities. Additionally, UAV operations in UK airspace are restricted by regulations, which often limits research to simulations and numerical modelling. Consequently, this project focuses on simulations rather than physical experiments. Hence, the methodology centres around quantitative research, focusing on numerical data and measurable outcomes.

Modeling and Simulation UAV operations in wildfire scenarios are normally applicable to large scales. However, simulating the large-scale behaviour of wildfire comes with certain costs and limitations. A large-scale simulation. would be inherently limited by the computational power and hence would limit the variability of simulation scenarios or the details and reliability of simulations. Hence, this study focuses on field scale simulations $200 \times 200 \text{ m}^2$ fields to maintain a balance between accuracy and computational costs as well as the variability of simulated scenarios.

Utilised models include the Fire Dynamics Simulator (FDS) developed by the National Institute of Standard and Technology (NIST), USA, as well as the FireProM-F an in-house reduced order wildfire propagation model, developed with the focus on providing faster than real-time physics-based simulations to model the wildfire behaviour.

AI models are mainly developed utilising the *Python* programming language, with the use of a variety of specialised libraries such as *scikitlearn* and *Tensorflow* for developing machine learning and deep learning models utilised in chapters 8 and 5.

Benchmarks CFD simulations carried out are validated against the field experiments carried out by the Commonwealth Scientific and Industrial Research Organisation (CSIRO) in Australia as detailed in (Cheney et al., 1993) and (Cheney et al., 1998). The fuel characteristics, time-dependent wind velocity, and profile of fire propagation are utilised to develop the model as well as validate the model outputs as detailed in Chapter 3.

Data Sources (Synthetic Data) As mentioned earlier, this project focuses on utilising simulation data or synthetic data rather than directly collecting field data as field data are solely used for the purpose of model validation and calibration. Considering the flexibility of CFD simulations, a large variety of simulations are performed and the spatial data of fire and wind velocity are obtained from these 3-dimensional physics-based simulations. The gathered data are then accumulated in the form of a dataset, which is used to train deep-learning models for the purpose of wind field reconstruction and uncertainty analysis.

Hypothesis Testing To answer the research questions and actually test the hypothesis of this research a series of experiments and procedures are taken. A systematic comparison of the effect of coupling and decoupling on the wildfire propagation dynamics is carried out by comparing the results of coupled and decoupled fire propagation models. Simulations carried out utilising the Fire Dynamics Simulator (FDS) level-set module. The effect of feeding wind field into decoupled models on the improvement of wildfire prediction accuracy is also studied in Chapter 6 through performing a series of simulations with decoupled models, recursively fed with the high-resolution near-surface wind field.

1.6 Thesis Structure

This thesis contains eight primary chapters plus a concluding chapter. This current chapter is the first of those—the Introduction. A graphical representation of the thesis structure is depicted in Figure 1.1.

Chapter 2 presents the introductory context and literature review on wildfire and combustion, propagation dynamics, wildfire modelling and developed models, wildfire emergency response (WER), the utilisation of UAVs in wildfire management and response, as well as the utilization of machine learning (ML) and deep learning (DL) models in wildfire science and management.

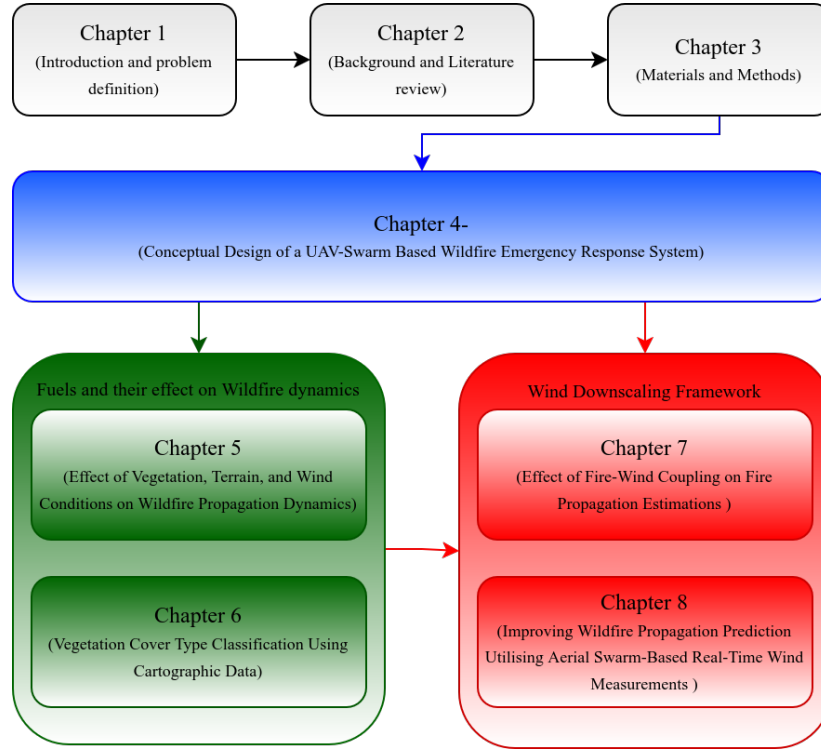


Figure 1.1: Thesis Structure

Chapter 3 presents the details and formulation of the utilised CFD codes including the fire dynamics simulator (FDS) and the FireProM-F. It also contains details on fuel model development, model calibration, and validation analysis performed for the 3D simulations of wildfire propagation conducted in field scale experiments.

Chapter 4 presents a conceptual design for a wildfire emergency response empowered by UAV swarms, supporting decision makers and land crews with a variety of activities including data gathering, participation in fire fighting activities, or assisting in search and rescue.

Chapter 5 focuses on addressing how vegetation height and bulk density affect wildfire propagation dynamics in grasslands. Consequently, a detailed analysis of the fire rate of spread in different configurations of wind speed and terrain slope, combined with varying vegetation height and bulk density is performed, combined with experimental data of two contradictory papers to accurately characterise if mowing grasses is a reliable wildfire management strategy.

Chapter 6 presents the details of the developed ML pipeline for improving the accuracy of vegetation classification utilizing cartographic data. The chapter presents the

details of the dataset, the ML models compared, and the optimal data pipeline including the feature engineering process, data cleansing, automated hyperparameter tuning and the utilisation of advanced ML models. This chapter's efforts toward developing a model for fast estimation of the fuel composition can later be used as input to the combustion model. However, it is acknowledged that the model is not inclusive of all types of data and is limited to the specific location and types of data considered.

Chapter 7 includes an examination of how coupling and decoupling affect the wild-fire propagation estimations provided by the level-set model of the FDS code. The obtained results provide the understanding and rationale for the system developed in Chapter 8.

Chapter 8 is the longest and the final working chapter of this thesis. This chapter initially details the pipeline for developing CFD simulations, extracting data, and creating datasets necessary for developing the framework or system to improve the accuracy of faster-than-real-time wildfire propagation simulations. Next, this chapter presents the system architecture, AI model development, training procedures and uncertainty analysis for the wind field downscaling. Finally, a short experiment highlights how the estimated wind field improves the faster-than-real-time wildfire propagation estimations in FireProM-F.

1.7 Derived Publications

During this research, multiple research papers and conference presentations have been delivered. These publications are as follows:

1. Tavakol Sadrabadi, M., Innocente, M., Gkanas, E., and Papagiannis, I. (2022). *Comparison of the effect of one-way and two-way fire-wind coupling on the modelling of wildland fire propagation dynamics*. In D. X. Viegas, and L. M. Ribeiro (Eds.), *Advances in Forest Fire Research* (Vol. 2022, pp. 115–121). Coimbra University Press <https://doi.org/10.14195/978-989-26-2298-9-18>.
2. Tavakol Sadrabadi, M., Innocente, M., (2023), *Vegetation cover type classification using cartographic data for prediction of wildfire behaviour*. *Fire*, 6(2). ISSN 2571-6255. doi:10.3390/fire6020076
3. Tavakol Sadrabadi, M., Innocente, M. (2024). *Enhancing wildfire propagation model predictions using aerial swarm-based real-time wind measurements: A conceptual framework*. *Applied Mathematical Modelling*, 130:615– 634. ISSN 0307-904X. doi: 10.1016/j.apm.2024.03.012
4. Tavakol Sadrabadi, M., Innocente, M. (2025). *To cut or not to cut: Effect of vegetation height and bulk density on wildfire propagation under different wind*

and slope conditions. International Journal of Disaster Risk Reduction, ISSN 2212-4209. doi: <https://doi.org/10.1016/j.ijdr.2025.105372>

5. Tavakol Sadrabadi, M., Joaquim P., Innocente, M., and Rein, G. (2025). *Conceptual design of a wildfire emergency response system empowered by swarms of unmanned aerial vehicles*. Under review at Elsevier, Preprint available at: <https://ssrn.com/abstract=4942867>
6. Tavakol Sadrabadi, Innocente, M. (2025). *Wind Field Reconstruction and Uncertainty Quantification at Wildland Fires Based on Sparse UAV-based Wind Measurements*. Preprint available at <https://doi.org/10.31224/4479>

Chapter 2

Background and Literature Review

Identifying research gaps and opportunities primarily relies upon developing a comprehensive understanding of the topic and the trending research paradigms. Consequently, this chapter's efforts to provide sufficient background and literature review to highlight existing research gaps and justify the stated research aims and objectives.

2.1 Wildfire Combustion Process

Fire as a process -even though it can take different forms- involves a chemical reaction between the combustible species and oxygen from the air and releasing heat. Flame is a gas phase phenomenon. Consequently, the combustion of solid and liquid fuels in a flaming manner requires that they be converted to gaseous form. The process of burning liquids typically involves simple evaporative boiling at the surface. Yet, for almost all solid fuels, pyrolysis or chemical decomposition is required to produce products with a minimal molecular weight that makes it possible to volatilise from the surface and enter the flame. Considering the higher energy demand for the chemical decomposition of solid fuels than simple evaporation of liquid fuels, their surface temperature is significantly higher than liquid fuel, around 400°C (Drysedale, [2011](#)).

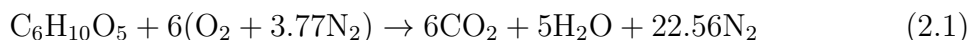
2.1.1 Fuel characteristics

The majority of fuels found in wildland areas are however woody, which contains a high percentage of cellulose (40-50%) a polymer consisting of long chains of carbohydrates, lignin (18-34%), and hemicellulose (25-35%). Attached chains of carbon (C), hydrogen (H) and hydroxyl group (OH) create carbohydrate molecules. Consequently, the general chemical formula of woody fuels could be expressed as $C_x(H_2O)_y$ with x denoting the number of carbon atoms, and y indicating the number of hydrogen and hydroxyl molecules, noting that H and OH typically form equal portions of the carbohydrate. Since cellulose typically consists of many glucose molecules ($C_6H_{10}O_5$), its formula could be presented as $(C_6H_{10}O_5)_{j'}$ where j' indicates the number of glucose

molecules in the chain (Finney et al., 2021a).

The bulk of the dry mass of the woody fuels in wildlands is made up of lignin, hemicellulose, and cellulose. However, this might only contain half of the dry mass of living plants, while the other half comprises different amounts of fats, sugars, proteins, and starches produced during photosynthesis. Due to the varying combustion properties of each of these constituents, the fuel's chemical composition can have a significant—and occasionally unidentified—impact on the burning behaviour as a whole. Considering the variety of fuels available in wildland fires, and the fact that the composition of pyrolysates formed by pyrolysis is highly dependent on the temperature of pyrolysis, it could be highlighted that, the real composition of gaseous fuels in wildland fires could be considered unknown. So normally, a global approach is adopted that simplifies the large set of possible chemical reactions into a few that adequately capture the overall behaviour for practical purposes. Part of these simplifications includes estimating the pyrolysis temperature (Finney et al., 2021a). It is normally unlikely that all the wooden fuel is consumed during the fire; there's always ash left behind, and often a layer of charred wood remains, which can be consumed in smouldering combustion (Finney et al., 2021a).

Air is composed of 21% oxygen (O_2) and 79% nitrogen (N_2), so for every mole of oxygen, air contains 3.76 moles of nitrogen. Utilising the abovementioned simplified approach for the combustion of cellulose it can be written as follows:



so it could be signified that for every mole of fuel, 6 moles of oxygen and 22.56 moles of nitrogen (28.56 moles of air) would be required. In the case of the perfect balance of fuel and air, the reaction is *stoichiometric*, implying that all fuel and oxygen would be consumed while nitrogen remains unchanged. A *fuel lean* reaction occurs when there is more air than needed, leaving extra oxygen in the products. Finally, a *fuel rich* reaction occurs when there's more fuel than the air, resulting in unburnt fuel in the combustion products (Finney et al., 2021a).

2.1.2 Premixed and non-premixed flame

Gaseous fuels can burn under two different regimes: (i) *premixed flames* in which the fuel and oxygen (or air) are thoroughly mixed before burning, and (ii) *diffusion flame* or *non-premixed* in which the fuel and oxygen (or air) are initially separate but burn in the area where they mix (Drysdale, 2011), which is the most frequent type of flame encountered. Diffusion flames are also more relevant to wildland fire behaviour. Whether it's a candle or a wildfire, all burning solids produce this kind of flame (Finney et al., 2021a).

Candle flames are an example of diffusion flames that burn wax vapour rather than solid or liquid wax; they resemble wildland fires in structure. At the flame front, the melted wax vaporises and then reacts with the air. Under stoichiometric conditions,

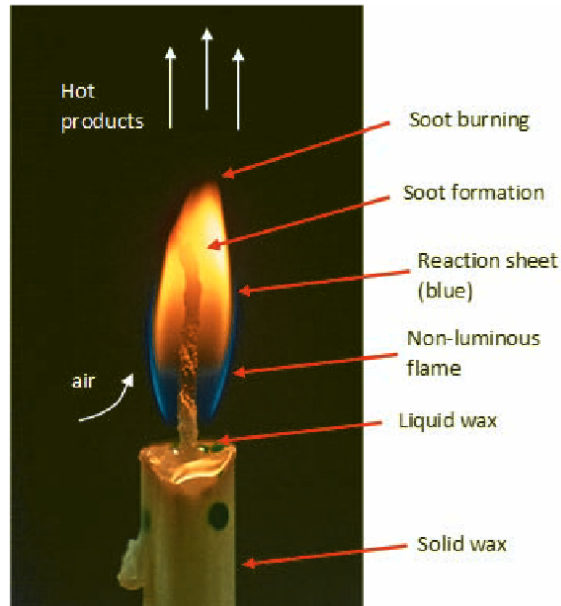


Figure 2.1: *Structure of a non-premixed flame, adopted from (Finney et al., 2021a)*

combustion occurs when air is outside the flame and fuel is inside. Because combustion only takes place within flammability limits, this results in a hollow flame as presented in figure 2.1.

The bright orange colour of a diffusion flame typically stems from the glowing of heated carbon (soot) produced as a by-product of the combustion. When carbon heats to 600–800°C, it emits orange and yellow light. the blue colour is more visible at the base of the flame here less soot is produced, while the blue colour is outshined by the bright orange and yellow at the upper levels of the flame(Finney et al., 2021a).

2.1.3 Laminar and turbulent flames

Generally, a series of parameters affect the flame length in a diffusion flame. For instance, the distance that fuel must travel to find enough oxygen to burn is a major factor in determining the height of a diffusion flame. The second parameter could be defined as the composition of the surrounding environment -i.e., flame is longer in the atmosphere than pure oxygen- which also denotes the level of available oxygen. Additionally, the fuel flow velocity has a positive effect on the flame height (Finney et al., 2021a). The height of a jet flame -such as flames generated by Bunsen burners- will normally increase roughly by the square root of the volumetric flow rate of the fuel. This, however, stands true only when the flow regime is laminar. As the flow velocity surpasses a certain level, turbulence begins to appear at the flame tip initially and then extends down toward the burner nozzle-though never reaches there. The

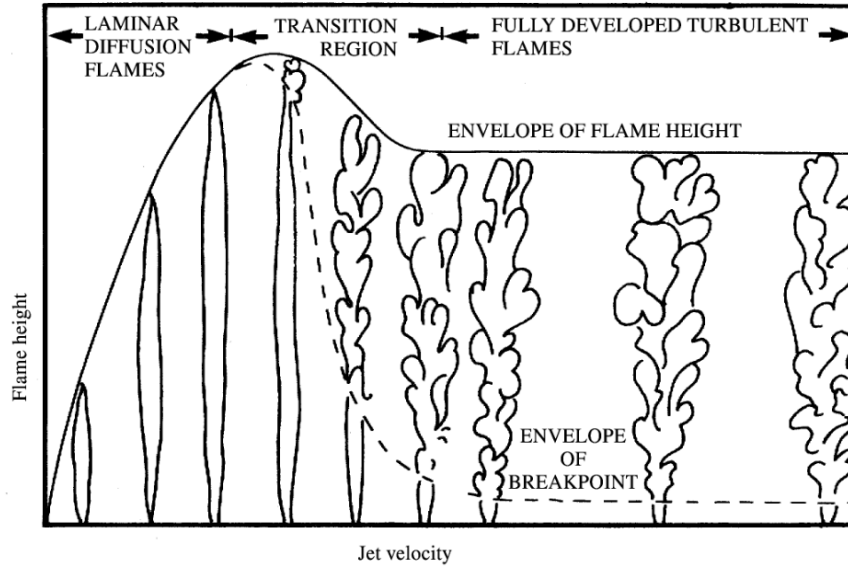


Figure 2.2: The transition of laminar flame into turbulent flame with height of flame as a function of nozzle velocity, adopted from (Drysdale, 2011).

propagation of turbulence within the flame leads to a reduction of the flame height towards a constant value, by further increasing the fluid flow rate (Drysdale, 2011) as presented in Figure 2.2. Consequently, a qualitative explanation for the flame height decrease from the maximum within the laminar region to a constant value in the fully turbulent regime is enhanced air entrainment through eddy mixing, leading to more effective combustion (Drysdale, 2011). However, if the gas jet velocity is too high, the flames will lift off the burner and will eventually blow off and go out with additional increases in flow rate (Finney et al., 2021a).

The spread of wildland fires depends heavily on convection heat transfer, which warms, dries, and ignites fuels through contact with hot gases and flames. It falls into one of two categories: forced convection, which is driven by external forces like wind, or natural convection, which is buoyancy-driven. Both varieties frequently mix to create mixed convection in wildland fires. Convection heat transfer rates in such environments are predicted using empirical correlations (Finney et al., 2021d).

The ratio of the viscous force to the inertial forces of fluid flow is known as the *Reynolds number*. It is an important criterion that can be used to define the flow regime (laminar, turbulent, transitional) in forced convection conditions and could be defined as:

$$\text{Re} = \frac{Ul}{\nu} \quad (2.2)$$

where U (m/s) indicates the flow velocity, l (m) is the characteristic length (usually defined as equal to diameter), and ν (m^2/s -for air $\approx 1.48 \times 10^{-5}$ -) is the kinematic

viscosity. In a fluid, viscous forces supersede inertial forces of flow when the Reynolds number is low. The flow is kept laminar by viscous forces, which stop spontaneous perturbations from growing in the flow. Larger Reynolds numbers (above a certain critical value) result in larger inertial forces of fluid flow than viscous forces. The flow becomes turbulent when the inertial forces outweigh the viscous forces, causing flow perturbations to increase in size and quantity. Enhanced mixing of a turbulent flow field, improves the convective heat transfer by attracting freestream fluid closer to the surface it is flowing over, which explains why the Reynolds number has a strong effect on the rate of convection heat transfer (Finney et al., 2021d).

When a temperature gradient creates a difference in density between two adjacent masses of fluid, the less dense fluid will rise relative to its surroundings due to buoyancy (Finney et al., 2021a). For buoyancy-driven flows, the *Grashof number* (Gr) could be utilised to determine the flow regime and hence, it plays a crucial role in understanding natural convection heat transfer. The Grashof number indicates the ratio of buoyant forces divided by the viscous forces and could be formulated as follows:

$$\text{Gr} = \frac{g\tau|T_s - T_\infty|l^3}{\nu^2} \quad (2.3)$$

where g (m/s²) is the acceleration of gravity, T_s (K or °C) is temperature at surface, T_∞ is the upstream or free stream temperature, and τ represents the volumetric thermal expansion coefficient (K⁻¹). Similar to the Reynolds number in forced convection, the Grashof number is important in natural convection. A laminar flow occurs when the Gr is less than a critical value ($\approx 1 \times 10^9$); a turbulent flow occurs when the Grashof number exceeds that value. Similar to the critical Re number, the critical Gr number also should be regarded as a very loose guideline. In wildland fires, the Gr typically ranges from 1 to 1×10^9 , implying that all problems involving natural convection are laminar. Purely buoyant flows, however, are uncommon in wildland fires because there is almost always some ambient or fire-induced wind present (Finney et al., 2021d).

2.1.4 Flame characteristics in wildfires

Wildland fires normally consume solid fuels for which the fuel flow rate is not controlled as opposed to the Bunsen burners and jet flames. Considering the required pyrolysis process, the fuel flow rate is equivalent to the rate of pyrolysis which is in turn controlled by heat feedback from the flames. Additionally, contrary to the jet flames, the generated gas velocity is not a fixed constant value in solid fuels, but it accelerates as it moves away from this solid bed. Consequently, wildland fire flames are called *buoyancy driven* while the jet flames are called *momentum driven*. As discussed in the previous section, the distance that the fuel gas needs to travel in order to come into contact with enough oxygen to burn basically determines the flame height. However, due to the complexity of the wildland fire process, -unlike jet flames- relationships for estimation of flame characteristics such as flame height are semi-empirical rather than being derived from first principles, meaning that equations are derived by measuring

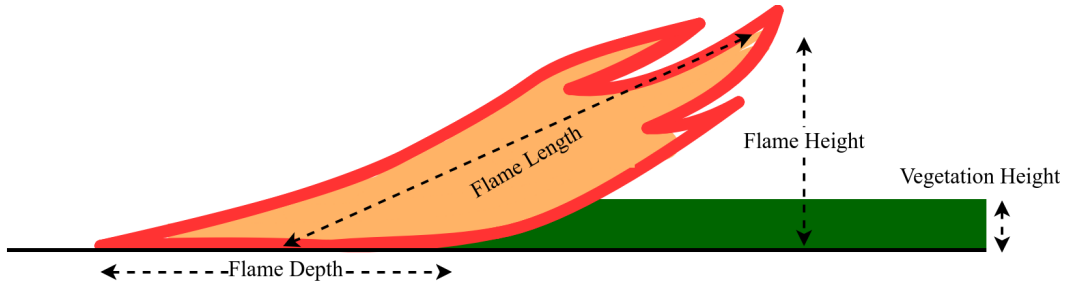


Figure 2.3: *Schematic representation of the cross-section of a wind-driven flame characteristics.*

key parameters in the process and then fitting an equation on the obtained results (Finney et al., 2021a). Figure 2.3 presents a schematic representation of the wildland fires characteristics including flame height, depth, and length. However, the pulsing and flickering of flames makes it difficult to measure flame characteristics in actual fires. Further complications in the estimation of flame height in wildfires also arise, mainly from sources like wind gusts as well as the significant height of the fuel layer -i.e. how to define the fire height in crown fires?-. Considering the tilting effect of wind on the flame, the flame length is mostly used instead of the flame height in wildland fire studies. Besides, since fuel requires time to fully burn, the flaming zone in a wildfire has a certain depth, rather than being confined to a single, narrow line (Finney et al., 2021a).

It is generally known that these flames consist of three regions including (i) a continuous flame zone at the bottom, (ii) an intermittent flame region, and (iii) the smoke plume (Finney et al., 2021a) or buoyant plume which in fact describes the convective column rising above the flame or the heat source. The plume's interaction with the surrounding fluid defines its structure. Besides, the temperature within the plume logically depends on the height above the flame and the strength of the fuel source, or the rate of heat release from the fuel (Drysdale, 2011). A visual illustration of the flame zones is presented in Figure 2.4.

2.1.5 Temperature and velocity profiles of the flame

The temperature and the fluid velocity are the two main factors controlling the convective heat transfer to solid fuel beds in wildland fires. In this case, both the flame and the hot combustion products in the smoke plume could be considered fluid in this instance. Hence, thoroughly comprehending the distribution of temperature and vertical velocity within and above the flame is essential in order to assess the heat transfer during such events (Finney et al., 2021a).

Considering the highly turbulent nature of the continuous flame zone, wildland fire is typically not hollow like a candle, and this turbulence improves conductive heat transfer through the flame height. This hence explains why the continuous flame

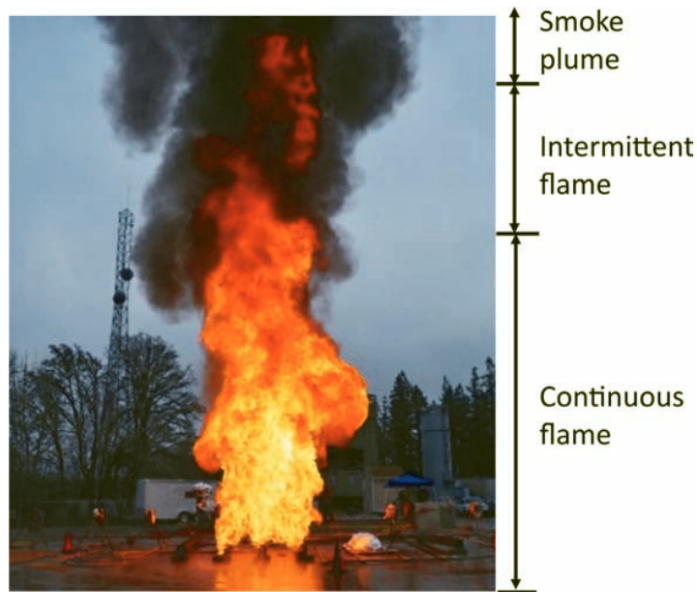


Figure 2.4: Visual illustration of the flame diagram, adopted from (Finney et al., 2021a).

region's time-averaged temperature at its centre remains relatively consistent from the bottom to the top. This, however, does not hold within the intermittent flaming zone and the smoke plume. In the area of intermittent flame, the centerline temperature starts to drop; in the smoke plume above, it drops even more quickly as presented in Figure 2.5. It could be highlighted that the x-axis presents the height above the base divided by the heat release rate (HRR) to the power of $2/5$, a scale empirically found by (Finney et al., 2021a; B. McCaffrey, 1979).

The distribution of the vertical velocity of a rising gas in a flame is directly related to the temperature profile. The gaseous fuels produced by pyrolysis have low velocity at the fuel base when they are generated from the solid fuel. However, they accelerate as they heat and burn due to the high variation in density, with the maximum velocity forming at the top of the continuous flaming zone. In the intermittent flame zone, the velocity stays relatively constant as the temperature decreases. However, for the non-reacting smoke plume, the temperature drops more quickly as cooler outside air is drawn in, slowing the upward movement of the gases as presented in Figure 2.6 (Finney et al., 2021a; B. McCaffrey, 1979).

2.1.6 Ignition

Ignition process

Ignition is the initiation of combustion. It normally occurs when flammable vapours produced by the pyrolysis of solid fuels burn visibly in the form of a flame. An impor-

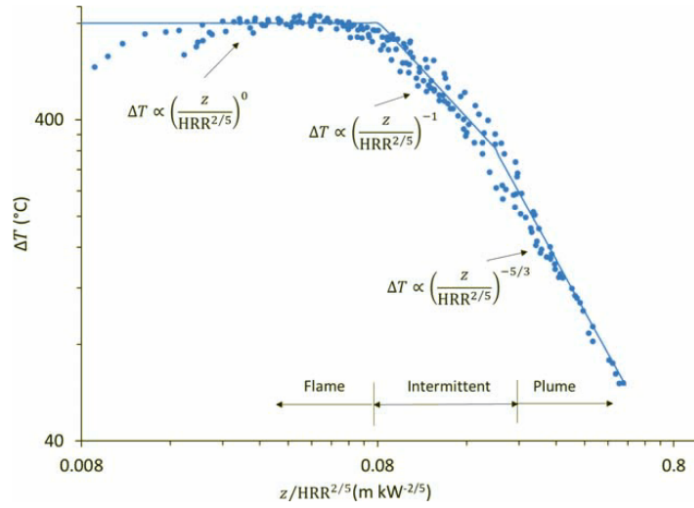


Figure 2.5: Relationship between the height (scaled) from the base of a small circular fire and the temperature along the flames' centreline, adopted from (Finney et al., 2021a).

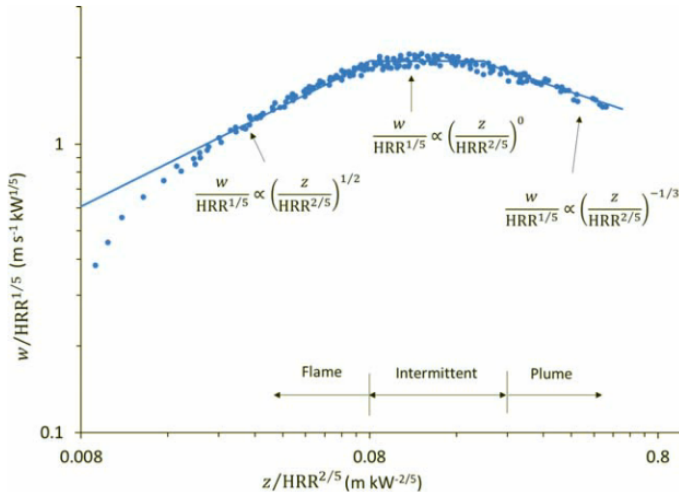


Figure 2.6: Relationship between the height (scaled) from the base of a small circular fire and the fluid vertical velocity along the flames' centreline, adopted from (Finney et al., 2021a).

tant characteristic of wildland fires is the discontinuity of the fuel bed as it consists of individual fuel elements. Consequently, the fire propagation or spread highly relies on the continuous ignition of different fuel elements. The ignition process naturally begins with heating the solid fuel up to a point that gaseous fuels begin to generate. This heating may be a result of direct contact with other burning fuels, or indirectly through thermal radiation and convection. Initially, heat may evaporate some moisture in the fuel, stalling temperature rise, especially in live fuels where water could be stored in two

different forms of *free water* stored typically in veins and *bound water* which is chemically attached to the cell walls, where the former evaporates faster than the latter. By further increase in the temperature, the pyrolysis—which is a temperature-dependent chemical reaction—begins at temperatures typically around 300°C and accelerates as the temperature increases. Initially, the generated gaseous fuel and air mixture would be too fuel-lean to burn; however, further increases in temperature lead to increased pyrolysis rate until the premixed gaseous fuel and air mixture passes the *lean flammability limit* and ignite at the presence of any hotspot with sufficient energy. The flame would then spread through the gas phase and towards the solid fuel. However, for the solid fuel to actually ignite, this approaching premixed flame should generate enough heat to overcome losses to the surrounding and the solid fuel itself. Hence, if the fuel mixture is near the lean flammability limit, the generated heat from the flame would not be sufficient and the resulting flame known as *flashing ignition* or *flash point* would be extinguished near the surface. By further increase in pyrolysis rate, the flame would be able to finally compensate for losses and lead to a stable diffusion flame which is anchored to the fuel's surface. This is known as the *fire point* (Finney et al., 2021c).

Ignition time

A measurable quantity is required to predict the amount of time it will take to ignite a fuel to flaming combustion. A physically accurate criterion can potentially be the *critical heat release rate* from the pyrolysis. However, this is impractical in actual wildland fires as it requires a deep understanding of the solid fuel heating up process, heat transfer between the gas and solid, as well as gas-phase reactions, which is challenging especially due to the unknown composition of the gases generated through pyrolysis. A simpler approach instead, would be using the *critical mass flux* criterion which only focuses on solid state to estimate the flaming ignition time. Generally, as the solid fuel heats, it loses mass through moisture evaporation and pyrolysis. As the surface temperature exceeds 300 °C, mass loss accelerates, producing enough gaseous fuel to ignite when heat from gas-phase reactions overcomes heat losses. For the fuel-lean mixtures typical during ignition, the bigger the volume of fuel vapours, the greater the amount of heat generated and the higher the temperature of the flame. Thus, the critical heat release rate requirement can be approximated by the critical mass flux rate. However, the critical mass flux criterion for ignition is not universally applicable because it does not account for gas-phase reactions. Factors like wind and changing pyrolysate composition due to temperature variation influence the required fuel production rate for ignition, making the criterion unreliable in the majority of conditions (Finney et al., 2021c). *Ignition temperature* could also be used as a criterion to predict the ignition time, considering that the pyrolysis gas production rate is temperature-dependent. However, similar to the critical mass flux, this criterion is also affected by ambient and heating conditions, implying that no single true ignition temperature could be defined; for instance, the wood ignition temperatures can range from 296 to 497°C for different environmental and testing conditions (Finney et al.,

2021c). With the ignition temperature, one may estimate the ignition time for fuel particles as follows:

$$t_{ig} = \left\{ \begin{array}{l} \frac{\pi}{4} k \rho_s c_s \frac{(T_{ig}-T_0)^2}{\dot{q}_s^2} \text{ for } \textit{thermally thick} \text{ fuels} \\ \frac{\rho_s c_s d (T_{ig}-T_0)}{\dot{q}_s} \text{ for } \textit{thermally thin} \text{ fuels} \end{array} \right\} \quad (2.4)$$

where t_{ig} is the ignition time, k represents the thermal conductivity of solid fuel ($\text{kW m}^{-1} \text{ } ^\circ\text{C}^{-1}$), ρ_s is the solid fuel's density (kg/m^3), c_s is the specific heat of the solid ($\text{kJ kg}^{-1} \text{ } ^\circ\text{C}^{-1}$), T_{ig} represents the temperature of ignition, T_0 represents the initial temperature of fuel ($^\circ\text{C}$), and \dot{q}_s^2 is the net heat flux on the fuel surface (kW m^{-2} , and d is the thickness or diameter of the fuel (Finney et al., 2021c).

It should be highlighted that the *thermally thick* assumption applies to fuel particles that are thick enough to provide a temperature gradient and possibly a significant temperature differential between the fuel particle's surface and centre. These particles take some time for heat to go through to the middle. On the other hand, the *thermally thin* assumption applies to very thin fuels. There is no temperature differential within the fuel in this instance because heat is transferred throughout the solid quickly enough to make the interior of the solid appear to be at the same temperature (Finney et al., 2021c).

The *thermal penetration depth* (l_{th}) can be used to determine which equation is more appropriate. Thus, for fuels heated on one side, if the fuel thickness is less than the calculated thermal penetration depth (l_{th}), the thermally thin assumption could be utilised, and vice-versa. However, half the thickness should be considered if the fuel is heated on both sides. The thermal penetration depth (l_{th}) can be calculated as follows:

$$l_{th} = \sqrt{\frac{k}{\rho_s c_s} t_{ig}} \quad (2.5)$$

Ignition of live fuels

Wildland fires are unique in the sense that a large variety of fuels are involved in the process, especially the living vegetation, or live fuels. Live fuels typically have a complex and varying chemical composition, including structural carbohydrates such as cellulose, lignin, and hemicellulose, as well as proteins, fats, sugars, and starches from photosynthesis. Due to the dynamically varying and constantly changing composition of the living fuels, estimating the gaseous fuels produced through pyrolysis. The second difference between living and dead fuels is that they differ notably in water storage types. While the living vegetation typically contains liquid water within their cell walls—that allows moisture content to exceed 100% of dry weight—, dead fuels can normally hold moisture levels of up to 30-40% (*fibre saturation point*) due to the collapsed cells. Furthermore, many living fuels have a waxy layer on their leaves that helps prevent dehydration, especially in hot and dry places that are prone to wildfires. This covering

is not at all like the softer texture of green grass. The way that live fuels burn and ignite is influenced by the water and sugary solutions they store. Live fuels, in contrast to dead vegetation, can forcefully release combustible gases and moisture when heated quickly. Certain species' ability to burn under particular circumstances can be affected by the high pressure that builds up inside their hard cell walls, which causes jets of moisture and gases to explode out (Finney et al., 2021c).

2.1.7 Burning and heat release rate

The rate of fuel consumption, expressed in (kg s^{-1}), is referred to as the burning rate of the fuel. Given that gaseous fuels are in the burn-ready form, the burning rate for these fuels is equivalent to the reaction rate, however, the burning rate for solid fuels depends on the production rate of gaseous fuels, as this limits combustion. It is therefore determined by the solid's mass loss over time and is directly related to the heat transferred to the solid fuel. The heat release rate of a fire is hence directly related to the burning rate of the fuel and could be described as follows:

$$\text{HRR} = \dot{m}_b H_{c,eff} \quad (2.6)$$

where HRR is the heat release rate (MJ s^{-1} or MW), \dot{m}_b is the burning rate (kg s^{-1}), and $H_{c,eff}$ is the effective heat of combustion (MJ kg^{-1}) indicating the amount of heat released when the fuel is consumed (Finney et al., 2021a).

However, *fire intensity* is the primary metric that is used in wildland fires and especially line fires to delineate the heat released by the fire. It indicates the rate of energy release per unit length of a linear flaming front, typically described in the unit of $\text{kJ.m}^{-1}.\text{s}^{-1}$, and has many applications in fire management practices and can be calculated as follows (Finney et al., 2021b):

$$I = H_c \dot{m}_c'' RoS \quad (2.7)$$

where I (KW or $\text{kJ.m}^{-1}.\text{s}^{-1}$) is the fire intensity, H_c is the heat yield, and \dot{m}_c'' (kg m^{-2}) is the mass of dry fuel per unit area consumed in the flaming and RoS (m s^{-1}) is the rate of spread of the fire. However, the fireline intensity is not directly observable and thus challenging to intuitively estimate the fire intensity. On the other hand, flame dimensions are observable and could be used as a useful indicator of fire intensity; so longer flames typically indicate a higher energy release rate in a spreading wildfire.

So far, a variety of studies have focused on developing empirical relationships to relate fire intensity and the length of flame (L), of which (Byram, 1959) with $L_{\text{Byram}} = 0.0775 I^{0.46}$, (Nelson Jr. & Adkins, 1986) with $L_{\text{Nelson \& Adkins}} = 0.0475 I^{0.493}$, (Thomas, 1963) with $L_{\text{Thomas}} = 0.0266 I^{0.666}$, $L_{\text{Newman}} = 0.0577 I^{0.46}$, (Weise & Biging, 1996) with $L_{\text{Weise \& Biging}} = 0.016 I^{0.7}$, (Barboni et al., 2012) ($L_{\text{Barboni}} = 0.062 I^{0.5336}$), and (Rossa et al., 2024) with $L_{\text{Rossa}} = 0.03885 I^{0.5112}$ could be mentioned. The results obtained through these models are highly divergent as depicted in Figure 2.7, highlighting the uncertainty involved when using flame length as a direct indicator of fire intensity.

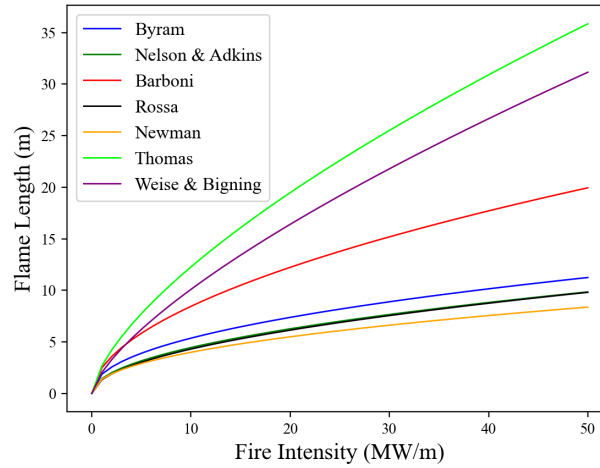


Figure 2.7: Comparison of flame length vs fire intensities estimated by different suggested equations.

2.1.8 Smouldering and glowing

Fire, as a combustion process, can be broadly divided into two types: flaming and smouldering. Smouldering is a flameless, lower-temperature form of combustion, while glowing combustion is a more intense type of smouldering that emits visible light (Finney et al., 2021a). Typically, smouldering occurs at 500°C, which is relatively low compared to the flaming combustion, and spreads in a creeping fashion, approximately around 1 cm per hour, which is two orders of magnitude slower than the spread rate of flaming fires (Rein & Huang, 2021). It is easier to start due to the lower temperature, however, it is typically more challenging to put out than flame combustion and hence is the most persistent type of combustion (Rein, 2013; Rein & Huang, 2021). Both smouldering and flaming types are typically present in wildfires. Although they differ fundamentally in chemical and physical characteristics, they can transition from one form to the other (Rein & Huang, 2021; Santoso et al., 2019). Large logs and duff can smoulder for long periods without anyone noticing before they transition into flaming combustion. Smouldering embers can be carried by the wind, cross firebreaks, and ignite new fires or structures. Smouldering usually consumes a significant amount of ground fuel, potentially negatively affecting the soil and underground organisms. Smouldering can also act as an ignition pathway from sources too weak to directly induce blazing combustion since it has the potential to abruptly turn into flaming (Finney et al., 2021a). since the fuel should be permeable to oxygen for the process to occur, not all solid fuels can burn in smoulder form. This is typically achievable with fuels like peat, rotting wood, trash, and small particles, as well as porous materials like furniture foam. The fuel must also be able to charring, or leaving behind a carbon residue that allows oxidation to continue the smouldering process. With its

pyrolysis and burning zone, char and ash zone, evaporation zone, and preheat zone, the smouldering front is organised similarly to a premixed flame (Finney et al., 2021a).

2.2 Wildfire Propagation Mechanisms

Generally, wildfires can be categorized into three groups: (i) *ground fires*, (ii) *surface fires*, and (iii) *Crown fires* ((Weise et al., 2018)):

1. Ground fire is a fire that burns the fuel at ground level (CIFFC, 2017) which are usually deposited by plants (Weise et al., 2018). Ground fuels include duff, roots, buried punky wood, and peat are all flammable elements that generally support smouldering or blazing combustion associated with ground fires (CIFFC, 2017).
2. Surface fire is a fire that normally consumes the fuels available below the level of tree crown either in the form of ahead fire, backfire or a flank advance. Surface fuel includes all flammable elements located above the duff layer between the ground and ladder fuels that contribute to the spread of surface fires (e.g. litter, herbaceous plants, low and medium shrubs, tree saplings, stumps, and downed dead roundwood) (CIFFC, 2017).
3. Crown fire is the stage in which the canopy cover of trees is in fire which is usually accompanied by a surface fire. The portion of the tree crown which is affected and burnt during the fire is called Crown Fraction Burned (CFB). Crown fire consumes crown fuel which contains forest trees canopy combustible material that are not in direct contact with ground such as foliage, twigs, and branches. The connection and transition between surface fires and crown fires usually depend on ladder fuels. In the context of a forest stand, ladder fuels are fuels that give vertical continuity between the surface and crown fuels (e.g. tall shrubs, small trees, bark flakes, tree lichens) (CIFFC, 2017).

Surface fires are the most prevalent type of wildland fires which consume the most fighting activities and costs. The fire environment greatly influences the spread of a surface fire, including factors such as fuel qualities, weather, and terrain. Composition, organic and moisture content of the raw material, mass per unit surface area, fuel-element size, shape (surface to volume ratio), porosity or packing ratio of the fuel bed, unevenness in vegetation distribution, and continuity of vegetative elements are all factors in determining the properties of the fuel (N. Liu et al., 2021). Among all the mentioned parameters, the fuel moisture content (defined as the percentage of water content in proportion to the dry mass of the fuel) is of major relevance (N. Liu et al., 2021).

2.2.1 Weather

Weather and atmospheric parameters significantly affect the fire propagation dynamics. Fire-atmosphere interaction is not limited to the interaction between the atmosphere

and the combustion flame. It also encompasses those interactions between the atmosphere and the fuel which is burning and will burn ultimately in a specific fire incident. However, it could be considered the fire-atmosphere interaction only while the induced disturbances from the ambient environment are smaller than those generated from the fire (Potter, 2012b). Different weather parameters could impact the behaviour of fire, however, three parameters including (i) *Temperature*, (ii) *Humidity or moisture*, and (iii) *Wind* could be considered most important.

Air temperature has a dual impact on the materials, a direct impact and an indirect impact which involves temperature effect on every other factor which affects to the weather. However, Wildland fire behaviour is heavily dependent on surface air temperature, which is well recognized (Potter, 2012b). Potter (Potter, 2012b) mentions that a possibility is that air temperature and fire behaviour are linked only by their dependence on fuel temperature, and not because air temperature affects fire behaviour in any way. Fuels on the surface are heated by the sun, which in turn warms the surrounding air. Moisture on the fuel's surface evaporates more quickly as fuel temperature rises, resulting in a more flammable fuel. A rise in the temperature of the atmosphere as well as an increase in flammability are both a consequence of a greater energy balance amongst the fuels, which is mostly determined by the sun's radiation as well as the heat emitted by any fires that do occur.

Despite the various field studies conducted, Potter (Potter, 2012b) suggested that clearly concluding the impact of humidity on wildfire propagation dynamics is inherently challenging due to the variation of fuel types, analysis and geographic locations where the studies are carried out. However, in some studies, it is shown that the fire RoS has a reverse relationship with atmospheric humidity as well as the fuel moisture content. It should also be highlighted that the effect of temperature and relative humidity is normally modelled through their effect on moisture content (i.e., see Sharples et al., 2009). Moinuddin et al., (Moinuddin et al., 2021) studied the effect of relative humidity on wildfire propagation dynamics utilizing Numerical simulations. They carried out a series of simulations with relative humidity ranging from 10 to 100% and compared the results with empirical models of fire propagation estimations. Their simulation results indicated a linear negative relationship between the RoS of fire and the relative humidity.

Wind, specifically ground-level or near-surface wind, is the most studied parameter in fire-atmosphere interaction (Potter, 2012b). Wind plays a complicated interaction with the fire which will be discussed in detail later. However, generally, wind accelerates the fire propagation rate by supplying it with fresh oxygen, tilting the flame towards the fresh unburnt fuel leading to an enhanced preheating of the fuel by increasing diffusion or radiation and transferring the hot air through the wet fuels through a convective process (Potter, 2012b). Additionally, it brings firebrands over long distances causing new ignited areas ahead of the main fire front. So far, various researchers have investigated the relationships between fire RoS and wind speed. For example, McArthur (McArthur, 1969) investigated the effect of wind on surface fire spread in Australian grasslands indicating that RoS is a function of the square of wind speed for winds up

to 10 m/s. Further, increasing the wind speeds above 12.5 m/s reverses this effect and decreases the RoS. One of the most important contributions to the topic is carried out by the Commonwealth Scientific and Industrial Research Organisation (CSIRO) through (Cheney et al., 1993) performing a large set of experimental grassland fires that examined the effects of the wind velocity, fuel moisture content (FMC), fuel load and fuel height on the behaviour of grassland line fires on the fire characteristic and propagation dynamics. They found that even though the wind was the most significant factor, other parameters, such as the length of the ignition line, also significantly affected the spread rate. They also found that the fires tend to propagate either (i) a narrow pointed head fire likely to be associated with the updraft from the burnt area restricting the lateral spread of fire due to the lateral inflow of wind towards the centre of the fire or (ii) a broad parabolic-shaped fire with flanks wider than the initial ignition length which tends to propagate faster than the point fire mechanism. In another study, aggregating data from experimental burns and real wildfires, (Cheney et al., 1998) proposed a new model for predicting the rate of spread of fires, highlighting the linear relationship between wind speed and RoS for wind speeds smaller than 5 km/h and the power law relationship for stronger winds. So far, different empirical and mathematical models are developed to predict wildfire behaviour in different vegetation types mainly driven by experimental data while incorporating some principles such as the Rothermel model (Rothermel, 1972), Albini fuel model (Albini, 1976), or even some simple rule of thumbs that assume the RoS to be equal to 10% (Cruz & Alexander, 2019a) or 20% (Cruz et al., 2022a) of the wind speed 10 m above ground level (AGL). These models are mainly adopted by fire services to predict the wildfire RoS during fighting operations or act as the basis of more complex models such as FARSITE (Finney, 1998b) to provide an estimation of spatial fire growth. On the other hand, physics-based models such as Fire Dynamics Simulator (FDS) (Mell et al., 2007) and FireProM-F (Grasso & Innocente, 2020a; Grasso & Innocente, 2018) try to solve the governing equations to capture the fire behaviour with different details, and numerous studies have utilised these models to study the wildfire behaviour. Performing 2D numerical simulations, (Morvan, 2014) studied the effect of fire intensity and wind conditions on the unsteady behaviour of the fire front. Analysing temporal variations in fire intensity, they indicated that plume-dominated flames oscillate more rapidly, showing erratic behaviour that makes them less predictable than wind-driven fires.

2.2.2 Terrain slope

The effect of terrain slope on fire behaviour is also extensively studied, often combined with wind speed. Rothermel (Rothermel, 1972) developed a mathematical model to describe the relationship between the RoS of fire with mid-flame height wind speed and slope. The model determines the additional propagating flux produced by wind and slope by defining wind and slope coefficients, ϕ_W and ϕ_S respectively, which are then related to the fire RoS in flat terrain and no wind condition known as (RoS_0) accord-

ing to $RoS = RoS_0(1 + \phi_W + \phi_S)$. Weise and Biging (Weise & Biging, 1994) studied the effect of wind speed and terrain slope on fire RoS and flame length and concluded that increasing the wind speed leads to an increased RoS and flame length. They utilised the obtained experimental data to validate the existing mathematical models and concluded that the existing formulations of empirical fire spread models are inaccurate and need to be revised. Wu et al., (Y. Wu et al., 2000) studied the interaction of a pool-fire plume with the terrain slope at no wind conditions. Their results indicated that the flame bends toward the surface, and the plume and the flame attach to the bed as the terrain slope increases, even in no wind conditions. They concluded that this is mainly due to the asymmetric formation of the plumes on either side of the flame. (Morandini et al., 2018) studied the fire spread dynamics uphill in no-wind conditions utilising particle image velocimetry and video imaging. In the case of horizontal surfaces with radiation as the dominant preheating mechanism, the fire plume maintains a quasi-vertical shape due to the lateral air flow into the fire from either side. Yet, by increasing the terrain slope, a strong convective flow forms ahead of the flame due to the pressure difference upstream and downstream of the flame that blows towards the top of the surface, contributing to the fuel preheating. Performing numerical simulations with WFDS, (Sánchez-Monroy et al., 2019) studied the effect of fuel depth and packing ratio on fire propagation dynamics at different uphill angles. Similar to other studies, they found a critical angle of $\approx 22^\circ$ beyond which rapid increase of the RoS occurs with increasing the slope. Overall, it could be summarised that the terrain slope highly affects the RoS of fire, as it increases in the case of uphill and decreases in downhill.

2.2.3 Fuel properties

The effect of fuel on fire dynamics is controversial as contrasting results are reported in the literature. An important effort to evaluate the effect of the fuel characteristics on the fire spread dynamics was carried out through CSIRO experiments (Cheney et al., 1993). The obtained results indicated that even though fuel load and vegetation species do not significantly affect fire spread, fires in natural undisturbed vegetation burnt approximately 18% faster than those in cut or grazed ones. (Moinuddin et al., 2021) utilised FDS to study the effect of relative humidity and fuel moisture content (FMC) on grass fire dynamics. They concluded that decreased FMC leads to faster fire propagation and higher burn intensity. They also mentioned humidity and FMC can potentially impose a shift in fire propagation mode. Cruz et al., (Cruz et al., 2018) studied the effect of fuel load on fire behaviour in Australian grasslands performing 58 experimental fires. They found that when fuel load is not a limiting factor, a negative correlation between the fuel load and fuel height with the RoS of fire is observed, contrary to the community's common assumptions. Conducting a series of numerical simulations, Moinuddin et al., (Moinuddin et al., 2018) studied the effect of fuel height on the RoS of fire, considering different heights from 0.m to 0.6 m. They concluded that increasing the grass height while keeping a constant bulk density reduces the RoS of

fire. Additionally, they mentioned that increasing the grass height leads to higher fire intensity (I) and heat release rate (HRR), which change the fire propagation mode from wind-driven to plume-dominated. In another study and performing 45 experimental burns, Cruz et al., (Cruz et al., 2020) studied the effect of fuel structure on the RoS of fire in wheat crops. They found a positive correlation between vegetation height and the RoS, where unharvested grass yielded the fastest RoS and largest flames. Commenting on the results of this study, Cruz et al., (Cruz et al., 2021) stated that the proposed conclusions are counter-intuitive, as robust empirical evidence supports the positive correlation between fuel height and RoS of fire. They reanalysed the data from (Cheney et al., 1993; Cruz et al., 2020) and stated that the positive correlation of fire RoS with vegetation height is not a matter of debate. They also stated that other studies failed to find this relationship (i.e. (Cruz et al., 2018)) mainly due to the structural variations between different grasslands utilised in such studies. Responding to the mentioned comments, Sutherland et al., (Sutherland et al., 2021) performed a reanalysis of (Cruz et al., 2020) data, combined with a series of numerical simulations and stated that below a certain grass height ($\approx 0.2 - 0.24$ m), RoS increases with height which is consistent with (Cheney et al., 1993) and (Cruz et al., 2020) where the majority of fires were wind-driven. However, for grass heights above the mentioned threshold, where fires are generally plume-dominated, the RoS decreases with increasing the grass height.

2.3 Wildfire Propagation Modeling

Sullivan (Sullivan, 2009a, 2009b, 2009c) classifies wildfire propagation models into three types: (i) *physical and quasi-physical* models, which are based on fundamental physics or chemistry of combustion (Sullivan, 2009a); (ii) *empirical and quasi-empirical* models, which are based on the statistical analysis of obtained data (Sullivan, 2009b); and (iii) *mathematical analogues and simulation* models, which are based on some mathematical conceit that coincidentally simulates the spread of fire (Sullivan, 2009c). Innocente and Grasso (Grasso & Innocente, 2020b; Innocente & Grasso, 2019a) classify them into three types (see Figure 2.8, yellow boxes): (i) *theoretical* models, which are physics-based and involve conservation laws; (ii) *data-driven* models, which are constructed or fitted using actual or synthetic data; and (iii) *mechanistic surrogate* models, which make use of mechanisms not directly related to fire dynamics. In turn, Bakhshaii and Johnson (Bakhshaii & Johnson, 2019) classify wildfire propagation models into three categories based on the level of their interaction with wind models: (i) *non-coupled*; (ii) *semi-coupled*; and (iii) *fully-coupled*. A wildfire model in which fire and wind models interact locally without being coupled with an atmospheric model would fall under the *semi-coupled* category. In this chapter, I classify wildfire models into (i) *coupled* and (ii) *decoupled* depending on whether fire and wind models interact (see Figure 2.8, blue boxes). This refers to the wildfire model alone, irrespective of whether it is coupled with an atmospheric model.

Seeking computational efficiency for operational use, models such as FARSITE (Finney, 1998a) and the Fire Propagation Model for Fast simulations (**FireProM-F**) (Grasso & Innocente, 2020b) are *decoupled* from wind models, neglecting the impact of the fire on the wind field. This increases epistemic uncertainty. FARSITE is a *mechanistic surrogate* model, which mainly relies on a simplified analytical calculation of the RoS and on Huygens' principle to approximate the propagation of the fire perimeter as if it were a wave front. FireProM-F (Grasso & Innocente, 2020b; Grasso & Innocente, 2018) is a *theoretical* reduced-order model based on energy and species conservation laws with some calibrated physically-meaningful parameters (*light-grey-box* model). Despite being physics-based, it may run faster-than-real-time under certain circumstances (scenarios, settings, computing power), although this comes at the expense of being decoupled from wind models and therefore using a frozen wind field. While *decoupled* models may provide fast simulations of wildfire propagation (Bakhshaii & Johnson, 2019), they are unable to capture structures such as plume-driven fire, whirls, or horizontal roll vortices (VanWagner, 1987).

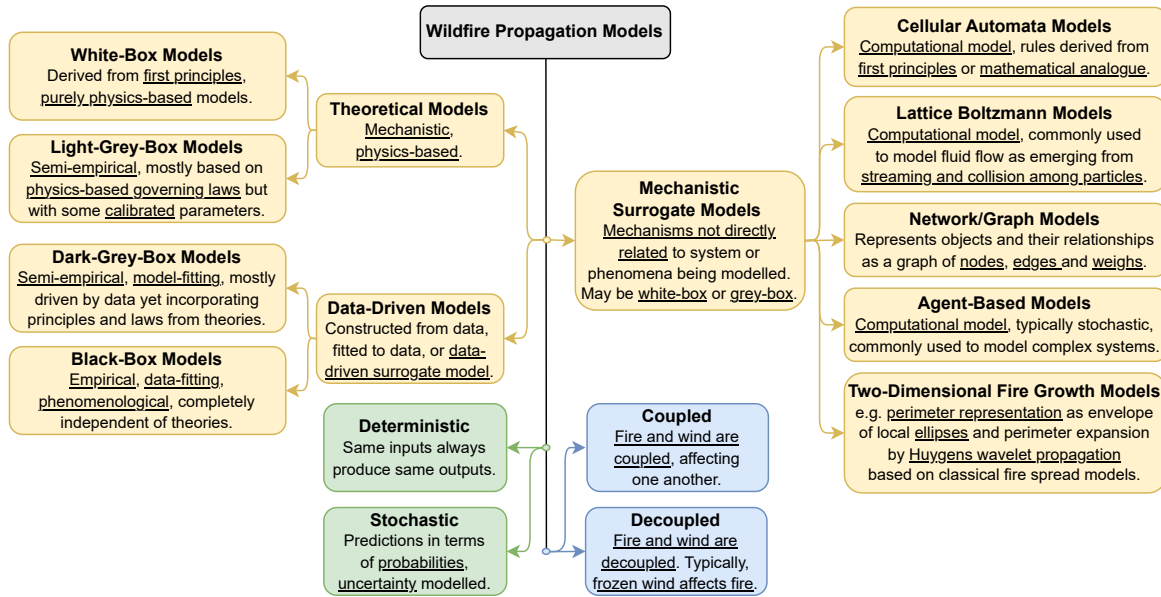


Figure 2.8: Classification of fire propagation models. Modified from (Innocente & Grasso, 2019a) to make it specific to wildfires and to explicitly differentiate coupled from decoupled models (Tavakol Sadrabadi & Innocente, 2024).

Conversely, *coupled* models such as the Fire Dynamics Simulator (**FDS**) (Mell et al., 2007) and FIRETEC (Linn et al., 2002) attempt to solve the fluid dynamics and thermo-chemical equations simultaneously in order to capture the dynamics of a wild-fire (Bakhshaii & Johnson, 2019). Even though some of these models (e.g. WRF-FIRE (Coen et al., 2013)) could potentially provide faster-than-real-time simulations under specific configurations and using high-performance facilities, an accurate numerical so-

lution over a large domain is prohibitively computationally expensive (Bakhshaii & Johnson, 2019). This restricts the practical use of this type of models.

Even though the fire–wind coupling strategy significantly affects the simulation results, this is rarely studied systematically in the literature. Lopes et al., (Lopes et al., 2017) studied the effects of the mesh size and of the wind update criterion on the fire propagation dynamics. They found that the mesh size has a high impact on the RoS and propagation dynamics of the fire, though this impact becomes less noticeable as the mesh size decreases. Nevertheless, a truly mesh-independent simulation is unlikely to be achieved. In turn, comparing the results of a series of coupled and decoupled wildfire simulations, they observed that coupled ones predict significantly smaller burned areas. Interestingly, it was also found that reducing the wind field update interval to once every five time-steps does not lead to significant variation in results, yet it notably reduces the computational effort (Lopes et al., 2017). Recently, Tavakol Sadrabadi et al., (Tavakol Sadrabadi et al., 2022) also found that the burned area and the RoS are smaller for coupled simulations.

2.4 Wildfire Emergency Response

The World Meteorological Organization (WMO) defines natural hazards as severe and extreme weather and climatic events. When a natural phenomenon destroys people’s lives and livelihoods, it becomes a disaster (World Meteorological Organization, n.d.). In this context, a wildfire could be considered a natural disaster that needs to be managed and controlled. Disaster or Emergency management is, hence, the process by which communities identify the hazards to which they are exposed and assess the physical and social impacts these hazards may inflict, as well as assess and develop their capabilities to mitigate, prepare for, respond to, and recover from these impacts (Lindell, 2013). The four integrated phases of disaster management in wildfire emergency management are prevention, preparedness, response, and recovery (Public Safety Canada, 2017) yet, these phases are not distinctly separated, and many activities that are carried out in one phase, such as fuel management, span two or more of the phases. These four phases, however, can be effectively reduced to three stages, including (i) pre-fire, (ii) amidst-fire, and (iii) post-fire. Figure 2.9 presents a broad overview of the Wildfire emergency response.

2.4.1 Pre-fire stage

The pre-fire stage generally entails all necessary steps and actions that need to be carried out in order to reduce the risk of ignition and limit the extent of probable wildfires. As such, it encompasses tactics and measures that may require years to complete as well as those that need to take place at short intervals before an ignition is detected. It should be noted that even though long-term forest management and safe building strategies are not part of a wildfire emergency response, this study provides a

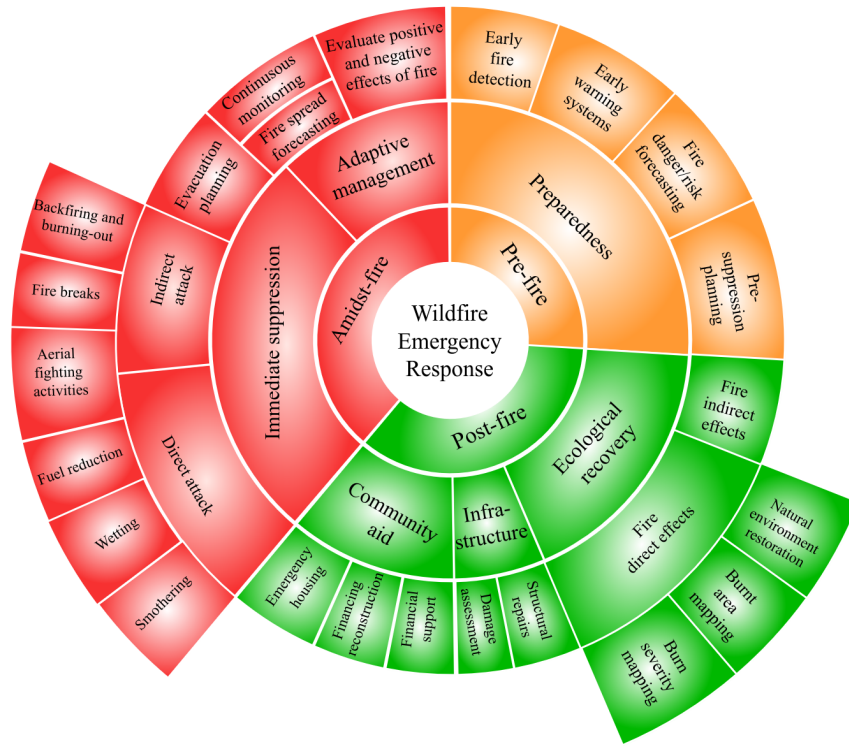


Figure 2.9: Overview of wildfire management and emergency response phases, strategies, and actions (Tavakol Sadrabadi et al., 2024).

brief overview. Consequently, the preparedness stage, which comprises those activities that must be carried out in the short term prior to the detection of a fire, could be considered as part of the emergency response and hence is of interest to the system design.

Prevention and mitigation

Generally, prevention and mitigation are frequently confused to imply activities that prevent or reduce the negative impact of an event. Yet, it should be noted that even though prevention limits the potential impacts of an incident, some actions, such as fuel management that are called prevention, do not completely prevent a fire from igniting but are capable of confining the span and intensity of the fire. Mitigation, hence, includes all actions that are taken in order to reduce the situational vulnerability and potential effects of an incident. Hence, prevention could be considered a specific type of mitigation (S. McCaffrey et al., 2020). When it comes to wildfires, the majority of mitigation strategies are then focused on strategies such as (i) *risk mitigation* and (ii) *ignition mitigation* (United Nations Environment Programme, 2022), and actions

such as reducing the vegetative fuels and increasing the fire resistance of structures and infrastructures (S. McCaffrey et al., 2020).

Ignition mitigation includes carrying out activities that help reduce the likelihood of a wildfire outbreak (United Nations Environment Programme, 2022). The majority of forest fires are started by the public (Balch et al., 2017); therefore, efforts to reduce the activity of wildfires involve education of the public, which is believed to be valuable and is used by many organizations (Prestemon et al., 2010). Media broadcasts, presentations, home visits, brochure distribution, and participation of communities in hazard assessments are among the methods for public education. It could be a highly effective and economically suitable method as it is shown that, for example, in Florida, such education has led to a reduction in the number and the burnt area of wildfires caused by preventable causes. It is also indicated that the expected benefits from averted damages could be nearly 35 times greater than the education costs (Prestemon et al., 2010). Under certain high-risk circumstances and periods, the capacity of law enforcement could also be used to restrict risky activities and public access to nature reserves and national parks (United Nations Environment Programme, 2022).

Risk mitigation of wildfires generally requires an integrated approach designed specifically for the target region, which takes into account different factors including but not limited to public awareness, fire regime, ignition and spread risk and estimations, and early detection and warning systems (United Nations Environment Programme, 2022). Even though a complete elimination of the wildfire risk is impossible, different measures and actions, such as fuel management, fire management, and fighting, could be taken to mitigate some of the economic and environmental impacts of wildfires (United Nations Environment Programme, 2022). The changes in climate significantly affect the likelihood and intensity of wildfires. A report published by the United Nations Environment Program (UNEP) states that the likelihood of catastrophic wildfires is expected to increase even under the lowest emission scenarios (United Nations Environment Programme, 2022). On the other hand, forest resilience that is the capacity to withstand and recover from natural and man-made changes has declined during the past two decades in large areas of the world, including tropical, temperate, and arid forests, most likely due to the climate change effects (Forzieri et al., 2022). Consequently, implementing plans to maintain and improve natural resilience seems to be of inherent importance.

Increasing the resilience of the natural environment is usually done in the form of landscape management. This involves the management of a section of nature in order to reduce the spread rate and intensity of a potential incident. This is often done through four strategies, including (i) fuel management, (ii) Firebreak creation and maintenance, (iii) land use planning, and (iv) fire regime restoration and management (United Nations Environment Programme, 2022).

Fuel management includes techniques such as vegetation thinning and felling, removing ride-side vegetation, connecting naturally resilient features like rivers and wetlands to fragment high-hazard areas (Forestry Commission, 2014), prescribed burns in mild conditions, planting low flammability vegetation, grazing practices, and even

controlling certain fires rather than putting them out right away (United Nations Environment Programme, 2022). The stakeholders responsible for this are usually local authorities such as forest services as well as the public or private organizations and land owners. Fire break and fire belts are linear features that serve as barriers, slowing down or stopping the spread of a wildfire. Fire breaks are gaps in vegetation and combustible fuel, while a fire belt is made of bands of fire-resistant species (Forestry Commission, 2014). The key challenge, however, is that the effectiveness of these methods are highly correlated with local conditions such as vegetation type and structure as well the burning conditions of the fire, including the weather, and it must be noted that these methods do not necessarily stop fires from propagating (United Nations Environment Programme, 2022).

The resilience of the built environment is also of importance when it comes to the effects of fire on the human-built environment. The public, local authorities, private organizations, and generally all stakeholders are required to work together to address the requirements of a fire-adapted community. This will take the form of fire-resistant building practices such as material choice, water supply practices, fire risk zoning, vegetation management, and land use management such as regulations on minimum distance between nature and property (United Nations Environment Programme, 2022). A study performed by (Dossi et al., 2023), examines data from 17,500 buildings exposed to 59 wildfires in California from 2013 to 2017 and 1,190 buildings exposed to the 2017 Pedrógão Grande Fire Complex in Portugal to study the relationship between building features in WUI fires and building damage levels. Their findings indicate that in California, vent screens and deck material flammability are strongly correlated with damage levels, while in Portugal, exterior wall and deck material flammability are the key factors related to damage levels.

Preparedness

Preparedness includes actions and measures that lead to an appropriate response for the management of wildfire outbreaks and consequences (Tymstra et al., 2020). In this context, it mainly focuses on the actions that are required to be carried out before and during a wildfire season, including (i) Preparation of suppression plans or pre-suppression planning, (ii) wildfire danger or risk forecasting, and (iii) utilizing fire detection and early warning systems (United Nations Environment Programme, 2022).

To organize a successful response operation, certain steps need to be taken before any incident happens (Council, Accessed in July 2023-b). To plan properly, a series of information is required: (i) general information such as details of land owners, land managers, tenants, access routes, and buildings; (ii) information on the water availability on-site and alternative water supply arrangements to the site; (iii) information on vehicles access and escape routes to the site and limitations such as bridge weight limits, (iv) utilities such as power lines, and gas or oil pipelines, (v) aircraft related information such as authorities, and potential impacts of a wildfire or fighting activities on the aircraft and airport, and (vi) military and shooting areas (Council, Accessed in

July 2023-b).

Identifying the endangered critical infrastructure and assets such as hospitals and transport systems and routes, preparing alternative plans and facilities in case of probable exposure of such infrastructure to the fire, and determining evacuation routes and safe shelter points (United Nations Environment Programme, 2022) could also be considered among the actions during the preparedness phase.

Forest Fire danger rating indices or systems provide the likelihood or probability of ignition, the fire rate of spread, ease of control, and its potential impacts (Food and Agriculture Organization (FAO), 2003). A variety of fire danger rating systems are used around the world that provide critical information to decision-makers and fire managers to prevent or mitigate fire effects (de Groot et al., 2015) among which Angstrom index (Chandler et al., 1983), Canadian Forest Fire Weather Index System (van Wagner, 1987), Forest Fire Danger Index, and the Keetch-Byram Drought index (Keetch & Byram, 1968), could be mentioned. Different technologies and methods have also been utilized in the development of such systems, including remote sensing and geographical information systems for satellite image analysis, statistical and machine learning methods, simulation models, and some miscellaneous methods, which are generally developed based on a combination of other methods (Zacharakis & Tsihrintzis, 2023).

Rapid and accurate fire detection is, however, the prerequisite for a fast and successful response. So far, different monitoring and detection systems have been used worldwide in order to facilitate early fire detection, which could be classified into three groups: (i) Land-based, (ii) Aerial, and (iii) satellite-based systems (Barmpoutis et al., 2020). Land-based systems generally rely on line-of-sight observations from a network of watchtowers either provided by human observers or optical sensors and digital cameras. However, with the advancements of technology, other imaging equipment, including infrared cameras, IR spectrometers, and Light Detection and Ranging (LIDAR) sensors, have also been utilized in these systems (Alkhatib, 2014) both as a single or multi-sensor network. In order to improve the accuracy and reliability of these systems, recent studies have mainly focused on utilizing the capabilities and advantages of the deep learning techniques and, more specifically, its automatic feature extraction capabilities in image processing and computer vision tasks (Barmpoutis et al., 2020). Another group of land-based monitoring instruments includes wireless sensors that are proposed to solve the limitations of the line of sight is the wireless sensors networks (WSN), which could be classified into two groups of scalar sensors and Multimedia sensors (Kizilkaya et al., 2022). Wireless sensor networks (WSN) are capable of sensing the environmental parameters such as temperature, humidity, pressure, as well as the concentration of gases such as carbon monoxide and carbon dioxide and transfer these data to the control station (Alkhatib, 2014). Despite the many improvements and capabilities, land-based systems have certain limitations. Growing trees could obstruct the line of sight, causing the system to fail. Each tower or sensor component is responsible for sensing and monitoring a large region, resulting in inevitable delays in fire detection, particularly at night and in severe weather conditions (Alkhatib, 2014).

Even though wireless sensor networks have some advantages over optical monitoring systems, such as not requiring watch towers and providing real-time data without the need for complex communication links, they have a shorter lifespan due to recharging issues, and the resolution and coverage area is directly limited by the number of sensors deployed (Alkhatib, 2014). As a result, they require constant maintenance and they carry the risk of being destroyed in fire incidents (Bumberger et al., 2013).

Satellite-based systems generally benefit from a combination of different sensors and large-scale coverage of the earth’s surface. Based on their orbit, satellites could be classified into five groups including (i) geostationary orbit (GEO), (ii) medium earth orbit (MEO), (iii) low earth orbit (LEO), (iv) sun-Synchronous orbit (SSO), and (v) geostationary transfer orbit (GTO). Among these GEO, LEO, and SSO have vast applications in earth observation tasks (Barmpoutis et al., 2020). Despite great advancements and significant improvements of satellite-based fire detection and monitoring systems, these systems are limited mainly due to the low spatial resolution sensors as well as the significant delay between consecutive surveys of the same geolocation (Akhloufi et al., 2021; Barmpoutis et al., 2020). Besides, as the intensity of thermal and infrared radiations of fires is negatively correlated with the distance, detecting fires in their early stages might not be readily feasible (Alkhatib, 2014). Smoke also poses another challenge as it might be difficult to distinguish it from clouds (Mohapatra & Trinh, 2022).

In order to address the shortcomings of land-based and satellite systems, aerial monitoring systems offer unrivaled advantages due to their high maneuverability as well as different designs, which makes them appropriate for different tasks in the context of wildfire monitoring and management (Akhloufi et al., 2021). They can carry different sensors, fly autonomously, and participate in different tasks, including fire detection and monitoring (Sudhakar et al., 2020), firefighting (Ausonio et al., 2021; Lattimer et al., 2023; Twidwell et al., 2016), and smoke particulate and aerosol measurements (Aurell et al., 2021; Z. Wu et al., 2022).

2.4.2 Amidst fire stage: response

When a wildfire occurs, those steps taken to manage and suppress it are referred to as the response phase (Tymstra et al., 2020). Wildfires in different areas of the world and ecosystems are highly varied due to the changes in fuels, geography, weather, and fire regime. Firefighting tactics also differ due to variances in fire characteristics as well as differences in the nations and individuals involved in fire management (Xanthopoulos et al., 2020).

Generally, two main strategies/options could be adopted during a response phase: (i) direct suppression, which includes actions and strategies to suppress fire immediately and effectively, and (ii) adaptive management of a wildfire, especially in areas that it is likely to have positive ecological effects (United Nations Environment Programme, 2022).

Generally, wildfire suppression management happens in different phases with re-

spect to the fire development stages. In an effort to put out a fire as soon as it is discovered, the closest fire management authority will often launch an early attack called an initial attack. In cases when the initial attack fails to contain the fire, the extended attack phase is launched, which normally involves more resources and control techniques. Spreading fires can potentially turn into Type 2 or Type 1 situations, requiring fire management teams to deploy increasingly more manpower and resources (Plantinga et al., 2022).

Since wildland fire managers have no control over the weather, attack plans within a direct response strategy mainly focus on (i) fuel reduction, (ii) specifying the location of suppression efforts, and (iii) considering minimum-cost suppression tactics. Suppression tactics could generally be classified to direct and indirect attacks. Wetting, smothering, or separating unburned fuels is how actively burning fuels are addressed by direct attack. A direct attack can be directly employed to put out a fire or reduce the intensity of a burning flame. In contrast, indirect attack, which is mainly used in case of fast propagating or intensely burning fires, tries to disrupt fuel continuity by creating fire-breaks and allowing the fire to reach a site that is optimal for suppression actions (NWCG, 2021; Wollstein et al., 2022). An approximate 95% of wildfires are contained during the initial attack (Murphy, 2004). Yet, understanding the ecosystem adaptability or vulnerability to fire, fuel distribution, infrastructure and lives at risk, and the probability of an uncontrolled fire development from the outbreak is crucial to be able to carry out a successful initial attack (United Nations Environment Programme, 2022).

Each suppression tactic type has its advantages and disadvantages (Council, Accessed in July 2023-a). The flame length could be used as a visual indicator of fire intensity to identify the most appropriate tactic to suppress a fire. Generally, building fire lines is one of the most important and widely used strategies during a response phase. These lines are generally located at a distance to the fire edge, where it is most likely that the fire will escape, which normally implies the fire front. Hot spotting, which is the technique to attack the fire's hotter burning points, is also usually adopted to stop fires from escaping the firelines. Apart from using hand tools and fire lines to fight the fire, water and other additives such as surfactants, which reduce the surface tension of water to improve its penetration, class A foams and retardants, which reduce the flammability of treated fuels and are more effective than water, and fire gels which perform like foams and expand water and adheres to the vegetation could also be used depending on the availability and situation (Group, 1996).

Tactical air operations could also be used in certain conditions to deploy significant amounts of water or retardants when it is required and could result in the overall reduction of suppression costs. Yet, there are a series of considerations that limit the use of these facilities. Factors that affect the use of an aircraft in suppression efforts include (i) heat and altitude of the operation, (ii) size, configuration, and speed of the aircraft, (iii) terrain shape and limitations, (iv) Environmental, atmospheric, and wind conditions, (v) turnaround times of the aircraft, (vi) possible flight and aircraft caused hazards, and (vii) policies. Their operation is normally affected by their large

physical dimensions, terrain specifications, high winds and turbulence generated by fire, atmospheric phenomena such as inversion, which keeps the smoke in low altitudes and prevents visibility, the significant time for returning and reloading the aircraft, which could also be increased by the distance from support facilities and resources, and the specific policies that can limit the flight time and duty hours of pilots and aircraft operation. On the other hand, firefighting aircraft are usually the most expensive single item in a fire scene (Group, 1996). Apart from the huge cost of acquiring air tankers, their operation is also extensively expensive. As a rough average, (Gabbert, 2018) reports that putting an air tanker with crew on hold would cost \sim \$30000 per day while flying it tops up the costs for \sim \$7600 per hour irrespective of the cost of the suppression liquids.

Another important strategy in fighting wildfires is to use fire. Generally, two strategies could be adopted to fight fire with fire, including (i) burning out and (ii) backfiring. Burning out implies the method to ignite a fire to consume the fuel between the constructed fireline and the edge of the fire, which reduces the chances of the fire line failure as well as the time required for mop-up. Backfiring, which is defined as setting fire along the inner edge of the fire line, is another technique that could be used to consume the fuel in the path of a wildland fire, change the direction or force of the fire's convective column, and to reduce the rate of spread of fire (Group, 1996).

According to the UK NFCC guidelines for wildfires, incident commanders should maintain situational awareness at all stages during the incident. It includes understanding the situation and anticipating how the situation may change. Consequently, they are required to continuously monitor the following data, which would help them make safe and informed decisions during the incident:

- fire data such as location, size, direction, and rate of spread
- topography of the site including slope, fire position on slope, aspect, or any probable topographical hazards
- fuel data including fuel type, moisture, and distribution
- weather data including the current values and predictions for wind speed and direction, temperature, and humidity
- endangered properties, heritage, livestock, and citizens
- location of nearby infrastructure such as wind farms and pipelines

Irrespective of the time and money invested in a comprehensive direct response approach, there are always dangers that cannot be eliminated. Consequently, in some areas, a tangible approach would be to develop adaptive response strategies that facilitate fire management strategies instead of direct suppression. A shift towards a flexible management strategy could exert positive ecological and economic benefits. However, adopting such an approach requires a broad understanding and integrated management

approaches that bring into account different factors, including adopted fuel management strategies, fire spread estimations, dominant fire regime of the region, monitoring and early warning systems, population awareness and preparedness (United Nations Environment Programme, 2022), as well as other parameters such as fire intensity and annual rainfall of the forested areas (Volkova et al., 2019).

Once a wildfire starts to threaten the structures and assets, a series of actions are generally taken to mitigate the impact of wildfire, including asset protection and population evacuation (United Nations Environment Programme, 2022). Evacuation of residents is generally encouraged by the fire management services in order to prioritize resident safety and reduce the complexity of wildfire management. An early evacuation of populations at risk is hence widely suggested to be the safest course of action in such conditions (Stasiewicz & Paveglio, 2021). Generally, important components of evacuation modeling include population, the time before evacuation, variables impacting movement, judgments on routes and destinations, flow restrictions, events affected by policy decisions, wildfire propagation speed, and designated safety zones (Ronchi et al., 2023). It should be mentioned that serious negative outcomes may arise from inaccurately forecasting, planning, or timing an evacuation procedure, or the wildfire's advance rate (Kalogeropoulos et al., 2023). Consequently, different studies have focused on the development of reliable evacuation modeling platforms through the integration of pedestrians, traffic, and wildfire propagation models (e.g., see (Mitchell et al., 2023; Wahlqvist et al., 2021)). Understanding the household movement and behaviour in emergency conditions is also critical in order to be able to improve WUI resilience and safety to wildfires (Lovreglio et al., 2019) and positively affects the decisions and management strategies taken during an event such as evacuation orders, traffic management, and rescue missions (Zhao et al., 2022).

2.4.3 Post-fire stage: loss evaluation and recovery

Wildfires directly impact the natural environment, including Vegetation cover, wildlife, water and soil quality, and human communities and economies. The recovery phase includes all efforts to restore or reconstruct the vegetation, forest cover, or natural environment (Tymstra et al., 2020). The risks are not completely eliminated in any wildfire management system with any hazard reduction and suppression strategies. Hence, recovery planning remains an important element of a disaster management system. The recovery phase generally encompasses three main aspects, including (i) community aid, (ii) infrastructure, and (iii) environment (United Nations Environment Programme, 2022). Emergency housing of the affected population, providing financial support and financing for the community, and establishing long-term assistance plans could be considered as actions taken to aid the community. Wildlife and environmental rescue and restoration actions, as well as infrastructure damage assessments and repairs, are also examples of actions in the recovery phase of communities (United Nations Environment Programme, 2022). For example, the burned area emergency response (BAER) program established by the USDA, is designed to address the emergency situations

after fire through determining, recommending, and implementing emergency actions with the priorities focused on protecting life, property, and natural resources (USDA Forest Service, 2020).

Wildfires pose a great risk to the buildings and infrastructure located in the wildland-urban interface (WUI). When a fire breaks out in a WUI, homes are either directly ignited as the firefront reaches out to the buildings or through firebrands, which pose a threat to the buildings further from the main firefront yet close enough to the dense vegetation for the firebrands to reach them (Kramer et al., 2019). Numerous examples of destructive WUI fire incidents could be cited. For example, in 2018, the Camp Fire, which burnt an area of almost 62000 hectares, burnt more than 18000 buildings, destroyed Paradise City in California, and caused more than 85 deaths (NASA Earth Observatory, 2018). In the newest example of such devastating WUI fires, the Lahaina fire in Maui island burnt an area of approximately 900 hectares, burnt nearly 2200 buildings, destroyed the historic town of Lahaina, and left more than 115 people killed. Initial estimations have indicated that the costs of re-buildings would be equal to 5.52 billion dollars (CBS News, 2023). The post-disaster infrastructure must be matched to the community's anticipated demand for its constructed and virtual environments in order for the recovery process to be successful. In the larger natural hazards community, replacing what was destroyed is no longer considered to be a successful recovery. Instead, restoration initiatives must promote resilience in a community's built, social, and biological environments (Federal Emergency Management Agency, 2011). A study performed by (Knapp et al., 2021) examined the effect of housing arrangement (i.e. distance to closest homes and nearest burnt structure, and density of buildings in the area) and vegetation factors (such as grass and crown canopy cover close to the buildings) on the buildings' survival rate during the 2018 Camp Fire incident, taking into account the construction year and the adopted building regulations for each time period. Their results demonstrate that while higher quality construction and standards might help protect subdivisions against direct exposure to the flames, the proximity of the building to burning structures and vegetation is the most significant factor affecting the survival rate of a building during a wildfire. Consequently, in terms of wildfire recovery, a successful recovery implies rebuilding fire-resistant structures, enhancing vegetation management practices, improving social support systems that minimize susceptibility, and confining future growth into wilderness areas (Schumann et al., 2020).

Ecological rehabilitation following wildfires generally focuses on both the direct and indirect effects of the fire. Wildfires are an inherent process within the ecosystems, and as a result, some individual incidents can be beneficial to the ecosystem. Yet, long-term shifts in fire regimes put significant stress on ecological and evolutionary processes and patterns (Meyer et al., 2021). Wildfires generally affect the biological ((micro-organisms, biota activities, and soil invertebrates) and physio-chemical properties of soils (i.e. soil water repellency, aggregate stability, bulk density, and texture). Yet, these effects are highly correlated with the intensity, duration, and frequency of the fire. Hence, the effects of low-intensity prescribed fires and high-intensity wildfires on soil characteristics could be significantly different (Agbeshie et al., 2022). For example,

some studies such as (Hubbert et al., 2012; Weninger et al., 2019) have reported an increased water repellency (decreased infiltration) of soils after wildfires, which would result in increased runoff. The amount of sediment yield to the downstream basins is also highly affected by wildfires, with the peak value occurring in the first year following the wildfire. However, the sediment yield decreases as the vegetation recovers (Hubbert et al., 2012). Surface runoff then carries leftovers and ashes from burnt areas and deposits them in surface waterways, and degrades the quality of surface waters such as rivers and lakes by significantly increasing the concentration of pollutants such as heavy metals (Raoelison et al., 2023).

The goal of forest and landscape restoration is to restore ecological functionality and improve human well-being throughout damaged environments (Food et al., 2019). A variety of different strategies, such as unassisted recovery, the removal of succession obstacles (such as fire, competition, and erosion), restoring plant species, and the creation of commercial plantations or agroforestry systems could be utilized for this purpose (Food et al., 2019; Scheper et al., 2021). Natural regeneration is highly dependent on the forest's capacity to recover independently (Scheper et al., 2021), yet it is highly dependent on the natural capacity of the forest independent restoration and parameters such as the fire intensity and mean annual rainfall (Volkova et al., 2019). Standing plants, as well as soil layers storing seeds, can be burned by intense fires. Such fires can substantially impede the recovery process as propagule availability is necessary for a successful natural regeneration (Holl et al., 2000; Scheper et al., 2021). An assisted natural regeneration strategy, however, could be utilized under unfavorable conditions such as destroyed seed banks or frequent fire incidents (Scheper et al., 2021). An assisted natural regeneration strategy, hence, tries to promote natural regeneration through lowering biophysical obstacles to succession (Shono et al., 2007). It hence comprises relatively straightforward, affordable procedures like weed management and the development of firebreaks as well as more sophisticated and expensive ones like erosion control, topsoil replacement, hydrological restoration, and enrichment planting either through direct seeding or planting nursery-grown seedlings (Scheper et al., 2021). Commercial restoration, which includes plantation forests and agroforestry, is another strategy that accounts for a significant portion of restored forests that offers more immediate socioeconomic advantages but less ecological value compared to natural restoration strategies (Scheper et al., 2021). In artificial regeneration, accurately selecting the best strategies and the right tree species are crucial to ensure seedlings' early establishment and growth. Generally, two techniques could be utilized in order to plant tree seedlings, including (i) direct seeding, and the more reliable method of (ii) transplanting nursery-produced tree seedlings (Stelzer, 2019).

It is obvious that the adoption of strategies and post-fire recovery planning requires accurate and timely information on the amount and severity of losses caused by the fire incident, as well as the information regarding the natural potential of the environment to recover. For example, despite burning less frequently than dry forests, humid tropical forests are more susceptible to the impacts of fire and recover slower than forests with a longer fire history (Scheper et al., 2021). The extent and severity of the fire

and its ecological consequences on the ecosystem could be identified by locating the affected areas (Yilmaz et al., 2023). When deciding what immediate actions should be done after a fire, burn severity (BS) maps that represent changes in plant and forest soil properties (García-Llamas et al., 2019; Yilmaz et al., 2023) and burnt area (BA) maps (Chuvieco et al., 2019) have a high priority. Different techniques Historically, government organizations gathered BA data based on reports from fire management crews and ground estimations. Yet, with the launch of the first Landsat satellite in 1972, many researchers started using satellite imagery as a reliable method for burn area detection and mapping, which mainly relies on the difference between the level of spectral reflectance between pre-fire and post-fire conditions (Chuvieco et al., 2019). With the current developments in sensors and processing technologies, three main types of sensors are used in the burn area and burn severity mapping, including (i) optical sensors/cameras, including the visible light cameras (RGB), near-infrared (NIR), shortwave infrared (SWIR), middle infrared (MIR) and thermal domain, (ii) synthetic aperture radar (SAR) systems which transmit microwave impulses and are specially used for tropical and cloud covered areas, and (iii) Lidar sensors. However, recent research and products mainly utilize a combination of the available methods and sensors (Chuvieco et al., 2019).

2.5 Unmanned Aerial Vehicles in Wildfire Emergency Response

Unmanned Aerial Vehicles (UAV) generally imply a flying robot that is not controlled by a human pilot. Hence, control functions of the UAV must be performed automatically, either on-board or off-board. For some years, the term UAV, or unmanned aerial vehicle, has been used to designate unmanned aerial systems. (Dalamagkidis, 2015b). Later, the United States Department of Defence (DOD), the Federal Aviation Administration (FAA), and the European Aviation Safety Agency (EASA) came up with the new term Unmanned Aircraft System (UAS), which is used to imply the UAV and its airworthiness, and other components of the system including ground control stations, communications, and the launch and retrieval systems (Dalamagkidis, 2015b).

2.5.1 Terminology and classifications

Generally, different metrics such as mean take-off weight (MTOW), size, capabilities, or combinations of these metrics (Dalamagkidis, 2015a) could be used to classify UAVs, yet other factors, including engine type, endurance, speed, and production costs are also considered in some classifications (Hassanalain & Abdelkefi, 2017). The most widespread and contradictory classifications, however, are based on the UAV weight. (Brooke-Holland, 2012) classified the UAVs based on their weight into 6 classes of Nano ($W \leq 0.2\text{kg}$), Micro ($0.2 < W \leq 2\text{ kg}$), Mini ($2 < W \leq 20\text{ kg}$), Small ($20 < W \leq 150\text{ kg}$), Tactical ($0.2 < W \leq 2\text{ kg}$, and MALE/HALE/strike drones ($W \geq 600\text{ kg}$). Another

Table 2.1: UAV classification based on Airspace class of operation (Dalamagkidis, 2015a; Dalamagkidis et al., 2012)

Class	Airspace Class	Sense and Avoid System (S&A)	Transponder	two-way ATC communication
VLA/LOS*	Class G	Not required	Not required	Not required
VLA/BLOS**	Class G	required	required	Not required
MA***	Class A-E	required	required	required
VHA****	Above F1600	required	required	required

*very low altitude /line of sight

**very low altitude /beyond line of sight

***medium altitude

****very high altitude

classification by (Weibel & Hansman, 2004) suggests five categories of micro ($W \leq 2$ lbs), Mini ($2 \text{ lbs} < W \leq 30 \text{ lbs}$), Tactical ($30 \text{ lbs} < W \leq 1000 \text{ lbs}$), Medium and high altitude ($1000 \text{ lbs} < W < 30000 \text{ lbs}$), and heavy ($30000 \leq W$). Another important aspect of UAV specifications includes the UAVs' Operational Altitude and Control requirements. The proposed classification of UAVs based on the airspace class is presented in Table 2.1. Note that the G and FL600 airspaces normally denote altitudes below 500ft and above 30,000 ft, respectively.

In terms of mission capabilities, UAVs could be categorized into (i) horizontal take-off landing (HTOL), (ii) vertical take-off landing (VTOL), (iii) hybrid models, (iv) heli-wing, and (v) unconventional models (Hassanalian & Abdelkefi, 2017). VTOL systems have the advantage of vertical take-off as well as hovering over the desired location, which comes at the cost of reduced endurance and cruise speed of these UAVs. On the other hand, HTOL has higher cruise speed and flight time, which are valuable when long-range missions and monitoring of remote areas are of interest. Due to these limitations and advantages, different types of hybrid drones are developed to address different operational requirements (Hassanalian & Abdelkefi, 2017).

The United State's National Institute of Standards and Technology (NIST) defines autonomy to be the condition of being self-governing. Being autonomous makes it feasible for a drone to sense, perceive, analyze, communicate, plan, make a decision, and act in order to reach the desired goal of the system. The level of autonomy is determined by criteria such as mission complexity, environmental challenge, and the level of human-robot interaction required to complete the missions. (Huang, 2004). Based on the level of human-robot interaction in the system, a system could be categorized into four levels of autonomy: (i) fully autonomous, (ii) semi-autonomous, (iii) teleoperation, and (iv) remote control. A fully autonomous mode of operation is the state wherein the unmanned system is expected to carry on the desired mission without any human intervention. In contrast, a semi-autonomous system is expected to plan and accomplish the target while specific tasks are carried out through different levels of human-robot interaction. Teleoperation is the state of control wherein the human operator uses video or data feedback to control and assign tasks to the system components directly. Finally, a remote control system is established when the human operator directly controls the actuators of the UAV continuously (Huang, 2004).

2.5.2 UAVs in pre-fire stage

Aerial monitoring systems offer unrivalled advantages to address the shortcomings of land-based and satellite systems, mainly due to their high manoeuvrability as well as different designs, which makes them appropriate for different tasks in the context of wildfire monitoring and management (Akhroufi et al., 2021). They can carry different sensors, fly autonomously, and participate in different tasks. Normally, UAV utilization in the pre-fire emergency response phase encompasses monitoring flights for geographical terrain data collection, vegetation detection and classification, fuel load estimations, and Fire risk assessment. Different types of UAVs and Sensors, such as multispectral cameras and LIDARs, are used for these purposes in different studies (Keerthinathan et al., 2023). Generally, machine learning (ML) or deep learning (DL) techniques are used to classify the vegetation in UAV-based multi-spectral images or data points. For example, (Kattenborn et al., 2019) utilized DL models for detailed classification of plant communities and species based on high-resolution RGB imagery from UAVs. In another study, (Hillman et al., 2021) investigated the efficiency of UAV-based LiDAR and photogrammetric techniques for characterizing forest structure, which is essentially important in the estimation of wildfire behaviour. Their results show that UAS LiDAR successfully captures information on canopy cover and sub-canopy layers, providing comparable estimates to terrestrial LiDAR (TLS).

2.5.3 UAVs in amidst-fire phase

The current state of UAV utilization in the amidst-fire stage mainly focuses on fire detection and monitoring, yet fewer studies have considered fire suppression activities. Various spectral and atmospheric measurement sensors onboard UAVs are used in different studies for fire detection and propagation monitoring. Atmospheric sensors offer numerical data on environmental factors such as temperature and humidity and enable straightforward analysis using statistical and AI techniques. They can also process data onboard without a constant wireless connection to a central system. However, they can be inaccurate due to external disturbances (Keerthinathan et al., 2023). Spectral sensors such as RGB, thermal, and Infrared cameras are also extensively used for fire detection and monitoring purposes with UAVs (Akhroufi et al., 2021; Keerthinathan et al., 2023). For example, (Georgiev et al., 2020) introduced an autonomous early fire detection system using a convolutional neural network for object detection. It employs live video feed from a UAV patrolling high-risk areas, incorporating optical and thermal cameras for improved fire probability predictions. The software platform autonomously processes data from both cameras, filters false positives, maintains a gallery of patrol images, and provides real-time UAV location on a map. However, it should be highlighted that implementing DL algorithms on board UAVs is not straightforward due to the limited computational capacity of onboard processors. Consequently, some studies have proposed lightweight models that could be executed in real-time onboard the UAV for wildfire detection (i.e., see (Fouda et al.,

2022)). Some studies have also proposed using UAV swarms for wildfire detection and monitoring. Comparing the performance of four algorithms, including Random walk (RW), random walk with dispersion (RWDP), pheromone avoidance (PHA), and dynamic space partition (DSP), (Tzoumas et al., 2023) explored the use of UAV swarms with long endurance for early wildfire detection in large areas. Considering an area as large as California, the DSP proves to be the most effective, detecting 82% of fires with just 20 UAVs and achieving 100% coverage with 40 or more UAVs. The system also exhibited robustness in the face of agent failures and new fire outbreaks. (Karvonen et al., 2023) proposed a concept of operation for a semi-autonomous swarm of UAVs to support wildfire management and fighting through providing real-time fire detection and fire front monitoring. Another study performed by (Viseras et al., 2021) addresses the need for real-time wildfire monitoring using a cooperative reinforcement learning (RL) framework with autonomous UAVs. The framework extends previous methods by proposing two approaches: Multiple Single-Trained Q-learning Agents (MSTA) and Value Decomposition Networks (VDN). Results demonstrate that MSTa and VDN outperform the existing methods, with VDN excelling in complex fire scenarios requiring inter-UAV coordination. MSTa shows stability and scalability for larger UAV teams, while VDN exhibits higher learning complexity.

In addition to monitoring wildfires, some research have proposed frameworks for firefighting UAV systems with different levels of autonomy and functionality (e.g., see (Ausonio et al., 2021; Bhat et al., 2021; Gayathri et al., 2022; Viegas et al., 2022)). For example, (Peña et al., 2022) proposed a firefighting UAV called WILD HOPPER capable of suppressing fires by discharging its payload of up to 600 litres. As another innovative solution (Bhat et al., 2021) proposed a hexacopter framework capable of carrying and dropping fire extinguishing balls on the fire front. Apart from designing Firefighting UAVs, some studies have focused on the concept of UAV swarms of firefighting drones. Coupling a physics-based fire propagation model and a self-organization swarm intelligence algorithm, (Innocente & Grasso, 2019b) proposed a swarm of collaborative firefighting UAVs for autonomous fire suppression. (Ausonio et al., 2021) proposed a conceptual UAV-based framework that utilizes a swarm of hundreds of UAVs to extinguish the firefront in forest fires. Their proposed system ensures uninterrupted firefighting through automatic battery replacement and liquid refill. The research estimates the system's effectiveness by calculating the critical water flow rate based on various factors influencing fire behaviour and the number of meters of active fire front that can be extinguished depending on the drones and extinguishing fluid available. Another strategy for fighting fires with UAVs is dropping fireballs to ignite prescribed fires. A recent study performed by (Lawrence et al., 2023) evaluated the incorporation of Small Unmanned Aerial Systems (UAS) for aerial ignition in prescribed fire and wildland fire programs. A comparison is made between UAS and non-UAS burns, analyzing data from 2012 to 2021, which includes 58 UAS burns conducted from 2019 to 2021, with a focus on post-burn assessment data. The results show that UAS burns from 2019 to 2021 were 129% more efficient than non-UAS burns.

2.5.4 UAVs in post-fire phase

UAVs could generally be utilized in different aspects of the post-disaster recovery phase, including community aid, infrastructure surveillance and assessment, and environment recovery. In terms of community aid, even though UAVs are unlikely to replace conventional vehicles, different initiatives and programs are still exploring the viability of the use of UAVs in order to deliver critical humanitarian aid in a timely manner to the communities affected by disasters. These innovations and explorations include delivering vaccines or critical medical aid to affected individuals or communities, and establishing a network for emergency communications (World Food Programme (WFP), [n.d.](#)) when equipped with proper devices. In addition to that, UAVs could also be used to deliver food and water, lighting devices, and communication devices such as radios to communities and individuals affected by natural disasters (Estrada & Ndoma, [2019](#)). So far, various heavy lift or cargo delivery platforms have been developed by different companies, among which FlyingBasket's FB3 (FlyingBasket, [2023](#)) and Airbus's multi-mission cargo copter (Airbus, [n.d.](#)) delivery UAV can be mentioned. For example, the coaxial multi-rotor FB3 has a flight time of 9 minutes while carrying a payload of 75 kg at a cruise speed of 12m/s (FlyingBasket, [2023](#)), which makes it a potential candidate for carrying out post-wildfire or even amidst-fire delivery or participating fighting activities. Additionally, Airbus is creating a heavy-lift unmanned aerial vehicle (UAV) that can travel 300 km while carrying up to 250 kg (Airbus, [n.d.](#)) that is initially going to be developed for military purposes but has many potential applications in disaster management activities.

The idea of using Unmanned devices for aerial photography of disaster sites goes back to the early 20th century when George Lawrence built his large-format cameras and used a series of unmanned kites to fly his camera and obtain aerial views. Utilizing this technique, he was able to document the amount of destruction caused by the great San Francisco earthquake that was followed by the largest fire in the nation's history to that date, which lasted for three days and destroyed approximately four square miles of the city and killed nearly 3400 people (Library of Congress, [Year of Access](#)). Since then, damage mapping has remained a challenging problem despite numerous efforts and developments. It has seen the use of various sensors on airborne platforms, from tethered to autonomous and even satellites in various configurations, all aiming for more automated damage detection (Kerle et al., [2020](#)). In this context, UAV-based sensing of the site could be utilized for mapping damages within the interior spaces from a small building scale (Ali et al., [2021](#)) up to the landscape scale disaster damage assessment (Kakooei & Baleghi, [2017](#)). Aerial mapping and leak detection in oil and gas pipelines (Korlapati et al., [2022](#)) and district heating systems (Hossain et al., [2020](#)) are also becoming increasingly popular in the research community.

Environment recovery through afforestation and reforestation by tree planting is normally utilized for different purposes, including reducing soil erosion and runoff, reducing the likelihood of zoonotic disease outbreaks, offering ecosystem services to indigenous people, and conserving carbon dioxide (Mohan et al., [2021](#)). Robins et al.,,

(Robinson et al., 2022) suggest that UAVs could be used in planning, implementing, and monitoring the restoration of the environment. For example, UAVs could be used for Burnt area (Qurratulain et al., 2023; Ribeiro et al., 2023) and Burn severity mapping (Hillman et al., 2021), vegetation mapping (Hamilton et al., 2020; Sierra-Escrigas et al., 2020), plant water stress (Lacerda et al., 2022) or health assessment (Chin et al., 2023), water resources quality monitoring and sampling (R. Zhang et al., 2023), and wildlife tracking and census (A. Chen et al., 2023) during restoration planning (Robinson et al., 2022). UAVs are extensively used for forest recovery and monitoring purposes (Andrio, 2019; Guerra-Hernández et al., 2021; Salamí et al., 2014; J. Zhang et al., 2016); however, such systems need to be supported by proper decision-making systems and procedures as they require a vast amount of information regarding topography, vegetation coverage, and soil quality to decide the optimal location and specific species. The seed dispersal operation is then planned and executed based on the information gathered and the decisions resolved (Mohan et al., 2021). In general, aerial seeding for reforestation dates back to the middle of the 20th century. For instance, helicopters and fixed-wing aircraft were used to perform aerial direct seeding, which made up 50% of Canadian reforestation practices. Yet, the general seedling establishment rates are typically around 20%, which is considered low even though this is a quick and flexible option, especially for remote and difficult-to-reach or inaccessible terrains (Grossnickle & Ivetić, 2017). Consequently, a high-volume seed-firing from drones might not be an efficient solution. Rather, drones have the advantage of increasing success rates by accurately delivering seeds to areas where the establishment is most likely to occur. This can be done by scattering the seeds in predetermined areas (such as predetermined microhabitats) where the likelihood of seedling establishment is increased. Besides, it has the advantage of being considerably cheaper (up to 80%), much quicker (up to 25x (AirSeed Technologies, 2023)), more efficient, and in larger areas compared to human workers without exerting risk to humans (castro2021). Besides, such systems are scalable and could be utilized in the form of swarms, which could cover vast amounts of areas simultaneously.

In order to maximise the chances of success for seedling establishment, different innovative approaches are developed. For example, the US-based company Mast (Mast reforestation, 2023) has developed resistant seedlings with more robust root structures and greater root fibrosity with the intention of being used in nutrient deficit harsh post-fire environments. Seedpods, which contain the determined species of tree seed, water-retention agents, helpful bacteria and fungus, minerals and nutrients, and a conditioner for a healthy growing medium to maximise chances of successful establishment, is another innovation that is developed by different startups, such as the Australian AirSeed (AirSeed Technologies, 2023), and the Canadian FlashForest (Flash Forest, 2023) startups. These seedpods are scattered or fired toward the soil by high-pressure air systems (Grossnickle & Ivetić, 2017; Mohan et al., 2021) at a rate of up to 40000 pods per day. However, as each species has particular needs for collecting and storage, the supply of seed is a key constraint on seed pod production (Mohan et al., 2021). The post-planting monitoring phase starts immediately after seedlings have developed

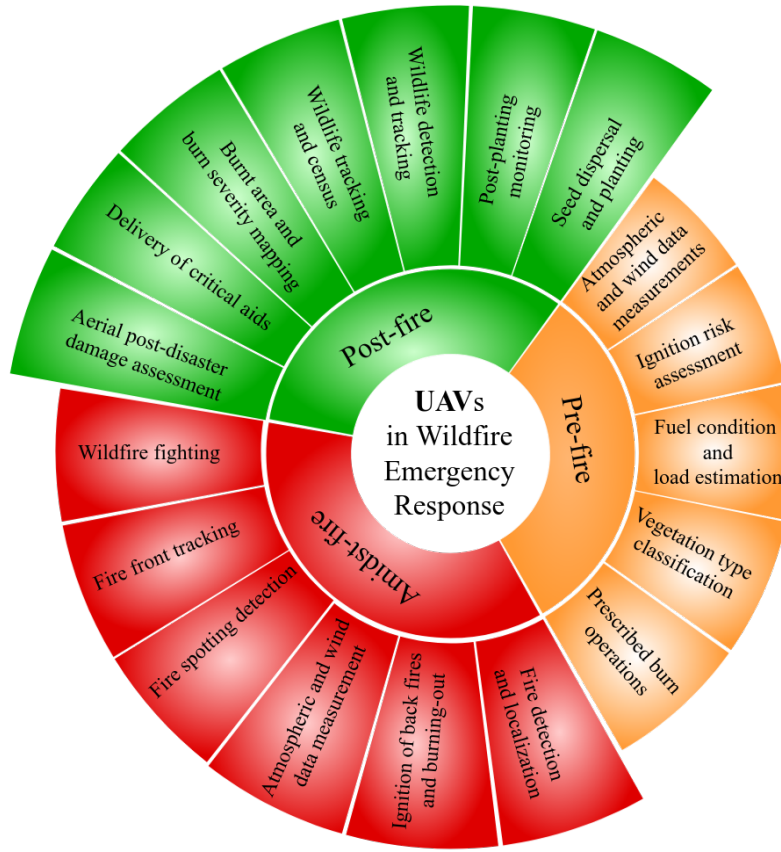


Figure 2.10: UAVs in different phases of wildfire emergency response (Tavakol Sadrabadi et al., 2024).

roots in the soil, where UAVs could be used for health and growth monitoring, as well as delivering water and nutrients to the seedlings (Mohan et al., 2021). For example, the Chinese company DJI (DJI, 2023) has developed different UAV models, such as the AGRAS T40 with a carry-on load of up to 50 kg, for agricultural purposes, including spraying water or fertilizers.

Figure 2.10 visualizes the general overview of UAV utilization in different phases of wildfire emergency response. Note that the majority of the mentioned tasks are either in the research phase or casual utilization.

2.6 Wind Measurements and Downscaling

The importance of the wind measurements lies in the synoptic structure of the atmosphere and the fire-atmosphere interaction. Considering that the wind field is heavily affected by the fire plume dynamics, and the wind reciprocally affects the rate of spread of fire (see (Potter, 2012b)), it would be ultimately useful to measure wind characteristics at different stages of fire. As mentioned in the previous section, even though UAVs

are less suitable for prolonged measurements due to the limitations that contribute to the limited flight time, they have mobility in three dimensions, which makes them flexible and cost-affordable instruments for providing spatiotemporal measurements of the desired variables such as the atmospheric wind (Thielicke et al., 2021). As a result, and due to their advantages over other options available such as wind LIDARs, balloons, and wind measurement towers, an increased number of studies have focused on the use of UAVs for wind field measurement tasks (e.g. (see Sasaki et al., 2021; Vasiljević et al., 2020)). Generally, both fixed-wing and rotary-wing UAVs could be used for atmospheric wind measurements, with fixed-wing UAVs more suited to measurement tasks that cover large areas and rotary-wing UAVs mostly suitable for measurements that need hovering on a spot for long periods such as validating wind measurements and in the proximity of the structures (Thielicke et al., 2021). Wind measurements using drones could be performed through the use of external wind sensors or onboard sensors of the avionic system of the UAV (Wetz et al., 2021). The idea of performing coordinated wind measurement with a group of UAVs was presented first by (Prudden et al., 2018) yet the first actual implementation of such a system in the field is performed by (Wetz et al., 2021) that utilizes a group of quadrotors hovering for a long period at certain locations, to provide spatiotemporal wind measurements.

However, it should be highlighted that it is the near-surface wind field that actually controls the instant fire behaviour and hence is of interest for wildfire propagation estimations. Still, accurately representing the wind field around a wildfire is highly computationally expensive, especially at large scales where utilising numerical weather prediction (NWP) models becomes inevitable. These models, however, have severe memory and performance requirements that restrict the availability of fine-scale (high-resolution) forecasts (Höhlein et al., 2020). Consequently, coarse-scale weather service models have often been employed in wildland fire decision support systems, where a domain-averaged wind field—often implied as uniform wind field—may be constructed from the outputs of these models and used as input to fire models (Forthofer et al., 2014).

To address this shortcoming, a series of downscaling techniques are developed to extract higher-resolution wind components from low-resolution NWP simulations. Downscaling is generally a method for avoiding expensive high-resolution simulations across large geographic scales by inferring information on physical characteristics at the local scale from freely accessible low-resolution simulation data using appropriate refinement techniques (Höhlein et al., 2020). *Dynamic* and *empirical-statistical* approaches are two major categories into which these techniques may be classified (Hewitson & Crane, 1996). Dynamic Wind downscaling models are physics-based models that solve a series of governing equations of the fluid and can be classified into two broad groups including (i) *prognostic* and (ii) *diagnostic* models. Prognostic models, such as those employed in numerical weather forecasting, solve mass, momentum, energy, and moisture conservation equations and advance in time. They often include detailed methods for the dynamics of boundary layers, land-atmosphere interactions, radiation, thermodynamics, and cloud processes. Due to the addition of physical processes, prognostic

model weather predictions demand a substantial amount of computational power, have complicated beginning and boundary conditions, and require highly skilled personnel to operate (Forthofer et al., 2014; Homicz, 2002). Diagnostic or steady-state models, on the other hand, are used to forecast the wind field at a certain point in time. The result may be used to depict winds over a period of time that is either quasi-steady or time-averaged. To account for the effects of terrain on an initial flow field obtained from point measurements or a coarse-scale weather model, diagnostic models employ mass, momentum, and energy conservation alone or in combination to account for terrain effects on an initial flow field obtained from point measurements or a coarse-scale weather model. Diagnostic models often have much lower processing needs than prognostic models due to the absence of time stepping. Diagnostic models are often employed in disaster response systems that demand rapid calculation times and are performed by casual users with minimal computer resources (Forthofer et al., 2014). Consequently, due to transient and thermal influences, diagnostic models are unable to mimic boundary layer evolution.

(Forthofer et al., 2014) examined the accuracy of three approaches for simulating high-resolution surface winds: (i) a uniform wind field, (ii) wind downscaling using a mass-conserving CFD model, and (iii) wind field simulation with a mass-momentum conserving CFD model (FLUENT). Results indicated that both CFD methods significantly improved accuracy compared to the uniform wind field. It was concluded that the error of the momentum conserving model compared to the measured values was among 10 to 32% with the lowest accuracy observed on the lee side of the hills which is the most difficult area to be simulated. Besides, the results of the mass-conserving model were between 0.3 to 3 times the measured values, indicating significant errors compared with measurements. Yet, the simulation time is significantly shorter than that of mass-momentum conserving models which makes them suitable for operational use. (Wagenbrenner et al., 2016) examined the capability of a mass-conserving diagnostic CFD model, titled WindNinja, to downscale surface wind predictions from four different mesoscale weather prediction models: Weather Research and Forecasting Reanalysis (WRF-NARR), High-Resolution Rapid Refresh (HRRR), Routine Weather Research and Forecasting (WRF-UW), and North American Mesoscale Model (NAM). Their results indicated that wind projections for all NWP models increased significantly when downscaled using WindNinja. The most significant gains occurred during high-wind situations (close to neutral atmospheric stability), when recorded wind speeds exceeded 10 m.s^{-1} . Besides, WindNinja could not forecast the observed recirculation of lee-side flow at BSB during externally induced high wind occurrences. This is largely owing to the WindNinja flow solution's absence of a momentum equation. This study illustrates how dynamic downscaling using a mass-conserving wind model may enhance NWP model wind predictions in difficult terrain, particularly during high-wind occurrences. These enhancements could result in more accurate predictions from additional model applications that are sensitive to surface wind fields, such as wildfire behaviour, local-scale transport and dispersion, and wind energy applications.

As an alternative, *statistical* downscaling utilizes predictor data from a large-scale

simulation to derive predictions at the smaller sizes (referred to as predictand data). Statistical models are trained on a given set of predictor–predictand data pairs to discover the fine and coarse correlations between the measured quantities (Höhlein et al., 2020). So far, different statistical downscaling methods have been developed (Abatzoglou & Brown, 2012; Rios et al., 2018) yet, with the recent advancements in machine learning (ML) and deep learning (DL) methods, different studies have focused on the use of the state-of-the-art DL algorithms and methods for this purpose (see Dujardin & Lehning, 2022; J. Zhang & Zhao, 2021). In particular, Convolutional Neural networks (CNN) and single image super-resolution (SR) tasks (see Cheng et al., 2020; Stengel et al., 2020) have proven to be effective in this manner due to their capabilities in learning multidimensional mappings, especially for spatially distributed data and generation of high-resolution data from low-resolution inputs (Höhlein et al., 2020). For instance, (Dujardin & Lehning, 2022) developed a multi-dimensional deep learning model called Wind-Topo to estimate the high-resolution wind field from large-scale estimations over the complex topography of Switzerland. They combined the low-resolution wind and topography data available from Intercantonal Measuring and Information System (IMIS) with high-resolution digital elevation models (DEM) to translate wind velocity components from a $1113 \times 1113 \text{ m}^2$ grid to $50 \times 50 \text{ m}^2$ grids. Le Toumelin et al., 2024 developed a deep learning model to correct and downscale the wind field from 1300 m to 30 m. The model consists of two fully connected neural networks for correcting wind speed and directions prior to feeding the corrected data to a convolutional neural network which is responsible for improving the resolution of estimations. They also developed two custom loss functions for training the fully connected neural networks to improve the wind speed and direction corrections.

This super-resolution procedure is however generally referred to as flow field reconstruction within the context of flow mechanics literature. An example would be to interpret a low-resolution fluid flow image (data matrix) as a collection of sparse sensor measurements. Utilising such an approach, super-resolution analysis could be extended to address the inverse problem of reconstructing global fields from local observations (Fukami et al., 2023). Different studies have utilised various deep-learning models for flow field reconstruction purposes. Examples include convolutional neural networks mostly with UNet structures (i.e. see Fukami et al., 2019; J. Zhang et al., 2023), artificial neural networks with autoencoder architectures (Dubois et al., 2022), and physics-informed frameworks (L. Wang et al., 2024; J. Zhang & Zhao, 2021).

2.7 Artificial Intelligence and Wildfire Science

With the recent advancements in AI capabilities, the application of different algorithms and methods in wildfire science and management has sharply increased. This section, however, does not intend to perform a comprehensive review of the applications of AI in wildfire science and management, rather it is dedicated to highlighting key aspects. Jain et al., 2020 classified the available literature on the applications of AI in wild-

fire science and management in six groups including (i) fire occurrence, susceptibility, and risk, (ii) fuels characterization, fire detection, and mapping, (iii) fire behaviour prediction, (iv) fire effects prediction, (v) fire weather and climate change, and (vi) fire management. Their review also indicated that the fire occurrence, susceptibility, and risk group has received the highest attention among others. They also indicated that the majority of studies performed before 2018, mostly utilize classical machine learning models such as random forests (RF), support vector machines (SVM), etc. However, a boost in the utilization of neural networks could be observed after 2019. Even though their study only considered published work before 2019, with the current trend in developing advanced deep learning models, it could be concluded that the same trend might still be valid and the majority of recent studies focus on advanced deep learning (DL) or even reinforcement learning (RL) models nowadays.

Vegetation or fuel characterization is one of the applications of AI in wildfire management that has received a substantial amount of interest within the past years. This is mostly because an accurate fuel classification and distribution throughout the landscape is necessary for making meaningful predictions of fire behaviour and propagation (Arroyo et al., 2008; Kim et al., 2009). Therefore, quick and precise mapping of vegetation type and land cover is essential to enable fire propagation prediction models, particularly those that are intended for faster or real-time simulations (Grasso & Innocente, 2020b). A variety of emergency management initiatives, such as evacuation, suppression, and prevention, can be aided by this knowledge (Ausonio et al., 2021; Campbell et al., 2019; Innocente & Grasso, 2019c; Martell, 2015). Research to characterise vegetation is generally concerned with (Tavakol Sadrabadi & Innocente, 2023):

1. *Capturing unique structural characteristics*, including height, single-tree biomass, branching structure, canopy volume, and diameter at breast height (DBH) (e.g. (Kato et al., 2009)).
2. *Estimating vegetation properties over a landscape* (metrics) including canopy biomass, canopy fuel load (CFL), moisture content, canopy base height (CBH), and canopy bulk density (CBD) (e.g. (Engelstad et al., 2019; Marino et al., 2022; Rao et al., 2020; Yebra et al., 2018)).

While certain structural traits are predicted using variables that are easier to measure, others are obtained directly, for example, through conventional field measurements. For instance, allometric equations are typically used to estimate single-tree biomass from tree data (Vorster et al., 2020). Traditional approaches can provide accurate measurements and biomass and cover estimations, but they necessitate difficult and time-consuming fieldwork to gather data in a highly localised way (not easily scalable) (Anderson et al., 2018; Hartley et al., 2022). On the other hand, three-dimensional point clouds produced by (terrestrial or aerial) laser scans are perfect for collecting the structural properties of trees via tree segmentation, while effective crown data acquired via laser scans can be used to estimate single-tree biomass (Zheng et al., 2019). It is helpful to both *characterise the fuel* and *classify the fuel type* (Hartley et

al., 2022) since the type of fuel has a significant impact on fire behaviour (Chuvieco et al., 2003; Tavakol Sadrabadi & Innocente, 2023). Anderson et al., 2018 mentions that laser scan point clouds and machine learning (ML) or deep learning (DL) techniques are the mainstays of current research on fuel characterisation and fuel type categorisation for both regression and classification problems. Y. Li et al., 2019 used three distinct machine learning algorithms—emphLinear Regression (LR), *Random Forest* (RF), and *Extreme Gradient Boosting* (XGB)—to examine the impact of variable selection. Their findings suggest that variable selection, particularly for the XGB technique, can greatly increase the accuracy of all models. Luo et al., 2021 estimated the above-ground biomass in forests using RF, XGB, and *Category Boosting* (CatB) regression models in conjunction with feature selection techniques. According to their findings, feature selection has a major impact on model accuracy, and *Recursive Feature Elimination* (RFE) and CatB work together to greatly outperform other models (Tavakol Sadrabadi & Innocente, 2023). In an early research, (Blackard & Dean, 1999) evaluated the prediction accuracy of forest cover types from cartographic variables using a *Feed-Forward Neural Network* (FFNN) model and the *Gaussian Discriminant Analysis* (GDA) method. With a huge dataset, FFNN yielded an accuracy of 70.5%, but GDA only managed 50.4%. Achieving an overall accuracy of 97.01%, (Macmichael & Si, 2017) outperformed all other models by a significant margin. Together with *Principle Component Analysis* (PCA) for feature selection, *k*-fold cross-validation, and model parameter optimisation, they employed an FFNN with five hidden layers. In a recent study, (Sjöqvist et al., 2020) implemented three classifiers, namely RF, *Naïve Bayes* (NB), and *Support Vector Machine* (SVM), integrated with PCA for the classification of different cover types from cartographic variables using the University of California Irvine (UCI) cover type dataset. The combination of RF with PCA achieved an overall accuracy of 94.7%, with class-wise accuracy of 93.7%, 96.7%, 95%, 77.9%, 77%, 86%, and 94.5% for Class 1 through Class 7, respectively. Comparing the results in Sameer et al., 2021 to those in Kumar and Sinha, 2020, it could be concluded that an RF model with automated hyperparameter tuning outperforms XGB with feature selection. This implies finding the optimal values of the hyperparameters might have superior effects compared to implementing feature selection methods (Tavakol Sadrabadi & Innocente, 2023).

Another important domain of research focuses on estimating the rate of spread of fire and wildfire propagation modelling utilizing AI algorithms. For instance, (Rubí et al., 2023) compared the accuracy of classical machine learning models in predicting the wildfire spread in Brazil’s Federal District, a region within the Cerrado biome that has frequent fire occurrences yet limited research. They compiled a dataset using governmental sources, by incorporating climate observation data, satellite data, and topographic, hydrographic and anthropogenic features. trying to predict the wildfire area, their examinations indicated that the AdaBoost model achieved the highest predictive accuracy at 91%, outperforming Random Forest (88%), Artificial Neural Network (86%), and Support Vector Machine (81%). Burge et al., 2023 evaluated the effectiveness of the effectiveness of deep learning models for time-resolved wildfire spread

prediction. They developed a convolutional recurrent deep learning model using an autoregressive process to simulate wildfire propagation in 15-minute increments. evaluating the model performance over 4 distinct datasets, their model estimations proved to be physically consistent and realistic achieving high accuracy with a Jaccard score between 0.89 and 0.94 in predicting fire scars. To address the challenge of monitoring vast and remote forest territories, (Shadrin et al., 2024) focused on large-scale wildfire prediction using remote sensing data. Utilizing a multi-scale attention-based network to predict wildfire propagation over a 5-day timeframe, the authors found that wind direction and land cover parameters were the most significant factors in predicting fire behaviour. The model achieved an F1-score between 0.64 and 0.68 depending on the day forecast timeframe and showed promise for adaptation in other regions.

2.8 Uncertainty estimation for flow field reconstruction

Deep learning and machine learning models are frequently used for various types of inference and decision-making procedures. However, assessing the effectiveness and reliability of these AI systems before deploying and utilising them is crucial as these models are susceptible to noise in data (aleatoric uncertainty) and model errors (epistemic uncertainty). Nowadays, uncertainty quantification (UQ) forms the basis of many important decisions; and predictions that lack UQ are typically unreliable Abdar et al., 2021. Generally, UQ methods could be categorised into two broad groups including (i) Bayesian methods and (ii) ensemble methods, where Bayesian methods encompass techniques such as the Markov chain Monte-Carlo (MCMC) algorithm, variation inference methods (VI), Monte-Carlo dropout (MCD), etc (Abdar et al., 2021). However, methods like Bayesian neural networks, MCMC, and the ensemble of models are heavily computationally intensive and time-consuming which limits their utilisation for large datasets and models (Abdar et al., 2021; Collins et al., 2023). As a result, the use of approximation techniques such as MCD Gal and Ghahramani, 2016 and Monte-Carlo batch normalisation (MCBN) (Teye et al., 2018) which could be used to estimate the epistemic uncertainty of a single trained model has gained traction.

Gal and Ghahramani, 2016 showed that an approximation to the probabilistic deep Gaussian process can be obtained mathematically by using a neural network with arbitrary depth and non-linearities, where dropout is applied before each weight layer. The dropout layer would then be active during model inference where an ensemble of estimations is output to act as the Monte Carlo samples to calculate the mean and variance of the prediction distribution (Collins et al., 2023; Teye et al., 2018). The Monte Carlo batch normalisation (MCBN) is another technique that could be used to approximate the Bayesian inference in neural networks (Teye et al., 2018). In this approach, many mini-batches are created by selecting random samples to go along with a particular query during inference. The predictive distribution is then estimated using the mean and variance of the ensemble of outputs (Collins et al., 2023).

2.9 Highlighting Research Gaps

Reviewing the literature the following research gaps could be highlighted:

1. Despite the flexibility, scalability and potential applications of UAVs, their utilisation in wildfire response systems is arbitrary and unstructured which prevents them from benefiting the full potential of UAVs.
2. A systematic evaluation of the effect of coupling strategy on the wildfire propagation dynamics and model estimation is missing in the literature.
3. Even though a series of solutions are proposed in the literature to address the accuracy limitations of decoupled models such as assimilation of fire front location into models, utilising mass-conserving wind models such as Wind Ninja, or even developing fully data-driven models for wildfire propagation estimation, yet these solutions fall short in establishing a direct and real-time connection of fire front and wind patterns.
4. Although some studies have focused on the combined effect of vegetation height and wind speed on wildfire propagation dynamics, a series of conflicting results are reported in the literature which keeps the door open to more research.

Chapter 3

Materials and Methods

This chapter presents the theoretical background as well as the calibration and validation procedures utilised for these models to be used in this thesis. Consequently, each section presents a brief description of the model, as well as the mathematical formulation and utilisation procedure. The following sections present a brief overview of the fire propagation models used for the simulations in this thesis.

3.1 Fire Dynamics Simulator

The Fire Dynamics Simulator (**FDS**) originally designed to simulate thermally-driven flows within buildings, numerically solves a variant of the Navier-Stokes (NS) equations suitable for low-speed, thermally-driven flow with a focus on smoke and heat transfer from fires, called the *Low-Mach* derivation of the Navier-Stokes equation. The main algorithm includes an explicit predictor-corrector method that is second-order accurate in space and time. Turbulence is modelled via Large Eddy Simulations (LES) with constant turbulent Schmidt and Prandtl numbers. A direct numerical simulation (DNS) method could be utilized instead, should the mesh be sufficiently fine. FDS employs a one-step, mixing-controlled chemical reaction with three bundled species for most applications: *products*, *fuel*, and *air*. Reactions that are not necessarily mixing-controlled and multiple reactions could also be considered under certain conditions. To approximate the governing equations and discretise the domain, a cartesian grid is used. It utilizes a simple immersed boundary method when dealing with flow obstructions (McGrattan et al., 2019).

As mentioned, the FDS utilizes the low Mach approximation of the NS equations. The Mach number (M) is equal to the ratio of flow velocity to the speed of sound ($M = u/C$). For low-speed flows where the energy of sound waves has negligible impact on the overall solution, using the fully compressible form of the Navier-Stokes equation is computationally inefficient. This inefficiency mainly arises from the requirement of tracking sound waves, which forces very small time steps for stability. For instance, when using an explicit time-discretization approach, the Courant-Friedrich-Levy (CFL)

criterion restricts the timestep size so that information can propagate only one grid cell per timestep. Hence, while this is not necessarily correct for implicit algorithms, considering the explicit formulation of the FDS which imposes a Courant number of $Cou = C \frac{\delta t}{\delta x} < CFL$ where $CFL=1$, it implies $\delta t \approx \frac{\delta x}{C}$ where c is the speed of sound, δx is the spatial grid resolution, and δt is the time step. Such a solution would be inherently slow and computationally expensive. A desirable solution for velocities well below the speed of sound, however, would have a $\delta t \approx \frac{\delta x}{|u|}$ so that the solution would require much fewer timesteps. To achieve such a filtered version of the NS equations for low-speed applications ($M < 0.3$)—where motion-related temperature and density variations are small—, (Rehm & Baum, 1978) suggested that the total pressure can be decomposed into a *background* or *thermodynamic* pressure $\bar{p}(z, t)$, and a *perturbation* or dynamic pressure, $\tilde{p}(x, y, z, t)$, where the perturbation would be eliminated from the equation of state (ideal gas law), so that (McGrattan et al., 2024):

$$\bar{p} = \rho T R \sum_a \frac{Z_a}{W_a} = \frac{\rho R T}{W} \quad (3.1)$$

where Z_α is the mass fraction of species α , W_α is the molecular weight of species α , z is the spatial coordinate in the direction of gravity, so the stratification of the atmosphere is accounted for within the background pressure (McGrattan et al., 2024), and W is the mean molecular weight of the mixture, defined as: $W = \left(\sum_\alpha \frac{Z_\alpha}{W_\alpha} \right)^{-1}$. By replacing the total pressure with the background pressure in continuity, energy and state equations, the final derivation would normally be incompressible against velocity and compressible against temperature. A complete derivation of the equations however is beyond the scope of this research and could be found in (McGrattan et al., 2024; Rehm & Baum, 1978).

FDS offers various models for the simulation of wildfire spread based on the desired level of physics required and the available computing resources: the Lagrangian Particle Model (LPM), the Boundary Fuel Model (BFM), and the Level-Set (LS) model. In this thesis, FDS 6.7.9 is used for the simulations.

3.1.1 Level-set model

This model is used for wildfires propagating across large areas, which cannot be discretised with a grid sufficiently fine for physics-based models. FDS with the Level Set model (**FDS-LS**) uses the same elliptical spread model used by FARSITE (Bova et al., 2016; Finney, 1998a), which is based on Huygens' principle for wave propagation modelling. It also adopts Rothermel-Albini's RoS formula and Albini's 13 fuel models (McGrattan et al., 2019). The meaning of the font colours of some variables will be explained towards the end of this section.

A series of parameters must be set to define a fuel in FDS-LS, including the no-wind no-slope rate of spread (RoS_0) for unburned fuel, the packing ratio (β), the surface area-to-volume ratio (σ), and the fuel height (h) (Tavakol Sadrabadi & Innocente,

2024). These settings are used to calculate the mid-flame wind velocity (\mathbf{u}_{mf}) and the wind and slope coefficients ($\boldsymbol{\phi}_w$ and $\boldsymbol{\phi}_s$, respectively). Since wind and slope are generally not aligned with each other or with the direction of the fire spread, they are both coefficient vectors: (Andrews, 2012; Bova et al., 2016)

$$\boldsymbol{\phi}_w = (\phi_{w,x}, \phi_{w,y}) = C (3.281)^B \left(\frac{\beta}{\beta_{op}} \right)^{-E} \cdot \left(|u_{mf,x}|^B \text{sgn}(u_{mf,x}), |u_{mf,y}|^B \text{sgn}(u_{mf,y}) \right) \quad (3.2)$$

$$\boldsymbol{\phi}_s = (\phi_{s,x}, \phi_{s,y}) = 5.275 \beta^{-0.3} \left(\left(\frac{\Delta z}{\Delta x} \right)^2, \left(\frac{\Delta z}{\Delta y} \right)^2 \right) \quad (3.3)$$

with

$$B = 0.15988 \sigma^{0.54} \quad (3.4)$$

$$C = 7.47 e^{-0.8711 \sigma^{0.55}} \quad (3.5)$$

$$E = 0.715 e^{-0.01094 \sigma} \quad (3.6)$$

$$\beta_{op} = 0.20395 \sigma^{-0.8189} \quad (3.7)$$

$$\mathbf{u}_{mf} = (u_{mf,x}, u_{mf,y}) = \mathbf{u}_0 \frac{1.83}{\ln \left(\frac{20+1.18 h}{0.43 h} \right)} \quad (3.8)$$

where \mathbf{u}_0 is the wind velocity at 6.1 m Above Ground Level (AGL), and h is the fuel height in meters. FDS-LS calculates \mathbf{u}_0 by dividing \mathbf{u}_{10} (wind velocity at 10 m AGL) by 1.15, with \mathbf{u}_{10} defined by the user as a boundary condition (input).

The surface RoS is obtained following Rothermel's model using the magnitude of the combined wind and slope coefficient vectors as in Equation (3.9) (Bova et al., 2016):

$$RoS = RoS_0 \left(1 + \sqrt{(\boldsymbol{\phi}_w + \boldsymbol{\phi}_s) \cdot (\boldsymbol{\phi}_w + \boldsymbol{\phi}_s)} \right). \quad (3.9)$$

FDS-LS assumes that, under specific wind, slope, and vegetation circumstances, a surface fire will spread from a single ignition point with an ellipse-shaped fire perimeter that has a constant length-to-breadth (LB) ratio for the effective wind velocity (\mathbf{u}_{eff}) (McGrattan et al., 2019). The latter is defined as:

$$\mathbf{u}_{eff} = \mathbf{u}_0 + \mathbf{u}_{vir} \quad (3.10)$$

where \mathbf{u}_{vir} is the virtual wind velocity aimed at accounting for the effect of slope (Finney, 1998a):

$$\mathbf{u}_{vir} = 0.3048 \left(\frac{1}{c} \left(\frac{\beta}{\beta_{op}} \right)^E \right)^{\frac{1}{B}} \boldsymbol{\phi}_s. \quad (3.11)$$

Thus, the effective wind velocity (\mathbf{u}_{eff}) combines the prescribed wind velocity (\mathbf{u}_0) and the effect of slope (\mathbf{u}_{vir}).

Let $P(t)$ be a point on the fire front at time t . The LB ratio for the elliptical fire front originating from $P(t)$ is as in Equation (3.12) (Bova et al., 2016; Finney, 1998a):

$$LB = \max(1, \min(\overline{LB}, 8)) \quad (3.12)$$

where

$$\overline{LB} = 0.936 e^{0.2566 u_{\text{eff}}} + 0.461 e^{-0.1548 u_{\text{eff}}} - 0.397 \quad (3.13)$$

and $u_{\text{eff}} = \|\mathbf{u}_{\text{eff}}\|$ is the effective wind speed.

The heading-to-backing ratio (HB), which is the ratio of the fire propagation in the wind direction to its propagation in the opposite direction, is given by (Bova et al., 2016; Finney, 1998a):

$$HB = \left(LB + \sqrt{LB^2 - 1} \right) \left(LB - \sqrt{LB^2 - 1} \right)^{-1}. \quad (3.14)$$

Let $P(t+dt)$ be a point on the fire front at time $(t+dt)$. Its location is obtained by modelling the fire propagation from $P(t)$ as an ellipse with semi-minor and semi-major axes $(a dt)$ and $(b dt)$, respectively, where:

$$a = \frac{b}{LB}, \quad (3.15)$$

$$b = \frac{1}{2} \left(RoS + \frac{RoS}{HB} \right). \quad (3.16)$$

Note that a and b are the rates of spread corresponding to the semi-axes of the ellipse, while RoS is as in (3.9). The distance between $P(t)$ and the centre of the ellipse is given by $(c dt)$, where:

$$c = b - \frac{RoS}{HB}. \quad (3.17)$$

Thus, the components of the RoS in the axes of the computational grid are calculated as follows:

$$RoS_x = D \left[a^2 \cos \theta (x_s \sin \theta + y_s \cos \theta) - b^2 \sin \theta (x_s \cos \theta - y_s \sin \theta) \right] + c \sin \theta \quad (3.18)$$

$$RoS_y = D \left[-a^2 \sin \theta (x_s \sin \theta + y_s \cos \theta) - b^2 \cos \theta (x_s \cos \theta - y_s \sin \theta) \right] + c \cos \theta \quad (3.19)$$

where

$$D = \left[a^2 (x_s \sin \theta + y_s \cos \theta)^2 + b^2 (x_s \cos \theta - y_s \sin \theta)^2 \right]^{-\frac{1}{2}}, \quad (3.20)$$

the quantities x_s and y_s are related to the components of the vector normal to the elliptical fire front, and θ is the clockwise angle between the y axis of the computational grid and the direction of the maximum spread as a function of the local wind, terrain, and vegetation (Bova et al., 2016):

$$\theta = \text{atan2}[(\phi_{\mathbf{w},y} + \phi_{\mathbf{s},y}) + (\phi_{\mathbf{w},x} + \phi_{\mathbf{s},x})]. \quad (3.21)$$

Thus, this model predicts the propagation of the fire front (assuming it behaves like a wave) affected by the wind and the terrain slope. It is a *decoupled model* (see Figure 2.8), since the fire does not affect the wind field. The same is true for FARSITE (Finney, 1998a). Therefore, the conceptual framework proposed in this research for improving the accuracy of *decoupled* wildfire propagation models using real-time wind field measurements carried out by a swarm of UAVs could be applied. In order to do so, the wind velocity at 6.1 m (\mathbf{u}_0) shown in blue is to be measured. This affects the mid-flame wind velocity (\mathbf{u}_{mf}) shown in violet, which in turn affects the wind coefficient (ϕ_w) shown in red and therefore the RoS and the orientation of the ellipse (θ). The effective wind velocity (\mathbf{u}_{eff}) in violet is also affected by \mathbf{u}_0 , affecting *LB* and *HB* and therefore the shape of the ellipse.

However, the LS model within the FDS software may be coupled with its wind model, thus becoming a *coupled model*—albeit not fully physics-based. In this project, the author makes use of this capability of FDS-LS to study the effect of fire–wind coupling in Section 7.3. To this end, the combustion model must also be coupled. Thus, when the fire reaches a surface cell, fuel vapours are generated at a constant rate (\dot{m}_f'') (McGrattan et al., 2019):

$$\dot{m}_f'' = (1 - \nu_{char}) \frac{m_f''}{\delta_t} \left[\frac{\text{kg}}{\text{m}^2 \text{ s}} \right]; \quad \delta_t = \frac{75,600}{\sigma} [\text{s}] \quad (3.22)$$

where ν_{char} is the char fraction (default value of 0.2), δ_t is the duration of the burn at a given location, and m_f'' is the dry fuel loading [kg/m^2].

Coupling the LS fire propagation model with the wind model results in FDS-LS accounting for terrain-induced wind fields and fire–wind interaction by presenting a simple heat source at the fire front location (Bova et al., 2016). Thus, FDS-LS may be used in any of four modes:

- MODE 1: Wind field is uniform and unaffected by terrain or fire (frozen uniform wind field). Only the fire model runs. *Decoupled* wildfire model in Figure 2.8.
- MODE 2: Wind field affected by terrain but unaffected by fire (frozen non-uniform wind field). Fire affected by frozen wind. *Decoupled* wildfire model in Figure 2.8.
- MODE 3: Wind field follows terrain but there is no actual fire in the simulation (just front-tracking). (McGrattan et al., 2019)
- MODE 4: Wind field affected by terrain and fire. Fire affected by wind. *Coupled* wildfire model in Figure 2.8.

Readers are kindly referred to (Bova et al., 2016) for a more detailed description of FDS-LS. The literature on FARSITE (Finney, 1998a) is also helpful to understand the approach of modelling fire propagation using Huygens' principle.

3.1.2 Boundary fuel model

When discretizing a thin layer of vegetation, this model might be used if a coarse grid is preferred. Here, the vegetation is represented as a porous barrier made up of a layer of wetness, air, and dry vegetation. For grid sizes up to 10 m, the vegetation's height can be utilised, although it is not resolved on the grid (McGrattan et al., 2023; Vanella et al., 2021). In this model, the convective heat transfer is represented by a source term in the one-dimensional heat conduction equation. This equation is applied to both the vegetation layer and the solid ground. Additionally, the transmission of thermal radiation through the vegetation layer is modelled using a one-dimensional radiative transport equation designed for semi-transparent solids. Even though this model might be efficiently utilised in a variety of studies and simulations, our preliminary results indicated that the Lagrangian particle model provides better and more realistic results and consequently, this study utilises the LPM model to carry out the simulations (Tavakol Sadrabadi & Innocente, 2025).

3.1.3 Lagrangian particle model

A group of Lagrangian particles heated by convection-radiation heat transfer constitutes the vegetation in this model. These particles might be grass, trees, leaves, or anything else. LPM may be used to replicate the front, rear, and flank fire across the surface and high-level vegetation (e.g., trees) with appropriate grid refinement (Vanella et al., 2021). The drag force per unit volume exerted by the vegetation can be calculated as follows:

$$\mathbf{f}_b = \frac{\rho}{2} C_d C_s \beta \sigma \mathbf{u} \|\mathbf{u}\| \quad (3.23)$$

where ρ is the air density, C_d is the drag coefficient defined through laboratory experiments, C_s is the shape factor with the default value of 0.25, β is the packing ratio of vegetation calculated as mass per unit volume divided by material density, σ is the surface-area-to-volume ratio, and \mathbf{u} is the wind velocity.

3.1.4 Reference cases and fuel modelling in FDS-LPM

Numerical simulations are validated against the field scale grass fire propagation experiments carried out by the Commonwealth Scientific and Industrial Research Organisation (CSIRO) (Cheney et al., 1993; Cheney et al., 1998) during July and August 1986 with constant high daily temperatures. Air temperature, relative humidity, and solar radiation are measured 1.4 m above ground level (AGL), while the wind velocity is measured at 2 m AGL during experiments. Fuel load and height were sampled at 16 points for each experiment and averaged for each plot. Other fuel characteristics, including surface-area-to-volume ratio and the fuel moisture content (FMC), were measured and recorded for each experiment.

Measured properties of two of the experiments performed by (Cheney et al., 1993) are presented in Table (3.1). The C064 experiment was carried out in 100×100 m² field

Table 3.1: Measured properties of CSIRO C064 and F19 experiments (Cheney et al., 1993; Mell et al., 2007) adopted from (Tavakol Sadrabadi & Innocente, 2025)

Property	Unit	Case C064	Case F19
Wind speed (U_2)	m/s	4.6	4.8
Ambient Temperature (T)	°C	32	34
Surface Area to Volume Ratio (σ)	m ⁻¹	9,770	12,240
Grass Height (H_g)	m	0.21	0.51
Bulk Mass Per Unit Area (ρ_b)	kg m ⁻²	0.283	0.313
Moisture Fraction (M)	%	6.3	5.8
Measured RoS	m s ⁻¹	1.2	1.5

covered with dry Kerosene grass of 0.21 m high, while the F19 experiment was carried out in a 200×200 m² covered with dry Kangaroo grass of 0.51 m high. Two workers ignited fires, starting at the plot's midpoint and moving towards either side of the plot with the length of ignition equal to 50 m for C064 and 175 m for F19 experiments. The fire behaviour and the rate of spread (RoS) were studied through data gathered by ground observations and oblique aerial photographs.

Following (Mueller et al., 2023), the solid phase thermal degradation of the vegetation is modelled utilising a three-step reaction process including (i) endothermic moisture evaporation, (ii) endothermic pyrolysis of dry vegetation, and (iii) exothermic char oxidation. Thus, the rate of change of the total mass in terms of density of composite solid could be calculated as:

$$\frac{\partial \rho_s}{\partial t} = -r_{\text{H}_2\text{O}} - (1 - \nu_{\text{char}}) r_{\text{pyr}} - (1 - \nu_{\text{ash}}) r_{\text{char}} \quad (3.24)$$

where the reaction rates for evaporation of H₂O, pyrolysis of the dry vegetation and surface oxidation of char as a function of component densities of composite solid are calculated utilising Arrhenius kinetics:

$$r_{\text{H}_2\text{O}} = \rho_{\text{s,H}_2\text{O}} A_{\text{H}_2\text{O}} T^{-\frac{1}{2}} e^{\left(-\frac{E_{\text{H}_2\text{O}}}{R T}\right)} \quad (3.25)$$

$$r_{\text{pyr}} = \rho_{\text{s,dry}} A_{\text{pyr}} e^{\left(-\frac{E_{\text{pyr}}}{R T}\right)} \quad (3.26)$$

$$r_{\text{char}} = Y_{\text{O}_2,\text{surf}} \sigma A_{\text{char}} e^{\left(-\frac{E_{\text{char}}}{R T}\right)} \quad (3.27)$$

where σ is the surface area-to-volume ratio of the vegetation, $Y_{\text{O}_2,\text{surf}}$ is the oxygen mass fraction at the material surface, A and E (J.mol⁻¹) are the pre-exponential factors and activation energy in the context of Arrhenius equation, R is the universal gas constant equal to 8.314 (J.mol⁻¹.K⁻¹), and T is the absolute temperature in Kelvin (McGrattan et al., 2023). This approach allows for the possibility of parallel drying and pyrolysis, with series char oxidation taking place as char is produced during pyrolysis

(Mueller et al., 2023). Kinetic constants must be determined for this model, and as the data required for particular fuels is sometimes unavailable -including the vegetations in CSIRO experiments- in this study, the kinetic constants of Fir determined by Grishin (Grishin, 1997) are utilised for the pyrolysis model of Veg_1 and Veg_2 , though the physical properties of Veg_2 follows that of Case F19 in CSIRO experiments mentioned in Table 3.1. Veg_3 however represents the pyrolysis model of little bluestem grass obtained from (Amini et al., 2021). Table (3.2) presents the details for the pyrolysis constants as well as the soil and the Three vegetation models utilised in this Thesis.

Table 3.2: *Summary of fuel physical properties and thermal decomposition coefficients, adopted from (Tavakol Sadrabadi & Innocente, 2025)*

Property	Unit	Veg ₁ (Veg ₂)(Veg ₃)	Reference
Area to Volume Ratio (σ)	m^{-1}	9,770 (12, 240)	(Cheney et al., 1993)
Bulk density (ρ_b)	$kg.m^{-3}$	1.313 (0.616)	(Cheney et al., 1993)
Fuel	-	Cellulose	(Vanella et al., 2021)
Fuel Density (ρ)	$kg.m^{-3}$	512	(Vanella et al., 2021)
Moisture content (M)	%	6.3	(Cheney et al., 1993)
Specific Heat	$kJ kg^{-1} K^{-1}$	2.1	(Boardman et al., 2021)
Conductivity	$kJ kg^{-1} K^{-1}$	0.1	(Vanella et al., 2021)
Heat of Evaporation (H_{H_2O})	$kJ kg^{-1}$	2259	(B. Porterie & Loraud, 2005)
Heat of Combustion (H_c)	$kJ kg^{-1}$	17,400	(McGrattan et al., 2023)
Heat of Pyrolysis (H_{pyr})	$kJ kg^{-1}$	418	(B. Porterie & Loraud, 2005)
A_{pyr}	s^{-1}	1040 (24550)	(Grishin, 1997) ((Amini et al., 2021))
E_{pyr}	$J.mol^{-1}$	61041 (58200)	(Grishin, 1997) ((Amini et al., 2021))
Char Yield (ν_{char})	$kg kg^{-1}$	0.25 (0.23)	(McGrattan et al., 2023)
A_{char}	$kg.m^{-2}.s^{-1}$	465	(Boonmee & Quintiere, 2005)
E_{char}	$J.mol^{-1}$	68000	(Boonmee & Quintiere, 2005)
Ash Yield (ν_{ash})	$kg kg^{-1}$	0.04	(McGrattan et al., 2023)
Obukhov Length (L)	m	-500	(Vanella et al., 2021)
Roughness Length(z_0)	m	0.03	(Vanella et al., 2021)
Drag Coefficient (c_d)	-	2.8	(McGrattan et al., 2023)
Soil Specific Heat	$kJ kg^{-1} K^{-1}$	2.0	(Vanella et al., 2021)
Soil Conductivity	$W m^{-1} K^{-1}$	0.25	(Vanella et al., 2021)
Soil Density	$kg m^{-3}$	1,300	(Vanella et al., 2021)
Relative Humidity	%	40	(Vanella et al., 2021)

3.1.5 Turbulent wind model and boundary conditions

Wind field modeling

FDS offers four options for defining the inlet wind into the domain, including (i) specified wind speed and direction that does not change with height, (ii) the Monin-Obukhov similarity theory, (iii) advanced meteorological concepts such as a Geostrophic Wind for modelling huge spatial domains, and (iv) the wall of wind or the power law approximation wind model. The latter is widely used in different studies due to its simplicity, mainly with a power of 1/7 (i.e., see Innocent et al., 2023; Mell et al., 2007; Moinuddin

et al., 2018); Still, it has certain limitations, as the power value varies with height, surface roughness and stability conditions (Petersen et al., 1998) where the 1/7 exponent approximates a neutrally stable stratification of the atmosphere. On the other hand, it should be highlighted that the CSIRO C064 experiments were carried out during the daytimes of the summer months with consistently warm and dry conditions ($T_{C064}=32^{\circ}\text{C}$) (Cheney et al., 1993), which is more consistent with an unstable stratification of the atmosphere with the convective uprising of the warm surface air ((NWCG), n.d.). Thus, utilising the *Monin-Obukhov* similarity theory that estimates the vertical wind and temperature profiles based on surface and atmospheric conditions (see (McGrattan et al., 2023)) seems to be a more accurate approach.

The Monin-Obukhov theory assumes that wind speed (u) and potential temperature (θ) change with height as follows (McGrattan et al., 2023):

$$u(z) = \frac{u_*}{k} \left[\ln \left(\frac{z}{z_o} \right) - \Psi_m \left(\frac{z}{L} \right) \right] \quad (3.28)$$

$$\theta(z) = \theta_0 + \frac{\theta_*}{k} \left[\ln \left(\frac{z}{z_o} \right) - \Psi_h \left(\frac{z}{L} \right) \right] \quad (3.29)$$

Where u_* is the friction velocity, k is the von Karman constant equal to 0.41, z_o is the aerodynamic roughness length, θ_* the scaling potential temperature, θ_0 ground level temperature, L is the Obukhov length, and Ψ_h and Ψ_m represent similarity functions. A negative value of L (m) determines an unstable stratified atmosphere where the buoyancy-generated turbulence causes large fluctuations in wind velocity and direction and enhances mixing. Based on the suggestions provided by (Vanella et al., 2021), this study determines an Obukhov length of $L=-500$ m and a roughness length of $z_o=0.03$ m (Tavakol Sadrabadi & Innocente, 2025).

Turbulence modeling

The turbulence within the domain is simulated by utilising the very large eddy simulation (VLES) model with Deardorff's sub-grid scale (SGS) model for turbulent eddy viscosity closure terms. The Van Driest damping model is utilised to model the Reynolds stresses in near-wall regions. To replicate the turbulent nature of the natural atmospheric winds, which significantly affects their behaviour at domain boundaries, this study utilises the synthetic eddy method (SEM)(Jarrin et al., 2008) that introduces random eddies into the domain as adopted in other studies (i.e. see Innocent et al., 2023; Mueller et al., 2021). Considering that an accurate definition of the eddy characteristics requires measurements of the turbulent Reynolds stress within the ambient wind and canopy height (i.e. see Mueller et al., 2021), which are not applicable here, an arbitrary value of 10% turbulence intensity is determined here similar to (Innocent et al., 2023) to mimic the atmospheric boundary layer turbulence in reality. It should be highlighted that for all cases, the wind field is let to develop through the simulation

domain for 80 seconds, and the fire is ignited afterwards. Utilised boundary Conditions include a no-slip boundary condition for the ground surface and 'Open' boundary conditions for the rest of the boundaries (Tavakol Sadrabadi & Innocente, 2025).

3.1.6 Simulation domain and gridding

The burnable field simulated in this study includes a vegetation field of $200 \times 200 \text{ m}^2$ to provide sufficient time and domain for the fire to reach a quasi-steady state, especially in steep upslope conditions and high vegetation heights. Initial experiments indicated that a domain height larger than 40 m does not affect the model results. Additionally, to eliminate the effects of up and downwind boundaries on fire propagation, a minimum length of 150 m on either side was required. Consequently, The simulation domain of this study, as presented in Fig 3.1, includes a cuboid 600 m long, 320 m wide, and 60 m high.

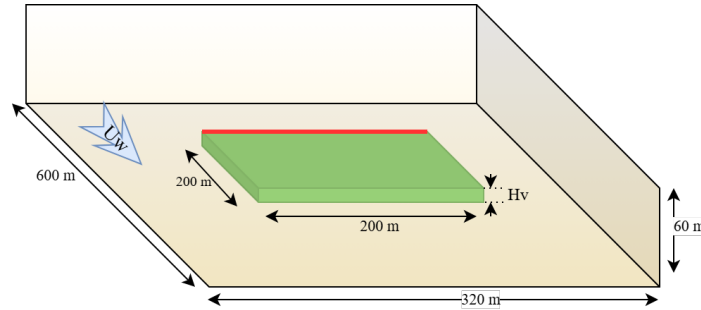


Figure 3.1: *Model Domain, adopted from (Tavakol Sadrabadi & Innocente, 2025).*

Every FDS computation needs to be carried out inside a domain composed of rectilinear volumes known as meshes. The number of rectangular cells that make up each mesh is determined by the required resolution of the flow dynamics. It is possible to define whether or not these mesh blocks overlap or come into contact. However, in the latter instance, there is virtually no communication between the calculations that are carried out in separate blocks (McGrattan et al., 2023). A grid sensitivity analysis is performed to determine the sensitivity of the estimated RoS of fire to the grid size. Three different grid sizes of $1 \times 1 \times 1 \text{ m}^3$ (coarse), $0.5 \times 0.5 \times 0.5 \text{ m}^3$ (fine), and $0.25 \times 0.25 \times 0.25 \text{ m}^3$ (very fine) were considered and tested as depicted in Figure 3.2a. It is acknowledged that the results are sensitive to the grid size up to a certain level, typically between 6% to 11% in different configurations of wind, vegetation height and terrain slope. Still, despite its potential benefit in accuracy, the utilisation of the very fine grid size is constrained by practical considerations of the computational cost required, mainly due to the large span of the vegetation area, the extended duration of simulations (particularly in downhill conditions), and the necessity for a considerable number of simulations.

Table 3.3: *Overview of the simulated Geometric and physical properties of the vegetation, terrain, and wind*

Veg model	Veg height (m)	Terrain Slope % (degrees)	Wind speed (m/s)	N. cases
<i>Veg₁</i>	0.2, 0.5, 10	-40%(-21.8°), -20%(-11.31°), 0(0°), +20%(-11.31°), +40%(-21.8°)	4, 6, 8, 10, 12	75
<i>Veg₂</i>	0.2, 0.5, 10	0 (0°)	4, 8, 12	9
<i>Veg₃</i>	0.2, 0.5, 10	-40%(-21.8°), -20%(-11.31°), 0(0°), +20%(-11.31°), +40%(-21.8°)	4, 6, 8, 10, 12	75

Thus, the final simulation domain consists of a rectangular block of $600 \times 320 \times 60$ m in x, y and z directions, respectively. A burnable area of 200×200 m is considered in this study to provide sufficient space for the formation of a quasi-steady state, especially for upslope and high wind conditions. Hence, to optimise the computational cost, the domain is discretised utilising a non-uniform grid with grid sizes of $0.5 \times 0.5 \times 0.5$ m³ used for the vegetation domain and its proximity (± 4 m) up to 44 m high, $1 \times 1 \times 1$ m³ cells for upstream and downstream areas up to a distance of ± 30 m, and $2 \times 2 \times 1$ m³ for the rest of the domain. Hence, each model includes a total number of 16687680 grid cells parallelised on 32 CPU cores for the duration of the simulation. The computational and simulation time, however, differs significantly from case to case. For example, the duration of simulation for the case with $u_{10} = 6$ m/s, $H_g = 0.2$ and on horizontal terrain was equal to ≈ 18 hours, while the same configuration but on downhill simulation required ≈ 80 hours of simulations for fire front to reach the end of the burnable domain due to the significantly lower RoS of fire downhills.

3.1.7 Model reliability and simulation scenarios

To study the effect of the turbulence model on the model estimations, three different variants of the large eddy simulation are compared in terms of the accuracy of the results as well as the computational cost, namely (i) Simple Very Large Eddy Simulation (SVLES), (ii) Very Large Eddy Simulation (VLES), and Large Eddy Simulation (LES) that determine the level of physics and accuracy of the numerical model. The estimated RoS and the heat release rate (HRR) of the combustion for all grid sizes and turbulence models utilised are presented in Figure (3.2-a) to (3.2-c). Figure (3.2-a) depicts the fire front location in C064 experiment for different grid sizes of $1 \times 1 \times 1$ m³ (coarse), $0.5 \times 0.5 \times 0.5$ m³ (fine), and $0.25 \times 0.25 \times 0.25$ m³ (very fine) and 2 different vegetation types considered in this study. The model shows grid dependence for the first vegetation type (Fir), and the RoS decreases by improving the grid resolution to 0.25 m. Further reduction in grid size did not lead to a change in the estimated RoS. However, no grid sensitivity is observed in the estimated RoS in the case of the second vegetation model (Little Bluestem) (Tavakol Sadrabadi & Innocente, 2025).

Consequently, as mentioned earlier, to find a balance between model accuracy and computational cost for a large number of simulations in this study, the fine grid size is adopted for the main simulations as it shows proper agreement with the experimental measurements. Figure (3.2-b) presents the front location in the C064 experiment for the first vegetation model (Fir) and different turbulence models utilised to carry out

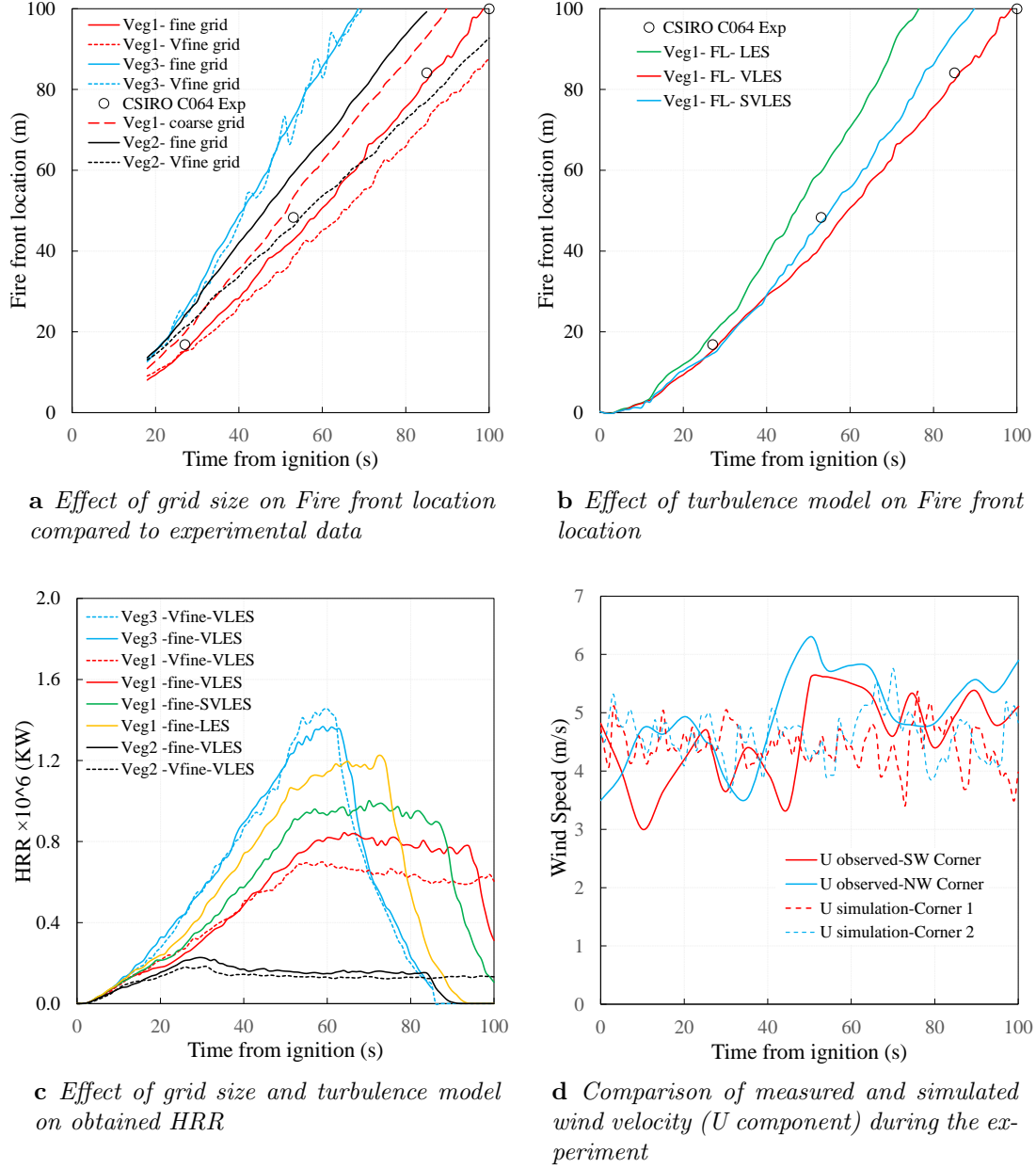


Figure 3.2: Model sensitivity and validation analysis, adopted from (Tavakol Sadrabadi & Innocente, 2025)

the simulations. It is indicated that Both LES and the SVLES provide faster RoS than the VLES, which agrees with the experiments. The estimated HRR of the combustion utilising different grid sizes and turbulence models is depicted in figure (3.2-c). It is evident that similar to the RoS, HRR is also sensitive to the grid size and turbulence model used. However, the level of this difference is limited to a maximum of 10% in most cases for 0.25 m and 0.5 m grid sizes. A comparison between the measured and simulated wind time-series as described in section 3.1.5 for the CSIRO C064 experiment is presented in figure (3.2-d), showing a proper agreement between the simulated wind time series and the field measurements.

Figure 3.3 compares the simulated and measured fire contours at the x-y plane for the CSIRO C064 experiment. Even though the simulated front location agrees with the experimental data, the simulated fire front width and flanks are not simulated accurately. This is mainly because flank flames are smaller than the front flames, requiring a finer grid size to accurately capture their dynamics. Consequently, to address this problem and limit the extent of the flank fire simulation problem and the effect of ignition line length on the estimated RoS, the length of the ignition line for all simulations is considered to be equal to the width of the field, 200 m. Finally, it should be mentioned that the simulation study presented here is generally idealised. Atmospheric conditions like wind velocity and direction vary rapidly with time in reality, affecting the fire propagation dynamics, while the idealised representation of the wind field for the whole duration of simulations and all cases studied here may not accurately mimic the real atmospheric situations.

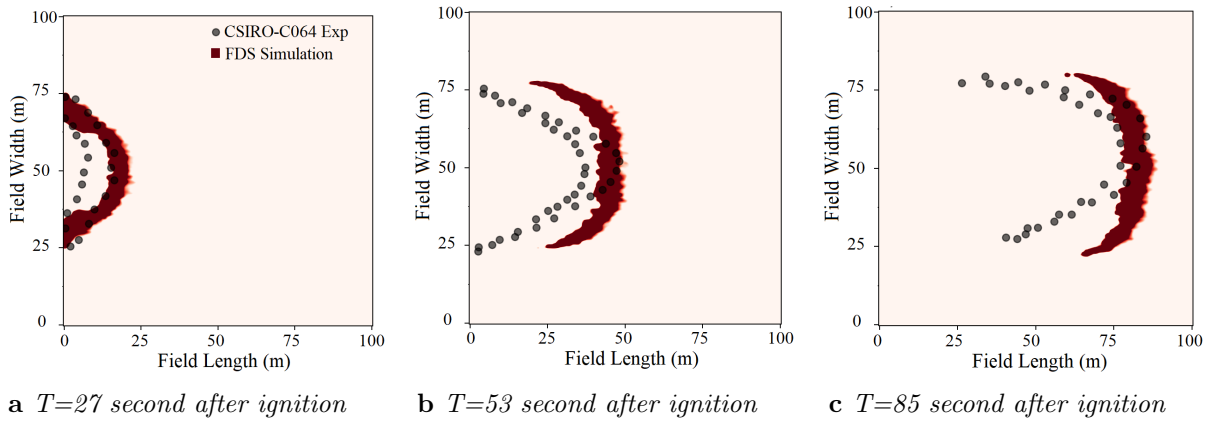


Figure 3.3: Comparison of simulated fire contours with the experimental results of CSIRO C064 experiment at different instants

Even though the estimations of the fire-front location agree with the experimental measurements while utilising the chosen grid size of 0.5 m, it is not guaranteed that this grid size is fine enough to adequately resolve a high fraction of the turbulent kinetic energy and ensure a valid Large Eddy Simulation (LES). Consequently, a posteriori grid quality analysis is conducted. This includes studying the effect of grid size on turbulence characteristics by calculating the spectral density of turbulence as well as

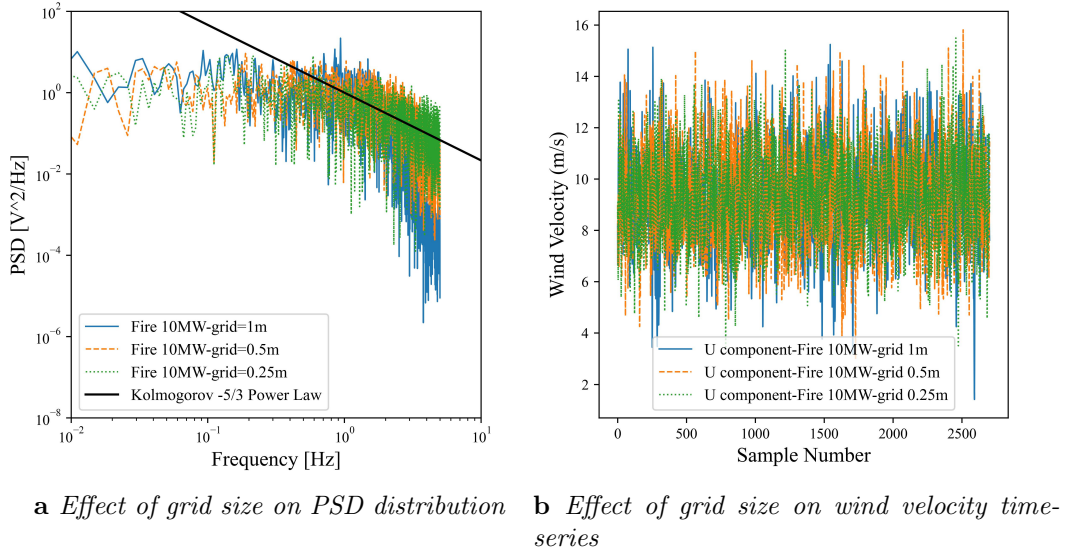


Figure 3.4: Effect of grid size and Fire Intensity on Spectral Density of turbulence.

evaluating the measure of turbulence resolution $M(x)$. The power spectral density is an important parameter, aiding in characterising the distribution of kinetic energy across different frequencies or scales of turbulent motion. Figure 3.4 presents the effect of grid size on the estimated spectral density (3.4a) and wind velocity (u_2) time series (3.4b) measured at $x=9$ m downstream of a 10MW/m pool fire with a width of 1 m at a sampling rate of 10Hz for 260 seconds, 2 meters above the ground level. It should be mentioned that the measurement point falls within the fire plume and hence reflects the fire-induced wind velocities. Generally, it could be observed that the simulated wind time series and the power spectral density distribution estimated using a 0.5 m grid and 0.25m grid are comparable, indicating that the 0.5 m grid might be sufficient for our purpose. It should be highlighted that the observed fire intensities in our experiments span a wide range yet, the 10MW fire here is selected as an average representative of obtained fire conditions during simulations for the calculation of PSD and $M(x)$.

The measure of turbulence resolution is a scalar quantity which could be calculated as follows (McGrattan et al., 2023):

$$M(x) = \frac{k_{sgs}}{k_{sgs} + TKE} \quad (3.30)$$

where TKE is the turbulent kinetic energy and could be calculated as follows:

$$TKE = \frac{1}{2} ((\bar{u} - u)^2 + (\bar{v} - v)^2 + (\bar{w} - w)^2) \quad (3.31)$$

and K_{sgs} is the subgrid kinetic energy and is estimated from Deardorff's eddy viscosity

model. It is also suggested that a valid Large Eddy Simulation is obtained such that $M(x) \leq 0.2$ (McGrattan et al., 2023).

Figure 3.5 presents the effect of grid size on the calculated values of the $M(x)$ at different locations downstream of the 10MW fire. It could be concluded that even though the best results are obtained when using the 0.25 m grid size, at all distances downstream of the fire, an approximate amount of 80-85% of turbulent kinetic energy is resolved by the 0.5 m grid except very close to the surface. This hence is a strong indicator that the 0.5 m grid is fine enough for a valid large eddy simulation of wildland fire propagations.

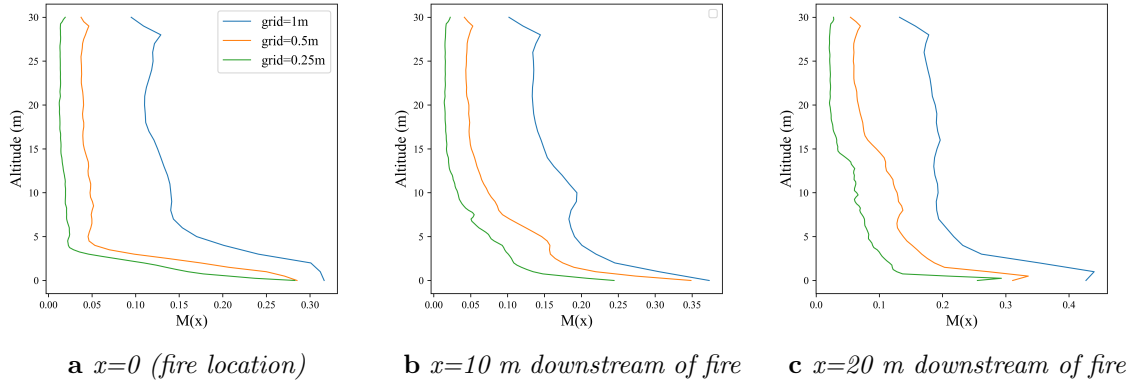


Figure 3.5: Effect of grid size on the measure of turbulence resolution $M(x)$ downstream of a 10 MW fire.

Consequently, it could be observed that a combination of a grid size of 0.5 m and the VLES turbulence model outputs satisfactory results and hence are utilised for the main simulations. It is however, acknowledged that the results are grid sensitive to a certain level and a true grid convergence has not been achieved, yet, practical considerations, including the large span of the vegetated area, as well as the need for a considerable height of domain, prevent the utilisation of a finer grid size.

Dimensional Analysis

Performing dimensional analysis utilising the Buckingham-pi theorem, (Morvan & Frangieh, 2018) stated that the propagation of fire in grasslands is governed by six parameters including RoS, wind speed (U_w), load of water and dry fuel inside combustible later, as well as the two opposing forces that affect the trajectory of flame and plume, characterised by the energy rate of fire p_f and the energy of wind P_w that could be defined as follows:

$$P_f = \frac{gI}{c_p T_0} \quad (3.32)$$

$$P_w = \frac{1}{2} \rho (U_w - \text{RoS})^3 \quad (3.33)$$

where I represents fire intensity, $\rho=1.225 \text{ kg.m}^{-3}$ is the air density, $c_p=1010 \text{ Jkg}^{-1}\text{K}^{-1}$, and T_0 is the ambient temperature in Kelvin. By applying the Pi-theorem, they concluded that the problem could be described by utilising three non-dimensional parameters including the ratio of RoS to wind speed (RoS/U_w), Byram's convective number (N_c), and the fuel moisture content (M) while these parameters could be related in the following form:

$$\frac{\text{RoS}}{U_w} = F(N_c, M) \quad (3.34)$$

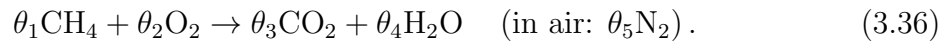
where

$$N_c = \frac{2 g I}{\rho c_p T_0 (U_w - \text{RoS})^3} \quad (3.35)$$

and the fire intensity I (kW/m) could be calculated as $I = W \times H \times \text{RoS}$ with W representing the fuel load (kg.m^{-2}), H (KJ.kg^{-1}) is the heat of combustion of the fuel and RoS is the rate of spread of fire. Nelson (Nelson, 2015) suggested that for values of $N_c < 2$, the propagation of fire is mainly dominated by the convective heat transfer between the flame and the unburnt vegetation ahead of the flame, namely the wind-driven fire propagation mode. On the other hand, $N_c > 10$ signifies a different type of fire propagation characterized by a vertical visible plume that is mostly governed by buoyancy forces and radiative heat transfer between fuel and flame. Consequently, values of $2 < N_c < 10$ could be considered a transitory state of fire. While the literature has traditionally treated U_w as interchangeable with both U_2 and U_{10} when calculating N_c , this study adheres to a consistent approach by exclusively utilizing U_{10} in all calculations for the sake of methodological uniformity (Tavakol Sadrabadi & Innocente, 2025).

3.2 Fire Propagation Model for Fast Simulations

The physics-based **Fire Propagation Model for Fast** simulations (**FireProM-F**) (Grasso & Innocente, 2020b) is a wildfire model developed with computational efficiency in mind, aiming for faster-than-real-time (FtRT) simulations. It is governed by a 2D reaction-diffusion equation that describes the combustion of a vegetation stratum represented by a mono-phase medium composed of pre-mixed gas of fuel and air. The fuel is assumed to be methane (after pyrolysis) whilst the air is assumed to be composed of oxygen, carbon dioxide, water vapour, and nitrogen. The reference chemical reaction (assumed irreversible) is the combustion of methane in air:



The model is formulated as a system of five partial differential equations (PDEs), where Equation (3.37) represents the conservation of energy whilst the four equations in (3.38) represent the conservation of chemical species.

$$\rho \frac{\partial}{\partial t} (c_p T) = R_c - \nabla \cdot (\mathbf{q}_c + \mathbf{q}_d + \mathbf{q}_r) + Q_{cz} + Q_{rz} + Q_w \quad (3.37)$$

$$\frac{\partial X_i}{\partial t} = -\frac{\theta_i}{\theta_1} \frac{M_i}{M_1} r; \quad \text{with } i = 1, 2, 3, 4, \quad (3.38)$$

where

T : temperature;
 ρ : mass density;
 c_p : specific heat capacity of the mixture;
 R_c : combustion energy;
 X_i : mass fraction of i^{th} chemical species;
 M_i : molar mass of i^{th} chemical species;
 r : combustion rate;
 \mathbf{q}_c : conductive heat flux;
 \mathbf{q}_d : interdiffusional enthalpy flux;
 \mathbf{q}_r : 2D radiation heat flux;
 Q_{cz} : vertical convection heat loss;
 Q_{rz} : vertical radiation heat loss;
 Q_w : transport term due to wind.

The specific heat capacity of the mixture is given by

$$c_p = \sum_{i=1}^5 X_i \frac{M_i}{M} c_{pi}, \quad (3.39)$$

where the molar mass of the mixture is a linear combination of the molar masses of each chemical species multiplied by their respective mass fraction:

$$M = \sum_{i=1}^5 X_i M_i. \quad (3.40)$$

The combustion energy is given by

$$R_c = -\rho c_h h_c \frac{M}{M_1} r \quad (3.41)$$

where h_c is the combustion enthalpy, and c_h is the enthalpy proportionality coefficient. The latter accounts for the possibility of burning fuels which have different R_c than that of methane. The combustion rate (r) follows Arrhenius law:

$$r = -\delta_{(T, X_{1,2})}^+ A_r T X_1^{0.5} X_2 \exp\left(-\frac{T_a}{T}\right) \quad (3.42)$$

where A_r is the pre-exponential coefficient and T_a is the activation temperature, which are empirical parameters that depend on the fuel structural and chemical properties. In turn, the Kronecker delta stands for the extinction model:

$$\delta_{(T, X_{1,2})}^+ = \begin{cases} 1 & \text{if } T > T_{\text{ig}} \wedge X_{1,2} > X_{1,2e} \\ 0 & \text{otherwise} \end{cases} \quad (3.43)$$

where T_{ig} is the ignition temperature (assumed to be the same as T_{a}), while $X_{1\text{e}}$ and $X_{2\text{e}}$ are the flame extinction values of the fuel and oxidant mass fractions, respectively. The combustion enthalpy is the summation of all formation enthalpies (H_i) at the specific local T :

$$h_{\text{c}} = \frac{H_{\text{c}}(T)}{M} = -\frac{1}{M} \sum_{i=1}^5 \theta_i H_i(T)$$

$$h_{\text{c}} = \frac{1}{M} \sum_{i=1}^5 \theta_i [H_{i,\text{ref}} + M_i c_{\text{pi}} (T_{\text{ref}} - T)] \quad (3.44)$$

where the reference empirical values $H_{i,\text{ref}}$ and T_{ref} can be found in (Mcbride et al., 1993).

The conductive heat flux is given by

$$\mathbf{q}_{\text{c}} = -\kappa \nabla T, \quad (3.45)$$

where the thermal conductivity (κ) is considered constant. In turn, the interdiffusional enthalpy flux is approximated by

$$\mathbf{q}_{\text{d}} \approx \frac{\kappa T}{c_{\text{p}} M} \sum_{i=1}^5 c_{\text{pi}} \nabla (X_i M_i) \quad (3.46)$$

while the 2D radiation heat flux is approximated by

$$\mathbf{q}_{\text{r}} \approx -4\sigma\varepsilon\delta_x T^3 \nabla T \quad (3.47)$$

where σ is the Boltzmann constant, ε is the emittance, and δ_x is the absorption length (a.k.a. optical thickness). The latter is assumed to be isotropic, and it must not be larger than the smallest cell size for the numerical solution to be valid.

With this dimensionality reduction, some fire dynamics phenomena like buoyancy are disregarded. Nonetheless, vertical convection (Q_{cz}) and vertical radiation (Q_{rz}) terms are added to the conservation of energy equation in (3.37), with:

$$Q_{\text{cz}} = \chi (T_{\text{amb}} - T)$$

$$Q_{\text{rz}} = \sigma\varepsilon\delta_z^{-1} (T_{\text{amb}}^4 - T^4) \quad (3.48)$$

where T_{amb} is the ambient temperature, χ is the convection coefficient, and δ_z is the vertical optical thickness.

FireProM-F does not account for conservation of mass or momentum, thus neglecting the effect of the fire on the wind field. The diffusion coefficient is augmented (via calibration) to compensate for this. Refer to (Grasso & Innocente, 2020b) for more details.

The transport term due to wind (Q_w) in Equation (3.37) is calculated as in Equation (3.49):

$$Q_w = -\rho c_w \mathbf{u} \cdot \nabla (c_p T) \quad (3.49)$$

where $\mathbf{u} = (u_x, u_y)$ is the atmospheric wind velocity, and c_w is the wind reduction coefficient (which may also be used as a calibration parameter).

The numerical scheme for the solution of Equations (3.37) and (3.38) is a finite difference method with a 2nd-order central difference for space and the 4th-order Runge-Kuta method for time discretisations. Refer to (Grasso & Innocente, 2020b) for the full formulation.

This reduced-order model, FireProM-F, is adopted in this Thesis as a fast yet still physics-based simulator to test the proposed framework. The latter aims to enhance the accuracy of the transport term (Q_w) by feeding the model with wind velocities (\mathbf{u}) measured by a swarm of UAVs. While the main purpose is to account for the effect of the fire on the wind field, it also serves the purpose of accounting for variable atmospheric wind.

3.3 Utilised Machine-Learning Algorithms

3.3.1 Support vector machine

With applications in both classification and regression, SVM (CorVap95) is a form of supervised ML technique which relies on the use of spatial coordinates to assign training samples in order to maximise the distance between the categories. New samples are then projected into that same region and estimated to belong to one of many categories depending on which side of the gap they fall. The complexity of real-world problems frequently requires more precise assumptions than those provided by contemporary linear learning machines, which have certain processing limitations. Thus, it would be beneficial to examine more complex relationships such as polynomial and radial basis function kernels (Aizerman et al., 1964). In this study, an SVM model with an RBF kernel is used as the first base model (Tavakol Sadrabadi & Innocente, 2023).

3.3.2 Decision trees

Despite the difficulties of reaching a universality given their core structure, the class of supervised learning techniques known as *Decision Trees* (DTs) (Breiman et al., 2017) represents an excellent example of a universal function approximator. Applications include regression and classification. A DT is made up of a number of branches connected by decision nodes, all of which end in leaf nodes. The decision node of the tree consists of a number of alternate leaf nodes that represent the output of the model, with each branch denoting a potential procedure. In classification and regression, this can be used as a label or a continuous value. The structure of the DT is largely composed of decision nodes. A basic goal when using this method is to minimise overfitting

by using the shortest feasible tree. In an ensemble DT model (EDT), many trees are used either simultaneously (using bootstrap aggregation or bagging) or sequentially to produce a final model (Jain et al., 2020).

3.3.3 Random forest

Random Forest (RF) is a mathematically solid ML method which aims to build more complex and robust models using bagging and random subspace as a base. Bagging is used to create a number of learner trees, which are then combined to obtain an overall prediction. Original training data are utilised to create bootstrap samples, which are then used to train the learning trees. A random selection of n instances from the initial training data (D), which consists of N instances, is used to construct each bootstrap sample (D_b). Fresh instances may be used in place of the bootstrap samples. D_b has a size of around two-thirds that of D , and does not have any duplicate instances (Jain et al., 2020). The main idea behind RF entails building numerous "simple" Decision Trees (DTs) during training and using a majority voting method for classification. Among other advantages, this voting method corrects for the unfavourable tendency of DTs to overfit the training data (Caie et al., 2021).

Extremely Randomised Tree, or *Extra Trees* (XT) (Geurts et al., 2006), is a tree-based method similar to RF that aims to increase accuracy by using the entire dataset rather than bootstrap samples to reduce bias, as well as to reduce the variance of the RF model by randomly selecting the optimal split points. Notably, XT executes faster than RF (Tavakol Sadrabadi & Innocente, 2023).

3.3.4 Stacked models

The method of stacking regressions, initially introduced in (Breiman, 1996), linearly combines several predictors to improve prediction accuracy. The approach primarily comprises two steps: (i) specifying a list of base learners and training each one on the dataset, and (ii) using the predictions of the base learners as input to train the meta-learner, which then predicts new values (Tavakol Sadrabadi & Innocente, 2023).

The defined structures of the stacked models in this study are depicted in Figure 3.6. Three different Stacking Classifiers (SC1 to SC3) were constructed based on combinations of different optimised base and ensemble algorithms in order to produce more complex classifiers. For consistency, the meta-learner of all models is the optimised RF model (Tavakol Sadrabadi & Innocente, 2023).

3.3.5 Extreme gradient boosting

Gradient Boosting Decision Tree (GBDT) (Friedman, 2001) is a supervised learning technique introduced by Jerome H. Friedman. Starting with a group of (x_i, y_i) values, where x_i stands for the input values and y_i for the associated target values, it involves iteratively creating a set of functions $F^0, F^1, \dots, F^t, \dots, F^m$ which are then used

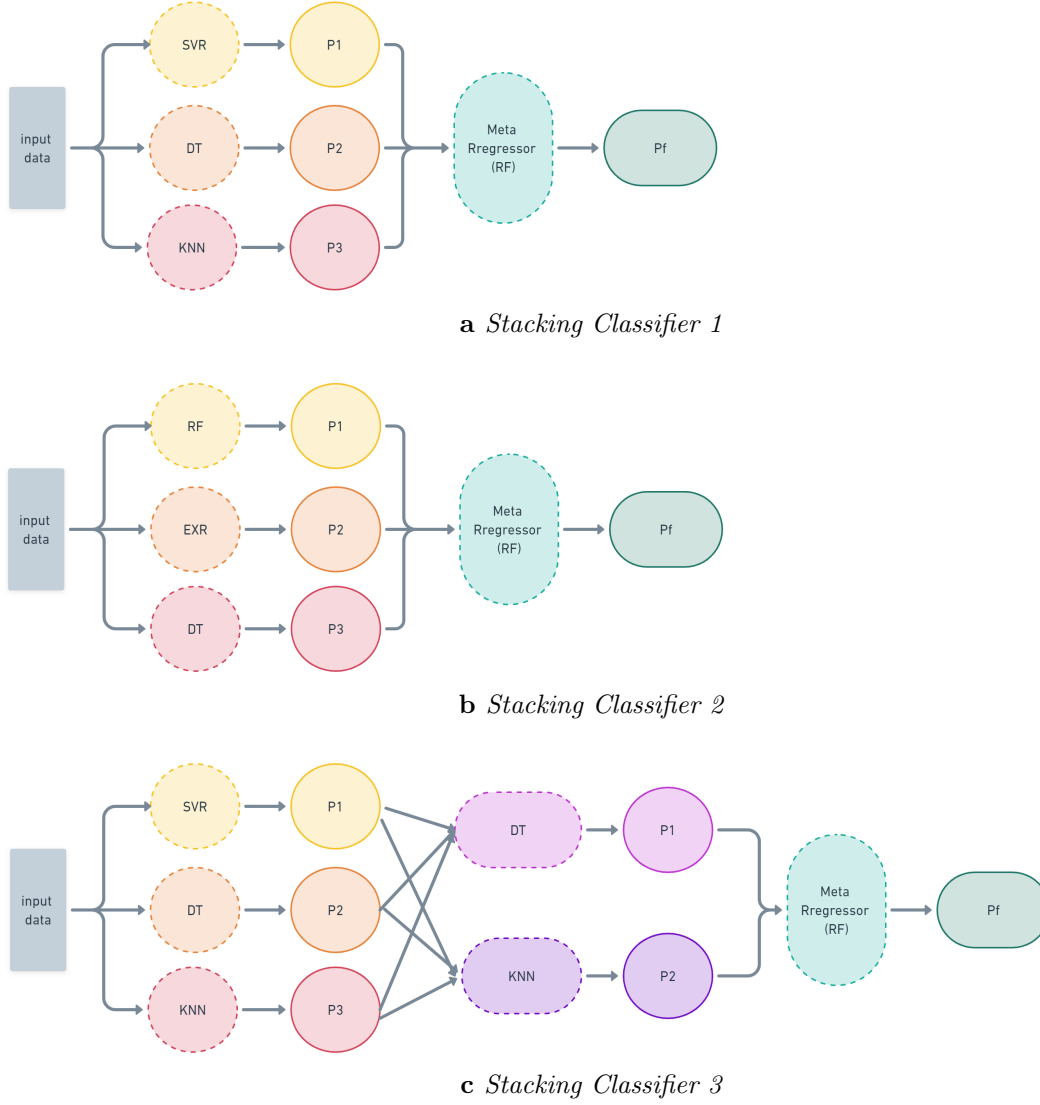


Figure 3.6: Structure used for the Stacked Classification models (Tavakol Sadrabadi & Innocente, 2023).

to form the corresponding loss function $L(y_i, F^t)$ that estimates y_i . To enhance the accuracy of estimations, another function $F^{t+1} = F^t + h^{t+1}(x)$ is created to calculate h^{t+1} as in Equation (3.50) (Gale et al., 2021; Rao et al., 2020):

$$h^{t+1} = \arg \min_{h \in H} EL(y, F^t) \quad (3.50)$$

where H is the group of potential DTs being taken into account for the ensemble. Thus, the loss function can be defined as in Equation (3.51) (Hancock & Khoshgoftaar, 2020):

$$EL(y, F^{t+1}) = EL(y, F^t + h^{t+1}) \quad (3.51)$$

A variant of GBDT called *Extreme Gradient Boosting* (XGB) was developed by (T. Chen & Guestrin, 2016). In general, the XGB approach combines several base learners (DTs) to create an aggregated model that is more resilient.

Overfitting may result from incorrectly specifying DT parameters such as the depth or number of iterations. XGB penalises overfitted models by incorporating regularisation techniques. However, numerous hyperparameters need to be adjusted (Tavakol Sadrabadi & Innocente, 2023).

3.3.6 K-nearest neighbour

K-Nearest Neighbour (KNN or k -NN) is a supervised learning algorithm that can be used for both classification and regression tasks (Cover, 1968). It aims to classify an unknown sample according to its distance from surrounding samples called neighbours. The defined context of distance is the Euclidian distance from the k -dimensional input vector \bar{x} to its neighbour (\bar{x}_2). In a regression context, the result is equal to the average of the target values over the desired k -nearest neighbours.

3.3.7 Adaptive boosting

Adaptive Boosting (AdaB), formulated in (Freund & Schapire, 1997), is a boosting ensemble that attempts to produce a strong learner by combining the outputs of weak base learners (though the method works for strong base learners as well), producing a stronger boosted classifier. AdaB attempts to learn from the mistakes of previous weak learners by increasing the weights assigned to incorrectly classified samples (Schapire, 1999). Higher weights are assigned to more accurate base learners.

3.3.8 Categorical boosting

Categorical Boosting (CatB), proposed by (Prokhorenkova et al., 2018), is an enhanced variant of GBDT. It has several advantages over the basic GBDT model:

- It is generally more rigorous at handling categorical data, and uses one-hot encoding for categories with low cardinality.
- It utilises the *Ordered Boosting* technique, which means that it is able to use the same examples used for computation of *Ordered Target Statistics* to compute h^{t+1} by assuming D to be the set of all available data for training the GBDT model, keeping in mind that the DT h^{t+1} is the tree that minimises the loss function (L).
- Its approach to building DTs relies heavily on *Oblivious Decision Trees* (ODTs). CatB creates a number of ODTs, which are full binary trees. Hence, there will be $2n$ nodes if there are n levels. The ODT's non-leaf nodes divide according

to the same standard. In order to increase confidence in the selection of the most productive feature combinations by CatB during training, the capabilities of GBDT are expanded to enable it to consider feature interactions. (Hancock & Khoshgoftaar, 2020; Prokhorenkova et al., 2018).

Since CatB is highly sensitive to its hyperparameters’ settings, their tuning is crucial (Tavakol Sadrabadi & Innocente, 2023).

3.3.9 Deep learning and convolutional neural networks

Machine-learning technology is integral to many aspects of modern life. However, traditional machine-learning methods struggle to process raw data directly. Consequently, for a long time, creating a pattern recognition or machine-learning system required significant engineering and specialized domain knowledge to build a feature extractor. This extractor could be used to transform raw data like image pixels into a format or feature vector that a classifier could use to detect patterns or make classifications (LeCun et al., 2015). Representation learning enables machines to process raw data and automatically uncover the representations necessary for tasks like detection and classification. Deep-learning methods thus, are representation-learning methods that use multiple layers of non-linear transformations to build increasingly abstract data representations from raw input. In a sequential process, each layer captures more complex structures by combining non-linear modules, each of which transforms the representation at one layer into a more abstract representation at the next level. Deep learning has led to major advancements in previously challenging areas for the AI community. Due to its promising capabilities in extracting intricate features and structures from high-dimensional data, it can be applied in a variety of domains including science, business and government. Deep learning outperforms traditional machine learning models in different tasks including but not limited to speech and image recognition, and reconstructing brain circuits (LeCun et al., 2015).

Many deep learning applications primarily rely on feed-forward neural networks, which are designed to take fixed-size input (such as an image) and produce fixed-size outputs (such as probability for each possible category). When moving from one layer to the next one, each unit or neuron calculates a weighted sum of inputs from previous layers and applies a non-linear function– the activation function–to this value (LeCun et al., 2015). The *Universal Approximation Property* of neural networks indicates that a multi-layer neural network can represent any function. For example, it indicates that a neural network with a single hidden layer can approximate any bounded continuous function with arbitrary precision or a neural network with two hidden layers can approximate any function (including discontinuous functions) with arbitrary accuracy (H. Wang & Raj, 2017). However, these universal approximation properties of shallow neural networks come at the cost of an exponentially large number of neurons within the networks, making them virtually impractical (H. Wang & Raj, 2017). The solution,

however, is to build deeper networks (H. Wang & Raj, 2017) rather than shallow but wider networks.

Convolutional neural networks (CNNs) are a form of feed-forward neural network that includes convolutional computations. They are easier to train and better at generalizing than networks with full connections between adjacent layers. They are primarily designed to handle data in the form of multiple arrays such as images made of 2D arrays representing pixel intensities in different color channels. Multiple arrays can include many types of data such as 1D arrays of signals and sequences, 2D arrays of images, and 3D arrays for video or volumetric images. CNNs normally leverage four key principles that help them analyse the properties of natural signals including (i) local connections, (ii) shared weights, (iii) pooling, and (iv) using multiple layers (LeCun et al., 2015). A typical schematic diagram of the structure of convolutional neural networks is presented in Figure (3.7).

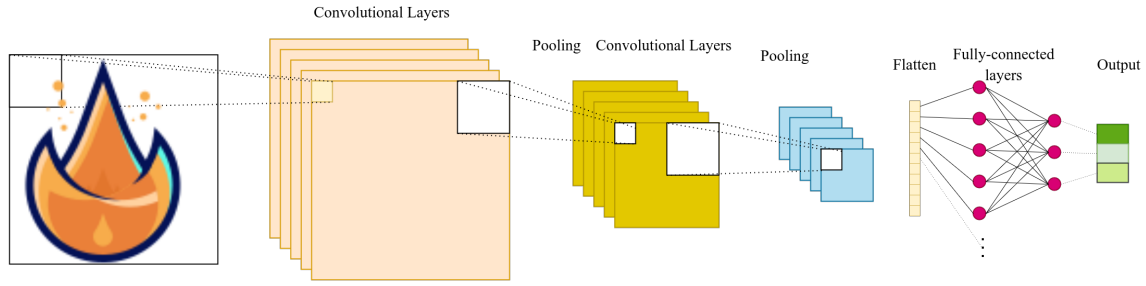


Figure 3.7: Schematic diagram of a CNN structure for regression or classification tasks.

Convolutional layer

Convolutional layers are a key part of the CNN structure, playing a crucial role in the feature extraction process. Unlike the fully connected layers, convolutional layers are sparsely connected, implying that only a subset of input neurons are connected to each output neuron. Assuming an input vector of $X = (x_1, x_2, \dots, x_k)^T$ and an output vector of $Y = (y_1, y_2, \dots, y_l)^T$, the input-output relationship can be described as (Yu et al., 2023):

$$Y = WX + b \quad (3.52)$$

where the weight matrix W is a sparse matrix, and b is the bias parameter. The convolution layer works by applying a convolution filter to transform the input image into a feature map, which is then passed to the next layer. A schematic representation of the convolutional layer for a filter size of 3×3 on an image or array with 3 channels is presented in Figure (3.8).

The convolutional kernel shifts horizontally and vertically on the feature map and converts data step by step. Hence, the filter- as shown in Figure 3.8—will have 27 weights ($3 \times 3 \times 3$), each representing a coefficient applied to each element in the corresponding

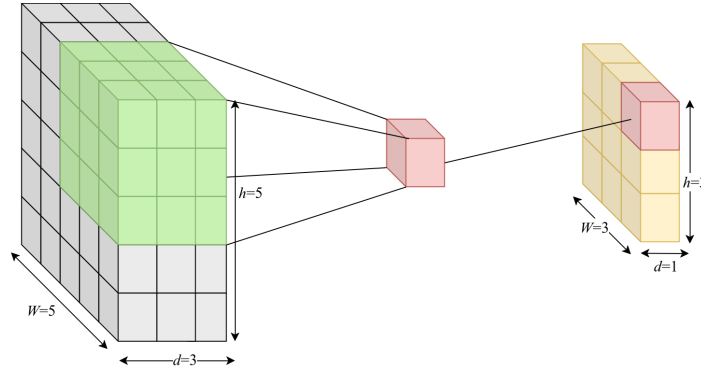


Figure 3.8: Schematic diagram of a convolutional layer operation.

positions of the feature map. Then each weight is multiplied by the corresponding element of the feature map and finally, the products are summed to form a single output value. Hence, the output feature map can be calculated as follows (Yu et al., 2023):

$$W_{out} = (W_{in} - K_{size}) / S_{size} + 1 \quad (3.53)$$

$$H_{out} = (H_{in} - K_{size}) / S_{size} + 1 \quad (3.54)$$

$$C_{out} = N \quad (3.55)$$

Where W_{in} and H_{in} are the width and height of input arrays, K_{size} and S_{size} are kernel size and step size, and N is the number of convolution kernels. The final output hence would have the dimension of $W_{out} \times H_{out} \times C_{out}$.

Activation functions

Activation functions are primarily used to apply non-linear transformations to the output features. This enhances the network's ability to represent non-linear relationships between input and output. So far various activation functions have been developed including but not limited to the Sigmoid function, Tanh function, Rectified Linear Unit (ReLU), and Softmax function (Yu et al., 2023). For instance, the formula of the Sigmoid function is:

$$S(x) = \frac{1}{1 + e^{-x}} \quad (3.56)$$

and Tanh is defined as:

$$\text{Tanh}(x) = \frac{e^x - e^{-x}}{e^x + e^{-x}} \quad (3.57)$$

Pooling layer

The pooling layer, which usually comes after the convolutional layer, is in charge of downsampling the feature maps that the convolutional layer produces. In addition to preventing overfitting, this method efficiently lowers the computing cost, training

complexity, and number of network parameters. Furthermore, feature invariance is introduced by pooling, which means that the network is more focused on the presence of features than their precise placement. Max pooling and average pooling are the two primary categories of pooling operations. The average value of every element in a region is calculated and utilised as the output in average pooling. The output of max pooling is, however, the highest value in the region. A pooling procedure with a stride of 2 reduces the image to a fourth of its initial size (Yu et al., 2023).

3.3.10 Attention mechanism and convolutional block attention module

Attention is a vital cognitive function that enables humans to selectively focus on important data while disregarding less significant details and information. Humans are naturally inclined towards processing information in pieces, focusing on the areas that are most urgently required. This ability to focus enhances perception efficiency and enables humans to rapidly select important information. Attention can be categorized into two types including (i) *top-down conscious attention* which is goal-directed and enables focus on particular tasks, and (ii) *bottom-up unconscious attention* which is motivated by external stimuli such as hearing loud noises—which is similar to the max-pooling mechanism (Niu et al., 2021). The majority of deep learning’s attention mechanisms are based on top-down focused attention. The problem of information overload can be addressed by using the attention mechanism as a resource allocation strategy. It aids in effectively prioritising and processing the most crucial information particularly when computational resources are limited. The attention mechanism can be used with the majority of models in a variety of deep learning domains as a way to enhance the neural network’s capacity to process information. Researchers have improved and modified the attention mechanisms to better tailor them to particular tasks, even though the basic idea behind attention models remains the same (Niu et al., 2021).

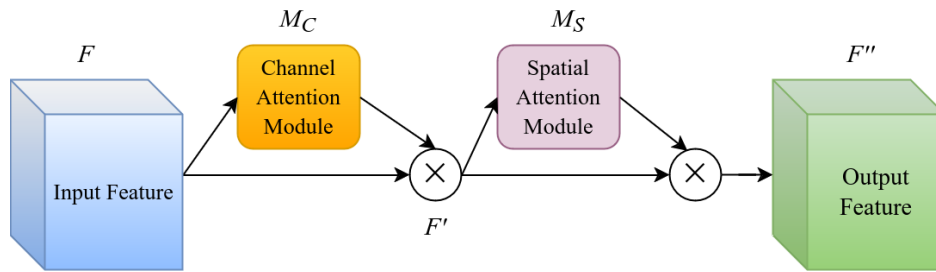


Figure 3.9: Schematic diagram of the CBAM module, adopted from (Woo et al., 2018).

Convolutional Block Attention Module (CBAM) introduced by (Woo et al., 2018), is a lightweight and efficient method to improve the representational capabilities of

feed-forward neural networks. It applies the attention mechanism in two dimensions: channel and spatial. For adaptive feature refinement, the input feature map is then multiplied by the attention maps (Woo et al., 2018). So the CBAM includes two main modules including (i) *Channel attention module* and (ii) *Spatial attention module*. The general structure of the CBAM module is presented in Figure (3.9). Given an input feature $F \in \mathbb{R}^{C \times H \times W}$, CBAM sequentially derives a 1D channel attention map $M_C \in \mathbb{R}^{1 \times 1 \times 1}$ as well as a 2D spatial attention map $M_S \in \mathbb{R}^{1 \times H \times W}$. Hence it can be formulated as follows:

$$F' = M_C (F) \otimes F \quad (3.58)$$

$$F'' = M_S (F') \otimes F' \quad (3.59)$$

where \otimes is the element-wise multiplication.

Channel attention module

A channel attention map is created by analyzing relationships between feature map channels and focusing on what is relevant in an image. Pooling is used to reduce the spatial dimension in order to calculate channel attention efficiently. While max pooling offers extra cues to differentiate distinctive object characteristics, average pooling, which is frequently used to aggregate spatial information, captures general object features. Hence, this technique enhances network representation power by integrating average and max-pooled features, providing a more sophisticated channel-wise attention (Woo et al., 2018). Calculated values are then forwarded into a shared fully connected network to produce the channel attention map $M_C \in \mathbb{R}^{C \times 1 \times 1}$, while a reduction ratio in the form of C/r is applied to the number of hidden layer cells to reduce the computational overhead. Here r represents the reduction ratio—mostly set to 8. The output feature vectors are then merged using element-wise summation (Woo et al., 2018). The general structure of the channel attention module is presented in Figure (3.10).

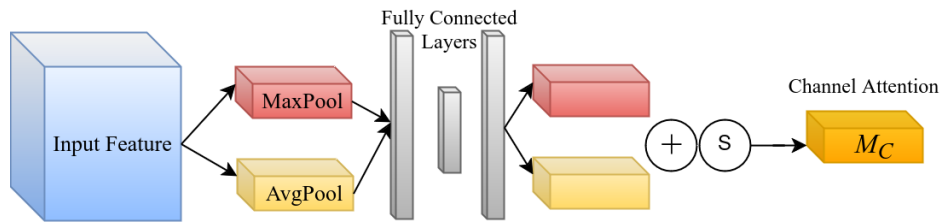


Figure 3.10: Schematic diagram of the channel attention module, adopted from (Woo et al., 2018).

In summary, the channel attention can be calculated as:

$$M_C(F) = \sigma (W_1(W_0(F_{avg}^c)) + W_1(W_0(F_{max}^c))) \quad (3.60)$$

where σ is the sigmoid function, F_{avg}^c and F_{max}^c are the, averaged pooled features and maxpooled features, and W_0 and W_1 are the weights of the fully connected network with $W_0 \in \mathbb{R}^{C/r \times C}$ and $W_1 \in \mathbb{R}^{C \times C/r}$.

Spatial attention module

In addition to the "what" that channel attention identifies, spatial attention is produced by examining spatial relationships within feature maps and concentrating on "where" the most instructive elements of an image are located. An effective descriptor that highlights important regions is created by combining the results of applying average and max pooling along the channel axis to compute spatial attention. A convolutional layer is then applied to this descriptor, producing a spatial attention map in the form of $M_S(F) \in \mathbb{R}^{H \times W}$ that identifies areas to emphasize or downplay in the image. Channel Information The general structure of the channel attention module is presented in Figure (3.11).

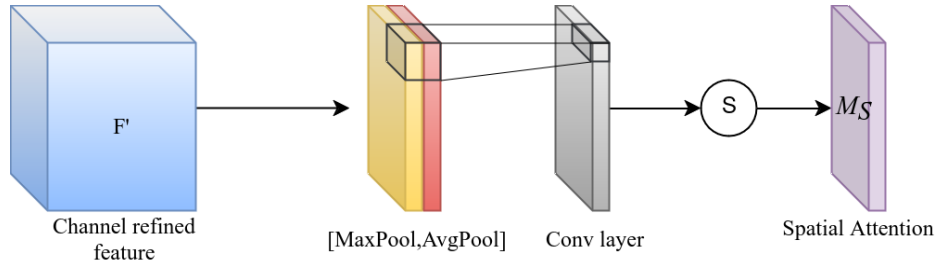


Figure 3.11: Schematic diagram of the spatial attention module, adopted from (Woo et al., 2018).

In summary, the spatial attention can be calculated as:

$$M_S(F) = \sigma (f^{7 \times 7} ([F_{avg}^s; F_{max}^s])) \quad (3.61)$$

where σ is the sigmoid function, $f^{7 \times 7}$ is a convolutional operation with kernel size equal to 7, F_{avg}^s and F_{max}^s are the, averaged pooled features and maxpooled features across channels with $F_{avg}^s \in \mathbb{R}^{1 \times H \times W}$ and $F_{max}^s \in \mathbb{R}^{1 \times H \times W}$.

Chapter 4

Conceptual Design of a UAV-Swarm Based Wildfire Emergency Response System

Systems for wildfire emergency response (WER) should ideally be planned systematically. In reality, however, they usually rely on ad hoc dynamic modifications and ad hoc design of some components because of budgetary limitations, shifting environmental conditions, developing threats, or any other unforeseen circumstance. Consequently, this chapter, the first working chapter of the thesis, presents the conceptual design of a UAV-swarm-based wildfire emergency response system, utilising a systems engineering approach aiming to identify and highlight the opportunities for maximum exploitation of the UAV's power and flexibility in empowering existing wildfire emergency response systems. However, it is acknowledged that firefighters and land crew are the core elements of every firefighting response system. Hence the presented chapter focuses on developing a human-centred framework to improve their safety and efficiency, rather than replacing these elements.

4.1 Systems Engineering Overview

Using a systems engineering framework (Faulconbridge & Ryan, [2002](#); NASA, [2020](#)), the author proposes here a conceptual design of a WER system explicitly leveraging intelligent UAV swarms. The main motivation for the design of such a WER system is that the use of UAVs has the potential to cut costs, boost efficiency, and improve safety in various existing forest service programs, including risky operations in which piloted aircrafts are not actively employed (Markiewicz & Nash, [2016](#)). This is reinforced by the use of intelligent self-organising UAV swarms. Although UAV-based systems cannot undertake all actions of a WER, as the presence of firefighters on the ground is indispensable, they can significantly improve its functionality and performance while reducing economic and human losses.

The life cycle of a system can be broadly divided into an *acquisition* and a *utilisation* phases. The acquisition phase comprises four main stages, illustrated in Fig. 4.1: (i) *conceptual design*, (ii) preliminary design, (iii) detailed design and development, and (iv) construction or implementation. This thesis is concerned with the *conceptual design*, which aims to define the system in functional terms (Tavakol Sadrabadi et al., 2024).

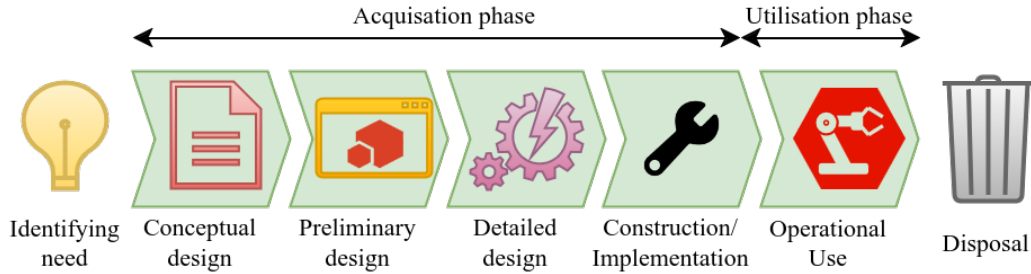


Figure 4.1: Life cycle of a system, which starts with the statement of a need and ends with the system’s disposal. The focus here is on the conceptual design, which is aimed at defining the system in functional terms, adopted from (Faulconbridge & Ryan, 2002).

It is crucial to unambiguously define the functional requirements of the system to avoid future problems during the system development and operational stages. The main steps comprising a *conceptual design* are (Faulconbridge & Ryan, 2002):

1. Stakeholder requirements identification.
2. System feasibility analysis.
3. System requirements analysis.
4. System-level synthesis.
5. System design review.

4.2 Stakeholder Requirements Identification

The first step in the conceptual design of a system is to identify stakeholders and their requirements, which involves defining the system’s functions, objectives, constraints, operational features, interactions with third-party systems, and operational environment. These requirements are specified in layman’s terms rather than technical language (Faulconbridge & Ryan, 2002).

4.2.1 Stakeholders

A stakeholder is any party that has a stake or an interest in the system (Vogwell, 2003). The UK Forestry Commission identifies the following stakeholders when planning for wildfires (Commission-England, 2020): (i) fire and rescue services, (ii) local authorities and resilience forums, (iii) local wildfire groups, (iv) local and adjacent tenants and property owners, and (v) managers and owners of national infrastructures. In addition, public law authorities such as police forces (Karvonen et al., 2023; United Nations Environment Programme, 2022), public health agencies, meteorological organisations, aerial flight crews, and telecommunication operators and companies may be added to the list. At a broader scale, governmental organisations and departments such as agricultural departments, forest and rangeland management services, water management services, municipalities, insurance companies, and the military may also be considered stakeholders. Finally, the natural environment comprises an external stakeholder, as it is highly affected by a wildfire and the strategies adopted during the emergency response. For example, the effects of fire suppression activities on the environment are so high that they could surpass the impacts of the fire itself (Backer et al., 2004).

With specific regard to the swarm-related components of the response system, their users and operators also comprise internal stakeholders. Examples are (i) swarm operators, (ii) data analysts, and (iii) U-space operators. *Swarm operators* communicate with operators of other components of the response system, whilst commanding, monitoring and controlling the mission—including launch and return of the swarm (i.e. command, control, and communication). *Data analysts* make use of sensor data and AI-based analytics to monitor and assess the situation, make recommendations to the incident commander, and inform external stakeholders. *U-space operators* establish U-space areas and provide traffic control, maintaining communications with pilots of manned and unmanned aerial vehicles (Karvonen et al., 2023).

Table 4.1 summarises the requirements of some important stakeholders related to the UAV swarm within the wildfire emergency response system, including internal stakeholders, nature, and regulatory authorities (Tavakol Sadrabadi et al., 2024).

4.2.2 Objectives and constraints

Since the *need* in Fig. 4.1 is typically loosely stated, system-level objectives must be clearly articulated at the beginning of the conceptual design. Common *objectives* of a WER system are (Tavakol Sadrabadi et al., 2024):

1. Reduce the risk of a fire.
2. Limit the consequences of a fire should one break out.
3. Monitor area of interest (surveillance).
4. Detect and localise fire outbreaks.

Table 4.1: Overview of some important stakeholders of the WER system empowered by aerial UAV swarms and their requirements (Tavakol Sadrabadi et al., 2024).

Type of stakeholder	Stakeholder	Requirements
External	Governmental organisations	The swarm-based WER system must be safe, economically viable, adaptable to regulations, and publicly acceptable.
	Aviation and regulatory organisations	The system must function within the specific aerial domain to maintain safety for other aerial vehicles.
	Insurance companies	The system must be able to protect human crew, valuable property, businesses, heritage sites, and infrastructure to reduce exerted damage and reconstruction/repair costs.
	Local authorities, landowners, tenants, etc.	Minimising damage to local property, lands, tenants, and environment.
	Nature	1- minimising the damage to all components of the ecosystem either caused by the fire or firefighting activities. 2- accelerating rehabilitation of the environment through performing timely and large scale recovery missions.
Internal	Forest management services	The UAV swarm is to be capable of carrying out Inspection missions, fire and environment monitoring and sensing, fire propagation estimations, fire fighting activities, damage assessment missions and recovery actions efficiently and economically to reduce the costs compared to current approaches.
	Fire and rescue services	The UAV swarm should be reliable, accessible, maintainable, and operable for the mission's duration. It must be capable of carrying out fighting activities, logistic and support missions, and continuous monitoring
	UAV system operators and maintainers	The UAV swarm must be (1) maintainable in a timely and cost-efficient manner, (2) energy efficient, (3) operable for the duration of the mission, and so on.
	Data analysts	The UAV swarm must be capable of providing reliable and accurate data throughout the entire mission time from desirable locations and with desirable resolutions.

5. Alert firefighters, incident commander, and other decision-makers.
6. Gather and assess fire data.
7. Forecast fire propagation.
8. Identify natural resources and map roads.
9. Monitor and assist evacuations (assets, people).
10. Suppress the fire.
11. Map burned area.

Project *constraints* include organisational policies, procedures, standards, resource allocations, and time frames guiding and restricting the system development. External *constraints* include compliance with laws, regulations, and industry standards, and capabilities to interface to other systems (Tavakol Sadrabadi et al., 2024).

Currently, there are no UAV regulations that directly address forest firefighting activities, as the majority of UAV regulations are focused on operations over populated and urban areas (see (D. Lee et al., 2022)). However, most of these regulations are still generally applicable and valid in WER situations. Even though a comprehensive review of regulations is beyond the scope of this research, the aim here is to discuss limitations imposed by some countries and modifications required to take advantage of UAV capabilities such as autonomous flights beyond the visual line of sight (BVLOS) (Tavakol Sadrabadi et al., 2024).

The U.S. Federal Aviation Administration (FAA) passed regulations in 2014–2015 stating that every UAV with a mass of at least 0.25 kg and a maximum speed higher than 100 mph is permitted to fly only during daytime and controlled by certified operators no younger than 17 years old. Furthermore, UAVs may not be used for deliveries or fly BVLOS (D. Lee et al., 2022; K. Lee, 2015). In 2021, the FAA published a new set of rules permitting operations over people and moving vehicles, and night operations as

long as UAVs are equipped with anti-collision lights (Federal Aviation Administration, 2021). In August 2023, the FAA authorised the “Phoenix Air Unmanned” company to perform BVLOS operations for aerial work, aerial photography, survey, as well as powerline and pipeline patrol and inspection (Federal Aviation Administration, 2023a). In September 2023, two other companies were granted BVLOS mission authorisations for small package delivery, and for testing detect-and-avoid technologies (Federal Aviation Administration, 2023b).

The European Aviation Safety Agency (EASA) and the Civil Aviation Authority (CAA) in the UK classify UAV flights into three categories, namely (i) *open category* (low risk), (ii) *specific category* (medium risk), and (iii) *certified category* (high risk) (European Union, 2019; D. Lee et al., 2022). The *open category* is sub-divided into three sub-categories: A1 (UAVs mass below 0.25 kg, which may be flown over people but not crowds), A2 (UAV mass under 4 kg according to EASA, and under 2 kg according to CAA), and A3 (general operations, including UAV mass up to 25 kg) (Tavakol Sadrabadi et al., 2024). *Open category* flights do not require authorisation from the National Aviation Authority (NAA), although Operator ID registration and some certification of competency may be required for sub-categories A2 and A3. The CAA requires a Flyer ID from anyone piloting a UAV. The *specific category* is for flights posing higher risks which may nonetheless be mitigated, requiring risk assessment and authorisation from the NAA. The *certified category* applies to complex operations, typically with larger and/or more sophisticated UAVs, requiring the highest levels of safety assurance. The levels of risk are determined with respect to cargo, population density, UAV dimensions, and whether the flight is within visual line of sight (VLOS) or BVLOS (European Union, 2019). UAVs must fly lower than 122 m in the open category, may fly higher in the specific category, whilst special permission is required in the certified category. For all UAVs with a mass of 0.25 kg or above, operators must have some level of training (European Union, 2019; D. Lee et al., 2022).

BVLOS flights are typically prohibited in the USA, the UK, and the EU, unless prior authorisation is obtained from the NAA and within well-defined geo-fenced zones (D. Lee et al., 2022; Matalonga et al., 2022). Nevertheless, regulatory bodies anticipate a variety of parties that will benefit from autonomous UAV missions (Matalonga et al., 2022), and hence are striving to adapt and define regulatory frameworks to allow for this. For example, the UK has established the airspace modernisation strategy (AMS) program, which aims to examine how RPAS flying BVLOS will be incorporated into the UK airspace system by 2040 (Civil Aviation Authority, 2023). EASA has developed the concept of *U-space*, which consists of a set of services and procedures to facilitate safe and efficient airspace access for multi-UAV missions. The aim is to allow for automated UAV management and integration, coexisting safely with the current air traffic management system (European Civil Aviation Conference (ECAC), 2021; European Union Aviation Safety Agency (EASA), 2020). The NASA Ames research centre is developing a so-called *UAV traffic management* (UTM) platform to safely integrate large numbers of UAVs operating at low-altitude airspace into existing air traffic (National Aeronautics and Space Administration (NASA), 2021).

WER missions are carried out largely under uncontrolled and uncertain situations. For instance, aircrafts and land crew mostly operate within smoky, windy, and highly turbulent environments. Consequently, a UAV swarm system must be adaptive, and able to operate autonomously and BVLOS (Matalonga et al., 2022). These are precisely defining features of a swarm intelligent, self-organising, multi-UAV system. However, regulations—especially in the context of wildfires—do not yet support such missions. In fact, the FAA states that “drones and wildfires are a toxic mix” as fire response services have to halt their airborne support vehicles to avoid midair accidents if unauthorised UAV flights are observed near the wildfire event (Federal Aviation Administration, 2019). Therefore, an autonomous aerial swarm-based system must be designed as an integral component of the WER system rather than incorporated *a posteriori* to enable coordinated and safe operations for both manned and unmanned vehicles in wildfire airspace. As such systems are progressively developed and tested, proving themselves efficient, reliable and safe, it is reasonable to expect regulations to become less restrictive in the near future (Tavakol Sadrabadi et al., 2024).

4.2.3 Operational scenarios

Operational scenarios take into account (i) *operational environments* (external factors) and the (ii) *modes of operation of the system* (internal factors) so as to meet the stakeholders requirements.

Wildfires can happen in diverse areas, including remote locations and wildland-urban interfaces (WUI). As a result, a WER may unfold within diverse environmental, topographical, and societal contexts. Environmental factors which may affect the system’s operations include “difficulty in accessing the terrain”, “fuel type”, “availability of natural bodies of water”, “weather”, “wildlife”, “human population”, “infrastructure”, and “natural barriers to fire propagation”. Missions addressing different objectives such as “detection and localisation of fire outbreaks”, “fire propagation monitoring”, “fire suppression”, and “mapping of the burned area” (see Section 4.2.2) require different *modes of operations* within each *operational environment*. In order to cope with diverse *operational environments* and meet *stakeholders* requirements, the WER system must exhibit adaptability and flexibility. For example, the detection and localisation of fire outbreaks heavily depends on visibility, which can be affected by day-night status, smoke, and weather (Alkhatib, 2014). Such conditions can affect the accuracy and detection speed, and limit the use of some reconnaissance resources available to the system. In turn, suppression operations are affected by the characteristics of the fire (type, size, intensity, rate of spread), smoke, terrain, vegetation, weather, and day-night status (Walsh et al., 2020). These conditions inform the intensity and strategy of the response, and constrain operations. Responding to larger, more severe, and faster spreading wildfires evidently requires more resources such as water or fire retardants, larger UAV fleets, higher numbers of firefighters, and more equipment. It is important to highlight here that a swarm of self-organising UAVs comprises a robust, resilient, adaptable, and scalable system (Tavakol Sadrabadi et al., 2024).

Whilst leveraging the power of autonomous, intelligent UAV swarms, the WER system is still human-centred, with human firefighters at its core. The UAV swarm is the WER sub-system that provides *(i)* real-time aerial monitoring and situational awareness, *(ii)* precise estimations of fire behaviour and propagation, *(iii)* decision-making support for fire management, search and rescue, and evacuations, *(iv)* delivery capabilities (e.g. firefighting tools, first aid kits, food, water), and *(v)* autonomous fire suppression capabilities (Tavakol Sadrabadi et al., 2024).

4.3 System Feasibility Analysis

Once the stakeholders requirements are stated (including objectives and constraints), feasible alternatives for the WER system must be considered taking into account the operational scenarios, costs, timeliness, and available technologies. For example, a variety of environmental and meteorological factors and conditions such as fog, haze, cloud cover, wind and turbulence, precipitation, temperature and humidity, lightning, tornadoes, and so forth, have the potential to impact UAV operations. Some of these may be defined as severe hazards or conditions, and impose serious risks on the operators and other personnel (Ranquist E, 2017), possibly rendering the system infeasible under such conditions (Tavakol Sadrabadi et al., 2024).

During operations aimed at early fire detection and localisation, the size of the area to be monitored, the estimated fire risk, and the estimated severity of the resulting hazard have a great influence on the design of the system and the technology adopted (e.g. static sensors, fixed-wings, multi-rotors, swarm-size, satellites). During fire suppression operations, the heat released from the burning front drives air temperatures to extremes and puts both UAVs and firefighting personnel in dangerous situations facing strong and turbulent wind conditions (Tavakol Sadrabadi et al., 2024).

The horizontal wind velocity within a wildfire may vary significantly under different fuel and topographical conditions, e.g. between 1.4 m/s and 26 m/s (Cruz & Alexander, 2019b). In turn, the vertical wind velocity may also be of great importance as it pushes the UAV upwards, with the potential to overturn it. For example, airborne cloud radar measurements (Rodriguez et al., 2020) indicated that, under extreme conditions of the Pioneer fire, the updraft and downdraft velocities reached maximums of 60 m/s and 30 m/s, respectively (Tavakol Sadrabadi et al., 2024). In order to address the wind effect on the UAVs, different approaches and methods are being utilised, such as the design of enhanced controllers (Olaz et al., 2023) and enhancing the structural design of UAVs (Peña et al., 2022). Alternatively, smaller off-the-shelf extreme-weather UAVs are available in the market. For example, the Sky Mantis 2 (Evolve Dynamics Ltd., 2024) is advertised to be able to operate with winds of 75 km/h and under heavy rain. With a payload of 2 kg, it may be used for dropping swarms of fire suppression balls, though it is limited to a maximum operational temperature of 50 °C. Nonetheless, the UAV temperature resilience issue is also being addressed by different studies (e.g. (Myeong et al., n.d.)).

Having said the above, the implementation of specific risk reduction and UAV safety technologies and methodologies can make such a system viable. A swarm like this should have a variety of sensors and safety systems to provide the necessary redundancy, thermal insulations to prevent thermal explosions or battery damage from high ambient temperatures, and continuous monitoring of the UAVs' internal devices and charge levels.

4.4 System Requirements Analysis

System requirement analysis is a crucial step in conceptual system design, establishing the basis for functional design by prioritising essential needs over implementation details (Faulconbridge & Ryan, 2002). When it comes to fully autonomous BVLOS firefighting missions, certain requirements and significant shortcomings need to be addressed to ensure these systems are reliable and safe enough to be utilised in such challenging and dangerous missions. This section briefly discusses the most important requirements and limitations of such a system, with Fig. 4.2 presenting an overview.

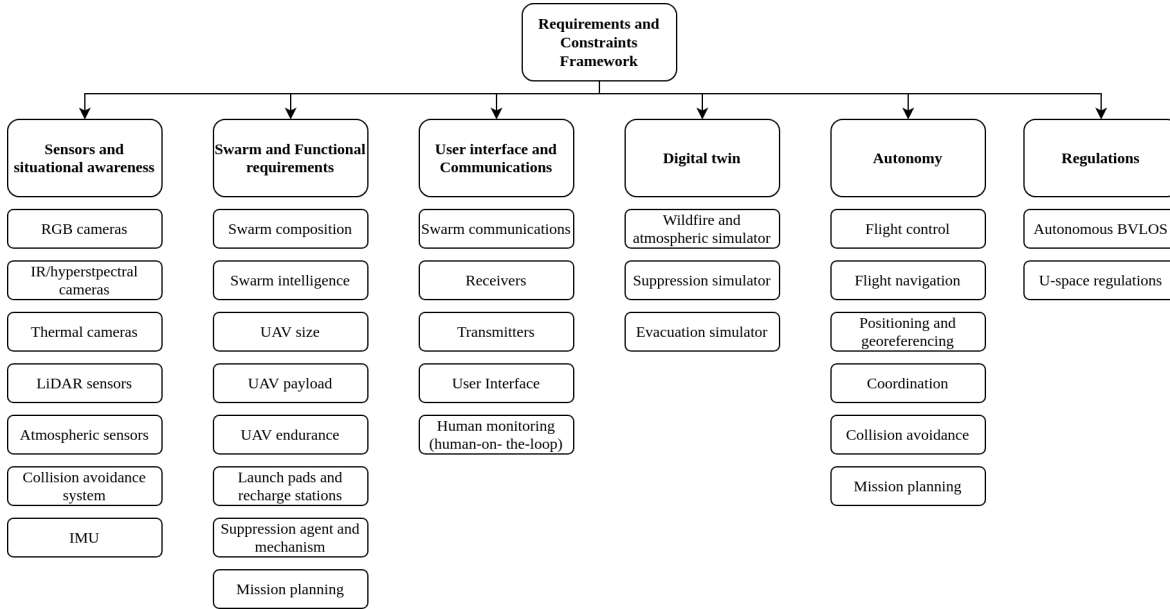


Figure 4.2: Overview of a UAV swarm system requirements (Tavakol Sadrabadi et al., 2024).

4.4.1 Mechanical and operational requirements

Safe operation of the individual UAVs within the system, and their interactions and cooperation with external elements such as manned aircrafts and human land crew is of high importance to the UAV swarm function. For example, UAVs operating

in a wildfire environment should be able to withstand extreme conditions, including high temperatures and turbulent winds. The temperature of the ambient environment during suppression operations could be as high as $\sim 80^{\circ}\text{C}$ (Belén et al., 2021), which can significantly affect the UAV performance. Currently, no commercial off-the-shelf UAV could operate in high temperatures close to the values that take place in a wildfire environment. It should be noted that even temperatures of up to $\sim 60^{\circ}\text{C}$ substantially reduce battery lifetime and its capacity, damaging the lithium-ion battery (N. Li et al., 2021), which is detrimental to the system’s functionality. Consequently, the UAVs should be temperature agnostic in order to be able to maintain safe operation, especially for those units that participate in direct suppression activities. Apart from the battery performance, temperature variations are also detrimental to the structural integrity of the UAV frame, while lower air density reduces the thrust generated by the motors (Ranquist E, 2017) and therefore the UAV payload capacity.

In addition to the high temperature, the turbulent wind and smoke in a wildfire environment could increase the probability of aircraft accidents. High wind speeds reduce the endurance time of UAVs and easily divert them from their original trajectory or even turn them upside down (Ranquist E, 2017). Therefore, the UAV resistance against horizontal and vertical gusts and turbulence is of great importance, and needs to be considered when designing UAVs for wildfire environments. Furthermore, smoke exhaled from the burned vegetation increases the noise in the data acquired by sensors like RGB cameras and LiDARs (Kyuroson et al., 2023), hence limiting their functionality required for maintaining situational awareness and autonomous operation of the UAV (Tavakol Sadrabadi et al., 2024).

Launch pads and recharging stations are essential components of any UAV-based system (Ausonio et al., 2021; Karvonen et al., 2023), supporting their continuous operation. A UAV launchpad or docking station is a multi-functional system that supports UAVs in various ways, including safe landing and take off, recharging and replacement of batteries and payloads, and possibly the required space for storing them. This enables the swarm to operate over long periods of time. UAV docking systems could be either mobile or fixed during the mission (Grlj et al., 2022). A range of fixed and mobile docking systems have been developed, including the DJI dock (DJI Enterprise, 2023). A detailed survey of these technologies is beyond the scope of this research.

Suppression agents and methods encompass a variety of different agents available for use in fire suppression activities, including water, surfactants (wetting agents), class A foams, fire retardants, and fire gels (Group, 1996). Compared to air tankers, UAVs have a limited payload capacity prompting researchers to propose some innovative solutions to tackle this limitation, including the use of fire extinguishing balls (Soliman et al., 2019), tethered firefighting hose (Viegas et al., 2022), or water spraying systems that mimic rainfall (Ausonio et al., 2021) to maximise the evaporation and hence reduce

the temperature of the burning fuel facilitating suppression (Tavakol Sadrabadi et al., 2024).

Generally, the amount of required suppressant is directly linked with fire intensity. Thus, the primary concerns of using suppression agents like water are using the right amount, with the correct form, and in the right place to increase the chance of success (Group, 1996). Apart from the considerably lower costs, one of the main advantages of UAVs over air tankers is that they can be equipped with advanced technologies that facilitate the calculation of the critical amount of suppressant required, and can deliver it in the optimal form and place to maximise the effectiveness of the suppression operation. Therefore, some researchers have tried to calculate the required amount of suppressant liquids, such as water, for different fire conditions (e.g., rate of spread or fire intensity) and fuel types when utilised in UAV systems (see (Ausonio et al., 2021)). In addition to the amount, the form of water delivery to the fire affects its effectiveness in absorbing heat and suppressing the flames. For instance, delivering water in a spray or fog form offers higher efficiency than a straight stream of water. (Group, 1996).

Distance from suppressant resources is also important for the uninterrupted operation of the system. Generally, air tankers and helicopters can access suppressant sources such as lakes and rivers located kilometres away from the main fire scene. Conversely, UAVs have limited endurance, which limits their flight range. Therefore, having access to a nearby water source or other suppression agents is critical for the effective operation of a UAV swarm (Tavakol Sadrabadi et al., 2024).

4.4.2 Sensors and situational awareness

Situational awareness could be defined as the ability to perceive elements in the environment within a volume of time and space, understand their meaning, and project their status in the near future (Endsley, 1995). A UAV swarm should be able to maintain its situational awareness, constantly transmit environmental information to the command and control centre, receive instructions, and carry out the assigned tasks autonomously throughout the operation. For the UAV system to carry out its mission safely within its operation environment, it must be able to evaluate its environment status and make timely decisions. Utilising data fusion and intelligent system health management can render such status assessments possible (Hussein et al., 2021).

Apart from structural and flight necessary sensors, UAVs are capable of carrying a range of sensors with various applications in environmental remote sensing, including RGB, infrared (IR), thermal, and multi-spectral cameras; light detection and ranging (LiDAR) sensors; and atmospheric measurement sensors such as temperature sensors, humidity sensors, PM and gas sensors (Akhloufi et al., 2021; Keerthinathan et al., 2023), wind probes, and anemometers (Prudden et al., 2018). Spectral sensors such as RGB, thermal, and IR cameras—e.g. near-IR (NIR), red-edge (RE), and shortwave IR (SWIR)—are the most prevalent type of sensors mounted on UAVs to assist in wildfire monitoring and response tasks. Spectral property analysis is made possible by the cameras' ability to record radiation from the material or object under observation at

various wavelengths and frequencies. A spectral image is hence created by recording the intensity of radiation that the camera detects at each frequency band as a value for each pixel (Akhroufi et al., 2021; Keerthinathan et al., 2023), which then needs to be localised or geo-referenced to be used as actionable data or as input into the fire predictive models. LiDAR sensors are also extensively used for various applications, such as vegetation mapping (Münzinger et al., 2022), fuel and burn severity mapping (Braziunas et al., 2022), and sub-canopy forest structure detection. The main drawback is that their performance deteriorates in adverse weather conditions such as snow, fog, or rain (Dreissig et al., 2023), potentially affecting UAV operations in smoke-covered environments during wildfires. Unlike LiDAR sensors, the performance of ultrasonic or sonar sensors is not affected by weather conditions. They are ideal for outdoor use because they offer broad coverage as well. However, radars' low output resolution prevents them from providing precise object dimensions (Partheepan et al., 2023), which limits their use in wildfire monitoring tasks. Hence, given that a single sensor may not be able to meet all the situational awareness requirements, each UAV in the swarm must be equipped with a specific set of sensors based on its unique operational needs, in addition to the standard sensors essential for autonomous flight and communications (Tavakol Sadrabadi et al., 2024).

4.4.3 Autonomy and decision making

The National Institute of Standards and Technology (NIST) defines autonomy as the ability of a drone to operate independently, including sensing, perceiving, analysing, communicating, planning, decision-making, and taking action to achieve its objectives (Tavakol Sadrabadi et al., 2024). It may be categorised into four levels: (i) full autonomy, when operation requires no human intervention; (ii) semi-autonomy, when tasks involve different levels of human-robot interaction; (iii) tele-operation, when a human operator uses feedback to control and assign tasks; and (iv) remote control, when the operator directly controls the UAV's actuators (Huang, 2004).

A UAV swarm system requires a high level of autonomy. The system requirements for an individual UAV to fly autonomously can be classified into: (i) *control*, (ii) *flight management*, and (iii) *path planning* (Hussein et al., 2021). In addition, *perception* is an inherent part of autonomous flight management and planning as the control algorithms of the UAV rely on the data provided by the perception sensors (Campion et al., 2019). Flight control and navigation, as well as the UAV positioning system, are also fundamental functions of the autonomous system that enable safe operation (Hussein et al., 2021). Besides, for the UAV to safely navigate from its current location to the desired destination, a series of functions, including flight planning, mission scheduling, fail-safe protocols, contingency management, conflict resolution, and obstacle detection and avoidance, must be executed (Tavakol Sadrabadi et al., 2024). UAV positioning is another important element for autonomous navigation, which may be achieved through technologies like *simultaneous localisation and mapping* (SLAM) or GPS sensors (Hussein et al., 2021).

In a multi-robot or swarm system, decisional autonomy comprises four main capabilities: (i) task allocation, which means dividing tasks among the robots; (ii) mission planning, scheduling, and refinement, which means converting tasks and missions into feasible sequences of actions while taking environmental conditions and UAV capabilities into account; (iii) coordination, which deals with resource conflicts and planning cooperative tasks to guarantee consistent actions among a group of robots; and (iv) supervision and execution control, which manages encountered circumstances and guarantees proper task execution (Lacroix et al., 2007).

4.4.4 Swarm communication and coordination strategy

An autonomous UAV swarm allows for a single operator to manage and control a group of UAVs instead of a group of operators controlling individual UAVs. UAVs in the swarm exchange information with one another, and self-coordinate to achieve a common goal. It is virtually impossible for human operators to process the shared information efficiently, reach consensus, and coordinate collective, cooperative actions. This makes autonomous swarms significantly more efficient, responsive, and timely than collections of human-controlled robots in a variety of situations (Arnold et al., 2019).

Swarm communication and coordination can be categorised into centralised (infrastructure-based) and decentralised architectures. Centralised communication involves direct communication between all UAVs and a central command center, making the system semi-autonomous (Akhroufi et al., 2021; Campion et al., 2019). While it benefits from real-time computation and optimisation, it has drawbacks like susceptibility to attacks and restricted communication range in remote and harsh wildfire environments. Decentralised architecture involves UAVs communicating with each other and planning collectively. They rely on onboard processing power, enhancing redundancy but increasing payload and reducing endurance. In addition, it introduces higher complexity, requiring distributed coordination algorithms for implementation (Campion et al., 2019). However, given the typical operational conditions of a UAV swarm suppressing a wildfire, which often involve BVLOS operations, a decentralised architecture would inherently be a superior choice provided that sufficient safety mechanisms are embedded into the system, such as emergency landing, return-to-home (RTH), and alternative communication such as satellite communications (SatCom) (Tavakol Sadrabadi et al., 2024).

Collective behaviours emerge from local UAV–UAV and UAV–environment interactions via self-organisation. This results in a swarm robotic system that is scalable (up and down), resilient to failure, and flexible in response to changing environmental conditions (Trianni & Campo, 2015) such as the harsh and highly dynamic environment of a wildfire event. These can be attained through meticulously hand-designed local rules

for a desired collective behaviour to emerge often accomplished through a bio-inspired strategy (reproducing baseline behaviours), or via some automatic design method using evolutionary-based techniques (evolutionary swarm robotics) or multi-agent reinforcement learning (MARL) methods. Some baseline behaviours include (i) synchronisation (coordination of actions); (ii) coordinated mobility (coordinated flight to preserve a stable spatial organisation); (iii) aggregation (gathering in a specific area), (iv) collective exploration, and (v) decision-making (Trianni & Campo, 2015). Whatever the design method, the swarm robotic system exhibits swarm intelligence (not every group of UAVs makes a swarm) (Tavakol Sadrabadi et al., 2024).

4.4.5 User interface and human-robot interaction

A user interface (UI) in a human-robot system is a communication platform that makes it feasible for human users to interact with the robot and exchange information (Thippeswamy et al., 2022). Conventional robotic systems require human decision-making, planning, action approval, and close human-system interaction. Such configurations are generally defined as *Human-in-the-Loop* systems. With the development of artificial intelligence, however, fully autonomous systems are now at the centre of attention. *Human-in-the-Loop* systems are capable of autonomous decision-making and execution without direct human control. However, human operators are still expected to perform monitoring and supervisory roles (Agrawal, 2022). The UAV swarm system may be supervised and monitored by fire managers and fire agencies, meaning that the UI should be simple and easy to use for user agencies (Tavakol Sadrabadi et al., 2024). On the other hand, it should be comprehensive and inclusive enough to facilitate situational awareness for the user or command and control centre as a poor UI can become a source of problems and failures in robotic systems (Agrawal, 2022).

4.4.6 System digital twin

The 2022 NASA workshop highlighted issues in the current firefighting operations, including an overload of unhelpful data, poorly scaled information from predictive services, and communication limitations that lead firefighters to rely on intuition rather than actionable data (NASA, 2020). In order to estimate wildfire behaviour and make informed decisions, the WER system needs real-time and accurate information about the wildfire's status, and reliable estimations of its future behaviour and extent (Tavakol Sadrabadi et al., 2024).

A digital twin may be described as an integrated model that incorporates different discipline-specific models (e.g. architecture, mechanical, electrical, software) and information from many existing technologies to monitor real-time situations and estimate future scenarios (D'Amico et al., 2019). Integrating these partial models is important as it provides the capability to study the multifaceted behaviours that occur from interactions between diverse system components (Vrabič et al., 2018). Different studies have focused on developing digital twin frameworks of UAV swarm monitoring systems

(Salinas et al., 2023) and wildfire incidents (Jiao et al., 2023). However, the digital twin required for a UAV swarm-based WER system interacting with the environment and participating in suppression, evacuation, and monitoring tasks must be able to consider (i) fire propagation, (ii) atmospheric conditions variations, (iii) UAV swarm actions and their effects on the environment, (iv) evacuation behaviour and traffic modelling, and (v) the effect of suppression activities on the fire dynamics. Besides, these simulations should be executed in faster-than-real time to be utilised in response activities. An accurate numerical solution over a large domain is prohibitively computationally expensive (Bakhshaii & Johnson, 2019); hence, a possible solution is to use faster-than-real-time reduced-order models (e.g. (Grasso & Innocente, 2020b)) and improve the estimations through other techniques such as data-assimilation (Tavakol Sadrabadi et al., 2024).

4.4.7 Performance requirements

In order to provide a basis for evaluating the effectiveness of the proposed system, it is necessary to define measurable quantities to offer insight into how the system is functioning. A Technical Performance Measure (TPM) is a measurable parameter that provides a way to compare the system function to the requirements that it needs to satisfy (Garrett et al., 2011).

Even though performing an exhaustive review of performance assessment metrics for such systems is beyond the scope of this thesis, it is fair to note that the technical performance measures for a UAV-swarm-based WER system encompass a range of aspects important to different stakeholders at different levels of the system. For example, at the system level and in terms of evaluating the effectiveness of the response system, performance assessment metrics may include parameters such as average response time, suppression costs, burned area, fire detection and alert time, fire and spotting localisation and mapping accuracy, system development, maintenance and operational costs, accuracy of fire behaviour estimations, human crew casualties, and facilities entrapment (Tavakol Sadrabadi et al., 2024).

On the other hand, the system can be evaluated based on the functional efficiency of the UAV swarm as a subsystem of the wildfire response system, which may include metrics for assessing the (i) system robustness and fault/error tolerance which may be discussed in terms of the effect of a failed agent on group performance and on other working agents, (ii) scalability which reflects on the system performance improvement with increasing the swarm size, and (iii) the system adaptability which reflects system capacity to adjust and respond to the external circumstances and dynamic environment (Milner et al., 2023). In terms of autonomous navigation and motion planning at the UAV level, the performance can be evaluated by utilising metrics for trajectory evaluation such as trajectory corrected distance, maximum curvature, minimum distance from obstacles, etc (Ermacora et al., 2020). From the standpoint of airworthiness and operational capabilities, the UAV system performance may be evaluated utilising metrics like flight endurance, range, collision avoidance, terrain following, energy con-

sumption, portability and deployment time, wind resistance, navigation and autonomy, safety measures, payload capacity, suppression effectiveness, communication range and quality, sensor resolution, scalability, cost-effectiveness, environmental impact, human-robot interaction, system reliability, and redundancy, among others (Tavakol Sadrabadi et al., 2024).

4.5 System-Level Synthesis

System-level synthesis is the step in which the abstract concepts and requirements are turned into a feasible architecture for implementation. It includes establishing relationships among system elements and forming an initial system configuration to satisfy system requirements even if such a configuration is not final and could be expected to undergo significant changes as the design matures (Faulconbridge & Ryan, 2002). This section of the paper proposes a possible swarm composition and defines the functional relationships among the WER system elements (Tavakol Sadrabadi et al., 2024).

4.5.1 Swarm composition

The proposed UAV swarm must be capable of carrying out WER missions autonomously, without direct human intervention other than having a human in the loop. However, a singular UAV type may be inadequate for the varied demands of different WER operations. For instance, heavy-lift UAVs may not be suitable for long-range inspection missions, while fixed-wing UAVs—with higher wind resistance than multi-rotors—prove more reliable for monitoring fire fronts and operations near visible plumes (Ranquist E, 2017). Nevertheless, the very important task of measuring atmospheric characteristics—which holds the main emphasis of this thesis—can be allocated to every type of UAV which in turn highlights the flexibility and scalability of the proposed model in chapter 8. Although there is research on the use of heterogeneous swarms, the original idea of swarm intelligence and swarm robotics is that agents are quasi-identical so that intelligence emerges from the interactions among similarly capable individuals in a massively redundant system (no single point of failure). Thus, single individuals are disposable with a graceful degradation of system performance. Likewise, UAVs may be incorporated into the swarm to enhance its performance, even during operations. Therefore, the WER system is proposed to have at least one quasi-homogeneous swarm composed of quasi-identical fixed-wing UAVs for tasks such as long-range monitoring, and one quasi-homogeneous swarm composed of quasi-identical multi-rotors for tasks such as fire suppression and precision deliveries. Although the spirit of swarm robotics is to make use of numerous relatively inexpensive robots, certain tasks may require a trade-off between many small and few heavy-lift UAVs. Hence, the multi-rotor swarm could potentially be split into one swarm of lightweight and another of heavy-lift multi-rotors for different tasks. There may—and usually will—be information

exchanged between swarms, but they will not self-organise to collaboratively perform a given task (i.e. they will not conform a single heterogeneous swarm). The preliminary proposed composition includes (i) swarm of fixed-wing UAVs for long-range and long-endurance reconnaissance and monitoring missions; (ii) swarm of small to medium-size multi-rotors for local monitoring tasks as well as for supporting or performing fire suppression (e.g. autonomous suppression or ignition of prescribed fires or backfires); and (iii) swarm of heavy-lift multi-rotors for supporting or performing fire suppression and equipment delivery missions (e.g. to support and protect firefighters). Heavy payloads requirements may also be met by means of collaborative transport using only relatively small multi-rotors, thus making use of only two swarms at the expense of adding complexity to the system. Figure 4.3 shows different tasks to which each of these swarms could be assigned (Tavakol Sadrabadi et al., 2024).

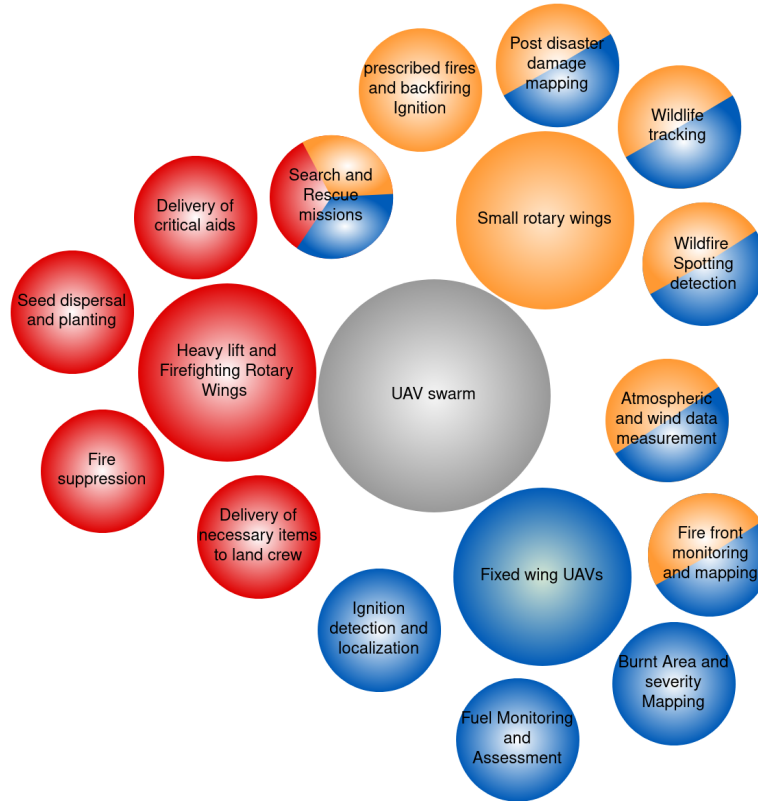


Figure 4.3: *WER missions to which each of the three proposed UAV swarms could be assigned, adopted from (Tavakol Sadrabadi et al., 2024).*

4.5.2 Potential UAV selection

A product planning matrix known as the *House of Quality* or the *Quality Function Deployment* (QFD) may be used to relate stakeholders' requirements to lower-level

Table 4.2: *Example of importance level of requirements for three different tasks or UAV types during a WER (Tavakol Sadrabadi et al., 2024)*

Requirement	Importance level from stakeholders'/customers' point of view		
	Long-range reconnaissance fixed-wing UAVs	Small multi-rotors for local monitoring and/or fire suppression	Heavy-lift multi-rotors for fire suppression and/or equipment deliveries
Portability	3	3	3
Fast deployment	0	3	0
High resolution data	9	9	9
Day and night operation	9	9	9
Controllability	9	9	9
Safety	6	6	6
Cost effectiveness	6	6	3
Long-time flight	9	0	0
Long-range flight	9	0	0
Disaster monitoring and assessment	6	6	0
Temperature resilience	3	6	9
Carrying dragon balls	0	9	9
Participation in fire suppression	0	6	9
Participation in emergency recovery	0	0	6

technological specifications that will meet them (Kiran, 2017). Quality Function Deployment (QFD) is generally a planning process that uses a quality approach to designing, developing, and implementing new products while considering the customer's needs and importance levels. It is a widely used method in industry and numerous companies active in the automotive, shipbuilding, electronics, aerospace, utilities, leisure and entertainment, financial, software, and other industries have used QFD with great success (Kiran, 2017). The Voice of the Customer (VOC) is the term used in QFD terminology to describe the process of determining customer requirements (Tavakol Sadrabadi et al., 2024). The other side of the QFD coin is called voice of the organisation (VOO), which assesses whether the business can meet the customers' needs under the current conditions by conducting a gap analysis of the team and the process to evaluate the company's capabilities. However, this can easily be translated into the "How questions" or the technical performance measures (TPMs). The first step in QFD is to form a planning matrix that outlines the relative importance of every requirement the team tries to meet. The next step is to identify the level of relationships between customer requirements and engineering specifications or TPMs (Kiran, 2017).

UAVs in a WER system will be used to perform a wide range of tasks during the different phases (see Fig. 2.10). The importance of TPMs can vary based on the specific function and the corresponding stakeholders' requirements for each phase or specific task. An example of key stakeholders' requirements and the corresponding importance levels is shown in Table 4.2 for the three types of UAVs discussed in the previous section. The QFD approach is used to determine the relative value of each TPM. The relative importance of TPMs may be used to design a system tailored to the requirements or to choose from commercially available options (Tavakol Sadrabadi et al., 2024).

Even though some companies are currently working on developing solutions such as UAV-based monitoring systems for supporting WER systems, they are still mainly in the research and development stages and typically utilise frameworks specifically tailored to their operational needs. As a result, public access to the specs is limited. Alternatively, a list of commercial off-the-shelf frameworks manufactured by different companies for use in precision farming and/or other activities such as land mapping may be utilised (see Tables 4.3 to 4.5), although they may lack high-temperature resilience. Considering that the UAV swarm system would be responsible for carrying out different tasks in the context of the wildfire emergency response, the UAV swarm is hence formed from a combination of different UAVs for different tasks. It is clear then that the requirements, their level of importance, and the relationship between different TPMS and those requirements for each UAV would be different. Consequently, three different QFD matrices are formed and presented in tables 4.6 to 4.8 for three different UAV types that would form a preliminary combination of the UAV swarm. The top row of the QFD matrix consists of potentially relevant technical performance measures (TPMs). The middle section then gives the relationships between customer requirements and these technical performance measures with zero representing no relationship and 9 representing a strong relationship in this example. The sum of the product of the customer requirement importance and the relationship value then gives the Importance value for each TPM. Finding the relative importance then yields the weighting importance matrix for each TPM that is then used in UAV ranking utilising a Multi-Criteria Decision Making (MCDM) method (Tavakol Sadrabadi et al., 2024).

It is worth mentioning that all importance levels and the values that represent the relationship between individual TPMs and customer requirements are estimated based on the author’s understanding of the topic and might not be necessarily accurate (Tavakol Sadrabadi et al., 2024).

Table 4.3: *Potential alternatives for long-range aerial imaging UAVs (Tavakol Sadrabadi et al., 2024).*

UAV type	Flight Range (km)	Data link range (km)	Max Endurance (hours)	Maximum payload (kg)	Cruise Speed (km/h)	Maximum windspeed (m/s)	Maximum temperature (deg celcius)	Camera resolution (megapixel)	weight (kg)	UAV Length	Wing span	Price (£)
WingtraOne Gen II	60	10	1	0.8	58	18	40	42	3.7	0.68	1.25	25.5k
Atmosuav Marlyn	50	7	0.83	1	65	15	40	61	5.7		1.6	26k
AgEagle eBee X	37	8	1.5		70	12.8		24	1.6		1.16	20k
deltaQuad Pro Map	120	150	2	1.2	65	14	45	42	5	0.9	2.35	17k
Quantum Systems Trinity F90+	100	7.5	1.5	1	61	12	50	42	4.5		2.4	19k
Delair UX11	53	160.934	1.33	0.2	54	12.5	49	21	1.6	0.75	1.2	15k
Boeing-Insitu ScanEagle	1500	100	20	5	148.2		49			3.1	1.7	2.64M
SkyRobot FX450	2500	2500	20	30	125		55		100	4.1	7.2	
Stalker VXE30	432.914	160.934	4	2.5	93		49		20	2.6	4.9	

MCDM focuses on organising and resolving multi-criteria planning and decision-making issues. The goal is to assist decision-makers who are dealing with these issues. Usually, there isn’t a single best answer for these kinds of issues, so decision-makers preferences must be used to distinguish between alternative options. Therefore, we require tools that assist the decision-maker in concentrating on the alternatives or chosen options. Typically, some criteria must be ”traded off” for others. Hence, an

Table 4.4: *Potential alternatives for small monitoring and response rotary wing UAVs (Tavakol Sadrabadi et al., 2024).*

UAVs	Max air speed (km/hr)	Max Endurance (mins)	Communication Range (km)	Max Wind speed (m/s)	Max payload (kg)	weight (kg)	MTOW (kg)	Max Temperature	folded volume (m ³)	Price (£)
DJI Mavic 3 Enterprise	75	45	15	12	0.1	0.92	1.05	40	0.0019	4800
Yuneec Typhoon H +	70	25	1.6	15			2.1	40	0.0700	2100
Autel robotics evo ii (Dual 640T)	72	35	15	20			2	40	0.0030	4600
Parrot Anafi USA	53	32	3.99	14.7	0.15	0.5	0.65	50	0.0020	7800
DJI Matrice 30T	83	41	15	12		3.77	4.1	50	0.0150	8500
FreeFly Alta X	95	50	3.2		15	11	34.86	50	0.2977	23000
DJI Matrice 600	65	35	5	8	5.5	9.6	15.1	40	0.2321	5000
Acecore Neo x8	91	25	10	20	9	7.3	16.3	50	0.3651	33000
Vulcan UAV D7	80	40		13.4	10	14	40	35		

Table 4.5: *Currently available UAV platforms potentially suitable for amidst-fire response and post-fire recovery phase (Tavakol Sadrabadi et al., 2024).*

UAV model	type	Max air speed (km/hr)	Max Endurance time With payload (min)	Communication range (km)	Max Wind speed (m/s)	payload	weight (kg)	MTOW (kg)	Max Temperature	Folded Volume M ³	max speed (km/hr)	price (£)
Aeronavics SkyJib	eight-motor coaxial multi-rotor	90	45			7		24			90	
Aeronavics ICON	eight-motor coaxial multi-rotor	100	20			25		50			100	
DJI Agras T40	eight-motor coaxial multi-rotor	36	6	5	6	51	50	101	50	0.71	36	\$26K+
DJI Agras T30	eight-motor coaxial multi-rotor	36	7.8	5	8	40	26	78	45	0.67	36	£23k+
Hylio AG-272	octocopter		10			68						£65k
Hylio AG-230	octocopter		10			30						£37k
DH- S.L.	octocopter-		30			600						~£220K
WILD HOPPER	thermal engines											
DH- S.L-agro hopper	hexacopter	90	10		11	16	24.5				90	
Vulcan UAV D8	eight-motor coaxial multi-rotor	80	40		13.4	25	16	55				

MCDM is necessary when evaluating off-the-shelf UAV options. The *Technique for Order Preference by Similarity to the Ideal Solution* (TOPSIS) is employed in this study to rank the available alternatives (Chakraborty, 2022). The general purpose of any generic multi-criteria decision-making (MCDM) method is to rank M available alternatives of $A_i (i = 1, 2, \dots, M)$ based on N criteria $C_j (j = 1, 2, \dots, N)$. The relative significance of each criterion for ranking alternatives is presented through a weighting vector of $W_j (j = 1, 2, \dots, N)$. The performance ratings for all alternatives against each attribute form a decision matrix (X) in the following form (Chakraborty, 2022):

$$X = \begin{bmatrix} x_{11} & x_{12} & \dots & x_{1N} \\ x_{21} & x_{22} & \dots & x_{2N} \\ \dots & \dots & \dots & \dots \\ x_{M1} & x_{M2} & \dots & x_{MN} \end{bmatrix} \quad (4.1)$$

The core concept of TOPSIS is that the optimal solution is the one that is furthest from the negative ideal and closest to the positive ideal. An overall index that is derived from the separations between the ideal solutions and the alternatives is used to rank

them. The first stage in TOPSIS is to normalize the X matrix utilizing the following equation:

$$y_{ij} = x_{ij} / \sqrt{\sum_{i=1}^M x_{ij}^2} \quad (4.2)$$

This will then be multiplied by the weighting vector to form the weighted-normalised decision matrix V :

$$v_{ij} = W_j \cdot y_{ij}; (i = 1, 2, \dots, M; j = 1, 2, \dots, N) \quad (4.3)$$

$$V = \begin{bmatrix} v_{11} & v_{12} & \dots & v_{1N} \\ v_{21} & v_{22} & \dots & v_{2N} \\ \dots & \dots & \dots & \dots \\ v_{M1} & v_{M2} & \dots & v_{MN} \end{bmatrix} \quad (4.4)$$

The positive and negative ideal solutions are then formed as:

$$A^+ = [v_1^+, v_2^+, v_3^+, \dots, v_N^+] \quad (4.5)$$

$$A^- = [v_1^-, v_2^-, v_3^-, \dots, v_N^-] \quad (4.6)$$

where v_j^+ and v_j^- are selected as follows:

$$v_j^+ = \begin{cases} \max v_{ij}; & \text{for benefit type attributes} \\ \min v_{ij}; & \text{for cost type attributes} \end{cases} \quad (4.7)$$

$$v_j^- = \begin{cases} \min v_{ij}; & \text{for benefit type attributes} \\ \max v_{ij}; & \text{for cost type attributes} \end{cases} \quad (4.8)$$

The next step is to calculate the Euclidean distance of each alternative from the positive and negative ideal solutions:

$$S_i^+ = \sqrt{\sum_{j=1}^N (v_{ij} - v_j^+)^2} \quad (4.9)$$

$$S_i^- = \sqrt{\sum_{j=1}^N (v_{ij} - v_j^-)^2} \quad (4.10)$$

Finally, the overall preference score V_i for each alternative A_i would be obtained, which is then used to rank the alternatives:

$$V_i = \frac{S_i^-}{S_i^- + S_i^+} \quad (4.11)$$

Table 4.6: *Long range monitoring UAV HOQ (Tavakol Sadrabadi et al., 2024).*

		TPMs											
Customer requirement	Importance level	Flight time	Cruise speed	Maximum wind resistance	Cost	Payload capacity	Autonomy level	Collision avoidance	Max Temperature	Communication range	Uav mass	UAV volume	Multi sensors
portability	3	0	0	0	0	0	0	0	0	0	9	9	0
Fast Deployment	0	0	0	0	0	0	0	0	0	0	6	6	0
High resolution data	9	0	0	0	6	3	0	0	0	6	0	0	9
Day and Night operation	9	0	0	6	6	6	9	6	3	0	0	0	9
Controllability	9	0	0	3	3	0	6	6	0	3	3	3	6
Safety	6	0	0	6	6	0	6	9	3	0	0	0	6
Cost effectiveness	6	6	0	3	9	3	0	3	3	0	3	3	9
Long time flight	9	9	9	6	0	0	3	3	0	3	0	0	0
name Long range flights	9	9	6	6	0	0	9	6	0	6	0	0	0
Distster monitoring and assessment	6	6	6	3	0	0	0	6	0	0	0	0	6
	Importance weight	234	171	261	225	99	279	297	63	162	72	72	342
	Relative Importance weight	0.103	0.075	0.115	0.099	0.043	0.123	0.130	0.028	0.071	0.032	0.032	0.150

Table 4.7: *Small monitoring and response rotary-wing UAV HOQ (Tavakol Sadrabadi et al., 2024).*

	TPMs												
Customer requirement	Importance level	Flight time	Cruise speed	Maximum wind resistance	Cost	Payload capacity	Autonomy level	Collision avoidance	Max Temperature	Communication range	Uav mass	UAV volume	Multi sensors
portability	3	0	0	0	0	0	0	0	0	0	9	9	0
Fast Deployment	3	0	0	0	0	0	0	0	0	0	6	6	0
High resolution data	9	0	0	0	6	3	0	0	0	6	0	0	9
Day and Night operation	9	0	0	6	6	6	9	6	6	0	0	0	9
Controllability	9	0	0	3	3	0	6	6	3	3	3	3	6
Safety	6	0	0	6	6	0	6	9	9	6	0	0	6
Cost effectiveness	6	6	0	3	9	3	0	3	6	0	3	3	9
temperature resilience	6	9	9	6	0	0	3	3	9	0	3	3	0
Carrying dragon balls	9	9	6	6	0	6	9	6	6	6	6	6	0
Disaster monitoring and assessment	6	6	6	3	0	9	0	6	6	6	0	0	6
	Importance weight	207	144	243	225	207	270	288	315	207	162	162	342
	Relative Importance weight	0.075	0.052	0.088	0.081	0.075	0.097	0.104	0.114	0.075	0.058	0.058	0.123

As an example, the TOPSIS method was applied to rank UAVs based on stakeholders' specifications and requirements weights from the QFD method (presented in Tables 4.6, 4.7, and 4.8), resulting in the preliminary selection of the DelatQuad Pro-Map for long-endurance/long-range monitoring tasks. DJI Matrice-600 and DJI Agras-T40 are potential selections for small and heavy-lift multi-rotors, respectively, as presented in Figure 4.4. All alternatives assume the same autonomy and collision avoidance capabilities, with missing values of TPMs filled with the minimum value of that TPM from other alternatives as a conservative assumption (Tavakol Sadrabadi et al., 2024).

It should be noted that the maximum endurance and flight range of the DeltaQuad is limited to 2 h and 120 km in ideal conditions, which exceeds what is achievable in a real wildfire. This suggests that multiple UAVs are required to ensure continuous area coverage, leading to increased expenses in terms of purchase and maintenance. Nonetheless, these costs remain considerably lower than those associated with military UAVs like ScanEagle or SkyRobot. Similar constraints are applicable to alternatives considered for smaller and heavy-lift multi-rotors in the preliminary swarm selection. Take, for instance, the DJI Agras T40, identified as the top commercially available option for heavy-lift firefighting UAVs. This model, however, offers a mere six-minute flight time when carrying its maximum payload. Furthermore, its maximum safe temperature and wind speed for operational conditions are limited to 50°C and 6 m/s, respectively, significantly lower than those encountered during a wildfire event.

Table 4.8: *Heavy-load response rotary-wing UAV HOQ (Tavakol Sadrabadi et al., 2024).*

	TPMs													
Customer requirement	Importance level	Flight time	Cruise speed	Maximum wind resistance	Cost	Payload capacity	Autonomy level	Collision avoidance	Max Temperature	Communication range	Uav mass	UAV volume	Multi sensors	
portability	3	0	0	0	0	0	0	0	0	0	9	9	0	
High resolution data	9	0	0	0	3	3	3	3	0	6	0	0	9	
Day and Night operation	9	0	0	0	6	6	9	9	9	0	0	0	9	
Controllability	9	0	0	6	3	0	3	3	3	3	3	3	6	
Safety	6	0	0	6	6	0	9	9	9	6	0	0	6	
Cost effectiveness	3	0	0	3	9	3	6	6	0	0	3	3	9	
temperature resilience	9	0	0	0	0	0	0	0	9	0	3	3	9	
Carrying Heavy payloads	9	9	0	6	9	9	0	0	0	0	6	6	0	
Participation in fire Suppression	9	9	6	6	9	9	9	9	9	6	6	3	6	
Participation in Emergency Recovery	6	9	6	3	9	9	9	9	0	6	6	3	6	
	Importance weight	216	90	225	387	306	342	342	324	207	234	189	450	
	Relative Importance weight	0.065	0.027	0.068	0.117	0.092	0.103	0.103	0.098	0.063	0.071	0.057	0.136	

Consequently, it can be inferred that existing commercially available alternatives for a heavy-lift response UAV require substantial enhancements in terms of resilience to temperature, endurance, and range before they can effectively contribute to a WER system (Tavakol Sadrabadi et al., 2024). To further elaborate on the gaps in commercially available UAVs identified above, Table 4.9 presents key hardware and operational requirements necessary for wildfire monitoring and response UAVs to operate in the wildfire environment.

Table 4.9: *Comparison of UAV hardware and operational requirements for wildfire operations at 40 m altitude.*

Requirement	Needed for Wildfire Ops	DeltaQuad Pro-Map	DJI Agras T40	Gap Identified
Endurance	> 2 hours (continuous coverage)	2 hours (ideal conditions)	6 minutes (full payload)	Severe (especially T40)
Max Temperature Tolerance	> 70°C	50°C	50°C	Insufficient
Max Wind Speed Tolerance	> 12 m/s	12 m/s	6 m/s	Insufficient (T40)
Flight Range	> 100 km (real conditions)	20 km (ideal conditions)	N/A	Moderate concern
Payload Capacity	> 30 kg	N/A	40 kg (but limited endurance)	Good (but endurance tradeoff)
Autonomy	Full collision avoidance, terrain following	Partial	Partial	Moderate
Redundancy	Required for safe operation in harsh conditions	Limited	Limited	Lacking

4.5.3 Functional relationships

The UAV swarm system will perform various functions to support the safety of human firefighters, shelter seekers, and other stakeholders. These may include reconnaissance, search and rescue, fire front monitoring, environmental data collection, data transmission for analysis and decision-making assistance, fire suppression, and delivery of critical supplies and equipment. Additionally, it may support post-fire damage assessment and emergency environmental recovery efforts. Figure 4.5 shows the functional process of the system's operational activities.

The operational process of the system typically commences with the onset of the wildfire season. At this stage, initial wildfire risk and danger estimations are made using satellite data and meteorological information. Next, long-range surveillance flights are planned using fixed-wing UAVs equipped with high-resolution cameras. They aim to identify potential ignition points in high-risk areas early, before the fire spreads.

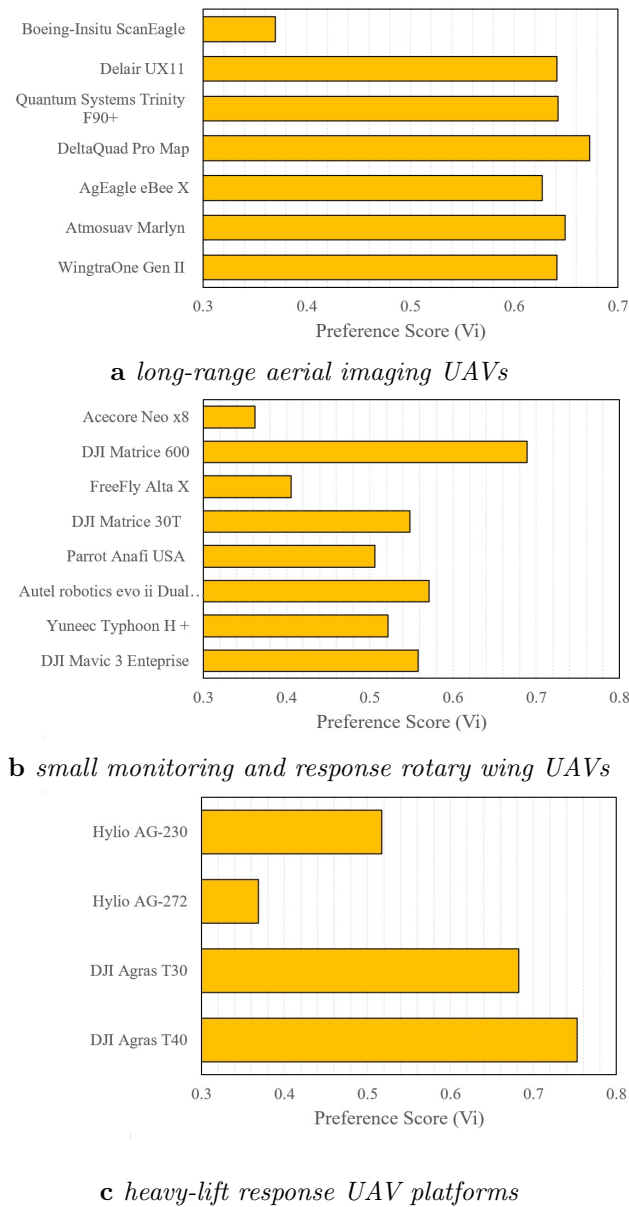
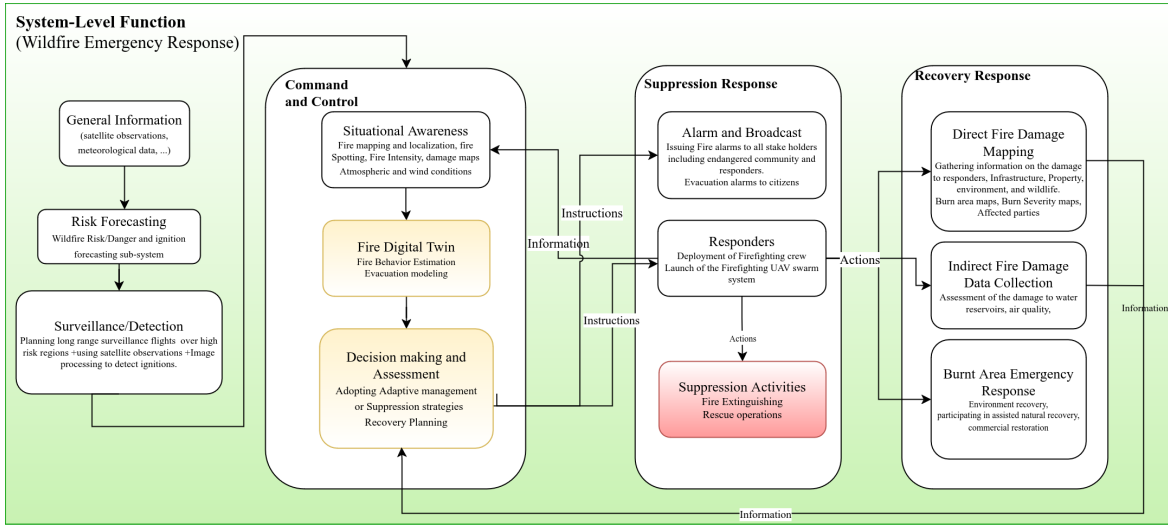
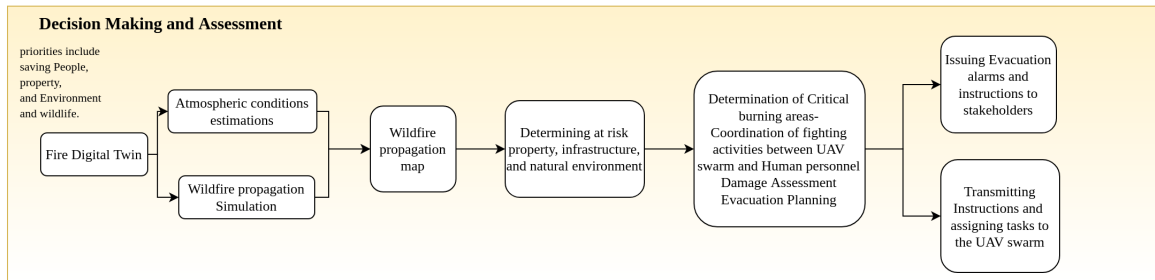


Figure 4.4: preference scores calculated for potential off-the-shelf alternatives for different types of UAVs in the swarm (Tavakol Sadrabadi et al., 2024).

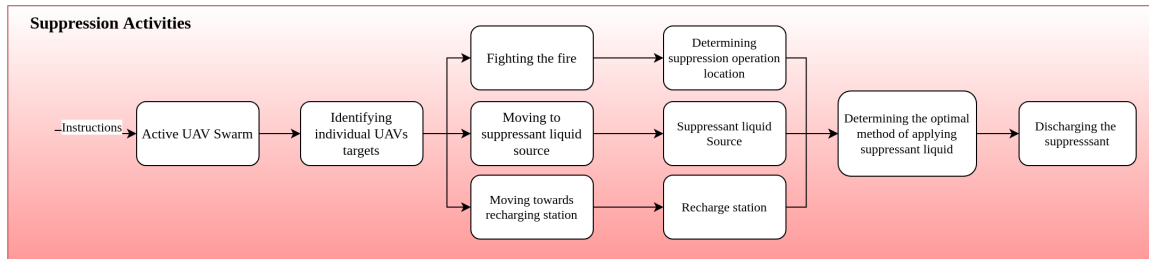
Confirmation flights and observations from other UAVs enhance accuracy, and reports from the public and/or other sources contribute to the reliability of the assessment. A detailed analysis of the fire's extent and conditions follows, considering factors like fire intensity, rate of spread, fuel conditions, and environmental variables. This data is crucial for maintaining situational awareness for the Command and Control Centre (CCC), and for creating a digital twin of the fire to predict its behaviour, plan its



a System level functional description



b Decision-making and assessment component level



c Suppression activities component level

Figure 4.5: Functional description of and relationships within the WER system, adopted from (Tavakol Sadrabadi et al., 2024).

suppression (required amount of suppressant, swarm size, suppression strategies), and design potential evacuation plans. While the CCC assigns tasks to the UAV swarm and other response teams, the swarm must operate autonomously (with a human in the loop) exchanging information with the fire digital twin. The latter is continually updated, enabling precise predictions of fire behaviour. The UAV swarm receives

instructions from a central hub, minimising human intervention. Management decisions are made in the CCC, ensuring coordinated operation (Tavakol Sadrabadi et al., 2024).

Emergency stabilisation is the top priority following a fire to save individuals, property, or natural resources (USDA Forest Service, 2020). The recovery response starts immediately after the fire is suppressed. In this phase, the UAV swarm would normally be responsible for carrying out high-resolution imagery and measurements of the burned area, and for delivering the information gathered to the CCC. This would then be used to provide accurate estimations of damage to infrastructure, property, wildlife, natural environment (e.g. soil and water bodies), and to construct burned area and burn severity maps to aid the design of emergency stabilisation programs and environmental recovery plans. The same swarm may be used for ecological recovery plans by planting seed pods and seedlings in vast areas within a short timeframe (Tavakol Sadrabadi et al., 2024).

4.6 System Design Review

The system design review (SDR) aims to *(i)* provide a formal evaluation of the conceptual design against specified requirements, *(ii)* communicate the intended design approach to key stakeholders, *(iii)* offer a platform for addressing and resolving interface issues, and *(iv)* document design decisions and approvals. Additionally, it aims to examine whether all requirements are fulfilled by the preliminary system architecture established during the system-level synthesis (Faulconbridge & Ryan, 2002). For example, the SDR should confirm that the system is feasible and would significantly improve the quality and effectiveness of the WER system, reducing the damage caused to the natural habitat, facilities, local properties, and infrastructure, and minimising human casualties. This would fulfil the requirements of insurance companies, authorities such as forest management services, land owners, and the natural environment (Tavakol Sadrabadi et al., 2024). With regards to the potential selection of UAVs in Section 4.5.2, the cost-effectiveness of UAVs was addressed by means of a multi-criteria decision-making process. A series of requirements such as those involving safety mechanisms, sensor fusion, autonomy units, and high-level swarm control algorithms can be progressively addressed as the design matures (Tavakol Sadrabadi et al., 2024).

Chapter 5

Effect of Vegetation, Terrain, and Wind Conditions on Wildfire Propagation Dynamics

Investigating the effect of vegetation type and height is of inherent importance when estimating fire propagation dynamics. Contrary to the effect of parameters such as wind and terrain, the effect of fuel characteristics on fire propagation dynamics is controversial and contrasting results are reported in the literature. This is even more challenging in sloped terrains where the combined effect of terrain slope, wind conditions and vegetation height could lead to unprecedented behaviours that are still not adequately studied. Consequently, this chapter attempts to cover this gap by performing a series of numerical simulations and combining the results with two contradictory experimental studies to investigate the effect of vegetation height and structure on fire propagation dynamics for different terrain slopes and ambient wind speed.

5.1 Grasslands and Wildfires

Wildfires can potentially devastate roads and other infrastructure, disrupt natural processes such as water supply, and cause immediate and long-term adverse effects on public health. In addition, such incidents may interfere with transport and supply chains, leading to road and business closures (United Nations Environment Programme, 2022). Grasslands cover up to 50 million square kilometres (37%) of the earth's terrestrial surface (O'Mara, 2012) and comprise more than 80% of the world's burned land (Leys et al., 2018). In the case of the United Kingdom, grasslands constitute almost 40% (Office for National Statistics, 2015), while in Australia, a substantial 70% (Innocent et al., 2023) of the land is covered by grasslands, which highlights the importance of studying grassland fires. The rate of spread of the fire (RoS) is generally a function of the intricate interplay of various topographical, weather, and fuel elements, including but not limited to atmospheric conditions -such as ambient wind speed, humidity,

temperature-, topographic conditions - such as slope-, and fuel condition -such as vegetation type, vegetation height, density, and moisture content- (Innocent et al., 2023; Moinuddin et al., 2021).

The next sections provide an overview of the simulation results performed in this study. This chapter aims to provide insight into the practical aspects of wildfire management concerning the effect of fuel structure on fire behaviour. Due to its importance in wildfire management and response planning, it mainly focuses on the rate of fire spread.

5.1.1 RoS as a function of wind speed

The rate of spread of fire (RoS) is inherently dynamic and oscillatory. However, a dynamic RoS is practically problematic for comparing different situations. Hence, a quasi-steady rate of spread of fire is calculated for each scenario, which reflects the average value of the dynamic behaviour of the fire. The quasi-steady rate of spread of fire is considered to be equal to the slope of the linear regression fitted on the fire front locations while it reaches a constant increase rate determined by a linear increase in the fire front location. However, determining the front location is challenging due to the variety of fuel height conditions. Consequently, the fire front location at each time instance is identified as the front point along the centerline of the field where the temperature exceeds 400 degrees Celsius, measured 25 cm above ground level. This height was chosen to minimize the pulsating effect of the flames on the measurements (Tavakol Sadrabadi & Innocente, 2025).

Figure 5.1 presents the calculated quasi-steady RoS as a function of the wind speed (u_{10}) for different terrain slopes, categorized with vegetation heights. Generally speaking, it could be observed that higher wind speed leads to a higher rate of spread regardless of the vegetation height and the bulk density. This increase mostly follows a linear trend, with the fuel with lower bulk density (Veg_2) indicating a higher RoS than the fuel with higher bulk density (Veg_1) on horizontal terrain conditions, except for very high wind velocities ($\approx u_{10} > 10$ m/s). Considering the combined effect of bulk density and wind velocity, it could be observed that regardless of vegetation height, for fuels with lower bulk density, the RoS is higher at moderate wind speeds (4–8 m/s). However, by increasing the wind speed, the RoS of fuel with higher bulk density experiences a sharper increase and ultimately exceeds that of fuels with lower densities at high wind velocities of $u_{10} > 10$ m/s (Tavakol Sadrabadi & Innocente, 2025).

for a constant bulk density (Veg_1), it could be observed that the RoS of shorter grass ($H_g = 0.2$ m) tends to be higher than that for taller grasses ($H_g = 0.5$ and 1 m), with RoS decreasing with increasing the grass height, which is consistent with the results reported by (Moinuddin et al., 2018). Under high wind speeds ($u_{10} > 10$ m/s) and steep slope conditions however, the combined effects of vegetation height and terrain can reverse the usual trend, resulting in a higher RoS for taller grass ($H_g = 1$ m) compared to shorter grass ($H_g = 0.5$ m), even with constant bulk density (see Figure 5.1b and 5.1c).

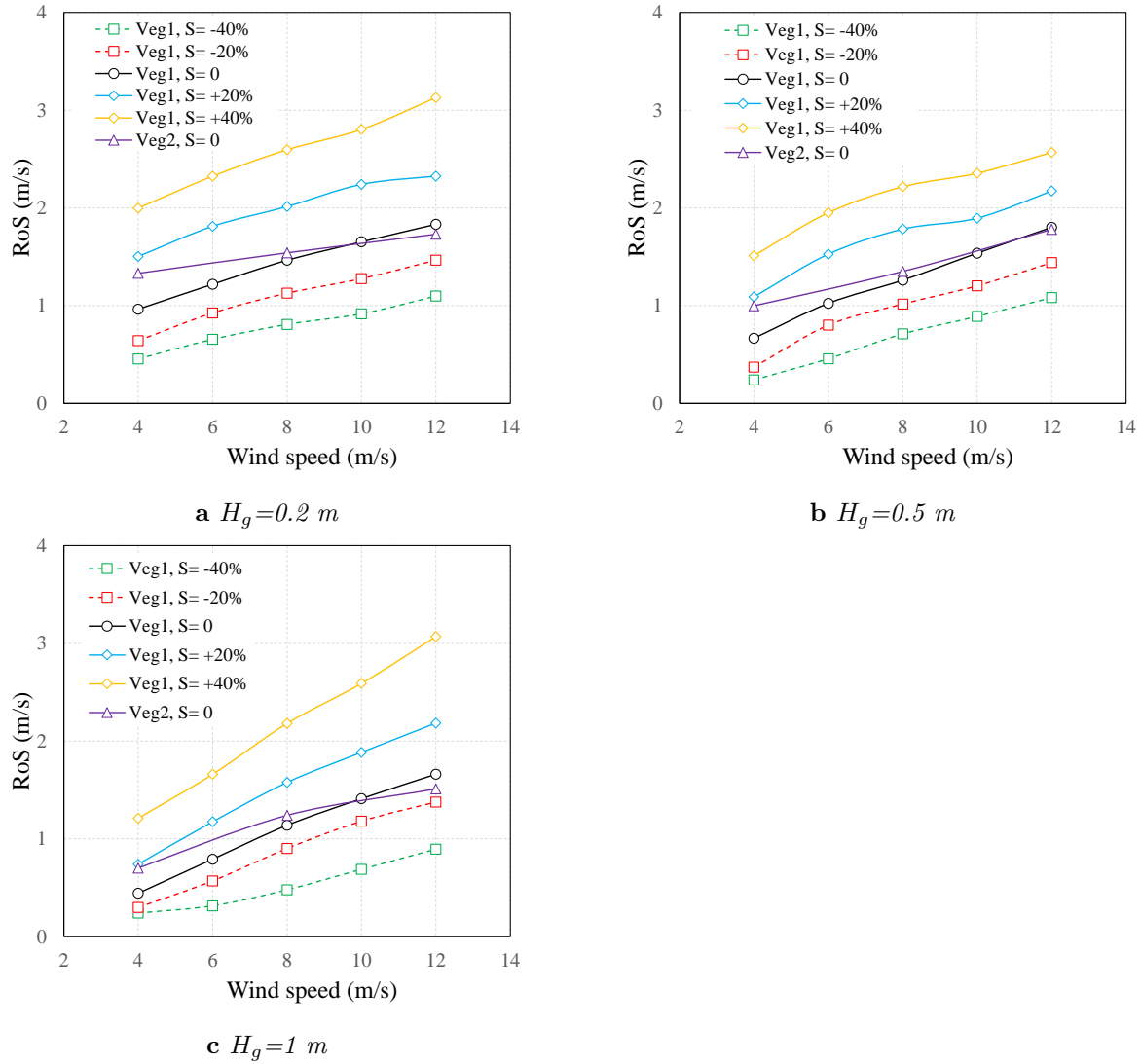


Figure 5.1: quasi-steady RoS at different wind speeds and terrain slopes, adopted from (Tavakol Sadrabadi & Innocente, 2025)

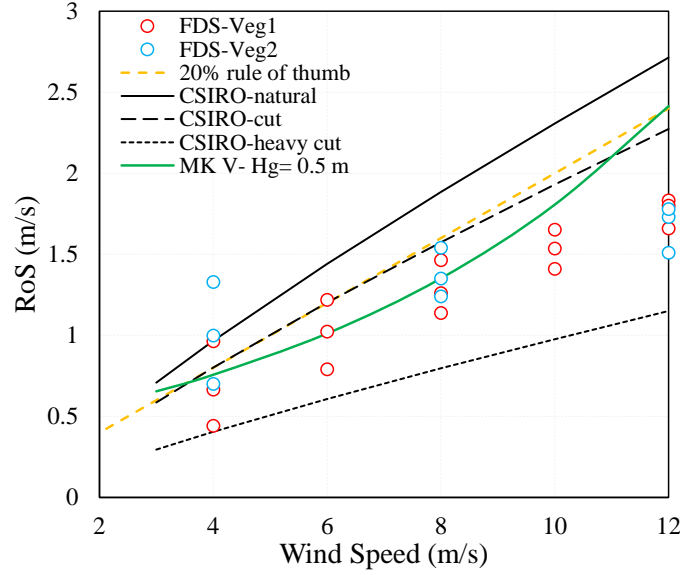


Figure 5.2: Comparison of the simulated RoS with experimental model estimations over horizontal terrain, adopted from (Tavakol Sadrabadi & Innocente, 2025)

Figure 5.2 presents a comparison between the quasi-steady RoS obtained from the empirical models of CSIRO (Cheney et al., 1998) developed by Cheney et al., the McArthur mark V model (Noble et al., 1980), as well as the 20% rule of thumb introduced by Cruz et al (Cruz et al., 2022b). The CSIRO model includes three different equations for estimating the RoS concerning the height or condition of fuels, including natural vegetation, cut or grazed, and heavy cut or eaten out vegetation as follows for natural grass:

$$\text{RoS}_{\text{natural}} = \begin{cases} (0.054 + 0.269u_{10}) \phi_M \phi_C, & u_{10} \leq 5 \text{ km.hr}^{-1} \\ (1.4 + 0.838(u_{10} - 5)^{0.844}) \phi_M \phi_C, & u_{10} > 5 \text{ km.hr}^{-1} \end{cases} \quad (5.1)$$

for cut grass:

$$\text{RoS}_{\text{cut}} = \begin{cases} (0.054 + 0.209u_{10}) \phi_M \phi_C, & u_{10} \leq 5 \text{ km.hr}^{-1} \\ (1.1 + 0.715(u_{10} - 5)^{0.844}) \phi_M \phi_C, & u_{10} > 5 \text{ km.hr}^{-1} \end{cases} \quad (5.2)$$

and for heavy cut or grazed conditions:

$$\text{RoS}_{\text{heavycut}} = (0.55 + 0.0357(u_{10} - 5)^{0.844}) \phi_M \phi_C, \quad u_{10} > 5 \text{ km.hr}^{-1} \quad (5.3)$$

Where ϕ_C and ϕ_M are curing coefficients and fuel moisture coefficients, respectively,

and could be calculated as follows (Cheney et al., 1998):

$$\phi_M = \begin{cases} e^{(-0.108M)}, & M \leq 12\% \\ 0.684 - 0.0342M, & M \geq 12\%, \quad u_{10} < 10 \text{ km.h}^{-1} \\ 0.547 - 0.0228M, & M \geq 12\%, \quad u_{10} \geq 10 \text{ km.h}^{-1} \end{cases} \quad (5.4)$$

and ϕ_C as follows (Cruz et al., 2015):

$$\phi_C = \frac{1.12}{1 + 103.99e^{-0.0996(C-20)}} \quad (5.5)$$

Where C represents the degree of grass curing. The estimations from all models are presented here assuming fully cured conditions ($C=100\%$).

The RoS in McArthur mark V model is directly related to the grassland fire danger index (GFDI) as follows:

$$\text{RoS} = 0.13 \text{ GFDI} \quad (5.6)$$

where for $M < 18.8\%$, the GFDI can be calculated as:

$$\text{GFDI} = 3.35 W e^{-0.0897M+0.0403u_{10}} \quad (5.7)$$

McArthur's model includes the effect of fuel load; hence, the equivalent fuel load for the Veg_1 with $H_g=50$ cm is utilised to calculate the corresponding RoS (Tavakol Sadrabadi & Innocente, 2025).

Comparing the estimated values with the simulated results presented in Figure 5.2, it could be inferred that although the CSIRO model is derived from controlled experimental burns and is expected to provide more accurate results compared to other models, estimated RoS for natural grass are significantly higher than the simulated ones except in low-velocity winds (i.e. 4 m/s). However, the estimations for heavy-cut grass indicate an under-prediction compared to the FDS. Simulated RoS values generally show good agreement for wind velocities below 6 m/s with the CSIRO cut grass model and the 20% rule of thumb, derived from a combination of experimental data and real wildfires. This agreement, however, declines with increasing wind speed. However, the best agreement between simulations and empirical models is observed for the McArthur mark V model (estimated for $H_g = 50$ cm) for wind speeds up to ≈ 9 m/s. However, it should be highlighted that the RoS estimated by the McArthur mark V model utilising the fuel load equivalent for $H_g = 0.2$ and $H_g = 1$ m indicated considerable underestimation and overestimation of the RoS values, respectively (not shown here). It is generally observed that the RoS simulated by the FDS at higher wind limits is considerably lower than that estimated by empirical models. Besides, the overall trend in the increase of RoS with wind speed is weaker than that of empirical models (Tavakol Sadrabadi & Innocente, 2025).

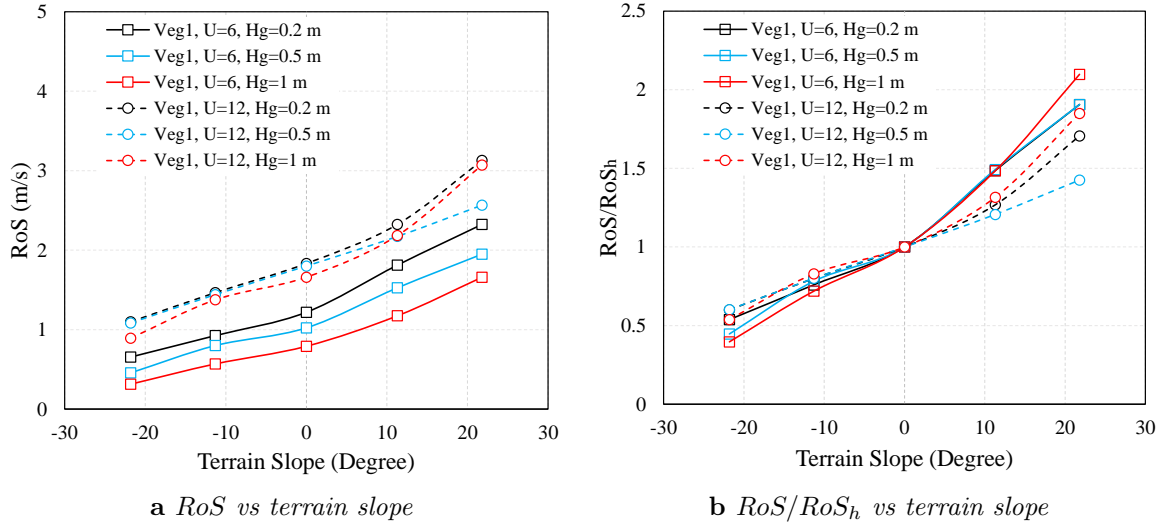


Figure 5.3: Variations of the RoS and RoS/RoS_h with terrain slopes at $u_{10} = 6$ (m/s), and $u_{10} = 12$ (m/s) for different vegetation heights, adopted from (Tavakol Sadrabadi & Innocente, 2025)

5.1.2 RoS as a function of terrain slope

As described earlier in section 3.1.7, the effect of bulk density on fire behaviour is studied solely on horizontal terrain and as a result, this section focuses on the first fuel type (Veg_1). Figure (5.3a) presents the simulated quasi-steady RoS against terrain slope for different vegetation heights, and wind speeds of $u_{10}=6$ and 12 (m/s). Generally, it is not surprising that the RoS of fires uphill is notably faster compared to horizontal and downhill scenarios, with the highest rate of spread occurring on $+40\%$ ($+22.8^\circ$) upslopes, while the lowest on downslopes with a slope of -40% (-22.8°). As previously mentioned, the calculated RoS for shorter grasses are higher than that for longer grasses. This is specifically clear in the case of $u_{10}=6$ (m/s) while this disparity tends to diminish as wind speed increases. This is particularly pronounced at higher wind speeds, such as $u_{10}=12$ (m/s) where the difference in RoS between fires in grasses of varying heights becomes minimal, especially over horizontal and low-angle slopes. Additionally, as mentioned in the previous section, the RoS of fire of taller grass ($H_g=1$ m) on a terrain slope of $S=+22.8^\circ$ exceeds that of the shorter grass ($H_g=0.5$ m) (Tavakol Sadrabadi & Innocente, 2025).

Figure (5.3b) presents the ratio of the rate of spread at each terrain slope and wind speed to the corresponding rate of spread on horizontal terrain (RoS/RoS_h) for different vegetation heights and wind speeds of $u_{10}=6$ and 12 m/s. Overall, it could be concluded that the combined influence of terrain slope and vegetation height on RoS is more significant in cases with taller vegetation. For example, the rate of increase of the RoS when increasing terrain slope from $S=+11.3^\circ$ to $S=+22.8^\circ$ for grass with $H_g=1$ m and $u_{10}=6$ is approximately 10% higher compared to that of other vegetation heights,

irrespective of wind speed. A similar pattern is observed in downslope conditions, where the ratio of RoS to RoS_h decreases more rapidly for taller grasses as the negative slope increases. When comparing the effect of slope on RoS variation across different wind speeds, it becomes clear that this effect is more obvious at lower wind speeds. In such conditions, fire propagation is primarily influenced by buoyancy forces which leads to a plume-dominated fire propagation. This effect tends to diminish at higher wind speeds where the fire propagation is more controlled by wind forces, known as wind-driven fire propagation (Tavakol Sadrabadi & Innocente, 2025).

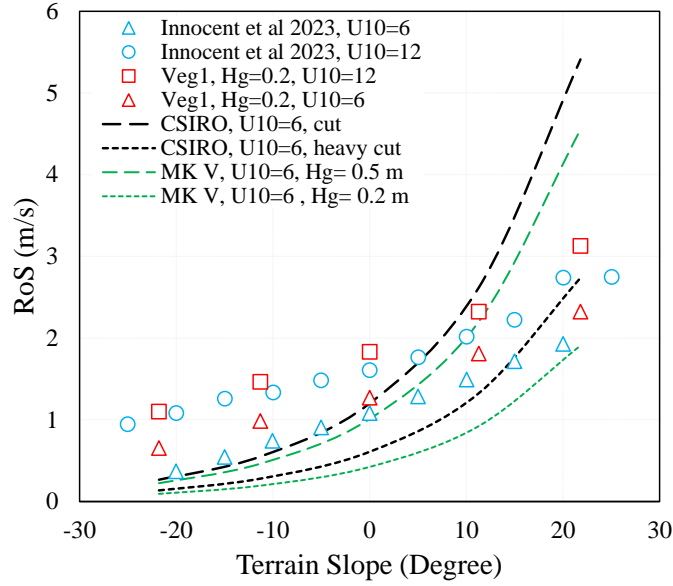


Figure 5.4: Comparison of the Simulated RoS with similar studies on different terrain slopes, adopted from (Tavakol Sadrabadi & Innocente, 2025)

Figure(5.4) compares the quasi-steady RoS obtained from simulations against terrain slope for vegetation height equal to $H_g=0.2$ m and wind speeds equal to $u_{10}=6$ and 12 (m/s) with simulation data from (Innocent et al., 2023) study and empirical models of CSIRO (Cheney et al., 1998) and McArthur mark V model (Noble et al., 1980) corrected for slope effect utilising the Noble et al (Noble et al., 1980) correction factors as it is adopted in Australia (Innocent et al., 2023) for upslope and downslope conditions:

$$RoS_{Corrected} = RoS e^{0.069S} \quad (5.8)$$

where RoS is the horizontal forward rate of spread ($km.h^{-1}$), and S is the slope of the terrain in degrees. Generally, the trend of simulated RoS of this study agrees with the simulation results of (Innocent et al., 2023), however, the differences are mainly due to the utilisation of different fuel models, wind models, grid size, as well as the longer ignition lines in our study. The Boundary fuel model and a two-step thermal degradation model are utilised in (Innocent et al., 2023) neglecting the exothermic char oxidation while our study utilises the three-step reaction model as well as the

Table 5.1: Average and range of measured environmental and fire variables in the (Cruz et al. 2020) wheatland and (Cruz et al. 2018) grassland experiments, adopted from (Tavakol Sadrabadi & Innocente, 2025)

Reference	Vegetation		T (°C)	RH (%)	u_{10} (m/s)	W (kg.m ⁻²)	H_g (m)	ρ_b (kg.m ⁻³)	M (%)	RoS (m/s)	RoS/U10	I (KW.m ⁻¹)
(Cruz et al., 2020) (Cruz et al., 2020)	Wheat	mean	30.2	21.6	8.0	0.42	0.37	1.6	7.5	1.5	0.19	12131
		[range]	[24.8-38]	[13.6-31.7]	[5.2-10.8]	[0.32-0.53]	[0.08-0.83]	[0.73-4.04]	[5.4-11.6]	[0.7-2.8]	[0.08-0.38]	[3858-27987]
(Cruz et al., 2018) (Cruz et al., 2018)	Grass	mean	25.7	27.8	5.3	0.49	0.39	1.38	7.96	1.0	0.18	7868
		[range]	[16-33]	[6-59]	[2-13]	[0.17-1.05]	[0.16-0.93]	[0.43-3.0]	[3.5-12.6]	[0.2-2.5]	[0.1-0.3]	[1260-18703]

Lagrangian particle model. Considering the empirical models, it is obvious that both CSIRO-heavy cut and MK-V with $H_g=0.2$ models have underestimated the RoS compared to the simulated values. However, the estimated values of the CSIRO-cut model are closer to the simulated ones (Tavakol Sadrabadi & Innocente, 2025).

5.1.3 RoS as a function of vegetation characteristics

In the previous sections, the combined effects of wind velocity, terrain slope, and vegetation height on the RoS of fire are examined. Simulation results indicate that generally, for a constant bulk density (ρ_b) increasing the vegetation height leads to a decrease in the fire spread rate, in agreement with reports of (Moinuddin et al., 2018). However, in some cases under high wind speeds and steep upslope conditions, the RoS of fire in taller grass is higher than that observed in shorter grass (Tavakol Sadrabadi & Innocente, 2025).

The practice of mowing grasses is widely adopted as a management strategy to control and slow down the wildfire spread in grasslands around the world, particularly favoured by the Australian fire authorities. It is believed that cutting the grass would result in a less intense and slower propagating fire (Cruz et al., 2021), a conclusion specifically supported by the experimental burns including (Cheney et al., 1993) and (Cruz et al., 2020). In contrast, some studies such as (Cruz et al., 2018) and (Moinuddin et al., 2018) suggest that RoS decreases with increasing vegetation height and the current practice of mowing grasses should be reconsidered. In this section hence, a data re-analysis is carried out utilising a combination of experimental and simulation data of wildfire RoS under varying wind velocities, over flat terrain to explore how changing vegetation height and bulk density affects the RoS of fire (Tavakol Sadrabadi & Innocente, 2025).

Two studies are selected with seemingly contradictory results regarding the relationship between fuel height and RoS of fire including grassland fire experiments by Cruz et al., (2018)(Cruz et al., 2018), and wheatland fire experiments by Cruz et al., (2020)(Cruz et al., 2020), aiming to highlight the sources of the contradictory results reported. The environmental and fuel conditions for both studies are summarised in Table (5.1). The two studies are performed in Australian territories under comparable temperature (T), relative humidity (RH), fuel height (H_g), and moisture content (M) conditions. It is important to highlight that the reported bulk density reported by Cruz et al., (2020)(Cruz et al., 2020) refers specifically to the standing fuel, while the burn-

ing experiments are carried out in the presence of matted fuel on the ground. However, for fire intensity calculations, the total fuel load includes 80% of the matted fuel load as well. Consequently, in this study, the bulk density is calculated as the consumed fuel divided by the fuel height. While both the standing fuel bulk density and this calculated bulk density yield similar trends and insights, the calculated bulk density is preferred for better visualization, and to maintain consistency with other calculations, such as fire intensity, as well as with Cruz et al., (2018)(Cruz et al., 2018).

The average fire RoS and intensity (I) obtained from wheatland experiments of (Cruz et al., 2020) equal to $\text{RoS}_{\text{wheat}} = 1.5$ m/s are higher than that from grassland experiments ($\text{RoS}_{\text{grass}}=1$ m/s) (Cruz et al., 2018) which seemingly are related to the higher average wind velocity during wheatland experiments. However, experiments diverge primarily in their findings concerning the correlation between the rate of fire spread and vegetation height. In the wheatland experiments, RoS is positively correlated with fuel height, in agreement with the conclusions made by (Cheney et al., 1993). In contrast, the grassland experiments reported a negative correlation between RoS and fuel height. To reconcile these conflicting outcomes, Cruz et al., (2021) (Cruz et al., 2021) state that the accurate conclusion should indicate a positive correlation between fuel height and the fire RoS. They attributed the grassland study's contradictory conclusion to structural differences in the grasslands, which likely obscured the effect of fuel height and led to misleading conclusions. However, (Sutherland et al., 2021) suggested that the variation between the conclusions from the two datasets is mainly due to the difference in their propagation modes as the wheatland experiments primarily represented wind-driven fires, while the grassland experiments were predominantly buoyancy-driven and concluded that for wind-driven fires, increasing the vegetation height leads to an increased RoS. Figure (5.5) presents the experimental data from both datasets alongside the simulated values, comparing fire RoS behaviour under different combinations of vegetation height, bulk density, and fuel load (Tavakol Sadrabadi & Innocente, 2025).

Figure (5.5a), illustrates the relationship between Rate of Spread (RoS) and fuel height, integrating experimental data from (Cruz et al., 2018) and (Cruz et al., 2020), alongside simulation results from the current study. The positive correlation between RoS and fuel height (H_g) in (Cruz et al., 2020) contrasts with the negative correlation in (Cruz et al., 2018) and our simulation results. A linear fit is applied for visualization purposes only, recognizing that it might not be appropriate for all datasets, each of which potentially requires a different fit. Notably, the RoS utilization could be misleading, as it is influenced by the ambient wind speed. Hence, utilising the ratio of fire spread rate to ambient wind speed RoS/u_{10} provides a more reliable representation of the data as depicted in Figure (5.5b). A strong positive correlation between RoS/u_{10} and H_g for the wheatlands experiments is evident, while the significant negative correlation in grassland experiments and our simulations no longer appears. This suggests that there is no correlation between RoS/u_{10} and H_g for grassland experiments of (Cruz et al., 2018) and FDS simulations. A similar behaviour is also observed between the RoS/u_{10} and Fuel load (W) in Figure (5.5c), suggesting that neither H_g nor W can suf-

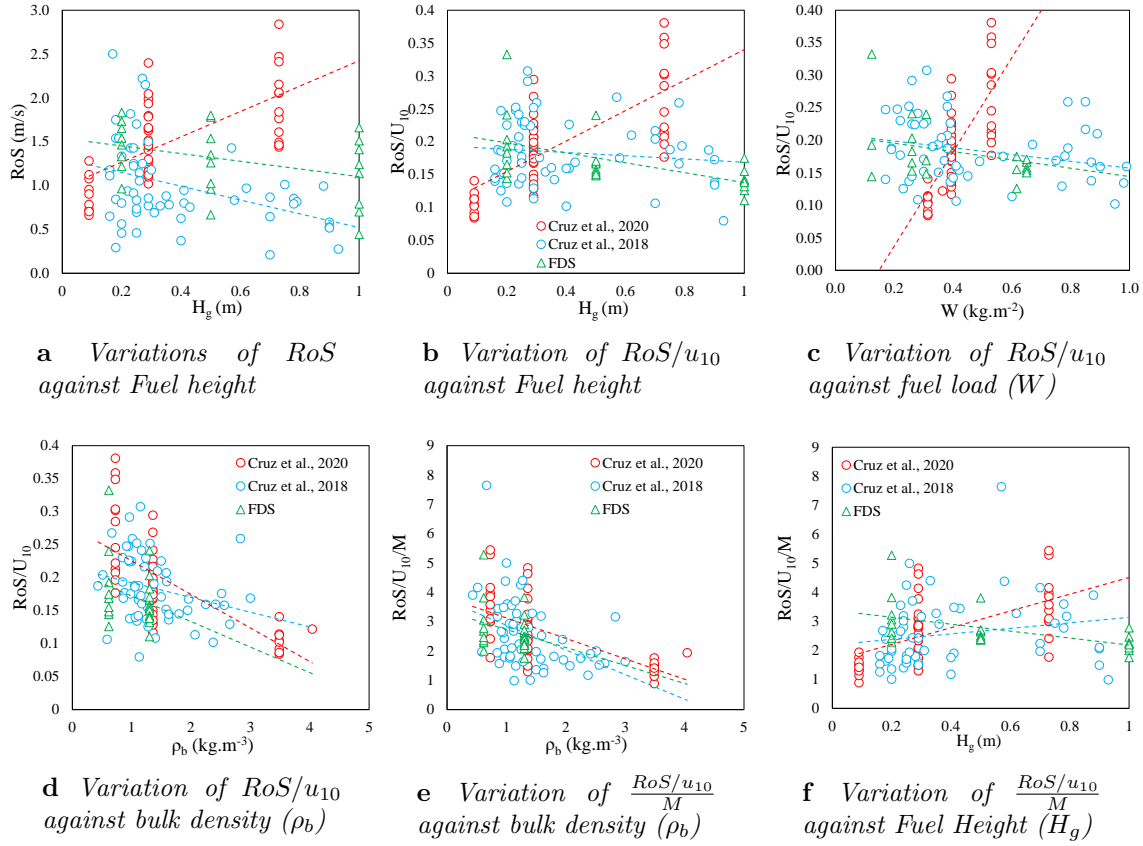


Figure 5.5: Comparison of the distribution and trend of the Observed RoS of the head fire versus fuel height and bulk density for different datasets, adopted from (Tavakol Sadrabadi & Innocente, 2025)

ficiently characterize the fire behaviour. However, when plotting the non-dimensional RoS/u_{10} against bulk density ρ_b of fuel, a clear negative correlation emerges across all datasets as depicted in Figure (5.5d). It is consistent with the findings of (Campbell-Lochrie et al., 2021) that increasing the bulk density leads to a reduction of the RoS for no-wind conditions. Here, however, it could be observed that this is still valid even in the presence of wind. By accounting for dead fuel moisture content (M) by simply dividing the RoS/u_{10} by the M , Figure 5.5e presents $RoS/u_{10}/M$ against bulk density, where a consistent negative correlation could be observed improved trend alignment and Pearson correlation coefficients equal to $R_p = -0.57$ for wheatland fire and -0.42 for grassland fire datasets. The most intriguing behaviour is found when plotting the $RoS/u_{10}/M$ against the fuel height (H_g) in Figure (5.5f). For both experimental datasets, a positive trend is found with a Pearson correlation coefficient equal to $R_p = 0.59$ for (Cruz et al., 2020) and 0.19 for (Cruz et al., 2018). This highlights a consistent relationship between RoS and fuel height when corrected for wind speed and moisture content, reconciling the seemingly disparate findings between the two datasets in the original studies (Tavakol Sadrabadi & Innocente, 2025).

Overall, it could be concluded that for a constant moisture content, the RoS/u_{10} increases with vegetation height. Nevertheless, the slopes of the trends in both datasets exhibit distinct magnitudes, reflecting the effect of various parameters such as atmospheric humidity and temperature, the surface area to volume ratio of fuel, etc, that affect the fire behaviour. However, contrary to the experimental data, the results of our simulations indicate a weak negative correlation which initially appears counter-intuitive. The following section however delves into the potential reasons behind this discrepancy and demonstrates that FDS is able to accurately reproduce the correct relationship between $\text{RoS}/u_{10}/M$ and H_g .

5.1.4 RoS as a function of propagation mode

Despite the diverse range of burning conditions, fuel types, vegetation heights, terrain conditions, and other atmospheric parameters such as moisture content, a unifying perspective can be achieved by examining their collective impact on fire intensity (I) and consequently on the equilibrium of buoyancy and inertial forces within the fire front (Morvan & Frangieh, 2018). Therefore, Figure (5.6) presents the ratio of RoS/u_{10} against the N_c values for all datasets utilised in this study along with the power law fit across the dataset. For wind-driven fires, particularly for $N_c < 1$, a saturation of data points is observed in the range $0.08 < \text{RoS}/u_{10} < 0.2$ for all datasets, converging towards a state independent of the Byram number which aligns with the observations of (Morvan & Frangieh, 2018) where they suggested that fire propagation in this state is solely a function of moisture content (M). However, for larger N_c values, a broad range of RoS/u_{10} values could be observed, from 0.05 to 0.4, increasing as N_c values rise (Tavakol Sadrabadi & Innocente, 2025).

5.2 Discussion

The previous section provided insight into the simulation results and the reanalysis of experimental datasets. However, certain questions were raised or remained partially unanswered, as they required the consideration of additional factors that affect the fire, including the fire propagation mode. Consequently, this section aims to combine analysis conclusions and fire propagation modes to address two key questions: (i) is FDS capable of accurately reproducing the effect of grass height on fire propagation as detailed by experimental studies?, and (ii) whether cutting grass effectively limits wildfires propagation (Tavakol Sadrabadi & Innocente, 2025)?

5.2.1 Are FDS results counter-intuitive?

The previous section revealed that FDS simulations indicate a negative correlation between $\text{RoS}/u_{10}/M$ and fuel height (H_g), whereas experimental data suggest a positive correlation. Additionally, previously it was mentioned that (Moinuddin et al., 2018)

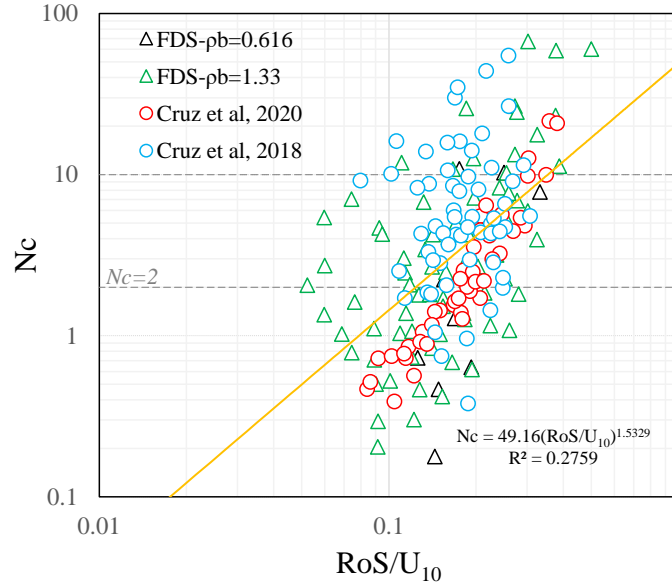


Figure 5.6: Ratio of RoS/u_{10} as a function of Byram convective number (N_C) for the combined dataset of simulations and experimental results; dashed line represent the values $N_C=2$ and 10 , implying two fire propagation regimes including wind-driven ($N_C < 2$) and plume-dominated ($N_C > 10$); solid orange line represents the best fit for the whole dataset, adopted from (Tavakol Sadrabadi & Innocente, 2025)

reported that the RoS of fire decreases with increasing the vegetation height. However, it is crucial to highlight that all simulations in (Moinuddin et al., 2018) and the majority of our simulations, assumed a constant bulk density across all vegetation heights. In contrast, the natural vegetation in the experimental datasets exhibits a decreasing trend in bulk density with increasing vegetation height. The Pearson correlation coefficient between H_g and ρ_b was found to be $R_p = -0.62$ and -0.37 for (Cruz et al., 2020) and (Cruz et al., 2018) datasets, respectively. As Cruz et al., 2021 mentions, changing the fuel bed height while keeping bulk density constant—as carried out in (Moinuddin et al., 2018) and partly in our study—solely changes the amount of fuel available for combustion. While it is not easily viable to explain the effect of these two fuel characteristics on the RoS . Besides, the representation of fuel as a homogeneous rigid layer that does not bend towards wind might have contributed to an incorrect estimation of drag coefficient and roughness length (Tavakol Sadrabadi & Innocente, 2025).

While ignoring the potential effect of vegetation representation and flexibility on the exerted drag and the RoS imposes certain limitations, the performed analysis suggests that the disparity in bulk density conditions between simulated and natural vegetation significantly contributes to the observed differences in $RoS/u_{10}/M$ and fuel height correlations between FDS simulations and experimental observations. To further examine the effect of bulk density on the RoS and mode of propagation of fire, Figure 5.7a to 5.7c presents the simulated variations in RoS against vegetation height across differ-

ent wind speeds (u_{10}), terrain slopes (S), and bulk densities (ρ_b). Additionally, the corresponding values of the Byram convective number (N_c) for each case are shown in Figure 5.7d to 5.7f. As previously mentioned, for a constant bulk density (ρ_b), increasing vegetation height leads to a reduction of the RoS irrespective of the terrain slope or fire propagation mode. The only exception occurs in the case with Veg_2 at $S=+40\%$ and $U_{10}=12$ where increasing the grass height from 0.5 m to 1m, increases the fire RoS. This, however, might be influenced by the shift in the fire propagation regime as characterised by N_c values (red line) crossing the $N_c=2$ threshold while increasing the vegetation height in Figure 5.7f. Consequently, our findings mainly contrast with (Sutherland et al., 2021) where they stated that for constant bulk density and wind-driven fires, the RoS increases with increasing the vegetation height. However, it is important to note that this effect was observed for $H_g \leq 0.2$ m, which is below the range considered in our simulations. Meanwhile, the wide range of wind speeds and terrain slopes considered in our study does not confirm their observations, suggesting that factors beyond the fire propagation mode may influenced the outcomes of their research (Tavakol Sadrabadi & Innocente, 2025).

Considering the effect of bulk density on the RoS and N_c values of fire, as shown in Figure 5.7b and 5.7e, it could be observed that for $N_c \gg 2$ —plume-dominated and transitory regimes—, the RoS of fire for Veg_1 —higher ρ_b —is smaller than that of Veg_2 —lower ρ_b . This observation aligns with the conclusion highlighted in Section 5.1.3, asserting that an increase in bulk density (ρ_b) leads to a reduction in the RoS of fire. Notably, this discrepancy tends to diminish as values of N_c approach 2 (blue lines in Figure 5.7b and 5.7e). However, for N_c well below the threshold of 2 (red lines)—corresponding to wind-driven fires—, an interesting trend emerges. Unlike the behaviour observed in plume-dominated fires, the estimated RoS for Veg_1 with $\rho_b=1.33$ kg/m³ is slightly higher than that for Veg_2 with $\rho_b=0.616$ kg/m³. This highlights a distinctive trend in wind-driven fires, deviating from the general pattern observed in plume-dominated conditions (Tavakol Sadrabadi & Innocente, 2025).

In summary, the discussion on the simulated RoS of fires indicates that FDS can realistically model the relationship between RoS/ u_{10} and vegetation height. This holds true provided that bulk density decreases as vegetation height increases—a characteristic observed in natural vegetation types considered in this study (Tavakol Sadrabadi & Innocente, 2025).

To clarify, Figure (5.8) depicts the RoS/ u_{10} and corresponding N_c values against vegetation height H_g , as an endeavour to imitate the reduced bulk density ρ_b seen in taller natural vegetation. Specifically, in each line, the RoS/ u_{10} of shorter grass corresponds to Veg_1 with $\rho_b=1.33$ kg/m³, while that of taller grass is extracted from Veg_2 with $\rho_b=0.616$ kg/m³. It is observed that for transitory and plume-dominated propagation modes $N_c > 2$, the RoS/ u_{10} increases with increasing vegetation height (and simultaneously reducing ρ_b). However, for wind-driven fires $N_c < 2$, RoS/ u_{10} decreases with increasing vegetation height (and simultaneously decreasing ρ_b). Still, it should be noted that this latter behaviour was not observed in experimental data of wheat-land (Cruz et al., 2020) experiments—possibly due to the complexity and variability of

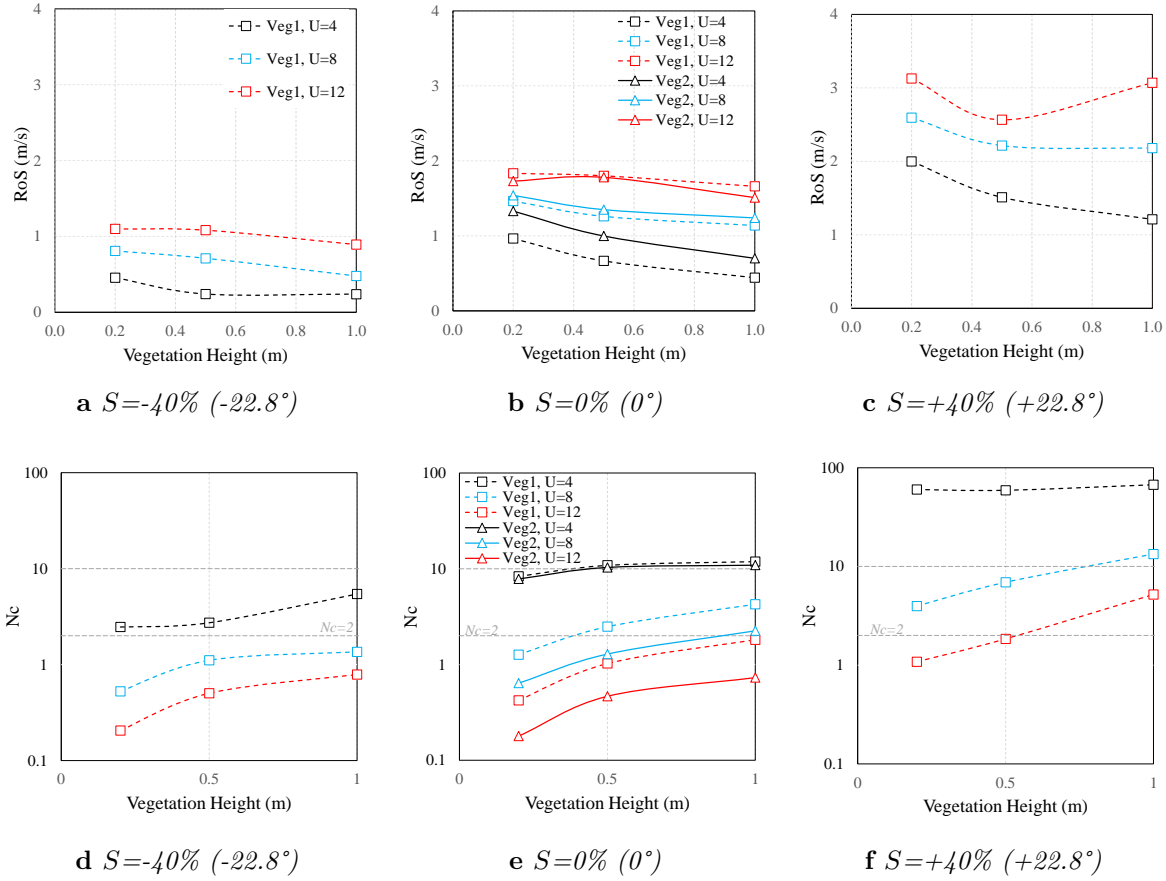


Figure 5.7: Variation of the RoS (a-c) and the corresponding Byram convective number N_c (d-f) against fuel height (H_g) for two different vegetations of Veg₁ and Veg₂ with bulk densities of $\rho_b = 1.313$ and $\rho_b = 0.616$ respectively, at different wind (u_{10}) velocities and varying terrain slopes; grey ; dashed line represent the values $N_C=2$ and 10 , implying two fire propagation regimes including wind-driven ($N_C < 2$) and plume-dominated ($N_C > 10$), adopted from (Tavakol Sadrabadi & Innocente, 2025)

experimental conditions and scattered data points—, underscoring the need for further controlled experimental investigation for wind driven conditions (Tavakol Sadrabadi & Innocente, 2025).

5.2.2 To cut or not to cut?

As mentioned earlier, mowing grasses is a widely accepted practice globally to curb the rate of spread (RoS) of wildfires. While reducing grass height can indeed decrease fire intensity—and hence easier to fight against—, it also makes the fire more prone to becoming wind-driven. Besides, our analysis indicated that in both experimental datasets considered, the bulk density of the vegetation layer decreases ($\rho_b \downarrow$) as the

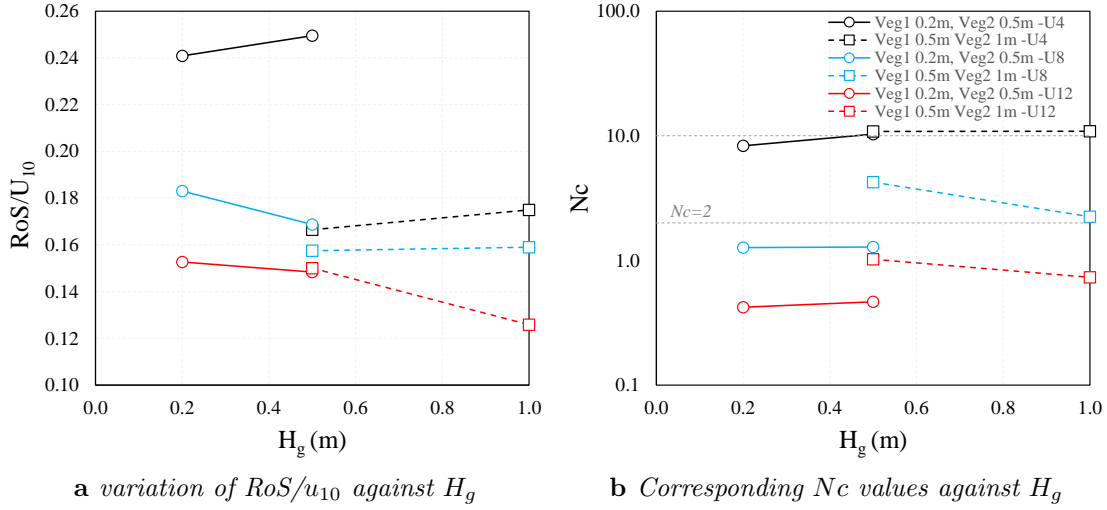


Figure 5.8: Variation of the RoS/u_{10} and the Byram convective number (N_c) against fuel height under different wind velocities, note that for each line the first point is extracted from Veg_1 with a bulk density equal to $\rho_b = 1.33$ and the second point from Veg_2 with bulk density $\rho_b = 0.616$, adopted from (Tavakol Sadrabadi & Innocente, 2025)

vegetation grows taller ($H_g \uparrow$) (Tavakol Sadrabadi & Innocente, 2025).

Wrapping up all the analysis from previous sections, it can be mentioned that for transitory and plume-dominated modes of fire propagation, increasing the bulk density of vegetation ($\rho_b \uparrow$) leads to a reduction of the RoS of the fire ($RoS/u_{10} \downarrow$). Hence, the RoS/u_{10} of fire decreases with decreasing the grass height ($H_g \downarrow$). Thus, mowing grasses could be an effective wildfire management strategy assuming that the bulk density of vegetation increases with decreasing the height of the vegetation. However, it should be highlighted that the above statements are valid for constant moisture content higher moisture content may overshadow the effect of vegetation height (Tavakol Sadrabadi & Innocente, 2025).

However, the probability of wind-driven fire also increases with cutting the grass. Although this behaviour was not observed in the experimental data of (Cruz et al., 2020), our simulation results indicate that for wind-driven fires $N_c < 2$, increasing the bulk density ($\rho_b \uparrow$) may lead to faster fire propagation ($RoS/u_{10} \uparrow$). Moreover, simulation results of (Sutherland et al., 2021) indicated that for wind-driven fires, even with constant bulk density, taller vegetation height can promote higher RoS. However, though unlikely, further experimental research is required to accurately determine if this effect can outweigh the benefits of reduced vegetation height (Tavakol Sadrabadi & Innocente, 2025).

Chapter 6

Vegetation Cover Type Classification Using Cartographic Data

The primary controlling factor of wildfire propagation is fuel availability. When fuel is present, wind becomes the main driver of fire spread. Different vegetation and fuel types exhibit varying combustion dynamics; therefore, accurately identifying the types of fuels and vegetation within the area of interest is essential for estimating wildfire propagation dynamics and planning firefighting operations effectively. However, the thermophysical properties of these vegetation types should be defined before they can be used as fuel input to combustion simulation models—though this is beyond the purpose of this research. This chapter presents the developed machine-learning methodology, which combines recursive feature elimination, state-of-the-art ML algorithms, and automated hyperparameter tuning utilising Bayesian optimisation to improve the accuracy of vegetation cover type classification.

6.1 Dataset

This study utilizes the University of California Irvine (UCI) cover type dataset, which contains 581,012 datapoints, twelve features, and seven cover type categories. Observations are taken from four wilderness areas, namely (1) Neota (3,904 ha), (2) Rawah (29,628 ha), (3) Comanche Peak (27,389 ha), and (4) Cache la Poudre (3,817 ha) within the Roosevelt National Forest in Northern Colorado, 70 miles northwest of Denver (Blackard & Dean, 1999) (see Figure 6.1).

The twelve features are: (1) *elevation* [m]; (2) *aspect* [degrees] (a.k.a. exposure or azimuth); (3) *slope* [degrees]; (4) *horizontal distance to hydrology* (HDH) [m]; (5) *vertical distance to hydrology* (VDH) [m]; (6) *horizontal distance to roadway* (HDR) [m]; (7) *hillshade index at 9:00 am* (HI9); (8) *hillshade index at noon* (HI12); (9) *hillshade index at 3:00 pm* (HI3); (10) *wilderness area designation* (four groups); (11) *soil type*

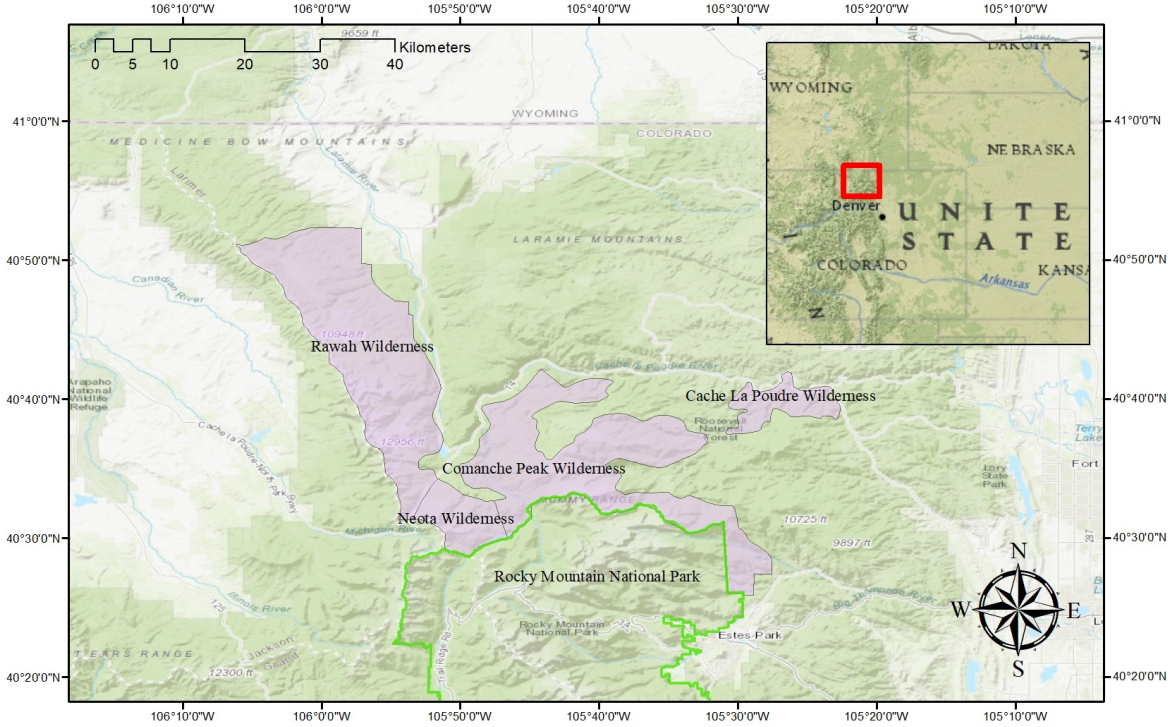


Figure 6.1: Study area location map: Roosevelt National Forest wilderness areas (Tavakol Sadrabadi & Innocente, 2023).

designation (40 one-hot encoded soil types); and (12) *horizontal distance to nearest wildfire ignition point* (HDF) [m]. The seven forest cover type categories are: Spruce/Fir (C1), with 211,840 datapoints; Lodgepole Pine (C2), with 283,301 datapoints; Ponderosa Pine (C3), with 35,754 datapoints; Cottonwood/Willow (C4), with 2,747 datapoints; Aspen (C5), with 9,493 datapoints; Douglas Fir (C6), with 17,367 datapoints; and Krummholz (C7), with 20,510 datapoints. Generally, Neota has the highest mean elevation and is mainly covered with spruce/fir, while Rawah and Comanche Peak are mainly covered with lodgepole pine, spruce/fir, and aspen (Tavakol Sadrabadi & Innocente, 2023).

This dataset (Blackard & Dean, 1999) was prepared using a combination of digital spatial data obtained from the US Geological Survey (USGS) and the US Forest Service (USFS). Thus, using digital elevation model (DEM) data with a resolution of 30 m, cartographic variables such as *aspect*, *slope*, and *hillshade indices* were extracted using the Geographic Information System (GIS). The distances from surface water resources were calculated by applying Euclidean distance analysis to the USGS hydrology and transport data, while soil type and wilderness areas were obtained from the USFS data. Hence a series of variables were obtained for each raster, comprising the input features

into the classifier. Its output is the vegetation cover type.

In order to improve model performance, 5,339 outliers based on the VDH were removed from the dataset, reducing the total number of data points to 575,576. This dataset was then split into two subsets, one for training the models (70%) and the other for testing their accuracy (30%). Pearson's correlation coefficients (r) and associated p -values between different input features and the cover type are shown in Figure 6.2. Elevation, slope, wilderness area, and soil type are among the features showing a higher correlation with the cover type. Because HI9 and HI3 were found to be highly correlated (Pearson's $r = 0.98$), the former was eliminated from the dataset and from Figure 6.2. The p -values show that the correlation coefficients (r) are statistically significant. The pairwise relationship of several of the most important features and their distributions are shown in Figure 6.3. It can be observed, for example, that elevation has a trimodal distribution, HDF and aspect have bimodal and right-skewed distributions, and HDH has a right-skewed distribution (Tavakol Sadrabadi & Innocente, 2023).

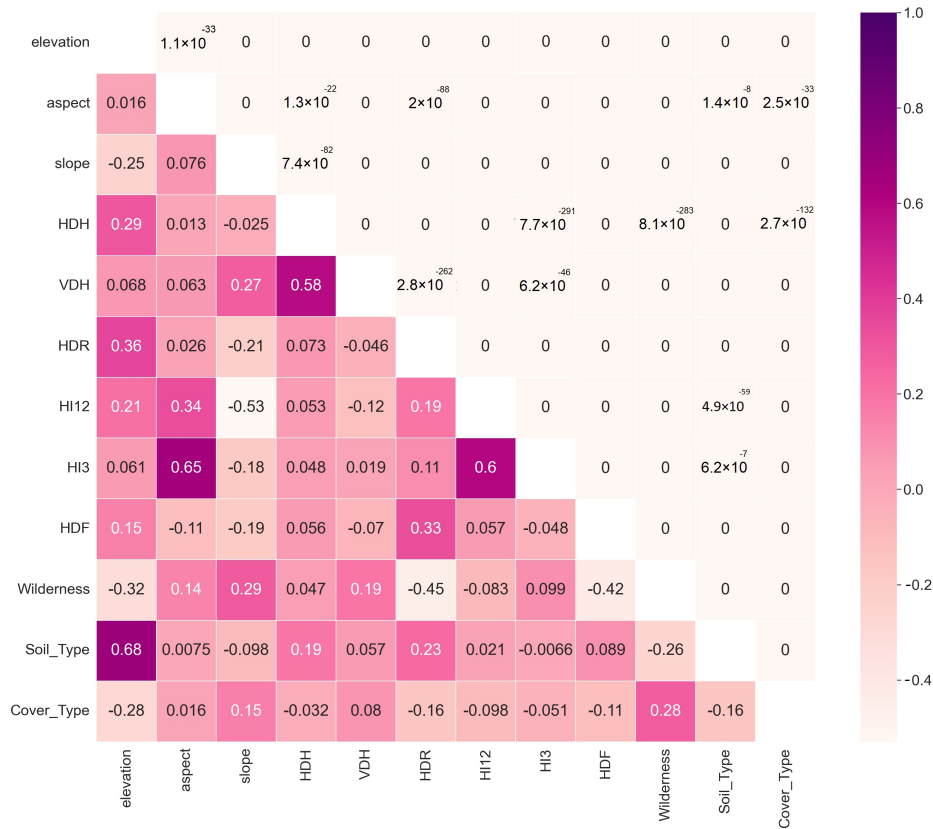


Figure 6.2: Feature correlation matrix (Pearson), with r below and p -value above the diagonal (Tavakol Sadrabadi & Innocente, 2023).

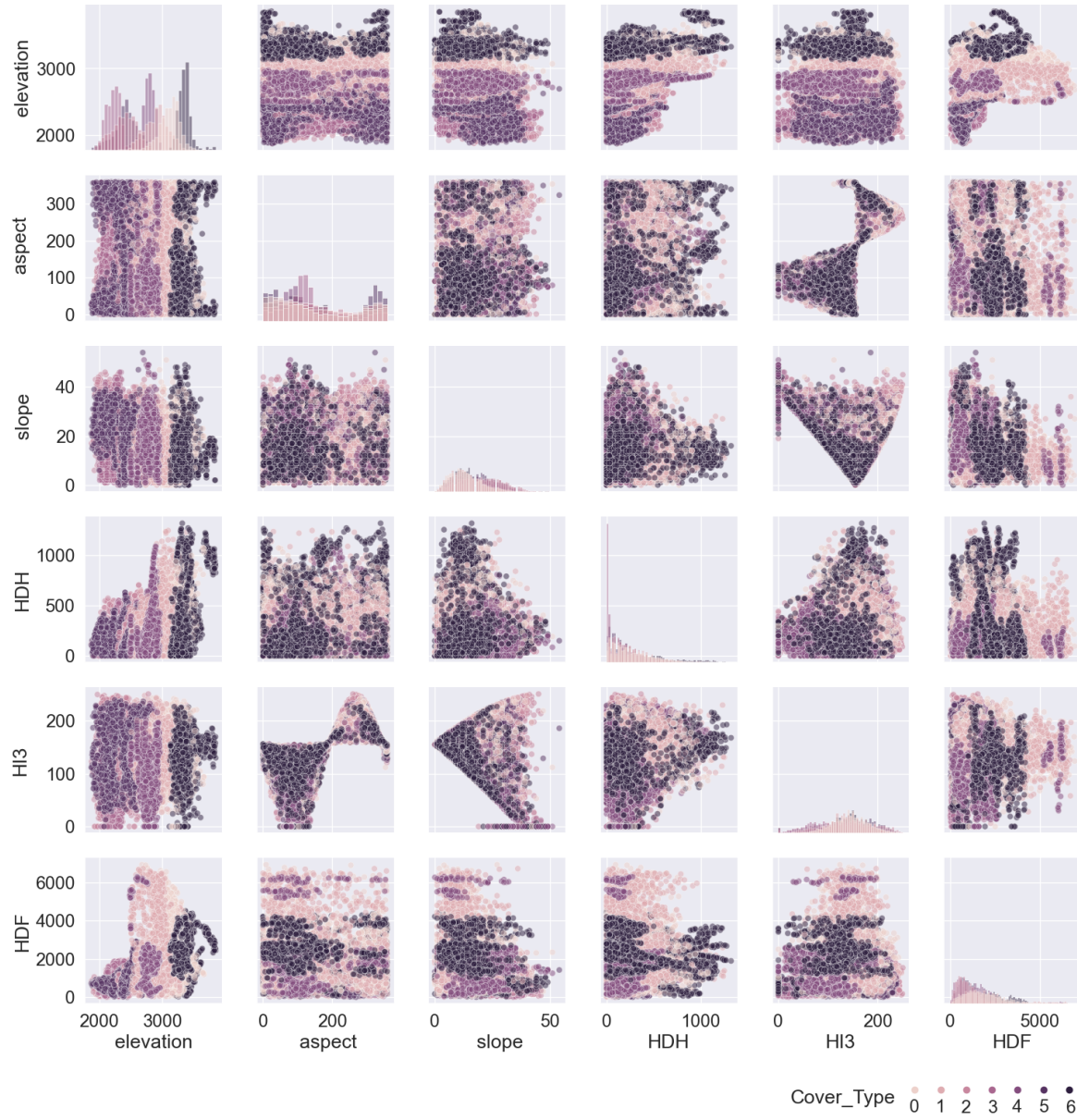


Figure 6.3: *Pairwise distribution and relationship of features in the dataset, adopted from (Tavakol Sadrabadi & Innocente, 2023).*

6.1.1 Hyperparameter optimisation

The performance of a ML model can be greatly improved by using AutoML (short for Automated ML), which automates complicated tasks without the need for human understanding (Tao et al., 2021). A crucial process is the optimal tuning of its hyperparameters.

Bayesian optimisation is a robust and potent technique for determining the extreme

values of computationally difficult functions (Brochu et al., 2009). It can be used to optimise non-convex functions or those with derivatives that are challenging to calculate or evaluate (J. Wu et al., 2019). Assuming that $\mathcal{F} : X \rightarrow \mathbb{R}$ is a well-behaved function defined on subset $X \subset \mathbb{R}^d$, the optimisation problem is formulated as shown in Equation (6.1).

$$\mathbf{x}^* = \arg \max_{\mathbf{x} \in X} \mathcal{F}(\mathbf{x}) \quad (6.1)$$

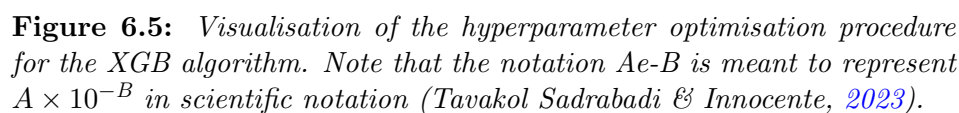
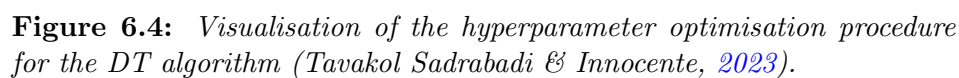
Bayesian Optimisation assumes $\mathcal{F}(\mathbf{x})$ to be unknown and treats it as stochastic, with a *prior* probability distribution that captures the beliefs about its structure. After collecting function evaluation data, the distribution is updated (the *posterior* distribution) and used to sample the next query point. Gaussian processes such as Kriging are typically used to define the probability distributions over $\mathcal{F}(\mathbf{x})$.

Bayesian optimisation is frequently used for optimal hyperparameter tuning (Nguyen, 2019). In this study, it is used to automatically tune all models' hyperparameters separately using the Optuna library (Akiba et al., 2019). The dataset is relatively large and highly imbalanced, with 211,840 data points for the C1, 283,301 data points for the C2, and 2,747 data points for the C4 cover types. This results in an imbalance ratio of $N_{\max}/N_{\min} = 77.1$. Therefore, a random under-sampling is utilised to ensure a balanced dataset, with 2,700 data points for each cover type extracted from the general dataset. Hyperparameter tuning was then performed on the smaller dataset using five-fold cross-validation for the model training corresponding to each candidate set of hyperparameters. Models were finally trained on the whole dataset with the obtained optimal set of hyperparameters, again using five-fold cross-validation.

Figures 6.4 and 6.5 show the multi-dimensional space of the hyperparameters searched during fine-tuning of the DT and XGB models. For each iteration, the corresponding values of the hyperparameters are linked to the resulting accuracy. The model parameters obtained from the optimisation process for all models are presented in Tables 6.1 and 6.2.

Table 6.1: *Hyperparameters for base learners and bagging ensembles (Tavakol Sadrabadi & Innocente, 2023).*

SVR	DT	RF	XT
<i>Kernel = RBF</i>	<i>Splitter : best</i>	<i>Splitter : best</i>	
<i>tolerance = 0.483</i>	<i>Criterion : entropy</i>	<i>Criterion : entropy</i>	<i>Criterion : entropy</i>
<i>Regularization(C) = 8.75</i>	<i>Min sample split = 3</i>	<i>Min sample split = 2</i>	<i>Min sample split = 2</i>
<i>gamma = 0.4</i>	<i>Min sample leaf = 1</i>	<i>Min sample leaf = 1</i>	<i>Min sample leaf = 1</i>
<i>Decision Function : 'ovo'</i>	<i>Max depth = 23</i>	<i>Max depth = 25</i>	<i>Max depth = 25</i>
		$N_{\text{estimators}} = 348$	$N_{\text{estimators}} = 348$



The models in this research made use of the Scikit-learn library (Pedregosa et al., 2011), XGBoost library (“XGBoost Project”, 2022), and CatBoost (“CatBoost”, 2022) library. Four measures were used to evaluate the accuracy of the models: accuracy,

Table 6.2: Hyperparameters for boosting ensembles (Tavakol Sadrabadi & Innocente, 2023).

AdaB	XGB	CatB
$Base_{estimator} = DT$	$objective = 'multi:softprob'$	$iterations = 3,500$
$N_{estimators} = 180$	$N_{estimators} = 1,073$	$loss_function MultiClassOneVsAll$
$Learning\ rate = 1.2$	$eta = 0.274$	$Learning\ rate = 0.47$
$algorithm = 'SAMME'$	$max\ depth = 25$	$depth = 10$
	$subsample = 0.5$	$subsample = 0.8$
	$colsample\ bytree = 0.6$	$l2_leaf_reg = 2.44$
	$tree\ method = 'exact'$	$model_size_reg = 2.62$
	$booster = 'gbtree'$	$bootstrap\ type : 'Bernoulli'$
	$min\ child\ weight = 2$	$boosting\ type : 'Plain'$
	$grow\ policy = 'lossguide'$	
	$lambda = 2.55 \times 10^{-5}$	
	$alpha = 3.95 \times 10^{-7}$	

precision, recall, and $F1$ score (Tavakol Sadrabadi & Innocente, 2023).

1. *Accuracy* is defined as the ratio of correct predictions over the total number of instances evaluated, and is calculated as in Equation (6.2).

$$acc = \frac{tp + tn}{tp + tn + fp + fn} \quad (6.2)$$

2. *Precision* is defined as positive patterns that are correctly predicted from the total predicted patterns in a positive class, and is calculated as in Equation (6.3).

$$prec = \frac{tp}{tp + fp} \quad (6.3)$$

3. *Recall* is defined as the percentage of positive patterns that are correctly categorised, as in Equation (6.4).

$$rec = \frac{tp}{tp + tn} \quad (6.4)$$

4. $F1$ score is the harmonic mean between recall and precision, and is calculated as in Equation (6.5) (Hoss).

$$F1 = \frac{2 \cdot prec \cdot rec}{prec + rec} \quad (6.5)$$

6.3 Results

6.3.1 Model feature importance

Increasing model accuracy via feature selection is an important step when implementing ML algorithms, especially for high-dimensional data structures. A reliable approach

to selecting the features which contribute the most and removing those which are detrimental is through feature importance analysis. The relative importance of features for the RF, XT, XGB, and CatB models is shown in Figure 6.6. The stacked models are not included here due to their hierarchical model fitting procedure.

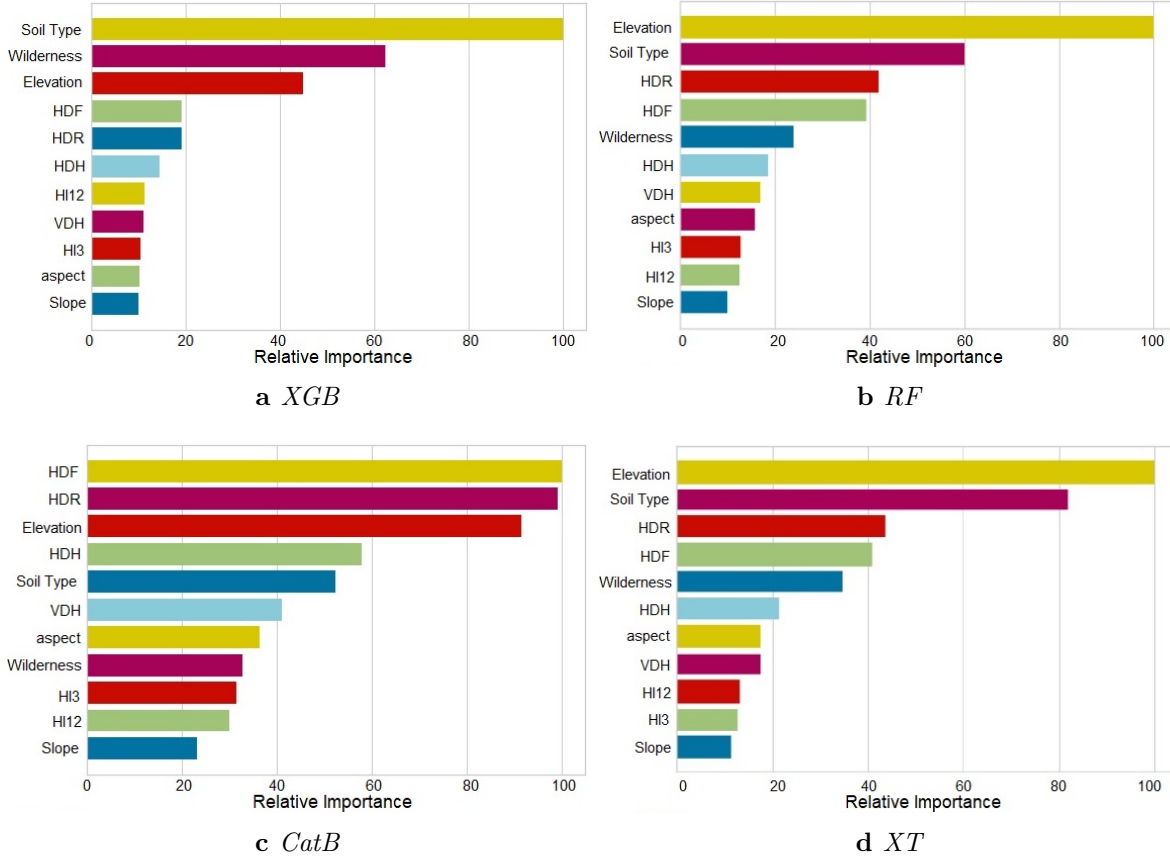


Figure 6.6: *Relative importance of features.*

It can be observed, for instance, that the slope of the terrain, HI12, and HI3 are among the least important features in the dataset (Tavakol Sadrabadi & Innocente, 2023).

6.3.2 Recursive feature elimination

Recursive Feature elimination is a feature selection technique which eliminates the weakest feature(s) from a model in a sequential manner until it reaches an optimal or predefined number of features. The obtained accuracy of the RF, XT, XGB, and CatB models during recursive feature elimination analysis is presented in Figure 6.7 for an increasing number of features. The highest accuracy for CatB is obtained using

ten features, excluding slope. For XGB and RF, the maximum accuracy is obtained using nine features, while XT achieves maximum accuracy using only seven features (Tavakol Sadrabadi & Innocente, 2023).

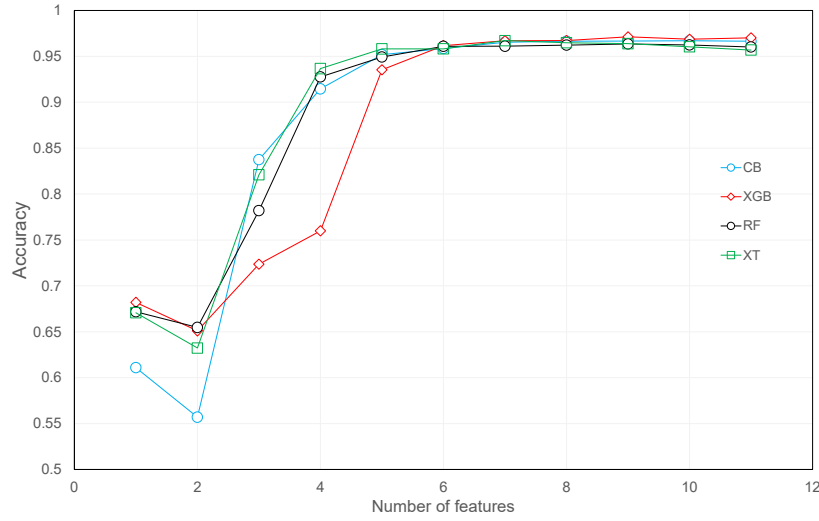


Figure 6.7: Accuracy during recursive feature elimination test (Tavakol Sadrabadi & Innocente, 2023).

6.3.3 Accuracy measures

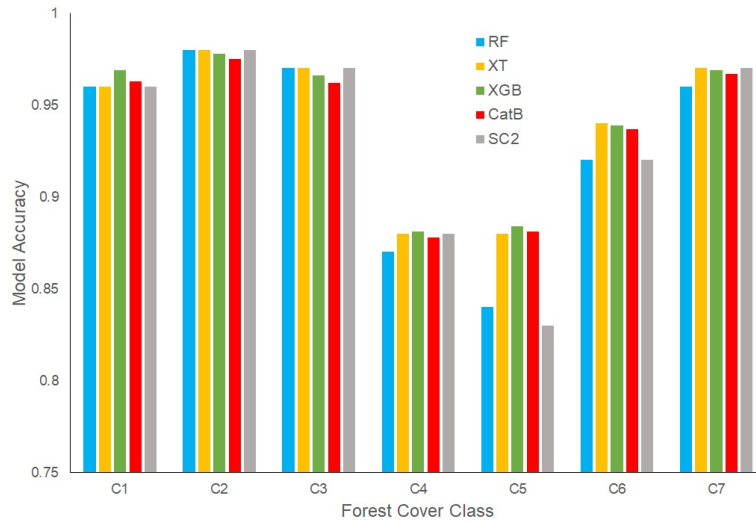
The overall classification accuracy (macro average) achieved by each of the different models studied here is shown in Table 6.3. It can be observed that the highest accuracy over the whole dataset equals 0.97, and is obtained by XGB. This is slightly higher than the accuracy achieved by CatB (0.967), SC3(0.967), and XT (0.968). Even though the optimised RF achieves an accuracy of "only" 0.964, this still surpasses other similar research results, including (Kumar & Sinha, 2020; Sjöqvist et al., 2020). Despite its higher overall accuracy, XGB exhibits lower precision compared to XT and SC2 and a lower $F1$ score compared to XT. The lowest overall accuracy is 0.913, achieved by SVM with radial basis kernel (SVR). Nonetheless, this value surpasses accuracy values previously reported in the literature using SVM on the same dataset.

Figure 6.8 presents the accuracy achieved by the five best-performing models for each of the seven cover types in the dataset. It is clear that all models perform poorly on the C4 and C5 cover types, with the highest accuracy values being 0.881 and 0.884, respectively. Unsurprisingly, these are the two classes with the fewest data samples. However, SC3 and RF performed significantly worse than other models for the C5 cover type. Figure 6.9 presents the confusion matrix for the XGB, XT, CatB, and SC2 models. It can be observed that the accuracy of estimations for the majority C1 and C2 cover type classes is higher than 0.96 for all models. It is interesting to note

Table 6.3: Accuracy metrics for the implemented models (Tavakol Sadrabadi & Innocente, 2023).

Metric	DT	SVR	KNN	RF	XT	Ada	XGB	CatB	SC1	SC2	SC3
<i>acc</i>	0.934	0.913	0.934	0.964	0.968	0.963	0.971	0.967	0.935	0.967	0.940
<i>prec</i>	0.901	0.897	0.897	0.951	0.955	0.952	0.952	0.951	0.898	0.955	0.895
<i>rec</i>	0.898	0.869	0.872	0.928	0.939	0.922	0.941	0.938	0.890	0.932	0.910
<i>F1-score</i>	0.900	0.882	0.884	0.939	0.947	0.936	0.946	0.943	0.893	0.943	0.902

that the most prominent misclassifications by all four models are "C5 misclassified as C2" and "C4 misclassified as C3", and not vice versa (Tavakol Sadrabadi & Innocente, 2023).

**Figure 6.8:** Accuracy of different classifiers for each cover class, adopted from (Tavakol Sadrabadi & Innocente, 2025).

6.4 Discussion

This research chapter proposes a methodology based on Machine Learning (ML) algorithms with automated fine-tuning of the model combined with recursive feature elimination to predict vegetation type from cartographic data. The overall accuracy obtained by the proposed approach using the XGB model on the UCI dataset is 97.1%, which surpasses those reported in other studies. For example, (Sjöqvist et al., 2020) reported an overall accuracy of 94.7%, (Sameer et al., 2021) reported 93%, and (Macmichael & Si, 2017) achieved an accuracy of 97.01% (the latter using deep learning models) (Tavakol Sadrabadi & Innocente, 2023).

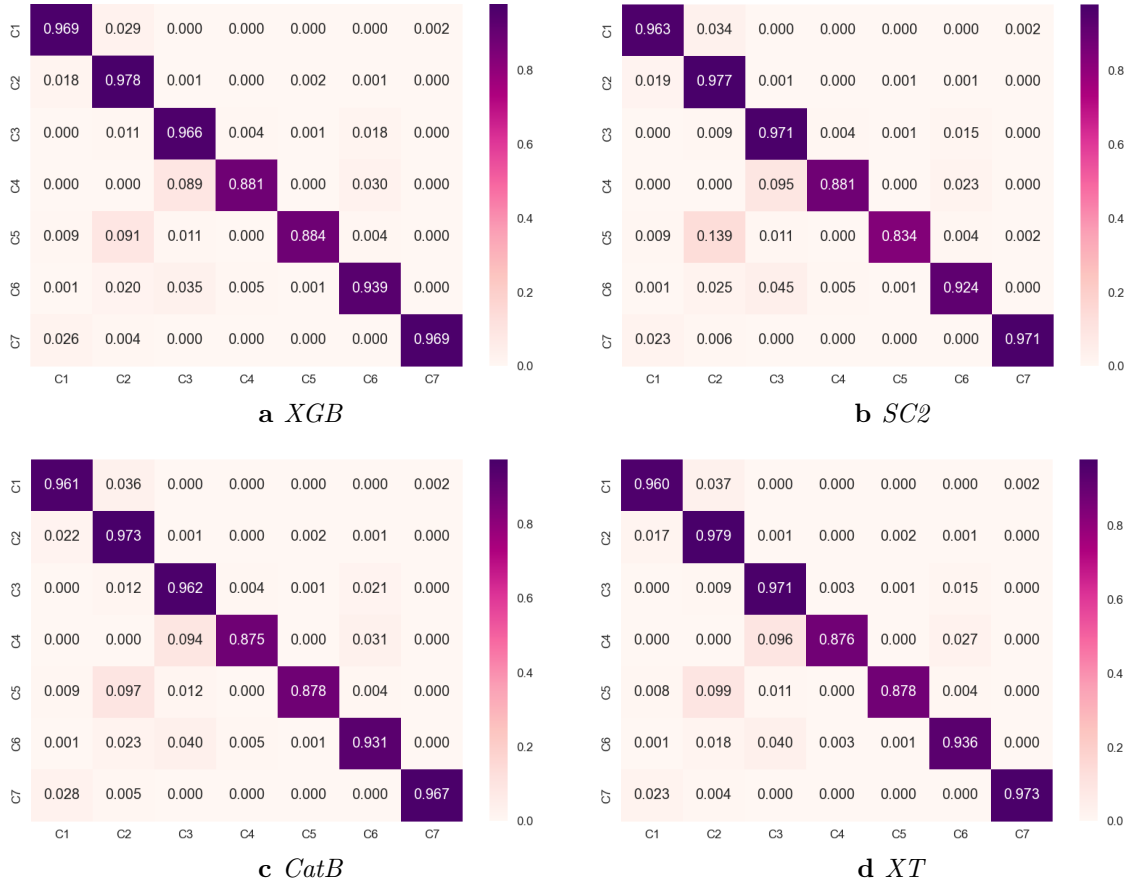


Figure 6.9: Confusion matrix of the four best-performing classifiers for predicted cover type classes (Tavakol Sadrabadi & Innocente, 2023).

Considering class-wise accuracy, Figure 6.9 shows that the four models are slightly overfitted on the majority class, the C2 cover type (283,301 datapoints), achieving the highest accuracy (97.3–97.9%). Unsurprisingly, the lowest accuracy (87.5–88.1%) corresponds to the minority class, the C4 cover type (2,747 datapoints). Somewhat surprisingly, all four models show high accuracy for the C7 cover type, despite its moderate sampling size (20,510 datapoints). Nonetheless, it is important to note that the proposed approach with all four models achieves higher accuracy for the undersampled classes than those reported by previous researchers. For example, while our proposed approach with XGB reaches 88.1%, 88.4%, and 93.9% for classes 4, 5, and 6, respectively, (Sjöqvist et al., 2020) reported respective accuracy of 77.9%, 77%, and 86%. This comprises a significant improvement. For classification of the C1 and C2 cover types, the same authors reported an accuracy of 93.7% and 96.7%, respectively, while our method using the XGB model achieved 96.9% and 97.8%, respectively. It is notable that using our proposed approach with the RF model used in (Sjöqvist et al., 2020) resulted in an overall accuracy of 96.4%, which is a significant improvement over

the results reported in their study (Tavakol Sadrabadi & Innocente, [2023](#)).

Chapter 7

Effect of Fire-Wind Coupling on Fire Propagation Estimations

As presented in section 2.3, wildfire estimation models could be classified into two broad groups of (i) *Coupled* and (ii) *Decoupled*, based on the level of interaction of fire and atmosphere in these models. Each of these models has specific advantages and disadvantages which makes them useful for different types of tasks. However, a structured evaluation of the effect of choosing the coupling strategy would be highly valuable when dealing with these types of models.

7.1 Coupled or Decoupled?

The choice of the right wildfire propagation model is highly dependent on the intended application: *coupled* models are more rigorous though computationally expensive (hence with limited operational use) whereas *decoupled* models decrease the computational cost at the expense of disregarding the effect of the fire on the wind field (hence sacrificing prediction accuracy). In order to compensate for this drawback, efforts have been made to increase the accuracy of the wind estimations; e.g. using Numerical Weather Prediction (NWP) models together with methods to downscale and refine these estimations over the terrain of interest (Höhlein et al., 2020). However, these large-scale models cannot capture wildfires local effects. Generally, it is clear that the level of fire-wind interaction considered by the model affects the accuracy and uncertainty level of the model outputs. Still, there is a gap for a detailed investigation of the impact of fire-wind coupling on wildfire propagation dynamics including the Rate of Spread of Fire in different terrain conditions. Hence, this section utilises the FDS-LevelSet model in order to study the effect of considering or neglecting the fire-wind interaction of wildfire propagation estimations as presented in (Tavakol Sadrabadi & Innocente, 2024).

7.2 Experimental Data and Model Calibration

7.2.1 Experimental data

Numerical simulations are validated against flat terrain grassland fire spread experiments carried out by the Commonwealth Scientific and Industrial Research Organisation (CSIRO) (Cheney et al., 1993; Cheney et al., 1998). As in (Mell et al., 2007), C064 and F19 are the selected experiments, which were performed in the middle of the dry season on flatlands of $100 \times 100 \text{ m}^2$ covered with dry Kerosene grass and of $200 \times 200 \text{ m}^2$ covered with dry Kangaroo grass, respectively. During each experiment, the reference wind speed (u_2) was measured at 2 m AGL whereas the air temperature (T_{amb}) and relative humidity were measured at 1.4 m AGL. Fuel load (m_f'') and height (h) were sampled at different locations and averaged within each plot. Other fuel characteristics, including surface area-to-volume ratio (σ) and fuel moisture content (FMC), were also measured and recorded. Two workers ignited fires, starting at the midpoint and moving towards either side of the plot. The length of ignition is around 50 m for $100 \times 100 \text{ m}^2$ plots and around 175 m for $200 \times 200 \text{ m}^2$ plots. Fire behaviour was then studied through data gathered by ground observations and oblique aerial photographs. The RoS was then calculated for each experiment as the maximum distance travelled by the fire between successive time steps.

7.2.2 Boundary conditions and grid Sensitivity

Open boundary conditions are used at the top, outlet, right, and left boundaries. Ambient wind is simulated using Monin-Obukhov similarity theory, with Obukhov length $L = -500 \text{ m}$, aerodynamic roughness length $z_0 = 0.03 \text{ m}$, $u_2 = 4.6 \text{ m/s}$ for C064, and $u_2 = 4.8 \text{ m/s}$ for F19.

Structured Cartesian grids with equal spacing in x , y , z directions are used to discretise a $120 \times 120 \times 40 \text{ m}^3$ domain for C064 and a $240 \times 240 \times 100 \text{ m}^3$ domain for F19. In order to study the sensitivity of the simulated fire propagation to the grid cell size, sizes between $1 \times 1 \times 1 \text{ m}^3$ and $5 \times 5 \times 5 \text{ m}^3$ are tested for the FDS-LS model (Tavakol Sadrabadi & Innocente, 2024).

FDS-LS uses Albin's fuel models (McGrattan et al., 2019) by default, which sets the values of h , σ , β , ν_{char} , m_f'' , and RoS_0 for different pre-defined fuel types. Following (Vanella et al., 2021) and as a first step, Albin's fuel type 1 (*short grass*) and fuel type 3 (*tall grass*) are used here to represent the fuel in C064 and F19 experiments, respectively. The evolution of the fire front is shown in Figure 7.1 for both experiments, cell sizes of 1 m, 2 m, 3 m and 5 m, and both *coupled* (C) and *decoupled* (D) configurations (Tavakol Sadrabadi & Innocente, 2024). It can be observed that the predicted fire front is sensitive to both cell size and fire-wind coupling. The C-configuration predicts higher RoS, which is closer to the experimental results. Increasing cell size generally leads to higher RoS as well, in agreement with results in (Vanella et al., 2021).

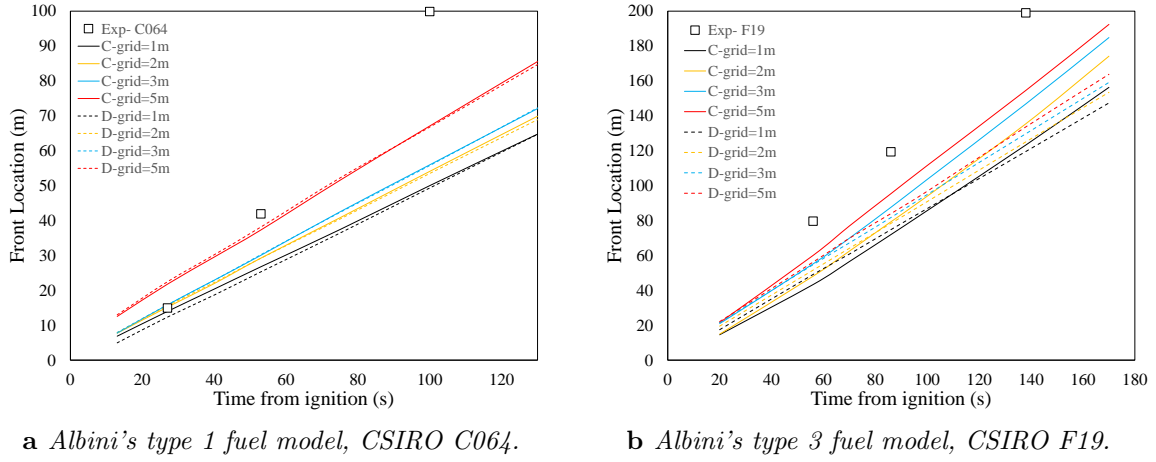


Figure 7.1: Evolution of simulated fire front location predicted by FDS-LS for CSIRO C064 and F19 experiments using Albini's fuel models, cell sizes of 1 m, 2 m, 3 m and 5 m, and both coupled (C) and decoupled (D) configurations. Results from field tests are also provided for reference (Tavakol Sadrabadi & Innocente, 2024).

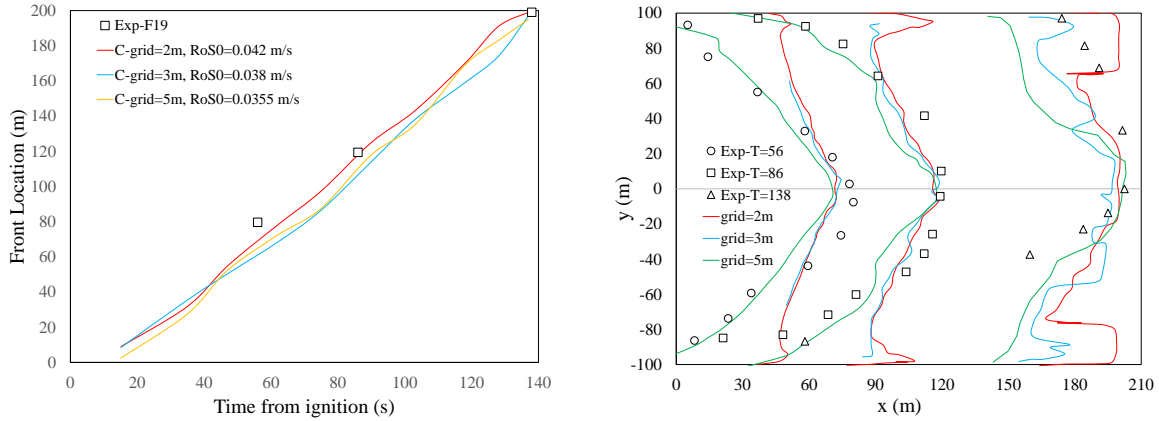
7.2.3 FDS-LS fuel definition and RoS_0 calibration

Although FDS-LS uses Albini's fuel models (McGrattan et al., 2019) by default, it is possible to define other fuels. Since the predicted fire front locations in Figure 7.1 do not accurately match the experimental results, a custom fuel type is defined with the physical characteristics in Table ?? to represent the Kangaroo grass in the CSIRO F19 field experiment. This experiment is chosen here due to its larger domain, which is more convenient to study the effect of the fire-wind coupling. Since FDS-LS does not require the thermal properties of the vegetation, only h , σ , β , ν_{char} , and m_f'' are required from Table ??, with RoS_0 being calibrated (Tavakol Sadrabadi & Innocente, 2024).

Calibration is carried out for three cell sizes and coupled FDS-LS (MODE 4). Figure 7.2 (a) shows that the evolution of the fire front location now matches the field measurements, with the calibrated RoS_0 only marginally larger than that of Albini's fuel type 3 (*tall grass*). Figure 7.2 (b) shows the predicted fire perimeter of the simulated fire predicted by the coupled FDS-LS with calibrated RoS_0 for cell sizes of 2 m, 3 m and 5 m at three time instances since ignition (Tavakol Sadrabadi & Innocente, 2024).

7.3 Effect of Coupling Strategies

Figure 7.2 (b) shows that the coupled FDS-LS with calibrated RoS_0 accurately predicts the CSIRO F19 experiment under no-slope conditions. The effects of fire-wind



a Evolution of simulated fire front location.

b Fire perimeter at 56 s, 86 s and 138 s since ignition (Tavakol Sadrabadi & Innocente, 2024).

Figure 7.2: (a) Evolution of simulated fire front location and (b) fire perimeter at three time instances since ignition, as predicted by coupled FDS-LS for CSIRO F19 experiment using custom fuel type defined by physical characteristics in Table 3.1, calibrated RoS_0 , and cell sizes of 2 m, 3 m and 5 m. Results from field test are also provided for reference (Tavakol Sadrabadi & Innocente, 2024).

coupling on the headfire position and the resulting RoS for a range of wind speeds and topography slopes during upslope propagation with the same custom fuel can be observed in Figure 7.3, where $2 \times 2 \times 1 \text{ m}^3$ cells are used for spatial discretisation. Given that FDS uses structured grids, a sloped topography is modelled using a staircase of cubic blocks (Tavakol Sadrabadi & Innocente, 2024).

Figure 7.3 shows (a) the headfire position (distance travelled) and (b) corresponding RoS for eight wind speeds in the range of 1–20 m/s and horizontal topography. It also shows (c) the head fire position and (d) corresponding RoS for a fire propagating upslope for all nine possible combinations of three slopes (5%, 15%, 30%) and three wind speeds (1 m/s, 5 m/s, 10 m/s). Both *coupled* (C) and *decoupled* (D) FDS-LS are used to model each scenario. Note that *wind speed* refers to horizontal reference wind speed (u_r), whilst the resulting upslope wind speed is higher. As expected, higher wind speed and higher topography slope (for upslope propagation) lead to higher RoS. Furthermore, higher wind speeds of up to 10 m/s and higher surface slopes of up to 30% also result in larger differences between predictions by corresponding coupled and decoupled fire–wind models, in agreement with experimental results in (Butler et al., 2007). For example, the difference between coupled and decoupled predictions of the RoS is 0.44 m/s for 30% slope and 5 m/s wind, whereas it is 1.51 m/s for 30% slope and 10 m/s. The RoS predicted by coupled FDS-LS appears to be generally higher than the one predicted by its decoupled counterpart for wind speeds of up to 12 m/s. For horizontal topography in Figure 7.3 (b), this trend seems to invert for wind speeds approximately between 12 m/s and 20 m/s, with the coupling strategy making little

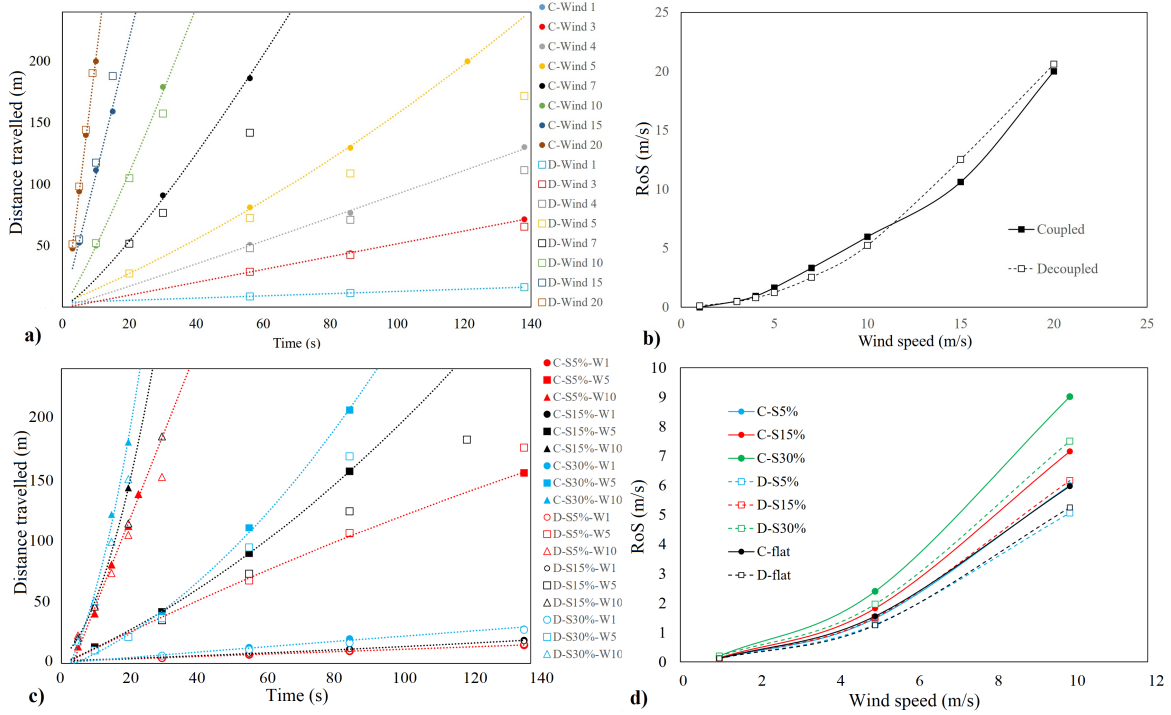


Figure 7.3: (a) Headfire position for eight wind speeds in the range of 1–20 m/s and (b) their corresponding RoS for horizontal topography; and (c) headfire position for nine slope–wind combinations in the range of 1–10 m/s and 5–30% and (d) their corresponding RoS with fire propagating upslope. Both coupled (C) and decoupled (D) FDS-LS are used to model each scenario (Tavakol Sadrabadi & Innocente, 2024).

to no difference for a wind speed of 20 m/s. More data points would be required to analyse this observation (Tavakol Sadrabadi & Innocente, 2024).

It is important to note that these simulations using FDS-LS suggest that increasing wind speeds always leads to increasing RoS. However, experimental results (McArthur & Australia., 1966; Potter, 2012a) showed that a turning point and a reduction of the RoS is to be expected. In fact, the model tends to overestimate the RoS for increasing wind speeds when compared to typical values reported in the literature, especially for extreme cases—in which model predictions are counter-intuitive. Since FDS-LS is not physics-based, it is reasonable to infer that it does not capture some of the relevant underlying fire propagation dynamics, and therefore may make unreliable predictions for higher wind speeds (here, higher than ≈ 10 –12 m/s).

Wildfires can propagate upslope surprisingly fast due to the preheating of unburned fuel ahead of the fire as the plume attaches to the slope surface (Torben P. Grumstrup, 2017). Under no-wind no-slope conditions, fuel preheating is governed largely by radiation, since upstream and downstream air entrainment is the same, hence forming a vertical uprising plume. As the angle between the fire plume and the fuel bed shrinks,

the length of the plume attachment increases, resulting in a higher RoS. This angle shrinks as the *flame tilt angle* (θ) and the *fuel bed inclination angle* (α) increase, where θ is the angle between the centerline of the individually pioneering flame and the vertical axis (M. Li et al., 2020). In turn, θ increases with increasing upslope *wind speed* and with increasing α due to the resulting asymmetric *air entrainment*. Since buoyancy has an upslope component, air entrainment into the fire from the burned side (upstream) is greater, hence tilting the plume towards the unburned downstream vegetation (Morandini et al., 2018). Therefore, higher upslope *wind speeds* and higher *surface slopes* lead to faster upslope fire propagation due to the resulting larger *plume attachment length*. Even though FDS-LS does not model the flame, radiative heat transfer, or fuel pre-heating effects, the larger RoS predicted for larger surface slopes when coupling fire and wind models during upslope fire propagation is likely due to the released latent heat from the fire front, which contributes to the formation of convective wind patterns upslope (Tavakol Sadrabadi & Innocente, 2024).

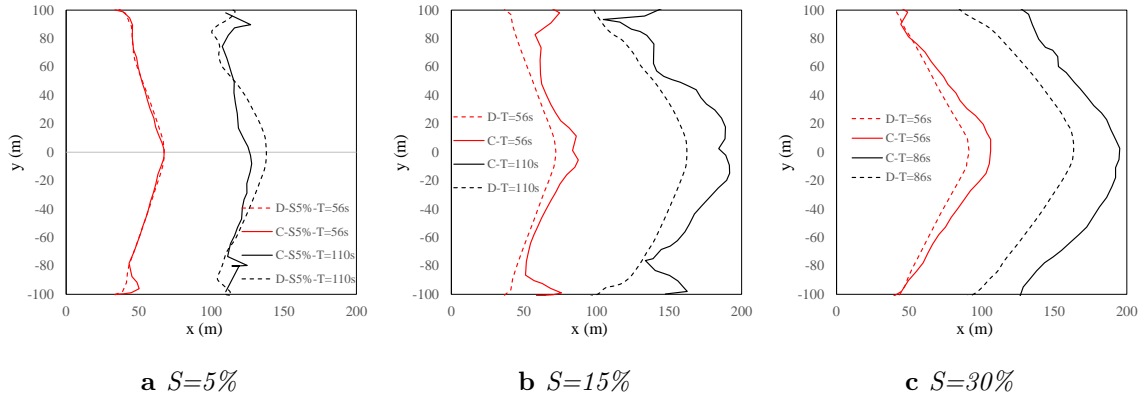


Figure 7.4: Fire perimeter as predicted by coupled (C) and decoupled (D) FDS-LS at three different times for three different slopes.

Thus, higher wind speeds and larger inclinations of the fuel bed result in faster upslope fire propagation. Coupled FDS-LS predicts faster propagation than its decoupled counterpart, presumably better capturing the relevant phenomena associated with fire-induced wind. Figure 7.4 also shows that decoupled FDS-LS displays smoother perimeters.

Chapter 8

Improving Wildfire Propagation Prediction Utilising Aerial Swarm-Based Real-Time Wind Measurements

Wildfire enhances the surrounding atmosphere and creates local wind patterns. These fire-induced local wind patterns, in turn, dynamically affect the behaviours of wildfire and its rate of spread. In the previous section, it was shown that this interaction has a strong effect on fire's RoS, and therefore should not be neglected when predicting its propagation. Still, this is exactly the approach adopted by decoupled wildfire models. Hence, this chapter proposes a framework to improve wildfire model predictions by feeding it with near-surface wind fields estimated from UAV measurements taken at higher altitudes. The idea is to capture the fire-wind interaction without having to solve the computationally expensive Navier-Stokes equations. Consequently, section 8.1 presents the proposed framework in a conceptual capacity; section 8.2 presents the details and actual steps for the development of the framework; and finally, section 8.3 studies how such a framework would help to improve the wildfire propagation estimations.

8.1 The Conceptual Framework

The proposed methodology is model agnostic and therefore can be implemented as a stand-alone module to be integrated with any wildfire model that includes wind in its governing equations. Since it aims to mimic the effect of fire-wind coupling, it was originally proposed with decoupled wildfire models in mind. Nonetheless, it could be applied to coupled models as well, potentially using data assimilation to correct the wind field predicted by the model. A top-level description of the methodology is shown in Figure 8.1 and summarised below (Tavakol Sadrabadi & Innocente, [2024](#)):

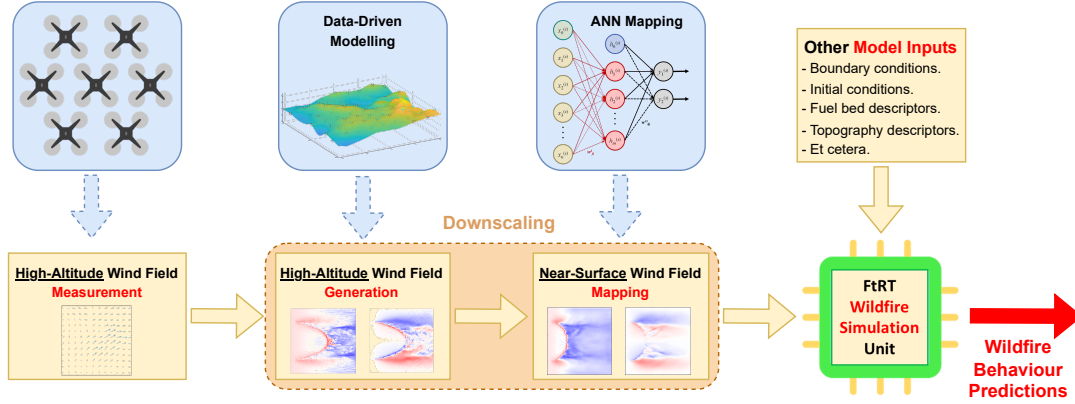


Figure 8.1: System-level description of the proposed methodology to enhance wildfire model predictions using near-surface wind fields approximated from measurements at a high altitude (specifically, at flight height) (Tavakol Sadrabadi & Innocente, 2024).

1. A swarm of UAVs measure wind velocity at different 2D locations at flight height (here assumed to be equal to $H=40$ m AGL), at a given time $t = t_i$.
2. The measured wind velocities are used to generate a high-resolution wind field using a data-driven super-resolution approach.
3. The high-resolution wind field at flight height is used to approximate the near-surface wind field employing a mapping method such as a neural network.
4. The downscaled near-surface wind field is fed into the FtRT simulator, which forecasts the fire propagation for the desired predictive horizon (\mathcal{T}). Thus, the fire propagation is simulated in the interval $(t_i, t_i + \mathcal{T}]$.
5. Once the desired time increment (Δt) for updates has elapsed, swarm-based measurements are re-taken at $t_{i+1} = t_i + \Delta t$ and the process is repeated to predict the fire propagation in the $(t_{i+1}, t_{i+1} + \mathcal{T}]$ interval. Thus, the predictive horizon moves forward by $\Delta t \ll \mathcal{T}$.

The fire propagation forecast during the predictive horizon (\mathcal{T}) can be used to assist firefighting operations, with the surface wind field remaining frozen during this time. Nonetheless, the outputs of the simulator after every Δt , together with the updated near-surface wind field at that time, comprise the inputs into the simulator to forecast the fire propagation during the next predictive horizon (Tavakol Sadrabadi & Innocente, 2024).

Although it may often be infeasible to have a swarm of UAVs airborne solely to take wind measurements, equipping them with appropriate sensors (and possibly effectors)

would enable the swarm to perform more than one task simultaneously. For example, consider the swarm of self-organising drones proposed by Innocente and Grasso (Innocente & Grasso, 2019a) or the drone fleet system proposed by Ausonio et al. (Ausonio et al., 2021), which could easily be taking imagery and measuring environmental variables like wind, temperature, or pressure whilst engaged in fire suppression and/or monitoring activities. A bird's eye view of an envisioned wildfire emergency response system is shown in Figure 8.2, which assimilates the methodology to enhance wildfire model predictions proposed in this research and shown in Figure 8.1.

The smaller the Δt between measurements the better, as the wind is kept frozen for shorter periods. A range of simulations are carried out in Section 8.3 to study how such model impacts propagation results and to study the effect of Δt on a flat grassland covered with a uniform fuel bed. Since actual wind measurements are *certain to be uncertain*, Section 8.3.2 provides also an initial attempt at studying the effect of uncertainty on the wildfire model predictions.

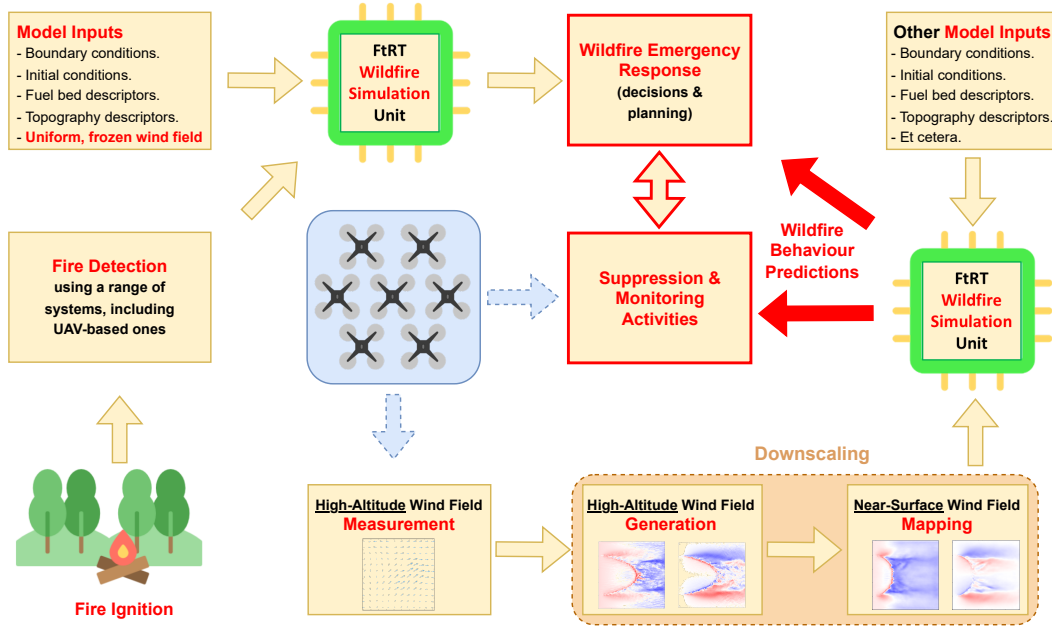


Figure 8.2: Bird's eye view of an envisioned wildfire emergency response system empowered by UAV swarms, which assimilates the proposed methodology shown in Figure 8.1 to enhance fire propagation model predictions. For the UAV swarm undertaking suppression activities, adopted from (Tavakol Sadrabadi & Innocente, 2024).

8.2 Wind Field Downscaling and Uncertainty Quantification

The previous section conceptually presents the framework proposed in this thesis for improving the accuracy of wildfire propagation estimations by using real-time UAV swarm-based wind measurements. This section presents the system development details including the dataset, approaches, models used, and results.

8.2.1 System description

Generally, downscaling refers to the process of obtaining information about physical quantities at a smaller local scale from lower-resolution available data through the use of appropriate refinement methods (Höhlein et al., 2020). Downscaling methods can be classified into two broad groups including (i) dynamical and (ii) empirical-statistical approaches (Sachindra et al., 2014). Dynamical downscaling refers to the procedure of using high-resolution mass-conserving or momentum-conserving numerical models to interpret the outputs of *NWP* models on a finer scale. Considering that this method is computationally expensive and timely, especially for large domains, it is mainly restricted to small domains (Höhlein et al., 2020). On the other hand, statistical downscaling efforts to train statistical models between quantities at coarse and fine scales. Such models would have a very short inference time and hence can provide instant estimations when fully trained. With the recent advancements in machine learning (ML) and deep learning (DL) methods, different studies have focused on the use of state-of-the-art DL algorithms and methods for this purpose (see (Dujardin & Lehning, 2022; J. Zhang & Zhao, 2021)).

Given that the fire plume in a wildland fire is tilted forward due to the ambient wind velocity, the turbulent fields near the surface and at the measurement height differ significantly. Therefore, downscaling atmospheric turbulence in the presence of fire cannot be directly addressed through a single-image super-resolution task. Hence, the developed system consists of three steps to provide real-time wind field maps near the terrain surface. The steps include (i) real-time UAV-swarm-based measurement of the turbulent wind above the fire, (ii) reconstruction of a high-resolution wind field at UAV flight altitude from sparse point measurements, and (iii) estimation of the high-resolution wind field close to the terrain surface based on the reconstructed wind field at UAV flight altitude. It is important to note that while the downscaling process is typically equated with the super-resolution or reconstruction step in the literature, this study considers downscaling to encompass both the super-resolution/reconstruction step and the estimation of the high-resolution near-surface wind field from the reconstructed high-altitude wind field.

Utilising the sparsely measured wind values at each time step as input data into the model, a high-resolution map of the wind field at the measurement altitude ($Z_m=40$ m) is generated which is in turn used to estimate the near-surface wind field $Z_e=2$ m

AGL. Considering that a high-res wind field is generated for the Z_m at the previous step through a super-resolution method, the equivalent high-res wind field for Z_e could be generated through a regression procedure. To achieve this, the study employs an image-to-image translation technique, which generates the required wind field at 2 m *AGL* from the wind field reconstructed from sparse measurements at 40 m *AGL*.

8.2.2 Simulations scenarios

Considering that actual measurements of wind velocity in wildfire situations are challenging to obtain and deep learning models require extensive amounts of data for training procedures, this study employs coupled three-dimensional computational fluid dynamics (CFD) simulations of wildland fire propagation to act as synthetic data. An overview of the physical and geometrical parameters of the simulation conditions including wind velocity, vegetation height and type, and terrain slope are presented in Table 3.3. This chapter utilises the simulated results from Veg_1 and Veg_3 . As shown in table 3.3, each vegetation type is utilised in 75 field-scale simulations carried out with three different vegetation heights of H_g , five different terrain slopes (S), and five different ambient wind speeds (u_{10}). Consequently, a total number of 150 simulations are carried out to provide the data required for developing the wind downscaling framework in this section. All simulations are performed utilising the Fire Dynamics Simulator (FDS) as discussed in details in sections 3.1.4 to 3.1.6 and validated in section 3.1.7. The details of the physical and thermal parameters of fuel utilised in this study are also presented in Table 3.2 in detail.

The turbulent flow field within the domain is simulated utilising the very large eddy simulation (VLES) model with Deardorff’s sub-grid scale (SGS) model for turbulent eddy viscosity closure terms. To replicate the turbulent nature of the natural atmospheric winds, this study utilises the synthetic eddy method (SEM)(Jarrin et al., 2008) that introduces random eddies into the domain as adopted in relevant studies (i.e. see (Innocent et al., 2023)). Considering that an accurate definition of the eddy characteristics requires measurements of the turbulent Reynolds stress within the ambient wind and canopy height which are not applicable here, an arbitrary value of 10% turbulence intensity is determined here similar to (Innocent et al., 2023). Utilised boundary Conditions include a no-slip boundary condition for the ground surface and ‘Open’ boundary conditions for the rest of the boundaries.

8.2.3 Model architecture, dataset, and training procedure

Architecture Briefly, this study effort to estimate the spatial distribution of the near-surface (2m *AGL*) wind velocity components of u_2 , v_2 and w_2 in the presence of an active grassland fire from the sparsely measured values (u_{40} , v_{40} and w_{40}) utilising a swarm of UAVs. As previously described, the problem is addressed through supervised training of two convolutional neural networks. Figure 8.3 presents the overall workflow

of the models and data utilised in model training. The first model is trained to reconstruct the high-resolution wind and temperature field at 40m AGL from the sparsely measured or low-resolution input data. The low-resolution input data are sampled from the original high-resolution simulations so that each sampled pixel represents a point measurement carried out by an individual UAV. Three different numbers of UAVs (n) are considered in this study so that $n \in (25, 49, 100)$. Sampled pixels $P \in \mathbb{R}^{n \times 4}$ are then used to generate the low-resolution input file $I_{lr} = \mathcal{F}_{\text{interp, KNN}}(P) \in \mathbb{R}^{13 \times 13 \times 4}$ through linear interpolation for areas that fall between at least two measurements and assigning values utilising the nearest available value (KNN) to outer regions (figure 8.3a-b). Extra information including the terrain slope (S) in degrees, the surface temperature ($T_{surf=2}$), Vegetation type (G_t) and the vegetation height (H_g) at corresponding coordinates of the terrain are inputted in the model through an encoder branch and is concatenated with the corresponding upsampled decoder block of the SR model (figure 8.3c&d). Hence, the output of the super-resolution model would be $I_{sr} = \mathcal{F}(I_{lr}, I_{\text{terrain}})$ where $I_{sr} = (u_{40}, v_{40}, w_{40}, T_{40}) \in \mathbb{R}^{416 \times 416 \times 4}$, and $I_{\text{terrain}} = (T_2, S, H_g, G_t)$.

The second model is trained on high-resolution input-output pairs of flow field at 40m AGL and the corresponding values at 2m AGL so that to estimate the near-surface wind field $I_{\text{surf}} = \mathcal{G}(C)$ where $I_{\text{surf}} = (u_2, v_2, w_2)$ from a concatenation of reconstructed high altitude wind field and the high-resolution data corresponding to the surface temperature, vegetation height and type, and terrain slope $C = \text{concat}(I_{sr}, I_{\text{terrain}}) \in \mathbb{R}^{416 \times 416 \times 8}$ (see figure 8.3d-e).

The utilized structure for both networks resembles a UNet with Residual blocks (He et al., n.d.) in both encoder and decoder branches empowered with the Convolutional Block Attention Module (CBAM)(Woo et al., 2018) blocks. A sensitivity analysis is performed and the optimal number of model parameters is selected based on a trade-off between obtained accuracy and training time. The activation function for the convolutional layers includes *tanh* activation for all layers except the output layer which uses the *linear* activation function. It should be emphasized that the linear activation showed better performance compared to *LeakyReLU*. It is worth mentioning that commonly used activation functions such as *relu* performed poorly on this task despite the promising results on actual image data. It is mainly based on the fact that even though the data is similar to an image, a large portion of values of the data matrix of inputs and outputs includes negative values which would be rounded to zero by using *relu*. Hence, a *linear* activation function is deemed necessary. All convolutional layers use zero padding, a *he – normal* kernel initializer, and a kernel size of 3×3 except for the first convolutional layer after the input layer, which benefits from a 7×7 kernel, and the output layer which uses a 1×1 kernel. Figure 8.3 also presents the structure of the encoder and decoder blocks in both models. All blocks include a dropout layer with a dropout ratio of 5% which is meant to assist in improving the model generalisability and uncertainty quantification analysis. All Models are then trained for 200 epochs with *MAE* loss function and the Adam optimizer with an initial learning rate of 0.0006 and an exponential decay rate of $\text{beta}_1=0.9$. During the training, accuracy metrics are observed after each epoch and the best models are saved for later use. To evaluate

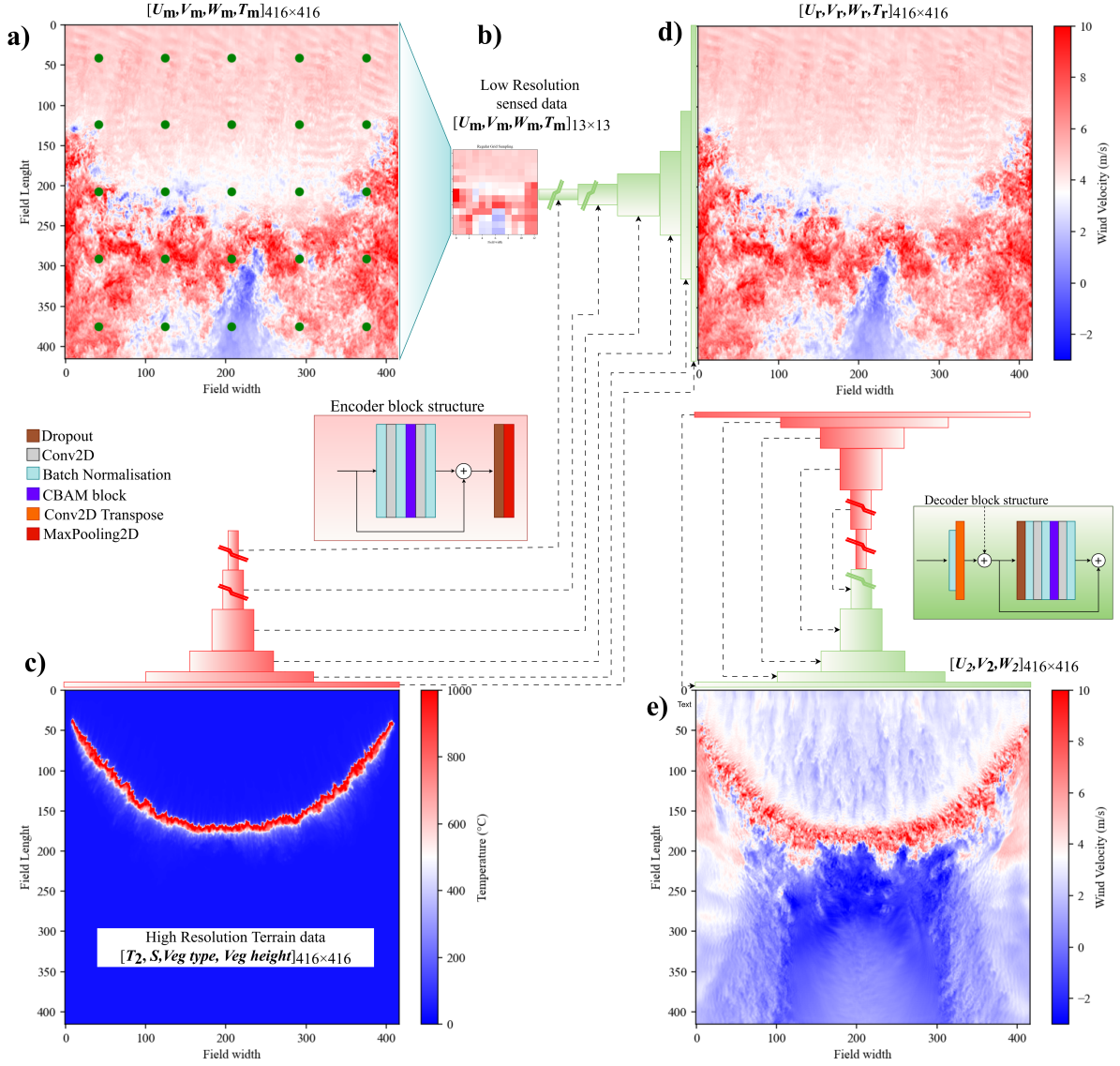


Figure 8.3: Architecture used for reconstructing the high-resolution wind field from low-resolution sensor data, showing: (a) high-altitude wind field sampled by UAVs in a structured formation, (b) generated low-resolution wind field as input to the super-resolution (SR) model, (c) terrain and fire data used as additional information for wind field reconstruction, (d) reconstructed high-altitude wind field, and (e) estimated near-surface wind field.

the performance of neural networks, the mean absolute error MAE , and root mean squared error $RMSE$ values are calculated as follows:

$$RMSE(y, y') = \sqrt{\frac{1}{n} \left(\sum_i^n |y_i - y'_i|^2 \right)} \quad (8.1)$$

$$MAE(y, y') = \frac{1}{n} \left(\sum_i^n |y_i - y'_i| \right) \quad (8.2)$$

Where y and y' are the ground truth and estimated values respectively.

Concerning probabilistic performance, three additional metrics including the standard deviation (Std), Prediction Interval Coverage Probability (PICP), and Prediction Interval Normalized Average Width (PINAW) are utilised to quantitatively assess the model performance. The standard deviation is a measure of variation or dispersion in a set of data values and can be calculated as follows:

$$Std = \sqrt{\frac{\sum_{i=1}^N (x_i - \mu)^2}{N - 1}} \quad (8.3)$$

where x_i is the value of i_{th} data point, μ is the population mean, and N is the number of datapoints.

The PICP on the other hand, is a fundamental characteristic of prediction intervals (PIs) and is calculated as the fraction of target values covered by the estimated PIs (S. Liu et al., 2022):

$$PICP = \frac{1}{N} \sum_{i=1}^N \epsilon_i; \text{ and } \epsilon_i = \begin{cases} 1 & , \text{if } \hat{k}_i \in [L_i, U_i] \\ 0 & , \text{otherwise} \end{cases} \quad (8.4)$$

where L_i and U_i are the estimated lower and upper limits at the i_{th} array, and N is the number of arrays. Generally, a larger PICP indicates more targets covered by the predicted prediction intervals (PIs). However, it does not necessarily denote an accurate model. Apart from the coverage probability, the width of the estimated PIs is an important metric, defining the quality of the PIs, so that for equal PICPs, a smaller PINAW would normally imply a better model. PINAW measures the average width of the prediction intervals normalized by the range of the actual observations and can be calculated as follows (S. Liu et al., 2022):

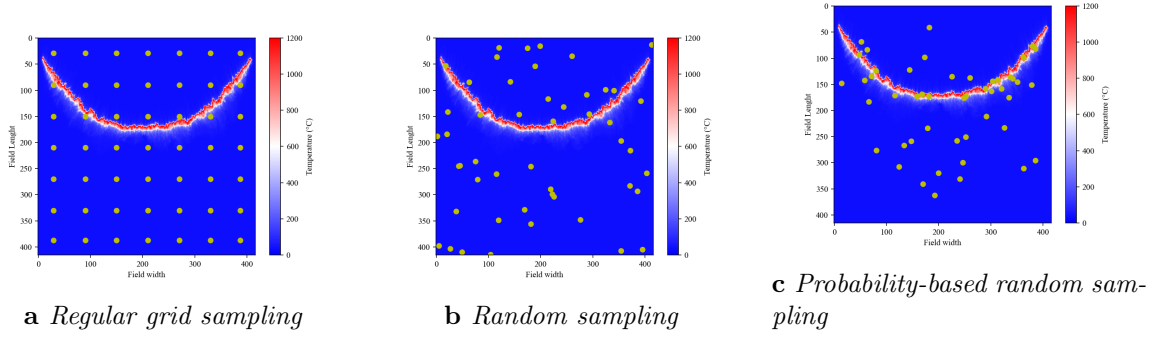
$$PINAW = \frac{1}{N} \sum_{i=1}^N \frac{U_i - L_i}{Y_{\max} - Y_{\min}} \quad (8.5)$$

where Y_{\max} and Y_{\min} are the maximum and minimum values of the actual observations, respectively.

Table 8.1: *Effect of the number of model parameters on the SR performance for $n=100$, utilising first sampling strategy*

	n. filters	N.params	U* (m/s)		V* (m/s)		W* (m/s)		T* °C	
			MAE	RMSE	MAE	RMSE	MAE	RMSE	MAE	RMSE
Attention	32/ 8,16,32,64,128 /128,64,32,16,8	1,030,358	0.744	1.277	0.724	1.241	0.875	1.535	3.860	14.891
	32/16,32,64,128,256/256,128,64,32,16	3,901,084	0.735	1.268	0.717	1.225	0.867	1.514	3.841	14.632
	32/32,64,128,256,512/256,128,64,32,16	8,332,602	0.732	1.268	0.715	1.223	0.866	1.525	3.889	15.142
No-Attention	32/32,64,128,256,512/512,256,128,64,32	15,334,136	0.736	1.274	0.720	1.234	0.864	1.510	3.797	14.626
Att+Physics Constrained	32/16,32,64,128,256/256,128,64,32,16	3,901,084	0.741	1.283	0.719	1.230	0.869	1.523	3.857	14.814
	32/16,32,64,128,256/256,128,64,32,16	3,901,084	0.737	1.275	0.721	1.235	0.868	1.516	3.845	14.683

* $U(\text{m/s}) \in [-18.7, 55.3]$, $V(\text{m/s}) \in [-38.4, 37.7]$, $W(\text{m/s}) \in [-22.2, 52.1]$

**Figure 8.4:** *Wind sampling strategies*

Dataset

As described before, a total number of 150 simulations are carried out with different combinations of wind speeds, terrain slopes and vegetation height and types. The wind field at 40m and 2m *AGL* (parallel to the terrain) along with the temperature field at the surface are extracted at different time steps after the start of ignition and are used for training the network. The dataset includes 24568 pairs of input-target data of which 17343 are randomly adopted for training, 3652 for validation, and 3573 for the test.

As mentioned before, the low-resolution input data to the SR model $I_{\text{lr}} \in \mathbb{R}^{13 \times 13 \times 4}$ are generated from the corresponding high-resolution images by sampling a prescribed number of pixels (25,49,100) and then creating a continuous response surface by performing linear interpolation between measured pixels and assigning nearest neighbour value to extrapolation areas to form a structured 13×13 low-resolution data matrix for each component of flow ($u_{40}, v_{40}, w_{40}, T_{40}$). To study the effect of sampling distribution on the system performance, three different sampling strategies are adopted in this study to provide the low-resolution input data as depicted in Figure 8.4. The first strategy as shown in Figure 8.4a assumes that the UAVs are positioned on a structured grid of points with equal distances and provide a regular grid of sampled pixels. Note that the yellow points reflect the fixed position of UAVs for the whole duration of the simulation. Two other strategies assume that measurements are carried out by UAVs

while flying above the domain and not positioned in a structured manner. Hence, the second strategy as shown in Figure 8.4b is a purely random sampling of the 416×416 flow field. In contrast, the third strategy assumes that pixels with higher near-surface temperatures have a higher probability of being sampled and is defined as follows:

$$P(x, y) = \frac{|T^{0.7}(x, y)|}{\sum_{(i,j)} T(i, j)} \quad (8.6)$$

where $T(x, y)$ is the temperature at pixel (x, y) and $P(x, y)$ defines the probability of that pixel being sampled. It should be highlighted that the value of 0.7 is selected arbitrarily to provide a visual balance between points sampled over the fire line and samples from the rest of the domain. This third strategy simulates a scenario where a greater number of UAVs are concentrated over the fire line to perform firefighting operations, while other UAVs are either en route to the fire line to discharge their payloads or returning to refill their payloads, battery, etc.

For the first strategy, only one low-resolution image is generated per each high-resolution image. Hence, models are trained on 17343 pairs of data, validated on 3652 pairs and tested on 3573 data pairs. In contrast, the second and third strategies produce varying distributions of sampling points for each image, leading to different low-resolution images every time the sampling process is repeated. This variability reflects the numerous possible distributions of UAVs over the terrain at any specific time, which can have infinite configurations. Therefore, for the second and third strategies, a sensitivity study is conducted to examine the effect of the number of low-resolution samples generated per each high-resolution flow field on the model's generalizability and accuracy in reconstructing a randomly sampled flow field. This is however discussed in more detail in the next section.

8.2.4 High altitude flow field reconstruction

The models are expected to learn the highly complex behaviour of the flow and the relationship between the high-altitude and near-surface flow fields, which is inherently intricate. First, the shape of the fire front changes over time, affecting the turbulent structure of the wind field at both measurement height (Z_m) and near the surface (Z_e) implying a highly dynamic environment. Additionally, by comparing the near-surface values to those from 40m *AGL*, it can be concluded that the wind fields are inherently different at measurement and estimation heights due to the ambient wind tilting the fire plume forward and creating complex behaviour at the plume flanks. The highest velocity regions near the surface are located immediately after the flaming front while the max velocity at (Z_m) is observed at a significant distance downstream of the fire location. Furthermore, the velocity field near the terrain surface includes two counter-rotating wake vortices downstream of the fire increasing the complexity of the flow field.

The models are designed to be time-independent as estimating the previous or future state of the wind is not of interest to this study. Meanwhile, it is intended to

Table 8.2: *Effect of the number of UAVs on the SR performance utilising first sampling strategy*

N. UAV	U* (m/s)		V* (m/s)		W* (m/s)		T* C	
	MAE	RMSE	MAE	RMSE	MAE	RMSE	MAE	RMSE
25 (5*5)	0.767	1.341	0.745	1.285	0.896	1.589	4.295	16.278
49 (7*7)	0.755	1.315	0.735	1.265	0.882	1.558	4.091	15.613
100 (10*10)	0.735	1.268	0.717	1.225	0.867	1.514	3.841	14.632

* U(m/s) \in [-18.7, 55.3], V (m/s) \in [-38.4, 37.7], W (m/s) \in [-22.2, 52.1]

be capable of estimating the distribution of the near-surface wind velocity components in real time from sparse measurements carried out by the UAV swarm. To prevent confusion, this section is divided into two parts where the first part discusses the experiments regarding the super-resolution model, and the second part explains the results obtained from a second model trained to estimate the high-resolution near-surface wind field.

Model sensitivity analysis

A sensitivity analysis was carried out to evaluate the effect of various parameters on the accuracy of super-resolution output. The number of filters in each layer of the network is the first parameter examined, focusing on how the quantity of the model's trainable parameters influences SR output accuracy. Table 8.1 presents the results for this preliminary examination. It is indicated that increasing the number of trainable parameters from 1M to 4M has impacted the model accuracy positively while further increase in model depth has resulted in a decline in the model performance. Comparing Model 2 and Model 5 highlights the impact of utilising Convolutional Block Attention Module (CBAM) blocks which has resulted in improved accuracy of the model outputs. To include some physics within the model training procedure, a weakly physics-informed (PI) version of the model is trained by incorporating the incompressible version of the continuity equation into the loss functions so that:

$$Loss_{total} = Loss_{residual} + |\nabla \cdot \vec{V}|$$

Where $Loss_{total}$ is the weak PI loss utilised to train the model. However, utilising this approach showed no positive impact on model performance as indicated in table 8.1 despite increasing the training time and complexity. Consequently, the second model architecture with 4M trainable parameters with 16,32,64,128,256 filters in convolutional layers within the first to fifth encoder and decoder blocks of UNet architecture, is adopted as the optimal architecture for the rest of the examinations.

The second examination involves evaluating the effect of the number of UAVs (sampling points) on the accuracy of the super-resolution output. Consequently, as previously discussed, three different numbers of UAVs including 25, 49, and 100 were considered while generating low-resolution inputs and one model was trained for each UAV quantity. Table 8.2 presents the effect of the number of UAVs or sampling points

Table 8.3: *effect of increasing the number of input randomly sampled low-resolution versions on SR model accuracy utilising random sampling strategy and $n=100$*

N. input samples	U* (m/s)		V* (m/s)		W* (m/s)		T* C	
	MAE	RMSE	MAE	RMSE	MAE	RMSE	MAE	RMSE
2	0.750	1.310	0.726	1.248	0.880	1.558	4.131	15.669
3	0.750	1.306	0.722	1.243	0.877	1.549	4.082	15.614
5	0.732	1.274	0.717	1.236	0.868	1.539	3.995	15.557

* U(m/s) \in [-18.7, 55.3], V (m/s) \in [-38.4, 37.7], W (m/s) \in [-22.2, 52.1]

Table 8.4: *performance evaluation metrics and uncertainty of the SR model against different testing subsets*

N. UAV (strategy)	U (m/s)		V (m/s)		W (m/s)		T	
	MAE (std)	RMSE (std)	MAE (std)	RMSE (std)	MAE (std)	RMSE (std)	MAE (std)	RMSE (std)
25 (1)	0.755 (0.0095)	1.315 (0.0161)	0.731 (0.0088)	1.261 (0.0152)	0.883 (0.0106)	1.562 (0.0188)	4.158 (0.0501)	15.984 (0.1897)
49 (1)	0.752 (0.0092)	1.308 (0.0159)	0.730 (0.0090)	1.259 (0.0154)	0.881 (0.0106)	1.555 (0.0188)	4.111 (0.0494)	15.787 (0.1890)
100 (1)	0.748 (0.0094)	1.301 (0.0163)	0.729 (0.0088)	1.257 (0.0151)	0.878 (0.0107)	1.546 (0.0189)	4.052 (0.0496)	15.570 (0.1896)
25 (2)	0.762 (0.0087)	1.325 (0.0155)	0.732 (0.0088)	1.263 (0.0151)	0.884 (0.0106)	1.565 (0.0189)	4.189 (0.0495)	16.060 (0.1944)
49 (2)	0.756 (0.0097)	1.314 (0.0166)	0.731 (0.0088)	1.261 (0.0152)	0.882 (0.0106)	1.559 (0.0188)	4.145 (0.0499)	15.915 (0.1878)
100 (2)	0.752 (0.0096)	1.307 (0.0163)	0.730 (0.0088)	1.259 (0.0152)	0.880 (0.0106)	1.552 (0.0164)	4.097 (0.0434)	15.729 (0.1652)
25 (3)	0.759 (0.0075)	1.321 (0.0133)	0.732 (0.0077)	1.264 (0.0134)	0.884 (0.0093)	1.566 (0.0167)	4.189 (0.0434)	16.122 (0.1652)
100 (3)	0.755 (0.0088)	1.315 (0.0144)	0.732 (0.0077)	1.263 (0.0134)	0.883 (0.0093)	1.563 (0.0165)	4.164 (0.0440)	16.045 (0.1703)
Overall	0.755 (0.0101)	1.313 (0.0177)	0.731 (0.0088)	1.261 (0.0153)	0.882 (0.0108)	1.558 (0.0198)	4.138 (0.0736)	15.901 (0.2618)

* U(m/s) \in [-18.7, 55.3], V (m/s) \in [-38.4, 37.7], W (m/s) \in [-22.2, 52.1]

while generating the low-resolution input utilising the first sampling strategy, on the output accuracy of the super-resolution model. It can be observed that increasing the number of UAVs results in a marginal improved super-resolution accuracy. While this is not a surprising outcome, it should be highlighted that the difference between the estimated MAE values remained within 4% for velocity components and 10% for temperature, while the number of UAVs changed from 25 to 100, a 4x increase. It is however a very important conclusion as the model is capable of estimating a 416 by 416 pixel domain while receiving only a sum of 25 data as input, which can be accounted as a $\approx 83x$ super-resolution of the wind field.

The final examination investigates how training models with various low-resolution versions of a single high-resolution flow field affect model performance. Hence, three different models were trained utilising varying numbers of low-resolution input samples, ranging from 2 to 5, for each high-resolution wind field as presented in Table 8.3. The models are trained to treat each low-resolution and high-resolution pair as a distinct input pair. For example, the training time for a model with 5 input samples is five times that of a model with a single input sample. Consequently, it could be concluded that while increasing the number of low-resolution inputs slightly increases model performance and generalizability, it also increases the model training time linearly. This hence would make it impractical to account for a high number of inputs while training the primary model on the whole dataset.

Model performance and epistemic uncertainty

The main model, as previously mentioned, is trained to ensure accurate super-resolution estimations regardless of the sampling strategy or UAV number and distribution. Hence, the training dataset consists of low-resolution and high-resolution pairs extracted using all three strategies and varying UAV numbers. Consequently, by utilising three samples per UAV number for the second and third strategies, the training dataset includes 18×17325 input-output pairs of data, leaving the case with the third sampling strategy and $n=49$ out for testing the model. Besides, since the first strategy assumes UAVs are hovering at fixed locations, only a single sample is extracted for the scenario per UAV number. Finally, it is important to note that this model was trained for only 100 epochs due to the substantial computational time required and the observed lack of improvement after 40 epochs.

The model accuracy is evaluated utilising the average MAE, and RMSE of the model while the uncertainty of estimations is quantified utilising Std of accuracy metrics. For each testing subset, the model undergoes 15 inference cycles with randomly sampled low-resolution inputs to accompany each sample. Table 8.4 presents the average performance evaluation metrics of the SR model, along with the standard deviation of these metrics, evaluated against the testing sets of the low-resolution datasets used to train the model. It should be highlighted that since this section solely focuses on the model uncertainty, all inference cycles are performed on a fixed testing set for each scenario so that the data uncertainty does not affect the evaluations.

Overall, the model achieved an MAE and RMSE equal to 0.755, 1.313 (m/s) for the U component of velocity which ranges from -18.7 to 55.3 m/s. For the V component, which ranges from -38 to 37 m/s the MAE and RMSE were 0.731 and 1.261. The MAE and RMSE for the W component that ranges from -22.2 to 52.1 are equal to 0.882, and 1.558, while for temperature (T), they were 4.138 and 15.901. Generally, it could be concluded that the model presents acceptable accuracy based on a comparison of MAE and RMSE with the value ranges. Furthermore, the standard deviation of all metrics are bound within a range of 1.5% of the metrics, indicating a low uncertainty of model estimations within the training range of data.

In terms of the impact of the sampling strategy on the model output accuracy, while the first sampling strategy demonstrated a slightly lower MAE and RMSE, the differences between the three strategies were minimal and hence negligible, suggesting a proper model generalisation. In addition, increasing the number of UAVs from 25 to 100 also proved to have a negligible effect on the model output accuracy. In terms of the estimation uncertainty, however, it could be concluded that although indicating a marginally higher MAE and RMSE, the model exhibits a lower epistemic uncertainty in its estimation while the low-resolution input is obtained through the third sampling strategy. This outcome is however advantageous as the third strategy aims to replicate and is the closest scenario to the actual distribution of the UAVs within the field. Figure 8.5 presents a graphical representation of the SR model target, mean predictions, and error values while reconstructing the high-resolution wind and temperature field for

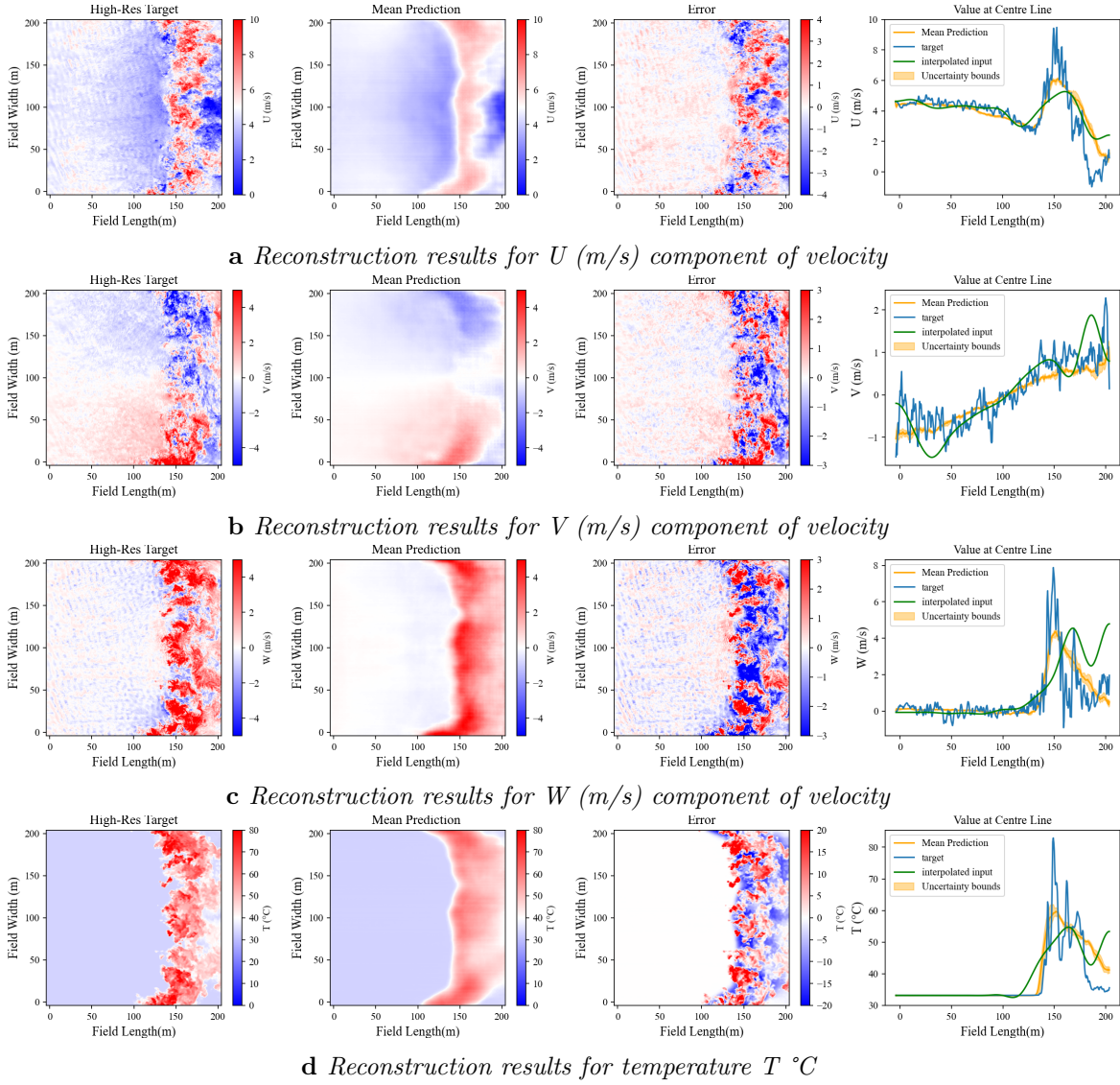


Figure 8.5: Results of the high-resolution wind and temperature field reconstruction for case 100(3) $u_{10} = 4$ m/s, $H_g = 0.2$ m and $S = 0\%$, depicting the high-resolution ground truth/target, mean prediction of the model, the reconstruction error, and comparison of the reconstructed value at the centre line of the field with model estimation and the model input.

the with case $u_{10} = 4$ m/s, $H_g = 0.2$ m, and horizontal terrain ($S = 0\%$). The low-resolution samples were generated from the scenario with 100 UAVs utilising the third sampling strategy (100(3)). The figure is organised into columns presenting the ground truth (first column), reconstructed field (second column), and the error values (third column), for the stream-wise component of velocity (U) 8.5a, transverse component of velocity (V) 8.5b, normal component of velocity (W) 8.5c, and the temperature field (T) 8.5d. It could be observed that while the model prediction is a smoothed version

of the true field, the overall performance of the model is satisfactory, capturing the general pattern of the wind field within the fire plume and surrounding area. The last column compares the ground truth, input, and the model estimated values at the centre line of the field. The model demonstrates accurate estimation of the upstream wind field as well as significantly improved estimations compared to the interpolated input values. Additionally, the narrow uncertainty bounds around estimations indicate the model's low uncertainty.

Table 8.5: *Evaluation of performance metrics and uncertainty of the SR model against unseen UAV numbers*

		N. UAVs (sampling strategy)				
		49 (3)	16 (3)	9 (3)	9 (2)	9 (1)
U	MAE	0.755	0.762	0.777	0.786	0.767
	RMSE	1.314	1.327	1.347	1.359	1.333
	PICP	0.107	0.123	0.142	0.144	0.134
	PINAW (%)	0.485	0.568	0.688	0.719	0.661
V	MAE	0.732	0.733	0.734	0.734	0.733
	RMSE	1.262	1.265	1.266	1.266	1.265
	PICP	0.057	0.059	0.061	0.063	0.060
	PINAW(%)	0.168	0.176	0.184	0.192	0.182
W	MAE	0.884	0.885	0.887	0.887	0.886
	RMSE	1.564	1.569	1.572	1.571	1.570
	PICP	0.058	0.060	0.063	0.065	0.064
	PINAW(%)	0.250	0.257	0.269	0.283	0.265
T	MAE	4.168	4.207	4.247	4.261	4.222
	RMSE	16.052	16.185	16.274	16.211	16.198
	PICP	0.188	0.194	0.202	0.200	0.191
	PINAW(%)	0.185	0.194	0.211	0.230	0.212

Effect of measurement uncertainties

Data measurement uncertainty typically stems from two sources: measurement devices and the measurement points' spatial distribution, which can result in infinitely different sampling combinations—or low-resolution versions—of the same high-resolution field. Wind measurements using UAV swarms are typically subject to different error sources, leading to high levels of uncertainty. Additionally, the number of UAVs in real-world scenarios may be significantly lower than those considered in our simulations. Therefore, the robustness and performance of the trained model are further investigated against the unseen number of UAVs, as well as various levels of noise in the measured wind values. Contrary to the previous section where the model was inferenced multiple times with a fixed dataset, in this section, each high-resolution wind field within the test subset, is randomly sampled multiple times to generate several Low-resolution versions of the same high-resolution wind field, replicating the infinitely possible spatial distribution of UAVs over the domain. These versions are then used to make multiple estimations of the same high-resolution field, capturing the combined effect of model uncertainty and data uncertainty. As a result, the inference time and complexity of

experiments in this section are significantly higher than those of the previous section. Table 8.5 presents the accuracy and uncertainty metrics of the model, while evaluated against previously unseen combinations of the number of UAVs and sampling strategies.

The first experiment quantifies the effect of decreasing the number of UAVs from 49 to 16 and subsequently to 9 while utilising third sampling strategies. Generally, it is indicated that even though the model is not trained on data from the case with 49 UAVs and third sampling strategy 49(3), it provides equally accurate estimations as those seen during the training phase, i.e. achieving an average MAE =0.755 and an RMSE=1.314 for U component of velocity. Further reducing the number of UAVs from 49 to 9 leads to a slight increase of MAE from 0.755 to 0.777, which corresponds to 3% increase. However, this increase is relatively minor, suggesting that the model can provide reliable estimations despite the low-resolution input field being significantly altered by the reduced number of sampling points. The model uncertainty is however quantified in terms of Prediction Interval Coverage Probability (PICP), and the Prediction Interval Normalized Average Width (PINAW) parameters. This is mainly due to the minimal variations of the MAE and RMSE standard deviations across different cases, making it difficult to identify trends based on that alone. As previously mentioned, a higher PICP indicates more target values are covered by the predicted prediction intervals (PIs), however, this does not necessarily imply a better model. Considering the accuracy and uncertainty metrics presented in Table 8.5, it can be observed that the PICP for the U component of velocity increases by decreasing the number of UAVs from case 49(3) to 9(3). Simultaneously, the averaged width of prediction intervals (PINAW) increased from 0.485% to 0.688%, equivalent to 42% increase, as the number of UAVs decreased from 49 to 9, suggesting that the higher PICP in cases with smaller UAV numbers primarily corresponds to the increased width of PIs, reflecting higher uncertainty of the model predictions along with the slightly reduced average accuracy of the model. This is however more pronounced in the U and T parameters, where the variations in PICP and PINAW are more significant. In contrast, it is less pronounced in the V and W parameters, as indicated by the smaller variations in their corresponding PICP and PINAW values. Comparing the PICP and PINAW metrics in cases with 9 UAVs and different sampling strategies, it could be observed that the average accuracy and uncertainty measures of the model for all cases are relatively similar with negligible variations of up to 3% for MAE and 0.002 and 0.01 in PICP and PINAW.

The second experiment revolves around quantifying the effect of measurement noise and uncertainty on the model's output accuracy and reliability. The model performance is hence evaluated using low-resolution inputs subjected to varying levels of measurement noise, replicating the uncertainties and errors that are likely to happen in real-world scenarios and environments. Similar to the previous experiment, multiple randomly sampled low-resolution versions of every high-resolution instant are generated. In this case, sampled data are subjected to random Gaussian noise and are then used to generate the low-resolution input file. This approach mimics the infinitely

Table 8.6: *Evaluation of performance metrics and uncertainty of the SR model against different measurement noise*

noise level		N. UAVs (sampling strategy)								
		9(2)				25(3)		49(3)		
		no noise	10%	30%	50%	50%	no noise	10%	30%	50%
U	MAE	0.786	0.936	1.513	2.038	1.736	0.755	0.790	1.143	1.579
	RMSE	1.359	1.530	2.138	2.730	2.369	1.314	1.358	1.743	2.190
	PICP	0.144	0.259	0.494	0.512	0.451	0.107	0.168	0.394	0.430
	PINAW(%)	0.719	1.462	3.765	5.121	4.006	0.485	0.865	2.533	3.516
V	MAE	0.734	0.736	0.750	0.766	0.757	0.732	0.733	0.738	0.750
	RMSE	1.266	1.270	1.293	1.321	1.304	1.262	1.264	1.273	1.280
	PICP	0.063	0.073	0.110	0.132	0.112	0.057	0.062	0.088	0.103
	PINAW(%)	0.192	0.228	0.363	0.456	0.378	0.168	0.187	0.271	0.336
W	MAE	0.887	0.890	0.911	0.935	0.921	0.884	0.884	0.894	0.912
	RMSE	1.571	1.579	1.628	1.676	1.650	1.564	1.566	1.588	1.628
	PICP	0.065	0.075	0.111	0.134	0.115	0.058	0.064	0.091	0.107
	PINAW(%)	0.283	0.335	0.524	0.656	0.553	0.251	0.278	0.404	0.501
T	MAE	4.261	4.501	5.263	5.937	5.523	4.168	4.233	4.714	5.292
	RMSE	16.211	16.381	17.016	17.624	17.274	16.052	16.094	16.418	16.913
	PICP	0.200	0.266	0.431	0.440	0.376	0.188	0.207	0.356	0.351
	PINAW(%)	0.230	0.327	0.621	0.818	0.666	0.185	0.242	0.444	0.595

possible spatial distributions of UAVs, as well as the potential errors of mounted sensors. The input Gaussian noise (N) is defined as a function of the input data standard deviation for each velocity component and each input batch which results in the noisy input data in the form of $U_{Noisy} = N \times U + U$. The obtained accuracy metrics for the test dataset with the prescribed noise levels including 10%, 30% and 50% are presented in Table 8.6.

Three different combinations of UAV number and sampling strategy are considered. The obtained results indicate that generally, increasing the measurement noise level decreases the model's output accuracy, and increases its uncertainty. For instance, in the case with 9 UAVs using third sampling strategy 9(3), introducing only 10% measurement noise has resulted in approximately 19% increase in MAE, and 12% in MSE corresponding to the U component of velocity, and 6% and 1% for the corresponding metrics concerning the the temperature. However, for V and W, changes are mainly limited to 1%. In addition, the model uncertainty is also increased as indicated through increased normalised average width of PI (PINAW) values, from 0.719% to 1.462% for the U, from 0.192 to 0.228% for the V, from 0.283 to 0.335% for W, and from 0.230 to 0.327% for temperature (T).

Concerning the impact of varying numbers of UAVs, it could be concluded that typically increasing the number of UAVs improves the model accuracy and reduces the model uncertainty under all input noise conditions. However, this effect is more pronounced when input noise levels are higher. For example, increasing the number of UAVs from 9 to 25 under 50% measurement noise conditions leads to a reduction of the MAE and PINAW values from 2.038 to 1.736 and from 5.121 to 4.006, representing

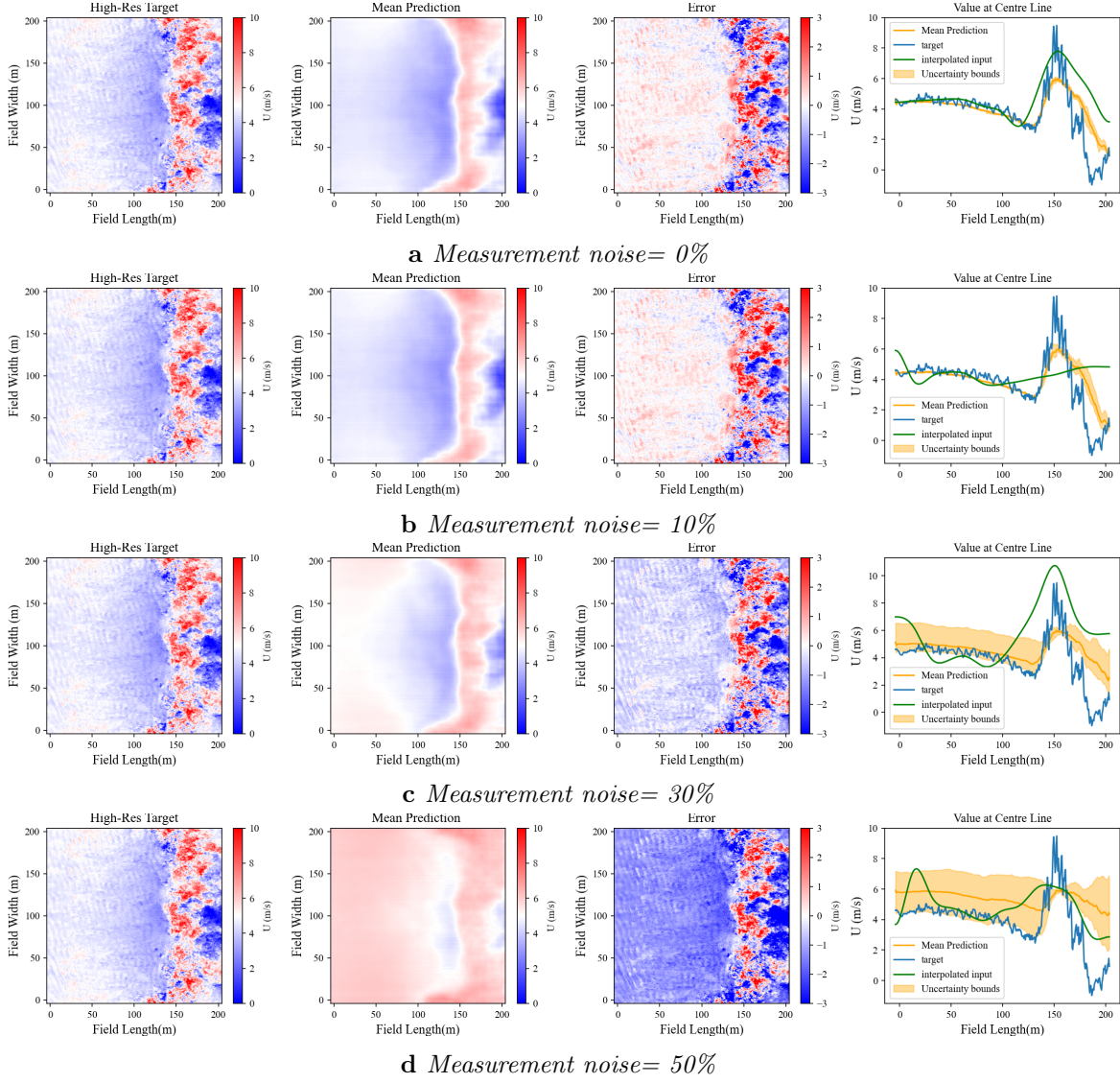


Figure 8.6: Results of the high-altitude reconstruction of the U -component for case 49(3), $u_{10} = 4$ m/s, $H_g = 0.2$ m and $S = 0\%$ under different measurement noise levels, depicting the high-resolution ground truth/target, mean prediction of the model, the reconstruction error, and comparison of the reconstructed value at the centre line of the field with model estimation and the model input.

a 15% reduction in MAE and 22% reduction in PINAW values, respectively.

Figure 8.6 presents a graphical representation of the super-resolution reconstruction of the U component of velocity with 49 UAVs and utilising the third sampling strategy, under different measurement noise levels. The environmental conditions of this instant include $u_{10} = 4$ m/s, $H_g = 0.2$ m, and horizontal terrain ($S = 0\%$). Generally, it could be observed that the quality and accuracy of reconstruction reduce as the input noise

increases. Increased width of PIs corresponding to the increased levels of input noise are also evidently presented.

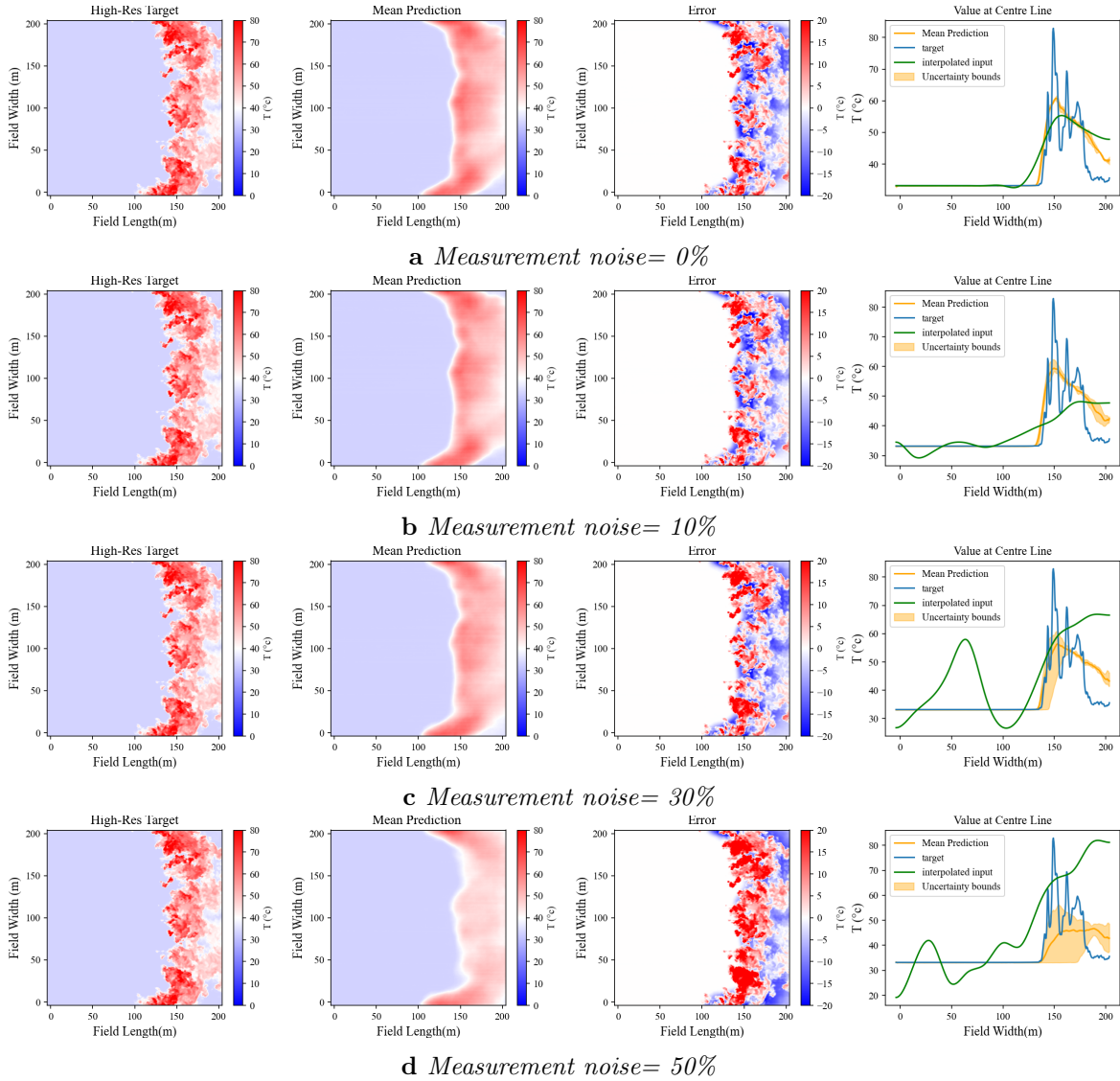


Figure 8.7: Results of the high-altitude reconstruction of the temperature (T) for case 49(3), $u_{10} = 4$ m/s, $H_g = 0.2$ m and $S = 0\%$ under different measurement noise levels, depicting the high-resolution ground truth/target, mean prediction of the model, the reconstruction error, and comparison of the reconstructed value at the centre line of the field with model estimation and the model input.

Notably, by increasing the input noise level, the average estimations of the velocity tend to overestimate the wind velocity at regions behind the fire plume, resulting in a smoother and more uniform estimation of the wind field estimation under high levels of noise. This, however, holds while $u_{10} \leq 6$ m/s. Nevertheless, for higher wind velocities,

Table 8.7: *performance evaluation metrics and uncertainty of the near-surface wind estimations against different testing subsets*

UAV number (strategy)	U (m/s)		V (m/s)		W (m/s)	
	MAE (std)	RMSE (std)	MAE (std)	RMSE (std)	MAE (std)	RMSE (std)
perfect data	0.744	1.202	0.627	1.071	0.545	1.004
25 (1)	0.862	1.337	0.679	1.142	0.552	1.011
49 (1)	0.859	1.335	0.677	1.14	0.551	1.01
100 (1)	0.857	1.331	0.676	1.138	0.551	1.01
25 (2)	0.867	1.345	0.679	1.142	0.552	1.01
49 (2)	0.862	1.337	0.678	1.141	0.552	1.01
100 (2)	0.859	1.334	0.677	1.139	0.551	1.01
25 (3)	0.867	1.344	0.68	1.144	0.552	1.011
100 (3)	0.864	1.341	0.679	1.142	0.551	1.01
Overall	0.849 (0.040)	1.323 (0.046)	0.672 (0.017)	1.022 (0.023)	0.551 (0.002)	1.010 (0.002)

* U(m/s) \in [-26.1, 41.3], V (m/s) \in [-33.1, 27.35], W (m/s) \in [-25.6, 29.95]

increasing the input noise leads to an underestimation of the wind velocity, suggesting that the model outputs begin to converge to a mean flow field. For the temperature field (Figure 8.7), the model consistently underpredicts temperature values within the plume across varying noise levels. However, it indicates a similar trend to the velocity components for temperature values ahead of the fire plume, with the difference in predictions being small and mainly limited to 0.5 degrees.

8.2.5 Near surface wind field estimation

This section presents the accuracy metrics and uncertainty measures obtained from models trained to estimate the near-surface wind field. As previously described, the purpose of this section is to train a model such that it estimates the near-surface wind field velocity components $I_{\text{surf}} = (u_2, v_2, w_2) \in \mathbb{R}^{416 \times 416 \times 3}$ from a concatenation of reconstructed high altitude wind field -from previous section- and the high-resolution data corresponding to the surface temperature, vegetation height and type, and terrain slope $C = \text{concat}(I_{\text{sr}}, I_{\text{terrain}}) \in \mathbb{R}^{416 \times 416 \times 8}$. Similar to the previous section, the effect of embedding the attention mechanism in the model on the estimation accuracy is studied.

Model performance and epistemic uncertainty

The obtained results indicate that the fully convolutional model was able to provide accurate estimations of the wind velocity with MAE=0.785 and RMSE =1.255 for U , MAE=0.656 and RMSE =1.123 for V , and MAE=0.555 and RMSE =1.021 for W component of velocity, which are however up to 5.5% higher than corresponding values of the attention-based model presented in Table 8.7. It is also worth mentioning that the results generated by the fully convolutional model provide a smoother representation of the wind field compared to when the attention mechanism is utilized. Consequently, the attention mechanism is embedded into the final model. Table 8.7 presents the average performance evaluation metrics for the near-surface wind estimation model

evaluated against the testing subsets of the reconstructed wind fields used to train the model. Similar to the section 8.2.4, the model has undergone multiple inference cycles for each testing subset with randomly sampled batches to accompany each sample. Overall, the model achieved MAE and RMSE equal to 0.849 and 1.323 for the U , 0.672 and 1.142 for the V , and 0.551 and 1.01 for the W velocity component, respectively. Furthermore, the standard deviation of all metrics is bound in a range of 5% of the metrics, indicating relatively high confidence in model estimations and low epistemic uncertainty.

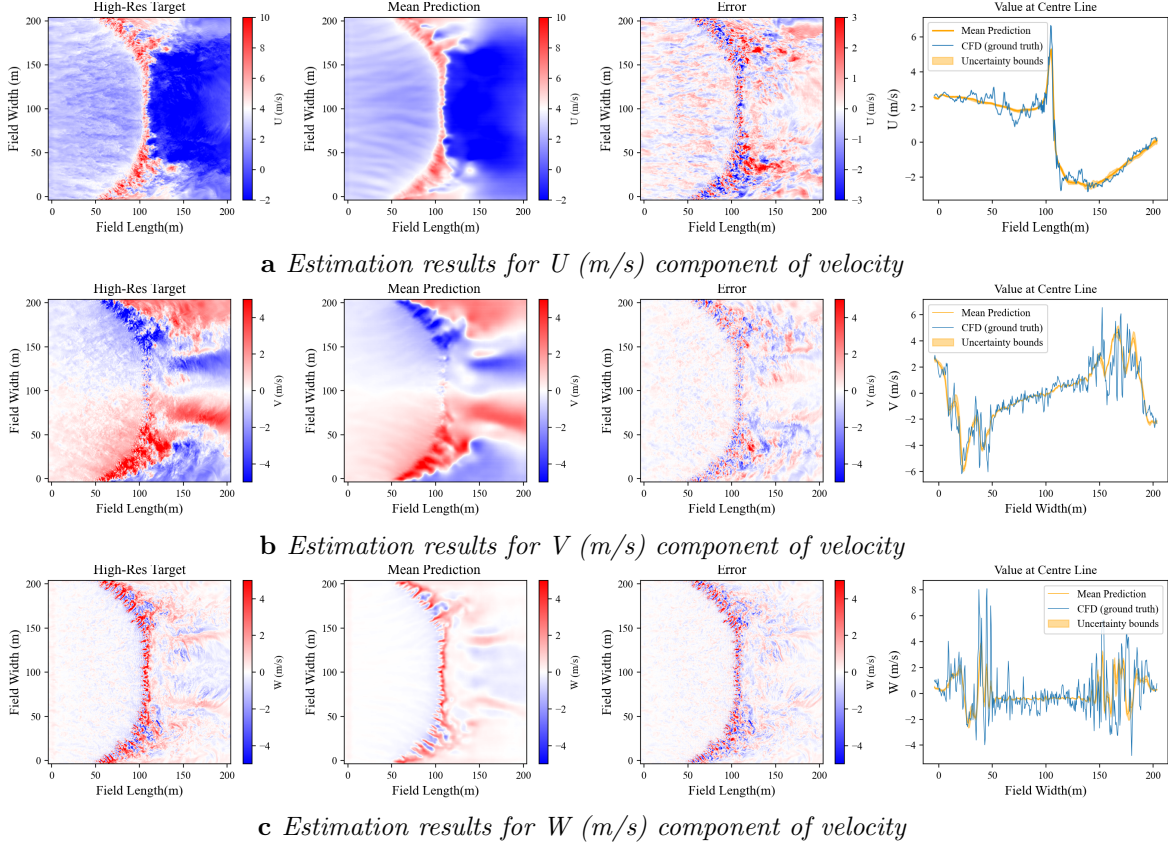


Figure 8.8: The near-surface velocity components (U , V , W) for case 49(3), $u_{10} = 4$ m/s, $H_g = 0.2$ m and $S = 0\%$, showing the high-resolution ground truth/target, the model's mean prediction, the reconstruction error, and a comparison of the estimated value along the centerline of the field with the ground truth (CFD)

Even though the third sampling strategy shows a slightly higher MAE and RMSE compared to the other strategies, the impact of the high-altitude wind sampling strategy proved to be negligible as indicated by the minor variation in MAE and RMSE metrics across different scenarios. Changing the number of UAVs from 25 to 100 on the near-surface wind field estimation accuracy described a negligible effect of less than 1% on the average accuracy of the model across different scenarios as presented in Table

Table 8.8: *Evaluation of performance metrics and uncertainty of the near-surface wind estimations against unseen UAV numbers*

		N. UAVs (sampling strategy)				
		49 (3)	16 (3)	9 (3)	9 (2)	9 (1)
U (m/s)	MAE	0.861	0.873	0.880	0.884	0.873
	RMSE	1.337	1.352	1.362	1.367	1.353
	PICP	0.0597	0.0653	0.0708	0.0725	0.0689
	PINAW (%)	0.6410	0.7210	0.7960	0.8270	0.783
	MAE	0.679	0.681	0.685	0.683	0.682
V (m/s)	RMSE	1.142	1.146	1.151	1.149	1.146
	PICP	0.075	0.078	0.080	0.081	0.07920
	PINAW (%)	0.449	0.472	0.489	0.502	0.48300
	MAE	0.552	0.552	0.553	0.552	0.552
	RMSE	1.011	1.011	1.012	1.011	1.011
W(m/s)	PICP	0.047	0.048	0.049	0.049	0.049
	PINAW (%)	0.2710	0.2770	0.2830	0.2860	0.2830

8.7, thus it could be considered negligible. Figure 8.8 shows the estimated velocity components (second column), ground truth (first column), error values ($y_i - y'_i$, third column), and a comparison of the estimated and ground truth values along the centerline of the field (fourth column) for the case of $u_{10} = 4, \text{ m/s}$, $H_g = 0.2, \text{ m}$, and flat terrain ($S = 0\%$) at a specific time instance. The near-surface wind is estimated utilizing the reconstructed high-altitude wind field from the scenario with 49 UAVs utilizing the third sampling strategy (49(3)). Overall, the model demonstrates a satisfactory performance while estimating the near-surface wind fields based the corresponding reconstructed instantaneous wind field at 40m *AGL* as depicted in Figure 8.8a, 8.8b, and 8.8c for U, V, and W component of velocity. Testing the model across various wind conditions and terrain slopes shows that it has successfully learned an accurate mapping between input and output values. The visualization of the errors indicates that the majority of the inaccuracies stem from the stochastic and instantaneous nature of the wind field, which complicates the estimation of its oscillatory behaviour. Overall, it can be concluded that the general trend is captured and estimated with satisfactory accuracy.

The results for the estimation of the U component of velocity -as depicted in Figures 8.8a, 8.12a, and 8.15a- indicate that the model accurately captures the span and formation of the fire-induced wind field, including the accelerated wind above the flaming front and the downstream vortex zone. The estimations of the V-velocity component -as depicted in 8.8b, 8.13a, and 8.16a- show that the model estimates the maximum and minimum values fairly well, particularly within the downwind turbulent structure of the fire-induced wind. However, the W component of velocity is highly oscillatory -as depicted in 8.8c, 8.14a, and 8.17a-, leading to higher estimation error values in certain areas, specifically within the downstream vortex zone. It is important to note that the W component is inherently the most oscillatory, making it the most challenging to estimate. However, it should be noted that in certain areas—particularly near the flaming front, where maximum velocity values occur—the estimates are less accurate

and can be underestimated up to 24% for the U component of velocity and up to 60% for the W component. This is however not surprising as the model is trained to estimate the average and large-scale behaviour of the flow rather than the oscillatory and vortical structure of the wind field at small scales from sparse measurements carried out at the UAVs' flying altitude.

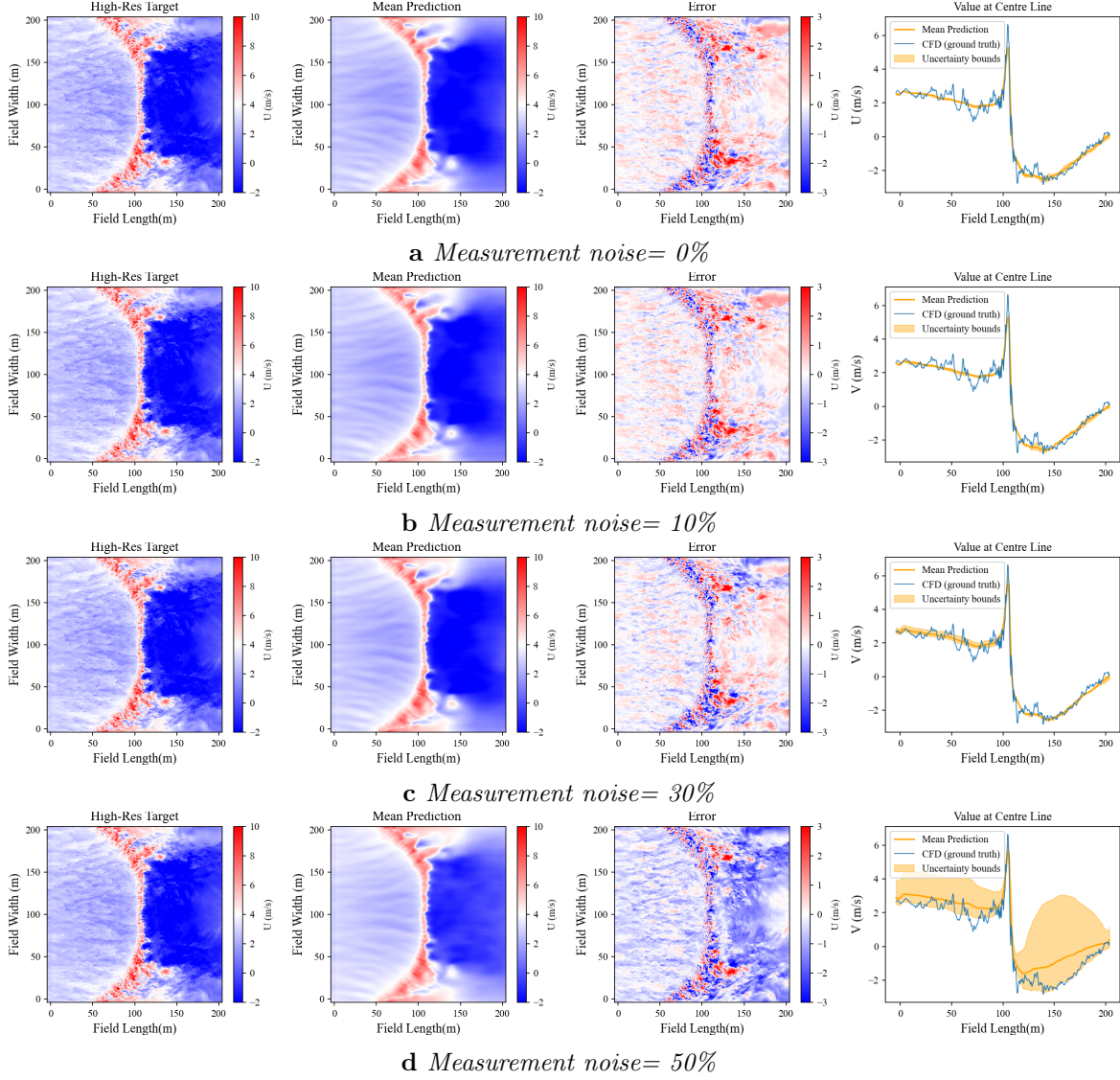


Figure 8.9: The near-surface U -component of velocity for case 49(3), $u_{10} = 4$ m/s, $H_g = 0.2$ m and $S = 0\%$, under different measurement noise levels, showing the high-resolution ground truth/target, the model's mean prediction, the reconstruction error, and a comparison of the estimated value along the centerline of the field with the ground truth (CFD)

Table 8.9: *Evaluation of performance metrics and uncertainty of the near-surface wind estimations against different measurement noise*

Noise level		N. UAVs (sampling strategy)									
		9(2)				25(3)		49(3)			
		0 %	10%	30%	50%	0 %	50%	0 %	10%	30%	50%
U (m/s)	MAE	0.884	0.965	1.123	1.490	0.867	1.358	0.861	0.893	1.057	1.267
	RMSE	1.367	1.460	1.742	2.073	1.344	1.875	1.337	1.374	1.544	1.766
	PICP	0.073	0.107	0.187	0.205	0.063	0.179	0.060	0.074	0.148	0.166
	PINAW (%)	0.827	1.283	2.642	3.479	0.687	2.734	0.641	0.837	1.798	2.384
V (m/s)	MAE	0.683	0.690	0.710	0.761	0.68	0.748	0.679	0.681	0.702	0.735
	RMSE	1.149	1.157	1.197	1.255	1.144	1.235	1.142	1.145	1.171	1.213
	PICP	0.081	0.096	0.137	0.156	0.0768	0.139	0.075	0.081	0.114	0.130
	PINAW (%)	0.5020	0.585	0.862	1.026	0.461	0.901	0.4490	0.488	0.693	0.831
W(m/s)	MAE	0.552	0.554	0.558	0.565	0.552	0.563	0.552	0.552	0.556	0.561
	RMSE	1.011	1.012	1.016	1.022	1.011	1.019	1.011	1.011	1.014	1.017
	PICP	0.049	0.057	0.078	0.088	0.0475	0.078	0.047	0.050	0.066	0.073
	PINAW (%)	0.286	0.316	0.401	0.451	0.275	0.414	0.271	0.286	0.351	0.392

Effect of measurement uncertainty

This section examines the effect of data measurement uncertainties including the spatial distribution of sampling points and the measurement device errors, on model performance and estimation reliability. As discussed in Section 8.2.4, multiple low-resolution versions were generated for each high-resolution wind field at flying altitude, which were then used to reconstruct the high-altitude wind field and conduct uncertainty analysis. These reconstructed high-altitude wind fields are subsequently utilized in this section to generate multiple representations of the near-surface wind field, providing both average estimations and uncertainty measures. Consequently, the uncertainty propagates throughout the entire process, as the uncertain estimations of the first model are used to generate uncertain near-surface wind field estimations in the second model, thereby accounting for the total uncertainty of the approach. Table 8.8 presents the accuracy metrics and uncertainty measures of the model, against unseen combinations of the number of UAVs and sampling strategies. The results indicate that the model is generally robust to changes in the number of sampling points or UAVs. Reducing the number of UAVs from 49 to 9 led to a slight increase in the MAE, corresponding to an approximate rise of 2.5% from 0.86 to 0.88 for the U component of velocity. The RMSE metric also shows a similar trend, with a slight increase, while the uncertainty metric, PINAW, grows from 0.6410 to 0.7960 as UAV numbers decrease, indicating a slightly wider range of uncertainty. However, the model indicates consistency in terms of accuracy metrics and uncertainty measures for the V and W components of velocity, regardless of the number of UAVs. As a result, it can be concluded that the model maintains high accuracy across various UAV configurations with a slight increase in uncertainty as the number of UAVs decreases.

Table 8.9 presents the evaluation of the near-surface estimations of the second model under different levels of measurement noise. The uncertainty caused by measurement noise propagates throughout the entire process, as multiple noisy low-resolution mea-

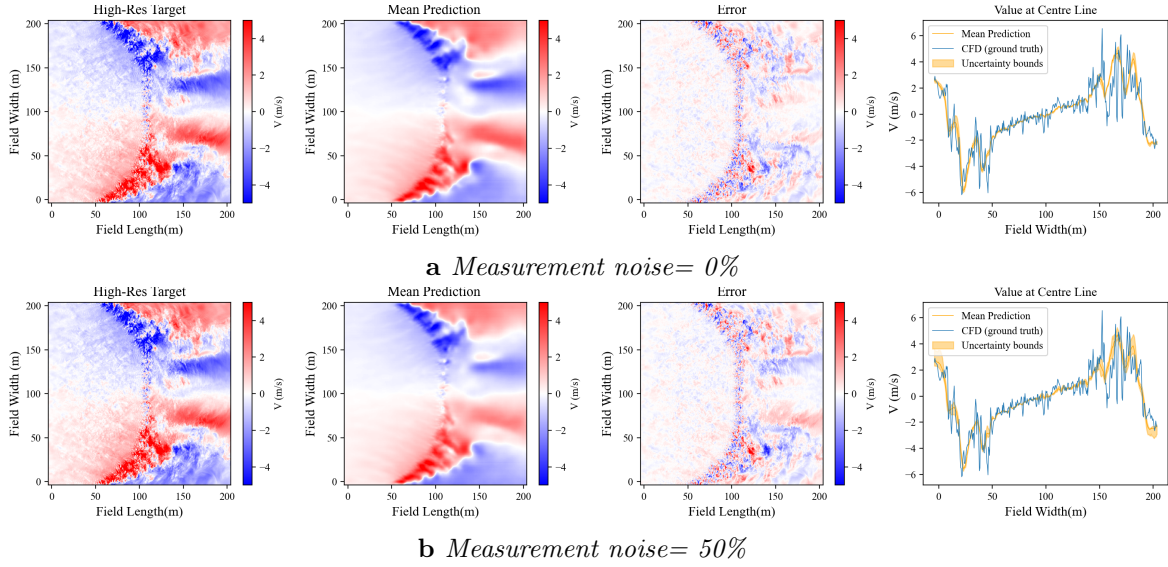


Figure 8.10: The near-surface V -component of velocity for case 49(3), $u_{10} = 4$ m/s, $H_g = 0.2$ m and $S = 0\%$, under different measurement noise levels, showing the high-resolution ground truth/target, the model's mean prediction, the reconstruction error, and a comparison of the estimated value along the centerline of the field with the ground truth (CFD)

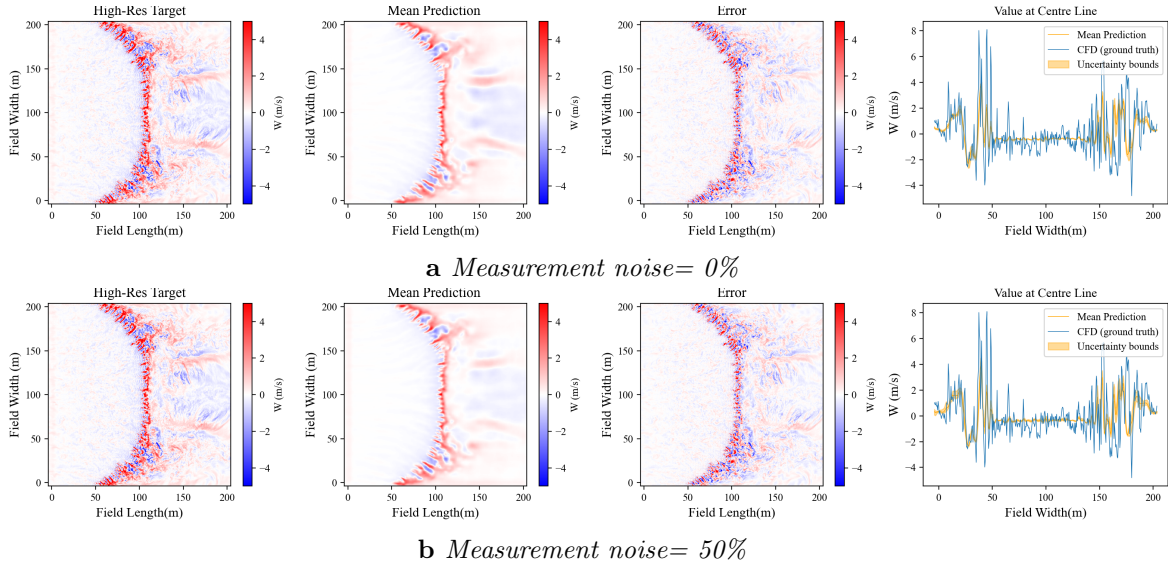


Figure 8.11: The near-surface W -component of velocity for case 49(3), $u_{10} = 4$ m/s, $H_g = 0.2$ m and $S = 0\%$, under different measurement noise levels, showing the high-resolution ground truth/target, the model's mean prediction, the reconstruction error, and a comparison of the estimated value along the centerline of the field with the ground truth (CFD)

surements are utilised to generate several versions of high-altitude wind fields. These in turn are subsequently used to generate multiple representations of the near-surface wind field, providing both average estimations and uncertainty measures. As expected, increased measurement noise leads to reduced estimation accuracy and higher uncertainty especially for smaller numbers of UAVs. For example, increasing the input noise to 50% leads to a rise in MAE from 0.884 to 1.49 for case 9(2), corresponding to 69% increase, which demonstrates a clear sensitivity to input noise. As noise increases, RMSE values also rise significantly, indicating larger discrepancies between predicted and true values. Both PICP and PINAW measures increase by increasing the input noise, particularly for case 9(2) where PICP for U increases from 0.073 to 0.205 (180%) and PINAW rises from 0.827 to 3.479 (320%). Considering the effect of UAV numbers, it could be concluded that increasing the number of UAVs, enhances the model robustness against input noise, as evident from the lower MAE, RMSE, PICP, and PINAW values for case 49(3) compared to 25(3) and 9(2). Regarding the V and W components of velocity, it could be highlighted that while uncertainty generally increases with noise -for example, PINAW values change from 0.502 to 1.026 for V and from 0.286 to 0.316 for W in case 9(2)-, this increase is less dramatic compared to the U component. This is however partly due to the fact that, despite their broad range, a significant portion of the V and especially W component values are near or equal to zero. When the model predicts these small values, the uncertainty has little impact on the estimations, resulting in lower average uncertainty metrics. Even as the uncertainty increases in regions with non-zero values, the overall average remains small because many of the predicted values are small or close to zero.

Figure 8.9 presents the estimated U component of the near-surface wind field for case 49(3), $u_{10} = 4$ m/s, $H_g = 0.2$ m and $S = 0\%$, under different measurement noise levels. Other examples of wind field estimations are also presented in Figure 8.12 and 8.15 for the U component, Figure 8.10, 8.13, and 8.16 for the V component, and Figure 8.11, 8.14, and 8.17 for the W component of velocity. It can generally be observed that although the model produces a satisfactorily smoothed version of the wind field, the quality and accuracy of the estimations decline as input noise increases. This is reflected in the widening of prediction intervals (PIs), which corresponds to the higher levels of input noise. The increased uncertainty in the predictions highlights the sensitivity of the model to noisy input data, leading to less precise estimations under higher noise conditions.

8.3 Enhancing Wildfire Model Predictions

The proposed system for wind field downscaling is presented in the previous section. However, the ultimate goal of developing such a system is to aid in improving the accuracy of wildfire propagation estimations. Consequently, this section addresses this purpose by studying how such a system could be used to improve wildfire propagations of *de-coupled* models and how it impacts the outputs.

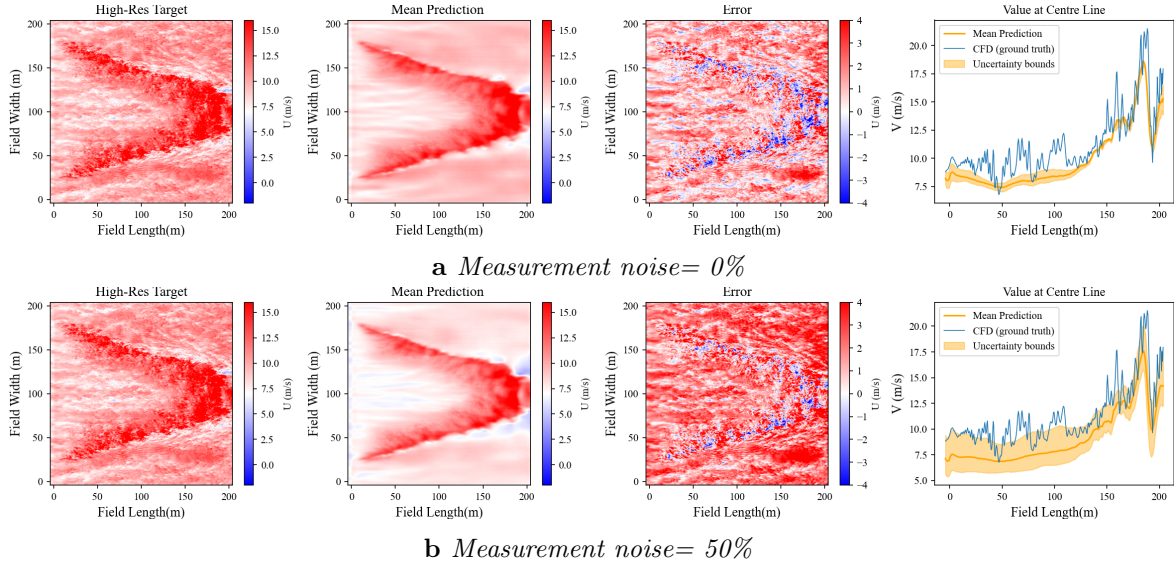


Figure 8.12: The near-surface U -component of velocity for case 49(3), $u_{10} = 12$ m/s, $H_g = 0.5$ m and $S = +20\%$, under different measurement noise levels, showing the high-resolution ground truth/target, the model's mean prediction, the reconstruction error, and a comparison of the estimated value along the centerline of the field with the ground truth (CFD)

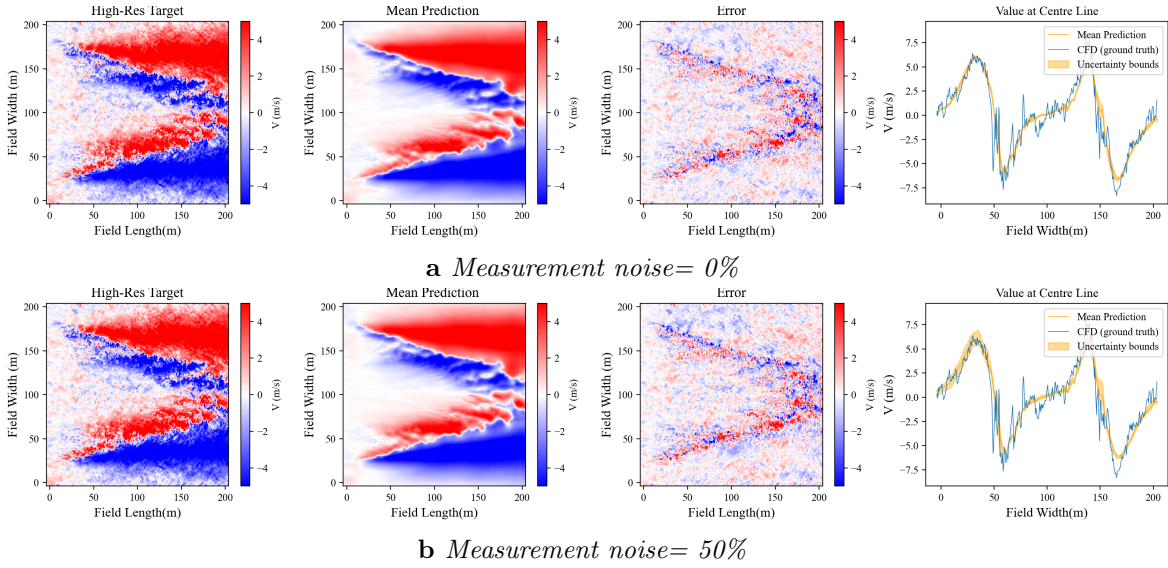


Figure 8.13: The near-surface V -component of velocity for case 49(3), $u_{10} = 12$ m/s, $H_g = 0.5$ m and $S = +20\%$, under different measurement noise levels, showing the high-resolution ground truth/target, the model's mean prediction, the reconstruction error, and a comparison of the estimated value along the centerline of the field with the ground truth (CFD)

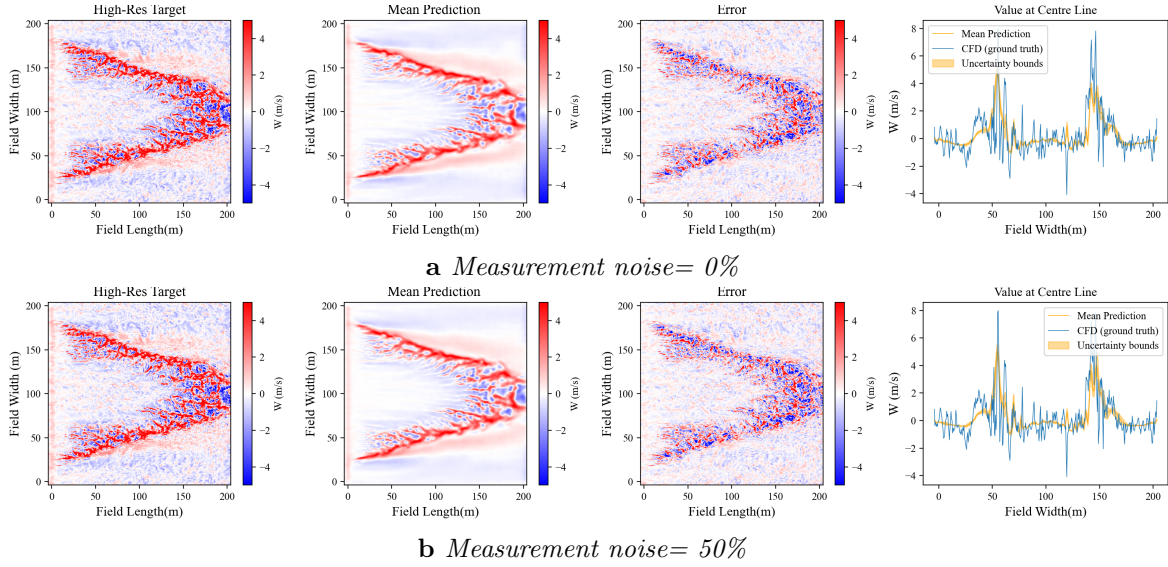


Figure 8.14: The near-surface W -component of velocity for case 49(3), $u_{10} = 12$ m/s, $H_g = 0.5$ m and $S = +20\%$, under different measurement noise levels, showing the high-resolution ground truth/target, the model's mean prediction, the reconstruction error, and a comparison of the estimated value along the centerline of the field with the ground truth (CFD)

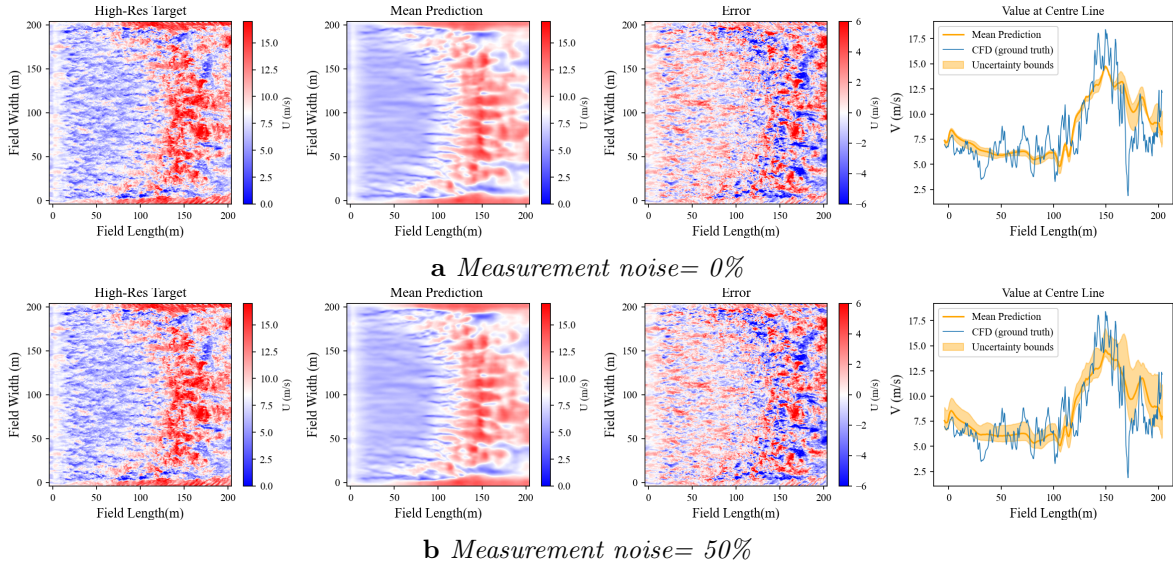


Figure 8.15: The near-surface U -component of velocity for case 49(3), $u_{10} = 12$ m/s, $H_g = 1$ m and $S = -20\%$, under different measurement noise levels, showing the high-resolution ground truth/target, the model's mean prediction, the reconstruction error, and a comparison of the estimated value along the centerline of the field with the ground truth (CFD)

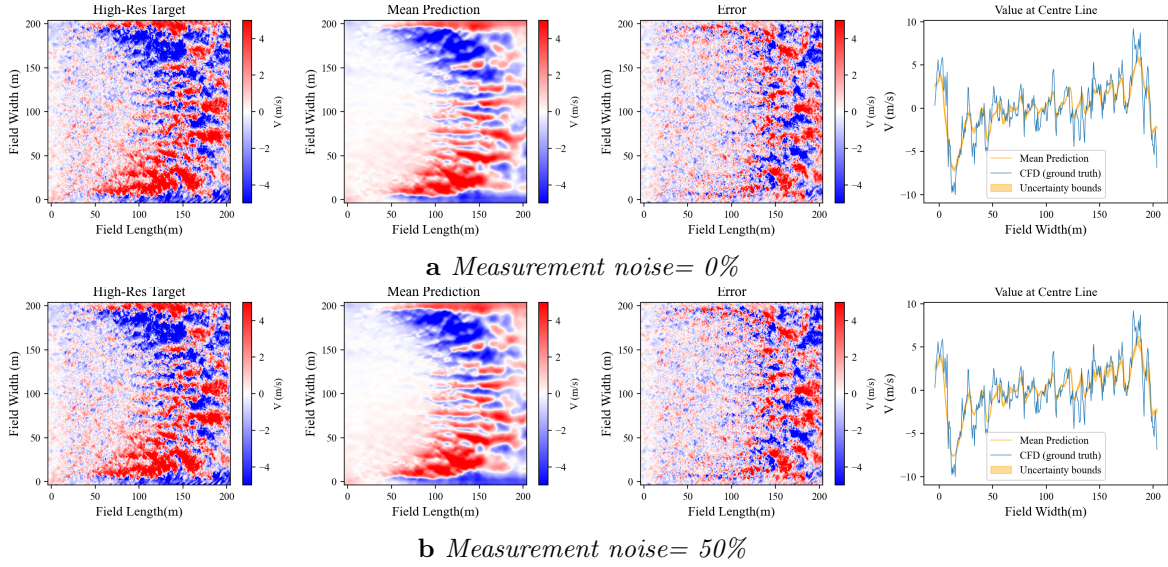


Figure 8.16: The near-surface V -component of velocity for case 49(3), $u_{10} = 12$ m/s, $H_g = 1$ m and $S = -20\%$, under different measurement noise levels, showing the high-resolution ground truth/target, the model's mean prediction, the reconstruction error, and a comparison of the estimated value along the centerline of the field with the ground truth (CFD)

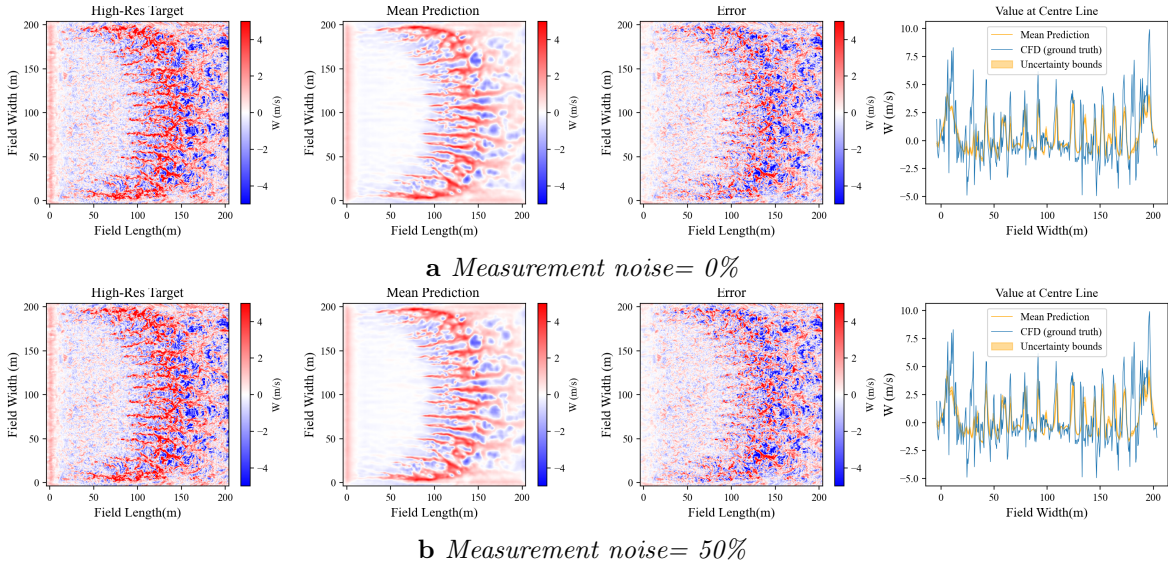


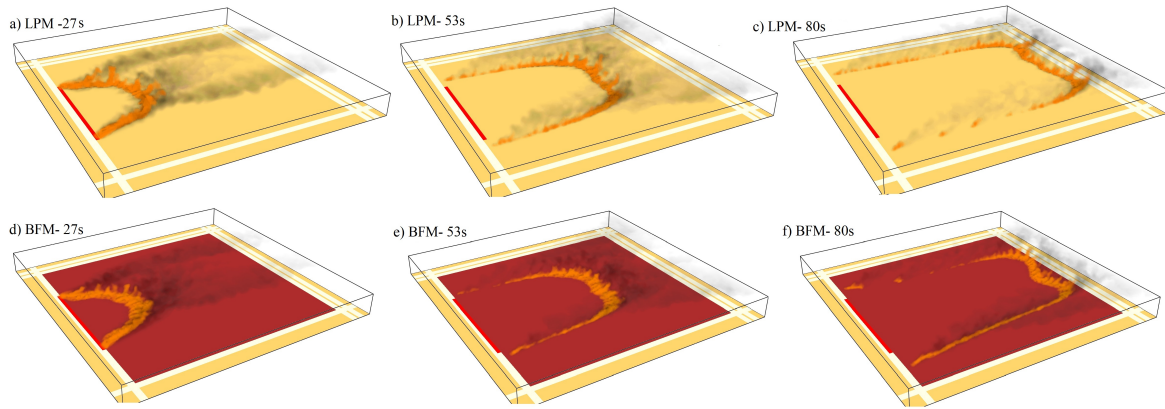
Figure 8.17: The near-surface W -component of velocity for case 49(3), $u_{10} = 12$ m/s, $H_g = 1$ m and $S = -20\%$, under different measurement noise levels, showing the high-resolution ground truth/target, the model's mean prediction, the reconstruction error, and a comparison of the estimated value along the centerline of the field with the ground truth (CFD)

Table 8.10: *Wind field inputs/updates during a 120 s simulation of wildfire propagation for different values of the time increment Δt .*

No. Wind Inputs	Δt (s)	Wind Input Times (s)
1	120	0
4	30	0, 30, 60, 90
6	20	0, 20, 40, 60, 80, 100
12	10	0, 10, 20, 30, 40, 50, ..., 100, 110
24	5	0, 5, 10, 15, 20, ..., 110, 115

8.3.1 Effect of wind field update time

In this section, a series of 3D grassland fire propagation simulations are performed using FDS-LPM and FDS-BFM, with the resulting wind field extracted at different time steps and provided to FireProM-F as if it were the output of the wind field *down-scaling module* in Figure 8.1. The effect of feeding the decoupled wildfire propagation model with the wind field is studied for a range of time intervals between consecutive "measurement" updates (Δt).

**Figure 8.18:** *Simulated wildfire propagation at three points in time for the CSIRO C064 experiment using FDS-LPM (top) and FDS-BFM (bottom) models and $0.5 \times 0.5 \times 0.5 \text{ m}^3$ cells.*

In order to investigate the effect of the time increment between wind measurements, the CSIRO C064 experiment is simulated with FireProM-F for 120 s and for five different values of Δt . The specific settings are provided in Table 8.10, whilst the temperature distributions are shown in Figure 8.19 at three points in time: 27 s, 53 s, and 100 s after ignition. In the first case, there is a single wind field input at the beginning of the simulation, which effectively means that the wind is frozen. The other cases consider decreasing values of Δt between measurements (and therefore between wind field inputs into the wildfire model) in order to somewhat account for the fire-induced wind without having to couple a computationally expensive wind model. For example, there are four wind field inputs into FireProM-F during the 120 s simulation

for $\Delta t = 30$ s.

The results for a uniform, frozen wind field are shown in Figures 8.19 (a), (b) and (c), providing a baseline against which to evaluate the effect of Δt . It can be observed that the fire front resulting from using a frozen wind field, thus disregarding the fire-induced wind, has a pointy shape that differs from the shapes displayed both in the field experiments and in the FDS-LPM simulations (see Figure 8.18). Conversely, the proposed periodic update of the wind field constructed from measurements every Δt leads to more realistic shapes of the fire front. Comparing Figures 8.18 and 8.19 at $t = 27$ s, it is clear that the shapes of the fire front are more similar to one another for smaller values of Δt (i.e. for higher frequencies of updates). For larger Δt , the fire front reaches the counter-rotating vortex pairs which form downstream before the next update (not shown here), affecting the formation of the fire front and the pace of its propagation. Therefore, reducing Δt , consequently increasing the frequency of wind field updates, may prevent or reduce the effect of this numerical (artificial) phenomenon. Furthermore, a visual comparison of Figures 8.19 (g), (h) and (i) ($\Delta t = 20$ s), Figures 8.19 (j), (k) and (l) ($\Delta t = 10$ s), and Figures 8.19 (m), (n) and (o) ($\Delta t = 5$ s) suggests that reducing Δt results in slightly faster propagation of the fire (i.e. higher RoS).

It is important to note that FireProM-F is deterministic. Therefore, the fire perimeter is symmetric for uniform wind and uniformly distributed fuel, as shown in Figures 8.19 (a), (b) and (c). The asymmetries in the remaining figures, in which the wind field is updated during the simulation, are due to FDS relying on LES to model turbulence, therefore introducing stochasticity. In fact, the fire perimeters predicted by FDS-LPM and FDS-BFM in Figure 8.18 are also asymmetric. Recall that the wind field modelled by FDS-LPM is taken here as ground truth to represent actual measurements, and are then provided to FireProM-F to enhance its predictions. Furthermore, a wind field extracted from the simulations corresponds to a specific point in time, which means that it is not time-averaged and is therefore affected by the oscillations of the dynamic combustion phase. This also contributes, albeit to a lesser extent, to the asymmetries observed in the simulated fire perimeters.

Figure 8.20 shows the simulated fire perimeter corresponding to the CSIRO C064 experiment at three points in time predicted by FireProM-F enhanced by wind field inputs derived from wind measurements every $\Delta t = 5$ s (red dotted lines). These predictions are in agreement with actual field measurements shown in the figure by black markers.

Figure 8.21 shows the burned area at three points in time after ignition: experimentally measured; predicted by FDS-LPM (coupled); predicted by FireProM-F (decoupled) with frozen and uniform wind; and predicted by FireProM-F (decoupled) enhanced by wind field inputs derived from wind measurements with different values of Δt . As can be observed, the burned area simulated by FDS-LPM is larger than the one experimentally measured. One source of this significant discrepancy is that *atmospheric wind* (i.e. disregarding fire-induced wind) velocities are variable both in intensity and direction during field experiments, whereas they are constant during

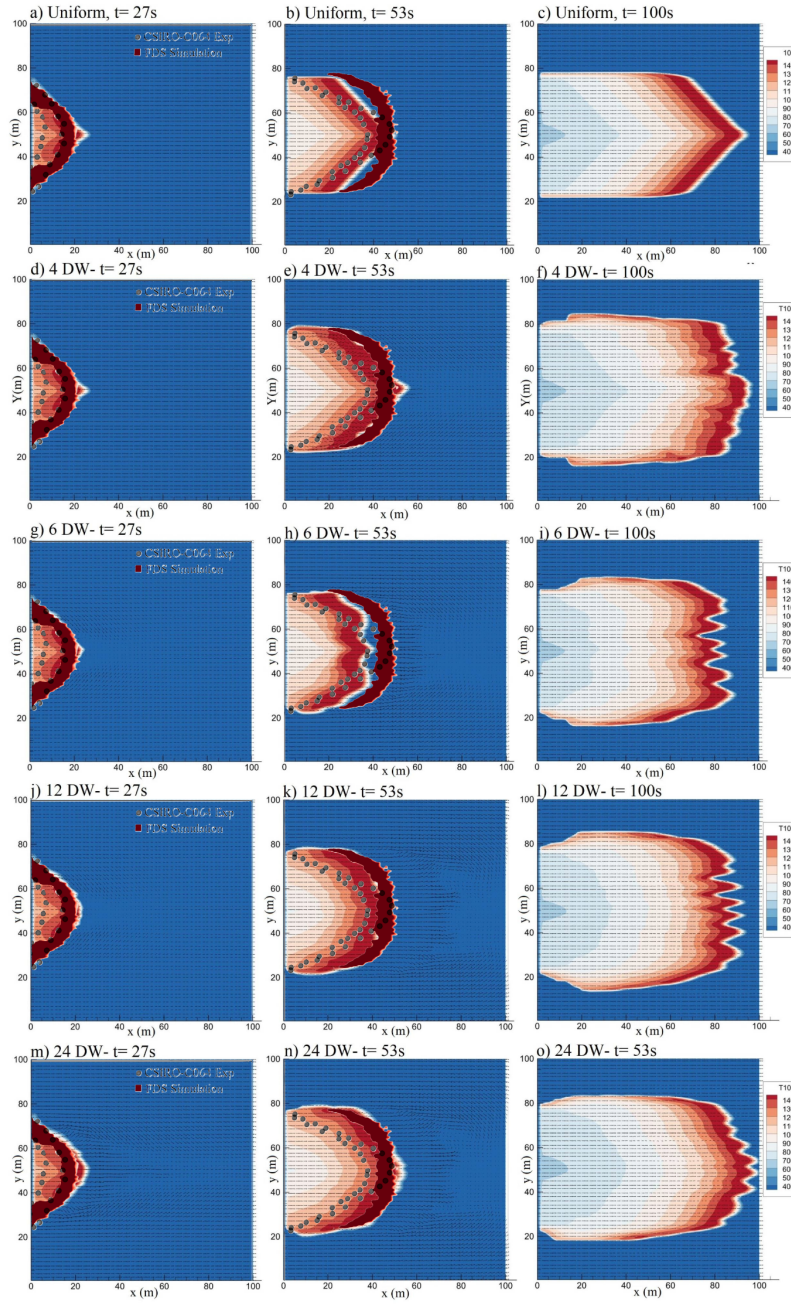


Figure 8.19: Temperature profile at three points in time from a 120 s simulation of the CSIRO C064 experiment by FireProM-F (decoupled) enhanced by wind fields inputs derived from wind measurements with update intervals (Δt) as in Table 8.10. For the first 2 time steps, simulation results of FDS and experimental data from CSIRO are also included for visual comparison. Note that "X DW" stands for "X dynamic wind field inputs during the simulation".

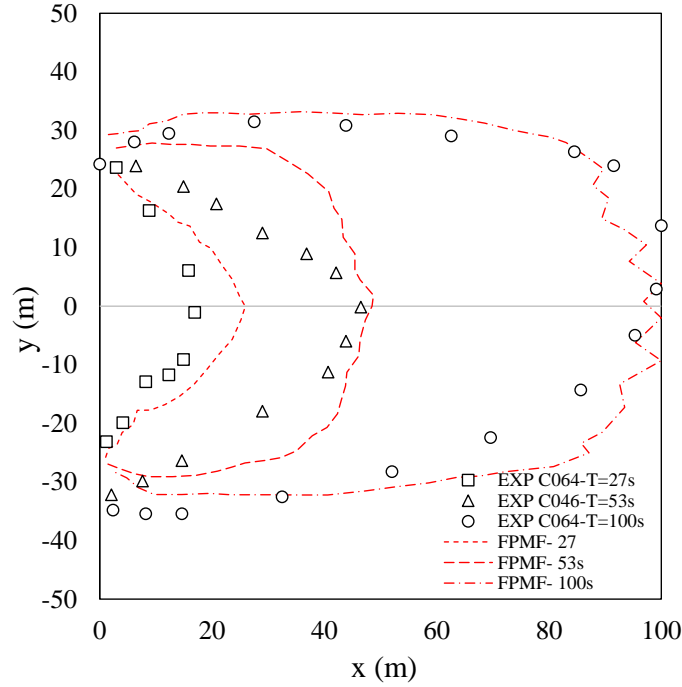


Figure 8.20: Three time instances of the CSIRO C064 experiment, where actual measurements are shown by black markers whilst the fire perimeter predicted by FireProM-F enhanced by wind field inputs derived from wind measurements every $\Delta t = 5$ s are shown by red dotted lines.

simulations. It can also be observed that the burned area predicted by the enhanced FireProM-F is closer to the one predicted by FDS-LPM than it is to the one experimentally measured. This makes sense since the wind fields provided to FireProM-F were extracted from FDS-LPM simulations. In fact, the smaller the Δt the better the agreement between them. In contrast, the burned area predicted by the decoupled Fire-ProM-F is closer to the one experimentally measured.

With regards to the computational effort, it is worth mentioning that simulating wildfire propagation within a 100×100 m² area discretised into 10,000 2D cells is performed up to 3.33 times faster than real time. That is to say that 1 min of wildfire propagation is simulated in 18 s on a single-core CPU. This may be reduced by orders of magnitude if implemented on parallel processing frameworks, which makes this approach especially suitable for operational settings.

8.3.2 Effect of wind measurement uncertainty

Wind speed measurement errors have been reported to be in the range of 20–50% when mounted on quadrotors (Donnell et al., 2018). In order to perform a preliminary study of the effect of these measurement uncertainties on the simulated wildfire propagation, two scenarios are considered: (i) 30% and (ii) 50% Gaussian noise added to the "mea-

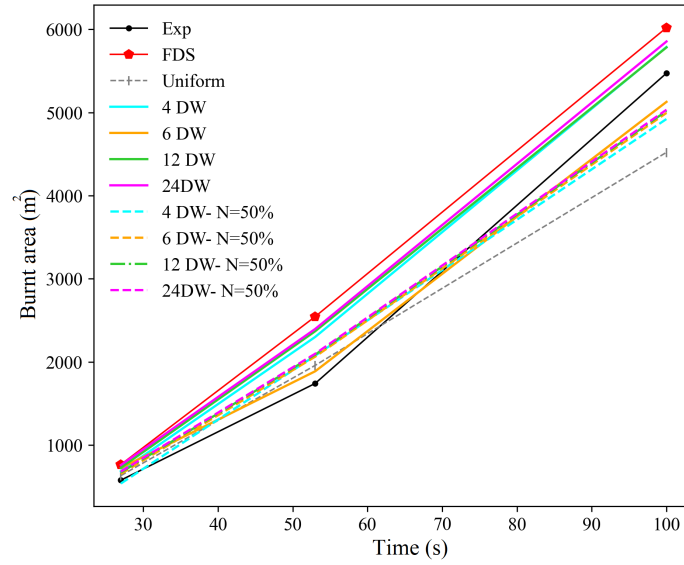


Figure 8.21: Burned area of CSIRO C064 experiment at three time instances after ignition: experimentally measured, predicted by FDS-LPM (coupled), predicted by FireProM-F (decoupled) with frozen wind, and predicted by FireProM-F (decoupled) enhanced by wind field inputs derived from wind measurements with different update intervals (Δt). Note that "X DW" stands for "X dynamic wind field inputs during the simulation", whilst the percentage refers to Gaussian noise.

surements". In other words, noise is sampled from a normal distribution with standard deviation equal to 30% and 50% of the wind velocity, respectively. Figures 8.22 and 8.23 show the temperature distribution at three points in time after ignition returned by FireProM-F simulating the CSIRO C064 experiment with noisy wind field inputs every 30 s and 10 s, respectively. As can be observed, the general shape of the burned area remains despite the noise, with the fire front displaying a more defined shape and faster propagation (higher RoS) for lower levels of noise (see also Figure 8.19). This is in agreement with the burned area decreasing when 50% noise is added to the "measurements" in Figure 8.21.

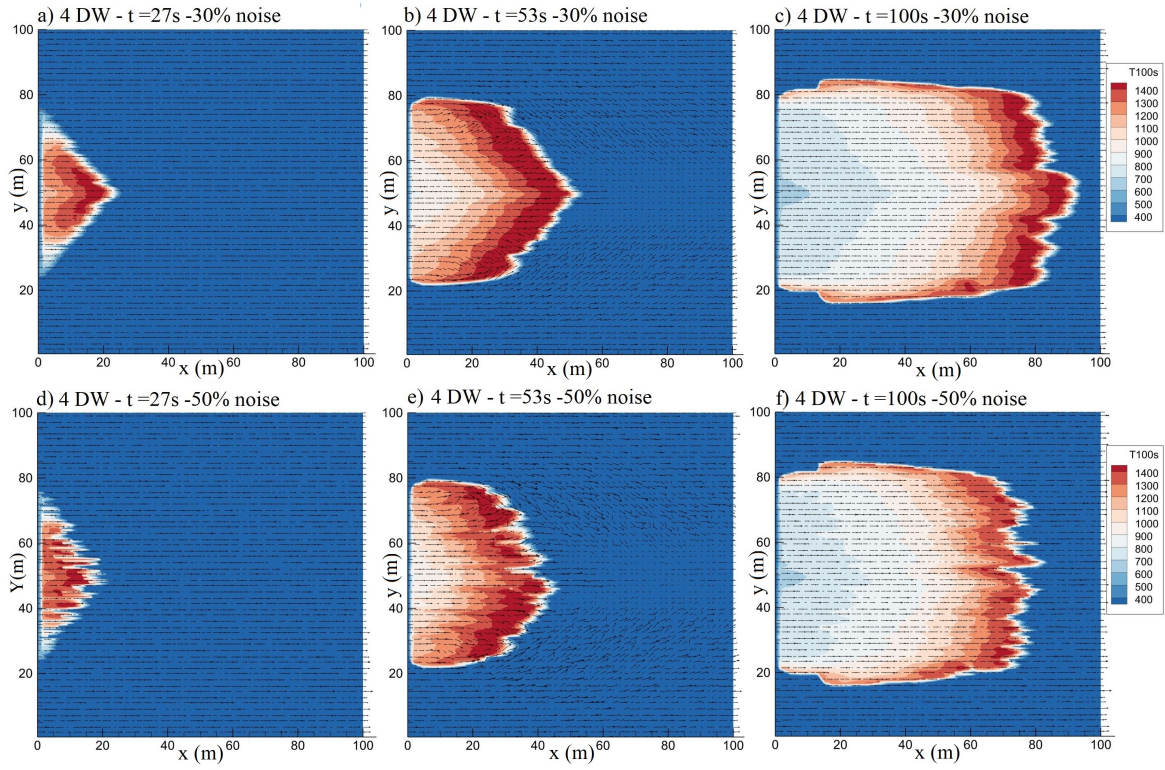


Figure 8.22: *Temperature profile at three points in time from a 120 s simulation of the CSIRO C064 experiment by FireProM-F (decoupled) enhanced by wind fields inputs with 30 % (top) and 50 % (bottom) Gaussian noise with update interval $\Delta t = 30$ s. Note that "X DW" stands for "X dynamic wind field inputs during the simulation".*

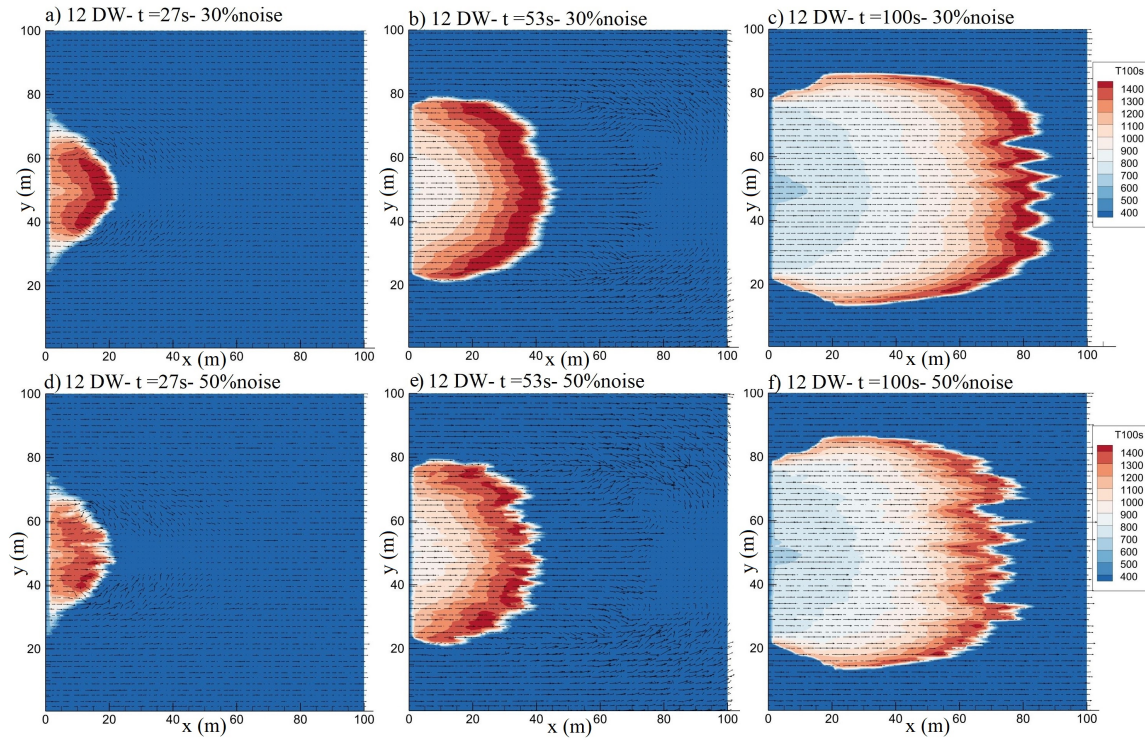


Figure 8.23: Temperature profile at three points in time from a 120 s simulation of the CSIRO C064 experiment by FireProM-F (decoupled) enhanced by wind fields inputs with 30 % (top) and 50 % (bottom) Gaussian noise with update interval $\Delta t = 10$ s. Note that "X DW" stands for "X dynamic wind field inputs during the simulation".

Chapter 9

Conclusions and Future Work

9.1 Conclusions

This research is mainly motivated by the importance of the need for providing reliable faster-than-real-time wildfire propagation predictions and better integration of UAVs into the existing wildfire emergency response systems which can benefit firefighters and decision-makers during wildfire fighting operations. Two types of models are mainly available for estimating the wildfire propagation considering the level of interaction between the fire front and the surrounding atmosphere namely (i) coupled, and (ii) decoupled models. However, coupled models are highly computationally demanding to solve a large set of underlying physics and can not be utilized in real-time wildfire fighting scenarios. On the other hand, decoupled models provide fast estimations but this comes at the cost of low accuracy and high uncertainty. Recognizing the potential for addressing this gap, this research proposed and developed a solution based on combining the power of computational fluid dynamics, deep learning, and UAV swarm-based wind measurements, aiming to reduce the risk of uncontrolled fire spread and support real-time decision-making in emergency settings.

In this thesis, firstly the current status of UAV utilization in wildfire emergency response was explored. A conceptual framework was then developed highlighting the requirements and approaches for successful UAV integration into the wildfire emergency response system, aiming to maximize the benefits of UAV utilization in wildfire emergency response operations. However, the main focus of the research was on designing and developing a framework for improving the accuracy of faster-than-real-time estimations provided by decoupled models. The developed framework includes a two-step procedure for estimating the high-resolution near-surface wind field from sparsely sensed wind velocity and temperature components at the UAV swarm flight altitude. The first step includes a model that creates a high-resolution representation of the wind and temperature field at flight altitude. The outputs from this model are then used as inputs to the second model to estimate the high-resolution wind field close to the terrain surface. The estimated wind field can be used as input to the de-

coupled wildfire propagation estimation models. The model's epistemic and aleatoric uncertainty are investigated by utilising probabilistic performance evaluation metrics including the standard deviation (Std), the Prediction Interval Coverage Probability (PICP), and the Prediction Interval Normalized Average Width (PINAW). The models' performance were tested under various numbers of measurement points—or number of UAVs in the swarm—, and inputs with high levels of measurement noise—up to 50%—to mimic the effect of swarm size and measurement uncertainties on the wind field predictions. The developed model proved to be capable of providing fast and fairly accurate estimations of the three-dimensional velocity components of the near-surface wind at 2m *AGL* from the measured wind field at 40m *AGL*, even under noisy conditions. A pilot test was designed and carried out to indicate the effectiveness of the proposed method to enhance decoupled wildfire propagation model predictions with the FireProM-F as the decoupled model. Results of the estimated fire perimeter and shape demonstrate that the enhanced FireProM-F makes more accurate predictions than the plain version.

Considering the importance of available fuel and vegetation structure on the wildfire propagation dynamics and its importance in estimating fire behaviour, a significant number of field scale simulations were carried out and combined with experimental data from the literature to provide a comprehensive understanding of fire behaviour in grassland fires under different vegetation heights, bulk densities, terrain slopes, and wind conditions. Obtained results indicated that a viable strategy to confine the fire propagation in grasslands would be to mow the grasses.

Finally, an AI-driven methodology was proposed for the accurate classification of vegetation cover type over a landscape from cartographic data. In essence, the proposed methodology is based on state-of-the-art Machine Learning (ML) classifiers combined with automated tuning of their hyperparameters and recursive feature elimination. The performance of three boosting (AdaB, XGB, CatB), two bagging (RF, XT), and three stacking ensemble models were investigated, with XGB outperforming the others. XGB with nine features and tuned with Bayesian Optimisation on a subsampled balanced dataset achieved the highest overall accuracy at 97.1% which was higher than previous values reported in the literature.

9.2 Research Contributions

This thesis primarily contributes to developing an AI-driven framework to improve the accuracy of decoupled wildfire simulation models, by leveraging comprehensive CFD simulations, and AI models. It delivers four contributions to the field as follows:

1. Conceptual Design of UAV Swarm Systems for WER Operations:

This research utilizes a system engineering approach to conceptualize a comprehensive wildfire emergency response (WER) system, leveraging UAV swarms for a variety of operational tasks such as fire detection and monitoring, supply de-

livery, real-time fire and atmospheric measurement, and participating in wildfire fighting operations. Besides, utilizing a multi-criteria decision-making procedure, this study compares commercially available UAV frameworks against the criteria that should be met and introduces the best readily available options to form a preliminary swarm of UAVs.

2. Vegetation Cover Classification Using Machine Learning:

As part of the contributions, this research introduces a machine-learning classification framework to improve the accuracy of vegetation cover mapping from cartographic data, utilizing state-of-the-art ML classifiers, automated fine-tuning algorithms, and feature engineering. Developing an accurate classifier for vegetation type is pivotal to wildfire fuel characterization as the thermal properties of the estimated vegetation type could be used as input to wildfire propagation models—though not carried out in this research— to provide a realistic and more accurate estimation.

3. Characterising the effect of vegetation characteristics on wildfire rate of spread:

As part of contributions, this research establishes a detailed analysis of the effect of vegetation characteristics—including vegetation height and bulk density—on wildfire rate of spread under different ambient wind velocities and terrain slopes. The work highlights the importance of bulk density as an important factor along with vegetation height, suggesting practical approaches for grassland fire management.

4. Enhancing Decoupled Wildfire Propagation Models Using Wind Measurements taken by a Swarm of UAVs:

This research designs and develops a novel framework utilising advanced AI models to improve the accuracy of decoupled wildfire propagation estimation models, by incorporating instantaneous sparse wind measurements collected by a UAV swarm into the wildfire propagation model after undergoing the downscaling process. This helps maintain the faster than real-time prediction speed while improving the accuracy of estimations. This methodological approach offers a practical, model agnostic and scalable solution for improving the accuracy of faster-than-real-time wildfire propagation models. A framework is developed that estimates the high-resolution near-surface wind field from sparse UAV-based wind measurements through a two-step process. First, spatial reconstruction of wind field from sparse UAV-based wind measurements is achieved by developing a data-driven super-resolution model, effectively reconstructing wind and temperature field at the flying altitude as detailed in Section 8.2.4. As detailed in section 8.2.5, a deep-learning-based model is developed and trained to provide high-resolution estimations of the near-surface wind field, taking as input the fire line characteristics and high-altitude wind patterns. Finally, as detailed in sections 8.2.4

and 8.2.5, this research quantifies uncertainties in high-altitude wind field reconstruction and near-surface wind estimation, to provide a quantitative basis for the model's estimation reliability.

9.3 Limitations

The presented work here presents an opening into the significant benefits of utilizing and integrating autonomous UAV swarms into existing wildfire management systems. It is highlighted that an accurate estimation of the wildfire behaviour over the future hours and days would be one of the main requirements for a successful wildfire management and fighting operation. Highlighting the limitations of currently available operational models which are capable of providing faster than real-time simulations including being disconnected from the atmosphere, leveraging the power of UAVs, AI and CFD simulations, a novel framework is designed and developed to improve the accuracy of wildfire propagation estimations by providing them with high-resolution wind fields near the terrain surface. This wind field is estimated through an AI model, trained to translate sparse UAV-based wind estimation into the high-resolution near-surface wind field.

The developed model, however, is currently valid within a limited range of data. The limitations could be summarised as follows:

1. only two different vegetation types
2. Wind speeds limited to the range of $4 < u_{10} < 12$ m/s
3. Terrain slopes limited to the range of $-22.8^\circ < S < +22.8^\circ$
4. Vegetation height limited to the range of $0.2 < H_g < 1$ m
5. the domain-specific limitations including limitation to square terrain of 200×200 m^2 area, with a uniform slope over the terrain
6. symmetric line fire
7. constant sampling height

9.4 Future Work

But the question here is "How applicable is this method to a large-scale wildfire"? The author suggests that this method could be generalised by a patching technique, where the desired area or firefront is divided into a series of square patches, with the wind field estimated independently for each patch. The fire could be treated as a line fire within each patch, making the proposed framework potentially feasible for larger wildfires. Nevertheless, the model in its current form has certain limitations

that require further improvements. For instance, the assumption of a symmetric line fire across all patches seems simplistic as fire fronts can vary significantly in shape within each patch. Additionally, the model is trained with input wind directed along the field length, necessitating that patches be aligned parallel to the ambient wind—an alignment that would be challenging in real fires and complex terrains. Finally, the model assumes that all data is collected at a constant height, directly parallel to the terrain, which may be difficult to obtain in actual fire conditions.

Additionally, it should be emphasised that the frameworks developed in this research, though not yet fully integrated, pave the road towards a fully deployable system which offers significant advantages. For example, the AI-driven model for vegetation classification is restricted to a specific geographic location and does not account for the atmospheric conditions of the area. However, it is hypothesised that the generalizability of the classifier can be enhanced by some methods, including removing region-specific features; emphasizing general features such as *slope*, *hillshade indices*, and *parameterised soil type*; incorporating climatic variables such as *temperature* and *precipitation*; and training on larger datasets covering different regions. Additionally, it should be highlighted that even though the model can classify vegetation accurately, it cannot be used directly as input to a wildfire estimation model as it should be first categorized as a fuel and the thermophysical properties of each species should be defined through appropriate laboratory experiments—steps that extend beyond the scope of this thesis.

Furthermore, the system development is developed and tested on simulated data both as input and targets. However, the adopted approach remains a reliable approach considering the validations against experimental data and the obvious lack of real-world data in the field. However, this inherently adds uncertainty to the model especially when employed on an actual UAV operating under highly chaotic field conditions, integrating highly uncertain UAV-based measurements.

These drawbacks, however, point to opportunities for further study to improve the system and make it more flexible for use in real-world situations. With additional development, the proposed technique has the potential to be useful for research projects as well as fire management and suppression tactics.

Bibliography

- Abatzoglou, J. T., & Brown, T. J. (2012). A comparison of statistical downscaling methods suited for wildfire applications. *International Journal of Climatology*, 32(5), 772–780. <https://doi.org/https://doi.org/10.1002/joc.2312>
- Abdar, M., Pourpanah, F., Hussain, S., Rezazadegan, D., Liu, L., Ghavamzadeh, M., Fieguth, P., Cao, X., Khosravi, A., Acharya, U. R., Makarencov, V., & Nahavandi, S. (2021). A review of uncertainty quantification in deep learning: Techniques, applications and challenges. *Information Fusion*, 76, 243–297. <https://doi.org/https://doi.org/10.1016/j.inffus.2021.05.008>
- Agbeshie, A. A., Abugre, S., Atta-Darkwa, T., et al. (2022). A review of the effects of forest fire on soil properties. *Journal of Forest Research*, 33, 1419–1441. <https://doi.org/10.1007/s11676-022-01475-4>
- Agrawal, A. (2022). *Human-drone collaborations in human-on-the-loop emergency response systems* [Doctoral dissertation, Computer Science and Engineering]. <https://doi.org/10.7274/hd76rx94g17>
- Airbus. (n.d.). Airbus’ multi-mission “cargo copter” is put to the test during a robotic military exercise [Accessed on 23-Sep-2023]. <https://www.airbus.com/en/newsroom/stories/2022-10-airbus-multi-%20mission-cargo-copter-is-put-to-the-test-during-a-robotic>
- AirSeed Technologies. (2023). AirSeed Technologies Website [Accessed: September 5, 2023]. <https://airseedtech.com/>
- Aizerman, M. A., Braverman, E. A., & Rozonoer, L. (1964). Theoretical foundations of the potential function method in pattern recognition learning. *Automation and Remote Control*, 25, 821–837.
- Akhloufi, M. A., Couturier, A., & Castro, N. A. (2021). Unmanned aerial vehicles for wildland fires: Sensing, perception, cooperation and assistance. *drones*, 5(1), 15. <https://doi.org/https://doi.org/10.3390/drones5010015>
- Akiba, T., Sano, S., Yanase, T., Ohta, T., & Koyama, M. (2019). Optuna: A next-generation hyperparameter optimization framework. *Proceedings of the 25th ACM SIGKDD International Conference on Knowledge Discovery & Data Mining*. <https://doi.org/10.1145/3292500.3330701>
- Albini, F. A. (1976). *Estimating wildfire behavior and effects* (tech. rep. No. INT-GTR-30). U.S. Department of Agriculture, Forest Service, Intermountain Forest and Range Experiment Station. Ogden, UT.

- Ali, R., Kang, D., Suh, G., & Cha, Y.-J. (2021). Real-time multiple damage mapping using autonomous UAV and deep faster region-based neural networks for GPS-denied structures. *Automation in Construction*, 130, 103831. <https://doi.org/10.1016/j.autcon.2021.103831>
- Alkhatib, A. A. A. (2014). A Review on Forest Fire Detection Techniques. *International Journal of Distributed Sensor Networks*, 10(3), 597368. <https://doi.org/10.1155/2014/597368>
- Amini, E., Safdari, M.-S., Johnson, N., Weise, D. R., & Fletcher, T. H. (2021). Pyrolysis kinetics of wildland vegetation using model-fitting methods. *Journal of Analytical and Applied Pyrolysis*, 157, 105167. <https://doi.org/https://doi.org/10.1016/j.jaap.2021.105167>
- Anderson, K. E., Glenn, N. F., Spaete, L. P., Shinneman, D. J., Pilliod, D. S., Arkle, R. S., McIlroy, S. K., & Derryberry, D. R. (2018). Estimating vegetation biomass and cover across large plots in shrub and grass dominated drylands using terrestrial lidar and machine learning. *Ecological Indicators*, 84, 793–802. <https://doi.org/10.1016/j.ecolind.2017.09.034>
- Andrews, P. L. (2012). *Modeling wind adjustment factor and midflame wind speed for Rothmel's surface fire spread model* (tech. rep. No. RMRS-GTR-266). U.S. Department of Agriculture, Forest Service, Rocky Mountain Research Station. Fort Collins, CO. <https://doi.org/10.2737/RMRS-GTR-266>
- Andrio, A. (2019). Development of UAV technology in seed dropping for aerial revegetation practices in Indonesia. *IOP Conference Series: Earth and Environmental Science*, 308(1), 012051. <https://doi.org/10.1088/1755-1315/308/1/012051>
- Arnold, R., Carey, K., Abruzzo, B., & Korpela, C. (2019). What is a robot swarm: A definition for swarming robotics. *2019 IEEE 10th Annual Ubiquitous Computing, Electronics & Mobile Communication Conference (UEMCON)*, 0074–0081. <https://doi.org/10.1109/UEMCON47517.2019.8993024>
- Arroyo, L. A., Pascual, C., & Manzanera, J. A. (2008). Fire models and methods to map fuel types: The role of remote sensing. *Forest Ecology and Management*, 256(6), 1239–1252. <https://doi.org/10.1016/j.foreco.2008.06.048>
- Aurell, J., Gullett, B., Holder, A., Kiros, F., Mitchell, W., Watts, A., & Ottmar, R. (2021). Wildland fire emission sampling at fishlake national forest, utah using an unmanned aircraft system. *Atmospheric Environment*, 247, 118193. <https://doi.org/10.1016/j.atmosenv.2021.118193>
- Ausonio, E., Bagnerini, P., & Ghio, M. (2021). Drone swarms in fire suppression activities: A conceptual framework. *Drones*, 5(1). <https://www.mdpi.com/2504-446X/5/1/17>
- B. Porterie, A. K., J. L. Consalvi, & Loraud, J. C. (2005). Predicting wildland fire behavior and emissions using a fine-scale physical model. *Numerical Heat Transfer, Part A: Applications*, 47(6), 571–591. <https://doi.org/10.1080/10407780590891362>
- Backer, D. M., Jensen, S. E., & McPherson, G. R. (2004). Impacts of fire-suppression activities on natural communities. *Conservation Biology*, 18(4), 937–946. https://doi.org/10.1111/j.1523-1739.2004.494_1.x

- Bakhshaii, A., & Johnson, E. (2019). A review of a new generation of wildfire-atmosphere modeling. *Canadian Journal of Forest Research*, 49(6), 565–574. <https://doi.org/10.1139/cjfr-2018-0138>
- Balch, J. K., Bradley, B. A., Abatzoglou, J. T., Nagy, R. C., Fusco, E. J., & Mahood, A. L. (2017). Human-started wildfires expand the fire niche across the United States [Publisher: Proceedings of the National Academy of Sciences]. *Proceedings of the National Academy of Sciences*, 114(11), 2946–2951. <https://doi.org/10.1073/pnas.1617394114>
- Barboni, T., Morandini, F., Rossi, L., Molinier, T., & Santoni, P.-A. (2012). Relationship between flame length and fireline intensity obtained by calorimetry at laboratory scale. *Combustion Science and Technology*, 184(2), 186–204. <https://doi.org/10.1080/00102202.2011.625373>
- Barmpoutis, P., Papaioannou, P., Dimitropoulos, K., & Grammalidis, N. (2020). A review on early forest fire detection systems using optical remote sensing. *Sensors*, 20(22). <https://www.mdpi.com/1424-8220/20/22/6442>
- Belén, C.-L., G, V. J., Jorge, L.-S., & A, R.-M. J. (2021). Study on the environmental adaptability of lithium-ion battery powered UAV under extreme temperature conditions. *International Journal of Wildland Fire*, 30, 475–483. <https://doi.org/10.1016/j.energy.2020.119481>
- Bhat, N. S., Shashidhara, K. S., & Dakulagi, V. (2021). Fire fighting un-manned air vehicle for remote areas. In P. M. Pawar, R. Balasubramaniam, B. P. Ronge, S. B. Salunkhe, A. S. Vibhute, & B. Melinamath (Eds.), *Techno-societal 2020* (pp. 593–601). Springer International Publishing.
- Blackard, J. A., & Dean, D. J. (1999). Comparative accuracies of artificial neural networks and discriminant analysis in predicting forest cover types from cartographic variables. *Computers and Electronics in Agriculture*, 24(3), 131–151. [https://doi.org/10.1016/s0168-1699\(99\)00046-0](https://doi.org/10.1016/s0168-1699(99)00046-0)
- Boardman, C. R., Dietenberger, M. A., & Weise, D. R. (2021). Specific heat capacity of wildland foliar fuels to 434°C. *Fuel*, 292, 120396. <https://doi.org/https://doi.org/10.1016/j.fuel.2021.120396>
- Boonmee, N., & Quintiere, J. (2005). Glowing ignition of wood: The onset of surface combustion. *Proceedings of the Combustion Institute*, 30(2), 2303–2310. <https://doi.org/https://doi.org/10.1016/j.proci.2004.07.022>
- Bova, A. S., Mell, W. E., & Hoffman, C. M. (2016). A comparison of level set and marker methods for the simulation of wildland fire front propagation. *International Journal of Wildland Fire*, 25(2), 229–241. <https://doi.org/10.1071/WF13178>
- Bowman, D. M. J. S., Balch, J. K., Artaxo, P., Bond, W. J., Carlson, J. M., Cochrane, M. A., D’Antonio, C. M., DeFries, R. S., Doyle, J. C., Harrison, S. P., Johnston, F. H., Keeley, J. E., Krawchuk, M. A., Kull, C. A., Marston, J. B., Moritz, M. A., Prentice, I. C., Roos, C. I., Scott, A. C., . . . Pyne, S. J. (2009). Fire in the earth system. *Science*, 324(5926), 481–484. <https://doi.org/10.1126/science.1163886>

- Braziunas, K. H., Abendroth, D. C., & Turner, M. G. (2022). Young forests and fire: Using LiDAR–imagery fusion to explore fuels and burn severity in a subalpine forest reburn. *Ecosphere*, 13(5), e4096. <https://doi.org/10.1002/ecs2.4096>
- Breiman, L. (1996). Stacked regressions. *Machine Learning*, 24(1), 49–64. <https://doi.org/10.1007/bf00117832>
- Breiman, L., Friedman, J. H., Olshen, R. A., & Stone, C. J. (2017, October). *Classification and regression trees*. Routledge. <https://doi.org/10.1201/9781315139470>
- Brochu, E., Cora, V., & de Freitas, N. (2009). *A tutorial on bayesian optimization of expensive cost functions, with application to active user modeling and hierarchical reinforcement learning* (tech. rep.). University of British Columbia’s Department of Computer Science.
- Brooke-Holland, L. (2012). Unmanned aerial vehicles (drones): An introduction. <https://irp.fas.org/world/uk/drones.pdf>
- Bumberger, J., Remmler, P., Hutschenreuther, T., Toepfer, H., & Dietrich, P. (2013). Potentials and Limitations of Wireless Sensor Networks for Environmental. *AGU Fall Meeting Abstracts, 2013*, Article H51F-1263.
- Burge, J., Bonanni, M., Hu, R., et al. (2023). Recurrent convolutional deep neural networks for modeling time-resolved wildfire spread behavior. *Fire Technology*, 59, 3327–3354. <https://doi.org/10.1007/s10694-023-01469-6>
- Butler, B. W., Anderson, W. R., & Catchpole, E. A. (2007). Influence of slope on fire spread rate.
- Byram, G. M. (1959). Combustion of forest fuels. In K. P. Davis (Ed.), *Forest fire: Control and use* (pp. 61–89). McGraw-Hill.
- Caie, P. D., Dimitriou, N., & Arandjelović, O. (2021). Precision medicine in digital pathology via image analysis and machine learning. In *Artificial intelligence and deep learning in pathology* (pp. 149–173). Elsevier. <https://doi.org/10.1016/b978-0-323-67538-3.00008-7>
- Campbell, M. J., Page, W. G., Dennison, P. E., & Butler, B. W. (2019). Escape route index: A spatially-explicit measure of wildland firefighter egress capacity. *Fire*, 2(3), 40. <https://doi.org/10.3390/fire2030040>
- Campbell-Lochrie, Z., Walker-Ravena, C., Gallagher, M., Skowronski, N., Mueller, E. V., & Hadden, R. M. (2021). Investigation of the role of bulk properties and in-bed structure in the flow regime of buoyancy-dominated flame spread in porous fuel beds [Fire Safety Science: Proceedings of the 13th International Symposium]. *Fire Safety Journal*, 120, 103035. <https://doi.org/https://doi.org/10.1016/j.firesaf.2020.103035>
- Campion, M., Ranganathan, P., & Faruque, S. (2019). UAV swarm communication and control architectures: A review. *Journal of Unmanned Vehicle Systems*, 7(2), 93–106. <https://doi.org/10.1139/juvs-2018-0009>
- Catboost [Available at <https://catboost.ai/>]. (2022). <https://catboost.ai>
- CBS News. (2023). How much of Maui has burned in the wildfires? Aerial images show fire damage as containment efforts continue [Accessed on 14-Sep-2023].

- <https://www.cbsnews.com/news/how-much-of-maui-has-burned-wildfires%20-aerial-images-acres-containment/>
- Chakraborty, S. (2022). Topsis and modified topsis: A comparative analysis. *Decision Analytics Journal*, 2, 100021. <https://doi.org/10.1016/j.dajour.2021.100021>
- Chandler, C. H., Cheney, P. H., Thomas, P. D., Traub, L., & Williams, D. (1983). Fire in forestry. volume 1. forest fire behavior and effects. volume 2. forest fire management and organization. <https://www.cabdirect.org/cabdirect/abstract/19850699124>
- Chen, A., Jacob, M., Shoshani, G., & Charter, M. (2023). Using computer vision, image analysis and UAVs for the automatic recognition and counting of common cranes (*Grus grus*). *Journal of Environmental Management*, 328, 116948. <https://doi.org/10.1016/j.jenvman.2022.116948>
- Chen, T., & Guestrin, C. (2016). XGBoost. *Proceedings of the 22nd ACM SIGKDD International Conference on Knowledge Discovery and Data Mining*. <https://doi.org/10.1145/2939672.2939785>
- Cheney, P., Gould, J., & Catchpole, W. (1993). The influence of fuel, weather and fire shape variables on fire-spread in grasslands. *International Journal of Wildland Fire*, 3(1), 31–44. <https://doi.org/https://doi.org/10.1071/WF9930031>
- Cheney, P., Gould, J., & Catchpole, W. R. (1998). Prediction of fire spread in grasslands. *International Journal of Wildland Fire*, 8, 1–13. <https://doi.org/https://doi.org/10.1071/WF9980001>
- Cheng, J., Liu, J., Xu, Z., Shen, C., & Kuang, Q. (2020). Generating high-resolution climate prediction through generative adversarial network. *Procedia Computer Science*, 174, 123–127. <https://doi.org/https://doi.org/10.1016/j.procs.2020.06.067>
- Chin, R., Catal, C., & Kassahun, A. (2023). Plant disease detection using drones in precision agriculture. *Precision Agriculture*, 24(5), 1663–1682. <https://doi.org/10.1007/s11119-023-10014-y>
- Chuvieco, E., Mouillot, F., van der Werf, G. R., San Miguel, J., Tanase, M., Koutsias, N., García, M., Yebra, M., Padilla, M., Gitas, I., Heil, A., Hawbaker, T. J., & Giglio, L. (2019). Historical background and current developments for mapping burned area from satellite earth observation. *Remote Sensing of Environment*, 225, 45–64. <https://doi.org/10.1016/j.rse.2019.02.013>
- Chuvieco, E., Riaño, D., Wagtenok, J. V., & Morsdorf, F. (2003, September). Fuel loads and fuel type mapping. In *Series in remote sensing* (pp. 119–142). WORLD SCIENTIFIC. https://doi.org/10.1142/9789812791177_0005
- CIFFC. (2017). CIFFC Canadian wildland fire management glossary. <https://www.cifc.ca/publications/glossary>
- Civil Aviation Authority. (2023). Airspace policy concept for BVLOS flying - A policy concept to develop how RPAS can be accommodated within airspace. *Civil Aviation Authority*. <https://www.caa.co.uk/drones/rules-and-categories-of-drone-flying/airspace-policy-concept-for-bvlos-flying/>

- Coen, J. L., Cameron, M., Michalakes, J., Patton, E. G., Riggan, P. J., & Yedinak, K. M. (2013). WRF-fire: Coupled weather–wildland fire modeling with the weather research and forecasting model. *Journal of Applied Meteorology and Climatology*, 52(1), 16–38. <https://doi.org/10.1175/jamc-d-12-023.1>
- Collins, A. M., Rivera-Casillas, P., Dutta, S., Cecil, O. M., Trautz, A. C., & Farthing, M. W. (2023). Super-resolution and uncertainty estimation from sparse sensors of dynamical physical systems. *Frontiers in Water*, 5. <https://doi.org/10.3389/frwa.2023.1137110>
- Commission-England, F. (2020). *Assessment of potential wildfire risk resulting from planned deforestation to open habitat* (Operations Note No. 40) (Appendix E: Stakeholders for Wildfire Planning). Forestry Commission-England. <https://www.gov.uk/government/publications/assessment-of-potential-wildfire-risk-resulting-from-planned-deforestation-to-open-habitat-operations-note-40>
- Council, N. F. C. (Accessed in July 2023-a). Control measure - emergency response plans: Wildfires. <https://www.ukfrs.com/guidance/search/emergency-response-plans-wildfires>
- Council, N. F. C. (Accessed in July 2023-b). Control measure: Consider appropriate wildfire suppression tactics and develop and implement a tactical plan. <https://www.ukfrs.com/guidance/search/insufficient-resources-wildfire%20bundle=control-measure%5C&id=14303>
- Cover, T. (1968). Estimation by the nearest neighbor rule. *IEEE Transactions on Information Theory*, 14(1), 50–55. <https://doi.org/10.1109/tit.1968.1054098>
- Cruz, M. G., & Alexander, M. E. (2019a). The 10% wind speed rule of thumb for estimating a wildfire’s forward rate of spread in forests and shrublands. *Annals of Forest Science*, 76, 44. <https://doi.org/10.1007/s13595-019-0829-8>
- Cruz, M. G., & Alexander, M. E. (2019b). The 10% wind speed rule of thumb for estimating a wildfire’s forward rate of spread in forests and shrublands. *Annals of Forest Science*, 76, 44. <https://doi.org/10.1007/s13595-019-0829-8>
- Cruz, M. G., Alexander, M. E., & Kilinc, M. (2022a). Wildfire rates of spread in grasslands under critical burning conditions. *Fire*, 5(2). <https://doi.org/10.3390/fire5020055>
- Cruz, M. G., Alexander, M. E., & Kilinc, M. (2022b). Wildfire rates of spread in grasslands under critical burning conditions. *Fire*, 5(2). <https://doi.org/10.3390/fire5020055>
- Cruz, M. G., Gould, J. S., Kidnie, S., Bessell, R., Nichols, D., & Slijepcevic, A. (2015). Effects of curing on grassfires: Ii. effect of grass senescence on the rate of fire spread. *International Journal of Wildland Fire*, 24, 838–848. <https://doi.org/10.1071/WF14146>
- Cruz, M. G., Hurley, R. J., Bessell, R., & Sullivan, A. L. (2020). Fire behaviour in wheat crops – effect of fuel structure on rate of fire spread. *International Journal of Wildland Fire*, 29, 258–271. <https://doi.org/10.1071/WF19139>
- Cruz, M. G., Sullivan, A. L., & Gould, J. S. (2021). The effect of fuel bed height in grass fire spread: Addressing the findings and recommendations of moinuddin

- et al. (2018). *International Journal of Wildland Fire*, 30, 215–220. <https://doi.org/10.1071/WF19186>
- Cruz, M. G., Sullivan, A. L., Gould, J. S., Hurley, R. J., & Plucinski, M. P. (2018). Got to burn to learn: The effect of fuel load on grassland fire behaviour and its management implications. *International Journal of Wildland Fire*, 27, 727–741. <https://doi.org/10.1071/WF18082>
- Dalamagkidis, K. (2015a). Classification of UAVs. In K. P. Valavanis & G. J. Vachtsevanos (Eds.), *Handbook of unmanned aerial vehicles* (pp. 83–91). Springer Netherlands. <https://doi.org/10.1007/978-90-481-9707-1-94>
- Dalamagkidis, K. (2015b). Definitions and terminology. In K. P. Valavanis & G. J. Vachtsevanos (Eds.), *Handbook of unmanned aerial vehicles* (pp. 43–55). Springer Netherlands. <https://doi.org/10.1007/978-90-481-9707-1-92>
- D’Amico, D., Ekoyuncu, J., Addepalli, S., Smith, C., Keedwell, E., Sibson, J., & Penver, S. (2019). Conceptual framework of a digital twin to evaluate the degradation status of complex engineering systems [7th CIRP Global Web Conference – Towards shifted production value stream patterns through inference of data, models, and technology (CIRPe 2019)]. *Procedia CIRP*, 86, 61–67. <https://doi.org/10.1016/j.procir.2020.01.043>
- de Groot, W. J., Wotton, B. M., & Flannigan, M. D. (2015). Chapter 11 - wildland fire danger rating and early warning systems. In J. F. Shroder & D. Paton (Eds.), *Wildfire hazards, risks and disasters* (pp. 207–228). Elsevier. <https://doi.org/10.1016/B978-0-12-410434-1.00011-7>
- DJI. (2023). DJI T40 Product Page [Accessed: September 5, 2023]. <https://www.dji.com/>
- DJI Enterprise. (2023). DJI dock [Accessed: Oct, 6, 2023]. <https://enterprise.dji.com/dock>
- Donnell, G. W., Feight, J. A., Lannan, N., & Jacob, J. D. (2018). Wind characterization using onboard IMU of sUAS. *2018 Atmospheric Flight Mechanics Conference*. <https://doi.org/https://doi.org/10.2514/6.2018-2986>
- Dossi, S., Messerschmidt, B., Ribeiro, L. M., Almeida, M., & Rein, G. (2023). Relationships between building features and wildfire damage in California, USA and Pedrógão Grande, Portugal. *International Journal of Wildland Fire*, 32, 296–312. <https://doi.org/10.1071/WF22095>
- Dreissig, M., Scheuble, D., Piewak, F., & Boedecker, J. (2023). Survey on LiDAR perception in adverse weather conditions.
- Drysdale, D. (2011). Fire science and combustion. In *An introduction to fire dynamics* (pp. 1–34). John Wiley & Sons, Ltd. <https://doi.org/https://doi.org/10.1002/9781119975465.ch1>
- Dubois, P., Gomez, T., Planckaert, L., & Perret, L. (2022). Machine learning for fluid flow reconstruction from limited measurements. *Journal of Computational Physics*, 448, 110733. <https://doi.org/https://doi.org/10.1016/j.jcp.2021.110733>

- Dujardin, J., & Lehning, M. (2022). Wind-topo: Downscaling near-surface wind fields to high-resolution topography in highly complex terrain with deep learning. *Quarterly Journal of the Royal Meteorological Society*, 148.
- Endsley, M. R. (1995). Toward a theory of situation awareness in dynamic systems. *Human Factors*, 37(1), 32–64. <https://doi.org/10.1518/001872095779049543>
- Engelstad, P. S., Falkowski, M., Wolter, P., Poznanovic, A., & Johnson, P. (2019). Estimating canopy fuel attributes from low-density LiDAR. *Fire*, 2(3), 38. <https://doi.org/10.3390/fire2030038>
- Ermacora, G., Sartori, D., Rovasenda, M., Pei, L., & Yu, W. (2020). An evaluation framework to assess autonomous navigation linked to environment complexity. *2020 IEEE International Conference on Mechatronics and Automation (ICMA)*, 1803–1810. <https://doi.org/10.1109/ICMA49215.2020.9233862>
- Estrada, M. A. R., & Ndoma, A. (2019). The uses of unmanned aerial vehicles –UAV’s- (or drones) in social logistic: Natural disasters response and humanitarian relief aid [ICTE in Transportation and Logistics 2018 (ICTE 2018)]. *Procedia Computer Science*, 149, 375–383. <https://doi.org/10.1016/j.procs.2019.01.151>
- European Civil Aviation Conference (ECAC). (2021). UAS bulletin. https://www.ecac-ceac.org/images/news/uas-bulletin/UAS_Bulletin_2021_02.pdf
- European Union. (2019). Commission implementing regulation (EU) 2019/947 of 24 May 2019 on the rules and procedures for the operation of unmanned aircraft. https://eur-lex.europa.eu/eli/reg_impl/2019/947/oj/eng
- European Union Aviation Safety Agency (EASA). (2020). What is U-space? <https://www.easa.europa.eu/en/what-u-space>
- Evolve Dynamics Ltd. (2024, June). Sky Mantis 2. <https://evolvedynamics.com/sky-mantis-2/>
- Faulconbridge, R., & Ryan, M. (2002). *Managing complex technical projects*. Artech House; Illustrated edition.
- Federal Aviation Administration. (2019). FAA drones and wildfires digital toolkit. Retrieved September 19, 2023, from https://www.faa.gov/sites/faa.gov/files/uas/resources/community_engagement/FAA_drones_wildfires_toolkit.pdf
- Federal Aviation Administration. (2021). Operations over people general overview [Accessed: Oct, 6, 2023]. https://www.faa.gov/uas/commercial_operators/operations_over_people
- Federal Aviation Administration. (2023a). The FAA authorizes Phoenix Air Unmanned to operate drones beyond visual line of sight for certain aerial work [Accessed: Oct, 6, 2023]. <https://www.faa.gov/newsroom/faa-authorizes-phoenix-air-unmanned-operate-drones-beyond-visual-line-sight-certain-aerial>
- Federal Aviation Administration. (2023b). The FAA authorizes UPS Flight Forward and uAvionix to operate drones beyond visual line of sight [Accessed: Oct, 6, 2023]. <https://www.faa.gov/newsroom/faa-authorizes-ups-uavionix>
- Federal Emergency Management Agency. (2011). *National disaster recovery framework: Strengthening disaster recovery for the nation*.

- Finney, M. A. (1998a). *FARSITE: Fire area simulator-model development and evaluation* (tech. rep. No. RMRS-RP-4, Revised 2004). U.S. Department of Agriculture, Forest Service, Rocky Mountain Research Station. Ogden, UT. <https://doi.org/10.2737/RMRS-RP-4>
- Finney, M. A. (1998b). *Farsite: Fire area simulator-model development and evaluation* (tech. rep.). U.S. Department of Agriculture, Forest Service, Rocky Mountain Research Station. <https://doi.org/10.2737/rmrs-rp-4>
- Finney, M. A., McAllister, S. S., Grumstrup, T. P., & Forthofer, J. M. (2021a). Combustion. In *Wildland fire behaviour*. CSIRO Publishing. <https://doi.org/10.1071/9781486309092>
- Finney, M. A., McAllister, S. S., Grumstrup, T. P., & Forthofer, J. M. (2021b). Fire and wildland fire behaviour. In *Wildland fire behaviour*. CSIRO Publishing. <https://doi.org/10.1071/9781486309092>
- Finney, M. A., McAllister, S. S., Grumstrup, T. P., & Forthofer, J. M. (2021c). Ignition. In *Wildland fire behaviour*. CSIRO Publishing. <https://doi.org/10.1071/9781486309092>
- Finney, M. A., McAllister, S. S., Grumstrup, T. P., & Forthofer, J. M. (2021d). Thermodynamics, fluid mechanics and heat transfer. In *Wildland fire behaviour*. CSIRO Publishing. <https://doi.org/10.1071/9781486309092>
- Flash Forest. (2023). Flash Forest Website [Accessed: September 5, 2023]. <https://flashforest.ca/>
- FlyingBasket. (2023). Fb3 - the most compact drone in the world able to carry 100 kg [Accessed on 14-Sep-2023]. <https://flyingbasket.com/fb3>
- Food, (FAO), A. O., & (WRI), W. R. I. (2019). *The road to restoration: A guide to identifying priorities and indicators for monitoring forest and landscape restoration*. FAO, Rome; WRI, Washington, D.C.
- Food and Agriculture Organization (FAO). (2003). Wildland fire management terminology [Accessed on August 18, 2023]. <https://www.fao.org/3/ag041e/AG041E13.htm>
- Forestry Commission. (2014). Building wildfire resilience into forest management planning. <https://cdn.forestresearch.gov.uk/2014/03/fcpg022.pdf>
- Forthofer, J. M., Butler, B. W., & Wagenbrenner, N. (2014). A comparison of three approaches for simulating fine-scale surface winds in support of wildland fire management: Part i. model formulation and comparison against measurements. *International Journal of Wildland Fire*, 23, 969–981. <https://doi.org/http://dx.doi.org/10.1071/WF12089>
- Forzieri, G., Dakos, V., McDowell, N. G., et al. (2022). Emerging signals of declining forest resilience under climate change. *Nature*, 608, 534–539. <https://doi.org/10.1038/s41586-022-04959-9>
- Fouda, M. M., Sakib, S., Fadlullah, Z. M., Nasser, N., & Guizani, M. (2022). A lightweight hierarchical AI model for UAV-enabled edge computing with forest-fire detection use-case. *IEEE Network*, 36(6), 38–45. <https://doi.org/10.1109/MNET.003.2100325>

- Freund, Y., & Schapire, R. E. (1997). A decision-theoretic generalization of on-line learning and an application to boosting. *Journal of Computer and System Sciences*, 55(1), 119–139. <https://doi.org/10.1006/jcss.1997.1504>
- Friedman, J. H. (2001). Greedy function approximation: A gradient boosting machine. *The Annals of Statistics*, 29(5). <https://doi.org/10.1214/aos/1013203451>
- Fukami, K., Fukagata, K., & Taira, K. (2019). Super-resolution reconstruction of turbulent flows with machine learning. *Journal of Fluid Mechanics*, 870, 106–120. <https://doi.org/10.1017/jfm.2019.238>
- Fukami, K., Fukagata, K., & Taira, K. (2023). Super-resolution analysis via machine learning: A survey for fluid flows. *Theoretical and Computational Fluid Dynamics*, 37(4), 421–444. <https://doi.org/10.1007/s00162-023-00663-0>
- Gabbert, B. (2018). Cost of exclusive use vs. call when needed air tankers [Accessed: Oct, 6, 2023]. <https://fireaviation.com/2018/02/21/cost-exclusive-use-vs-%20call-needed-air-tankers/>
- Gal, Y., & Ghahramani, Z. (2016). Dropout as a bayesian approximation: Representing model uncertainty in deep learning. <https://arxiv.org/abs/1506.02142>
- Gale, M. G., Cary, G. J., Dijk, A. I. V., & Yebra, M. (2021). Forest fire fuel through the lens of remote sensing: Review of approaches, challenges and future directions in the remote sensing of biotic determinants of fire behaviour. *Remote Sensing of Environment*, 255, 112282. <https://doi.org/10.1016/j.rse.2020.112282>
- García-Llamas, P., Suárez-Seoane, S., Fernández-Guisuraga, J. M., Fernández-García, V., Fernández-Manso, A., Quintano, C., Taboada, A., Marcos, E., & Calvo, L. (2019). Evaluation and comparison of landsat 8, sentinel-2 and deimos-1 remote sensing indices for assessing burn severity in mediterranean fire-prone ecosystems. *International Journal of Applied Earth Observation and Geoinformation*, 80, 137–144. <https://doi.org/10.1016/j.jag.2019.04.006>
- Garrett, C. J., Levack, D. J. H., & Rhodes, R. E. (2011). Using technical performance measures. *47th AIAA/ASME/SAE/ASEE Joint Propulsion Conference*. <https://ntrs.nasa.gov/citations/20110014436>
- Gayathri, K., Yasoda, K., & Roy, M. N. (2022). Automatic firefighting system using unmanned aerial vehicle. In R. Ibrahim, K. Porkumaran, R. Kannan, N. Mohd Nor, & S. Prabakar (Eds.), *International conference on artificial intelligence for smart community* (pp. 1023–1031). Springer Nature Singapore.
- Georgiev, G. D., Hristov, G., Zahariev, P., & Kinaneva, D. (2020). Forest monitoring system for early fire detection based on convolutional neural network and UAV imagery. *2020 28th National Conference with International Participation (TELECOM)*, 57–60. <https://doi.org/10.1109/TELECOM50385.2020.9299566>
- Geurts, P., Ernst, D., & Wehenkel, L. (2006). Extremely randomized trees. *Machine Learning*, 63(1), 3–42. <https://doi.org/10.1007/s10994-006-6226-1>
- Grasso, P., & Innocente, M. S. (2020a). Physics-based model of wildfire propagation towards faster-than-real-time simulations. *Computers & Mathematics with Applications*, 80(5), 790–808. <https://doi.org/10.1016/j.camwa.2020.05.009>

- Grasso, P., & Innocente, M. S. (2020b). Physics-based model of wildfire propagation towards faster-than-real-time simulations. *Computers & Mathematics with Applications*, 80(5), 790–808. <https://doi.org/10.1016/j.camwa.2020.05.009>
- Grasso, P., & Innocente, M. S. (2018). A two-dimensional reaction- advection- diffusion model of the spread of fire in wildlands. *Advances in Forest Fire Research*.
- Grishin, A. (1997). *Mathematical modeling of forest fires and new methods of fighting them*. Publishing House of the Tomsk State University. <https://books.google.co.uk/books?id=JGy-AAAACAAJ>
- Grlj, C. G., Krznar, N., & Pranjić, M. (2022). A decade of UAV docking stations: A brief overview of mobile and fixed landing platforms. *Drones*, 6(1). <https://doi.org/10.3390/drones6010017>
- Grossnickle, S. C., & Ivetić, V. (2017). Direct seeding in reforestation – A field performance review. *REFORESTA*, (4), 94–142. <https://doi.org/10.21750/REFOR.4.07.46>
- Group, N. W. C. (1996, April). *Wildland fire suppression tactics reference guide* (Report) (A publication sponsored by the United States Department of Agriculture and the United States Department of the Interior). National Wildfire Coordinating Group.
- Guerra-Hernández, J., Díaz-Varela, R., Álvarez-González, J., & et al. (2021). Assessing a novel modelling approach with high resolution UAV imagery for monitoring health status in priority riparian forests. *Forest Ecosystems*, 8, 61. <https://doi.org/10.1186/s40663-021-00342-8>
- Hamylton, S., Morris, R., Carvalho, R., Roder, N., Barlow, P., Mills, K., & Wang, L. (2020). Evaluating techniques for mapping island vegetation from unmanned aerial vehicle (UAV) images: Pixel classification, visual interpretation and machine learning approaches. *International Journal of Applied Earth Observation and Geoinformation*, 89, 102085. <https://doi.org/10.1016/j.jag.2020.102085>
- Hancock, J. T., & Khoshgoftaar, T. M. (2020). CatBoost for big data: An interdisciplinary review. *Journal of Big Data*, 7(1). <https://doi.org/10.1186/s40537-020-00369-8>
- Hartley, R. J. L., Davidson, S. J., Watt, M. S., Massam, P. D., Aguilar-Arguello, S., Melnik, K. O., Pearce, H. G., & Clifford, V. R. (2022). A mixed methods approach for fuel characterisation in gorse (*ulex europaeus* l.) scrub from high-density UAV laser scanning point clouds and semantic segmentation of UAV imagery. *Remote Sensing*, 14(19), 4775. <https://doi.org/10.3390/rs14194775>
- Hassanalian, M., & Abdelkefi, A. (2017). Classifications, applications, and design challenges of drones: A review. *Progress in Aerospace Sciences*, 91, 99–131. <https://doi.org/10.1016/j.paerosci.2017.04.003>
- Haynes, K., Short, K., Xanthopoulos, G., Viegas, D., Ribeiro, L. M., & Blanchi, R. (2019). Wildfires and wui fire fatalities. In S. L. Manzello (Ed.), *Encyclopedia of wildfires and wildland-urban interface (wui) fires* (pp. 1–16). Springer International Publishing. https://doi.org/10.1007/978-3-319-51727-8_92-1

- He, K., Zhang, X., Ren, S., & Sun, J. (n.d.). Deep residual learning for image recognition. *2016 IEEE Conference on Computer Vision and Pattern Recognition (CVPR)*, 770–778. <https://doi.org/10.1109/CVPR.2016.90>
- Hewitson, B., & Crane, R. G. (1996). Climate downscaling: Techniques and application. *Climate Research*, 7, 85–95.
- Hillman, S., Hally, B., Wallace, L., Turner, D., Lucieer, A., Reinke, K., & Jones, S. (2021). High-resolution estimates of fire severity — An evaluation of UAS image and LiDAR mapping approaches on a Sedgeland forest boundary in Tasmania, Australia. *Fire*, 4(1). <https://doi.org/10.3390/fire4010014>
- Höhlein, K., Kern, M., Hewson, T., & Westermann, R. (2020). A comparative study of convolutional neural network models for wind field downscaling. *Journal of Meteorological Applications*, 27(6), e1961. <https://doi.org/https://doi.org/10.1002/met.1961>
- Holl, K. D., Loik, M. E., Lin, E. H. V., & Samuels, I. A. (2000). Tropical montane forest restoration in costa rica: Overcoming barriers to dispersal and establishment. *Restoration Ecology*, 8(4), 339–349. <https://doi.org/10.1046/j.1526-100x.2000.80049.x>
- Homicz, G. F. (2002). *Three-dimensional wind field modeling: A review* (tech. rep.). Rocky Mountain Research Station. Sandia National Lab. (SNL-NM), Albuquerque, NM (United States); Sandia National Lab. (SNL-CA), Livermore, CA (United States). <https://www.osti.gov/biblio/801406>
- Hossain, F. A., Zhang, Y. M., & Tonima, M. A. (2020). Forest fire flame and smoke detection from UAV-captured images using fire-specific color features and multi-color space local binary pattern. *Journal of Unmanned Vehicle Systems*, 8(4), 285–309. <https://doi.org/10.1139/juvs-2020-0009>
- Huang, H. (2004). *Autonomy levels for unmanned systems (alfus) framework volume i: Terminology version 2.0* (Special Publication (NIST SP) No. 1011-I-2.0). National Institute of Standards and Technology. Gaithersburg, MD. Retrieved October 20, 2023, from <https://doi.org/10.6028/NIST.sp.1011-I-2.0>
- Hubbert, K. R., Wohlgemuth, P. M., Beyers, J. L., et al. (2012). Post-fire soil water repellency, hydrologic response, and sediment yield compared between grass-converted and chaparral watersheds. *Fire Ecology*, 8, 143–162. <https://doi.org/10.4996/fireecology.0802143>
- Hussein, M., Nouacer, R., Corradi, F., Ouhammou, Y., Villar, E., Tieri, C., & Castiñeira, R. (2021). Key technologies for safe and autonomous drones. *Microprocessors and Microsystems*, 87, 104348. <https://doi.org/10.1016/j.micpro.2021.104348>
- Innocent, J., Sutherland, D., Khan, N., & Moinuddin, K. (2023). Physics-based simulations of grassfire propagation on sloped terrain at field scale: Motivations, model reliability, rate of spread and fire intensity. *International Journal of Wildland Fire*, 32, 496–512. <https://doi.org/10.1071/WF21124>
- Innocente, M. S., & Grasso, P. (2019a). Self-organising swarms of firefighting drones: Harnessing the power of collective intelligence in decentralised multi-robot sys-

- tems. *Journal of Computational Science*, 34, 80–101. <https://doi.org/https://doi.org/10.1016/j.jocs.2019.04.009>
- Innocente, M. S., & Grasso, P. (2019b). Self-organising swarms of firefighting drones: Harnessing the power of collective intelligence in decentralised multi-robot systems. *Journal of Computational Science*, 34, 80–101. <https://doi.org/10.1016/j.jocs.2019.04.009>
- Innocente, M. S., & Grasso, P. (2019c). Self-organising swarms of firefighting drones: Harnessing the power of collective intelligence in decentralised multi-robot systems. *Journal of Computational Science*, 34, 80–101. <https://doi.org/10.1016/j.jocs.2019.04.009>
- Jain, P., Coogan, S. C., Subramanian, S. G., Crowley, M., Taylor, S., & Flannigan, M. D. (2020). A review of machine learning applications in wildfire science and management. *Environmental Reviews*, 28(4), 478–505. <https://doi.org/10.1139/er-2020-0019>
- Jarrin, N., Uribe, J.-C., Prosser, R., & Laurence, D. (2008). *Synthetic inflow boundary conditions for wall bounded flows* (Vol. 97). Springer Nature. https://doi.org/10.1007/978-3-540-77815-8_8
- Jiao, J., Lewis, R. H., Seong, K., Farahi, A., Navratil, P., Casebeer, N., & Niyogi, D. (2023). Fire and smoke digital twin – a computational framework for modeling fire incident outcomes.
- Kakooei, M., & Baleghi, Y. (2017). Fusion of satellite, aircraft, and UAV data for automatic disaster damage assessment. *International Journal of Remote Sensing*, 38(8-10), 2511–2534. <https://doi.org/10.1080/01431161.2017.1294780>
- Kalogeropoulos, N., Mitchell, H., Ronchi, E., Gwynne, S., & Rein, G. (2023). Design of stochastic trigger boundaries for rural communities evacuating from a wildfire. *Fire Safety Journal*, 140, 103854. <https://doi.org/10.1016/j.firesaf.2023.103854>
- Karvonen, H., Honkavaara, E., Rönning, J., Kramar, V., & Sassi, J. (2023). Using a semi-autonomous drone swarm to support wildfire management – a concept of operations development study. In D. Harris & W.-C. Li (Eds.), *Engineering psychology and cognitive ergonomics* (pp. 235–253). Springer Nature Switzerland.
- Kato, A., Moskal, L. M., Schiess, P., Swanson, M. E., Calhoun, D., & Stuetzle, W. (2009). Capturing tree crown formation through implicit surface reconstruction using airborne lidar data. *Remote Sensing of Environment*, 113(6), 1148–1162. <https://doi.org/10.1016/j.rse.2009.02.010>
- Kattenborn, T., Eichel, J., & Fassnacht, F. E. (2019). Convolutional neural networks enable efficient, accurate, and fine-grained segmentation of plant species and communities from high-resolution UAV imagery. *Scientific Reports*, 9, 17656. <https://doi.org/10.1038/s41598-019-53797-9>
- Keerthinathan, P., Amarasingam, N., Hamilton, G., & Gonzalez, F. (2023). Exploring unmanned aerial systems operations in wildfire management: Data types, processing algorithms and navigation. *International Journal of Remote Sensing*, 44(18), 5628–5685. <https://doi.org/10.1080/01431161.2023.2249604>

- Keetch, J. J., & Byram, G. M. (1968). *A drought index for forest fire control* (Vol. 38). US Department of Agriculture, Forest Service, Southeastern Forest Experiment ...
- Kerle, N., Nex, F., Gerke, M., Duarte, D., & Vetrivel, A. (2020). UAV-based structural damage mapping: A review. *ISPRS International Journal of Geo-Information*, 9(1). <https://doi.org/10.3390/ijgi9010014>
- Kim, Y.-H., Bettinger, P., & Finney, M. (2009). Spatial optimization of the pattern of fuel management activities and subsequent effects on simulated wildfires. *European Journal of Operational Research*, 197(1), 253–265. <https://doi.org/10.1016/j.ejor.2008.05.025>
- Kiran, D. (2017). Chapter 30 - quality function deployment. In D. Kiran (Ed.), *Total quality management* (pp. 425–437). Butterworth-Heinemann. <https://doi.org/10.1016/B978-0-12-811035-5.00030-1>
- Kizilkaya, B., Ever, E., Yatbaz, H. Y., & Yazici, A. (2022). An effective forest fire detection framework using heterogeneous wireless multimedia sensor networks. *18*(2). <https://doi.org/10.1145/3473037>
- Knapp, E. E., Valachovic, Y. S., Quarles, S. L., & Johnson, N. G. (2021). Housing arrangement and vegetation factors associated with single-family home survival in the 2018 Camp Fire, California. *Fire Ecology*, 17(1), 25. <https://doi.org/10.1186/s42408-021-00117-0>
- Korlapati, N. V. S., Khan, F., Noor, Q., Mirza, S., & Vaddiraju, S. (2022). Review and analysis of pipeline leak detection methods. *Journal of Pipeline Science and Engineering*, 2(4), 100074. <https://doi.org/10.1016/j.jpse.2022.100074>
- Kramer, H. A., Mockrin, M. H., Alexandre, P. M., & Radeloff, V. C. (2019). High wildfire damage in interface communities in California. *International Journal of Wildland Fire*. <https://doi.org/10.1071/WF18108>
- Kumar, A., & Sinha, N. (2020). Classification of forest cover type using random forests algorithm. In *Advances in data and information sciences* (pp. 395–402). Springer Singapore. <https://doi.org/10.1007/978-981-15-0694-9-37>
- Kyuroson, A., Koval, A., & Nikolakopoulos, G. (2023). Efficient real-time smoke filtration with 3D LiDAR for search and rescue with autonomous heterogeneous robotic systems.
- Lacerda, L. N., Snider, J. L., Cohen, Y., Liakos, V., Gobbo, S., & Vellidis, G. (2022). Using UAV-based thermal imagery to detect crop water status variability in cotton. *Smart Agricultural Technology*, 2, 100029. <https://doi.org/10.1016/j.atech.2021.100029>
- Lacroix, S., Alami, R., Lemaire, T., Hattenberger, G., & Gancet, J. (2007). Decision making in multi-UAVs systems: Architecture and algorithms. In A. Ollero & I. Maza (Eds.), *Multiple heterogeneous unmanned aerial vehicles* (pp. 15–48). Springer Berlin Heidelberg. https://doi.org/10.1007/978-3-540-73958-6_2
- Lattimer, B. Y., Huang, X., Delichatsios, M. A., Levendis, Y. A., Kochersberger, K., Manzello, S., Frank, P., Jones, T., Salvador, J., Delgado, C., Angelats, E., Parés, M. E., Martín, D., McAllister, S., & Suzuki, S. (2023). Use of unmanned aerial

- systems in outdoor firefighting [Published online: July 27, 2023]. *Fire Technology*. <https://doi.org/10.1007/s10694-023-01437-0>
- Lawrence, B. L., Mundorff, K., & Keith, E. (2023). The impact of UAS aerial ignition on prescribed fire: A case study in multiple ecoregions of texas and louisiana. *Fire Ecology*, 19. <https://doi.org/10.1186/s42408-023-00170-x>
- Le Toumelin, L., Gouttevin, I., Galiez, C., & Helbig, N. (2024). A two-fold deep-learning strategy to correct and downscale winds over mountains. *Nonlinear Processes in Geophysics*, 31(1), 75–97. <https://doi.org/10.5194/npg-31-75-2024>
- LeCun, Y., Bengio, Y., & Hinton, G. (2015). Deep learning. *Nature*, 521(7553), 436–444. <https://doi.org/10.1038/nature14539>
- Lee, D., Hess, D. J., & Heldeweg, M. A. (2022). Safety and privacy regulations for unmanned aerial vehicles: A multiple comparative analysis. *Technology in Society*, 71, 102079. <https://doi.org/10.1016/j.techsoc.2022.102079>
- Lee, K. (2015). FAA drone rule proposal: What they allow, who benefits, who doesn't [Accessed: Oct, 6, 2023]. <https://www.latimes.com/nation/nationnow/la-na-nn-proposed-drone-rules-20150216-story.html>
- Leys, B. A., Marlon, J. R., Umbanhowar, C., & Vannière, B. (2018). Global fire history of grassland biomes. *Ecology and Evolution*, 8(17), 8831–8852. <https://doi.org/10.1002/ece3.4394>
- Li, M., Shu, Z., Geng, S., & Han, G. (2020). Experimental and modelling study on flame tilt angle of flame spread over jet fuel under longitudinally forced air flows. *Fuel*, 270, 117516. <https://doi.org/10.1016/j.fuel.2020.117516>
- Li, N., Liu, X., Yu, B., Li, L., Xu, J., & Tan, Q. (2021). Study on the environmental adaptability of lithium-ion battery powered UAV under extreme temperature conditions. *Energy*, 219, 119481. <https://doi.org/10.1016/j.energy.2020.119481>
- Li, Y., Li, C., Li, M., & Liu, Z. (2019). Influence of variable selection and forest type on forest aboveground biomass estimation using machine learning algorithms. *Forests*, 10(12), 1073. <https://doi.org/10.3390/f10121073>
- Library of Congress. (Year of Access). Cyclones and earthquakes: Panoramic photographs [Accessed on 13-Sep-2023]. <https://www.loc.gov/static/collections/panoramic-photographs/%20articles-and-essays/selected-panoramic-photographs/%20cyclones-and-earthquakes.html>
- Lindell, M. K. (2013). Emergency management. In P. T. Bobrowsky (Ed.), *Encyclopedia of natural hazards* (pp. 263–271). Springer Netherlands. <https://doi.org/10.1007/978-1-4020-4399-4-114>
- Linn, R. R., Reisner, J. M., Colman, J., & Winterkamp, J. (2002). Studying wildfire behavior using FIRETEC. *International Journal of Wildland Fire*, 11, 233–246. <https://doi.org/10.1071/WF02007>
- Liu, N., Lei, J., Gao, W., Chen, H., & Xie, X. (2021). Combustion dynamics of large-scale wildfires. *Proceedings of the Combustion Institute*, 38(1), 157–198. <https://doi.org/10.1016/j.proci.2020.11.006>
- Liu, S., Luo, Y., Peng, L., Jiang, Y., Meng, E., & Li, B. (2022). Wind pressure field reconstruction based on unbiased conditional kernel density estimation. *Journal*

- of Wind Engineering and Industrial Aerodynamics*, 223, 104947. <https://doi.org/https://doi.org/10.1016/j.jweia.2022.104947>
- Lopes, A. M. G., Ribeiro, L. M., Viegas, D. X., & Raposo, J. R. (2017). Effect of two-way coupling on the calculation of forest fire spread: Model development. *International Journal of Wildland Fire*, 26(9), 829. <https://doi.org/10.1071/wf16045>
- Lovreglio, R., Kuligowski, E., Gwynne, S., & Strahan, K. (2019). A modelling framework for householder decision-making for wildfire emergencies. *International Journal of Disaster Risk Reduction*, 41, 101274. <https://doi.org/10.1016/j.ijdr.2019.101274>
- Luo, M., Wang, Y., Xie, Y., Zhou, L., Qiao, J., Qiu, S., & Sun, Y. (2021). Combination of feature selection and CatBoost for prediction: The first application to the estimation of aboveground biomass. *Forests*, 12(2), 216. <https://doi.org/10.3390/f12020216>
- Macmichael, D., & Si, D. (2017). Addressing forest management challenges by refining tree cover type classification with machine learning models. *2017 IEEE International Conference on Information Reuse and Integration (IRI)*. <https://doi.org/10.1109/iri.2017.89>
- Marino, E., Tomé, J. L., Hernando, C., Guijarro, M., & Madrigal, J. (2022). Transferability of airborne LiDAR data for canopy fuel mapping: Effect of pulse density and model formulation. *Fire*, 5(5), 126. <https://doi.org/10.3390/fire5050126>
- Markiewicz, A., & Nash, L. (2016, August). Small unmanned aircraft and the U.S. Forest Service: Benefits, costs, and recommendations for using small unmanned aircraft in Forest Service operations. <https://rosap.ntl.bts.gov/view/dot/12349>
- Martell, D. L. (2015). A review of recent forest and wildland fire management decision support systems research. *Current Forestry Reports*, 1(2), 128–137. <https://doi.org/10.1007/s40725-015-0011-y>
- Mast reforestation. (2023). Introducing FirePlug-The first seedling optimized for post-wildfire reforestation [Accessed: 07/Sep/2023]. <https://www.mastreforest.com/seed>
- Matalonga, S., White, S., Hartmann, J., et al. (2022). A review of the legal, regulatory and practical aspects needed to unlock autonomous beyond visual line of sight unmanned aircraft systems operations. *Journal of Intelligent and Robotic Systems*, 106(10). <https://doi.org/10.1007/s10846-022-01682-5>
- McArthur, A. G. (1969). The tasmanian bushfires of 7th february 1967 and associated fire behaviour characteristics. In T. T. C.-o. Programme (Ed.), *Mass fire symposium: The technical cooperation programme* (Paper A7, Vol. 1).
- McArthur, A. G., & Australia. (1966). *Weather and grassland fire behaviour / by a.g. mcarthur*. Forestry; Timber Bureau Canberra.
- Mcbride, B. J., Gordon, S., & Reno, M. A. (1993). *Coefficients for calculating thermodynamic and transport properties of individual species* (tech. rep.). NASA.
- McCaffrey, B. (1979, 1979-01-01 05:01:00). Purely buoyant diffusion flames ::some experimental results. <https://doi.org/https://doi.org/10.6028/NBS.IR.79-1910>

- McCaffrey, S., McGee, T. K., Coughlan, M., & Tedim, F. (2020). Understanding wild-fire mitigation and preparedness in the context of extreme wildfires and disasters: Social science contributions to understanding human response to wildfire. In F. Tedim, V. Leone, & T. K. McGee (Eds.), *Extreme wildfire events and disasters* (pp. 155–174). Elsevier. <https://doi.org/10.1016/B978-0-12-815721-3.00008-4>
- McGrattan, K., Hostikka, S., Floyd, J., McDermott, R., Vanella, M., & Mueller, E. (2023). *Fire dynamics simulator user's guide* (Sixth). https://github.com/firemodels/fds/releases/download/FDS-6.8.0/FDS_User_Guide.pdf
- McGrattan, K., McDermott, R., Hostikka, S., & Floyd, J. (2019). *Fire dynamics simulator user's guide*. NIST Special Publication 1019-5: National Institute of Standards and Technology (NIST). Maryland, USA.
- McGrattan, K., McDermott, R., Vanella, M., Mueller, E., Hostikka, S., & Floyd, J. (2024). *Fire dynamics simulator: Technical reference guide, volume 1: Mathematical model* (Sixth, NIST Special Publication No. 1018-1) (FDS-6.9.1-0-g889da6aU, April 8, 2024). National Institute of Standards and Technology (NIST). Gaithersburg, Maryland. <https://doi.org/10.6028/NIST.SP.1018>
- Meier, S., Elliott, R. J., & Strobl, E. (2023). The regional economic impact of wildfires: Evidence from southern europe. *Journal of Environmental Economics and Management*, 118, 102787. <https://doi.org/10.1016/j.jeem.2023.102787>
- Mell, W., Jenkins, M. A., Gould, J., & Cheney, P. (2007). A physics-based approach to modelling grassland fires. *International Journal of Wildland Fire*, 16(1), 1. <https://doi.org/10.1071/wf06002>
- Meyer, M., Long, J., & Safford, H. (2021). *Postfire restoration framework for national forests in California* (General Technical Report No. PSW-GTR-270). U.S. Department of Agriculture, Forest Service, Pacific Southwest Research Station. Albany, CA.
- Milner, E., Sooriyabandara, M., & Hauert, S. (2023). Swarm performance indicators: Metrics for robustness, fault tolerance, scalability and adaptability.
- Mitchell, H., Gwynne, S., Ronchi, E., Kalogeropoulos, N., & Rein, G. (2023). Integrating wildfire spread and evacuation times to design safe triggers: Application to two rural communities using peril model. *Safety Science*, 157, 105914. <https://doi.org/10.1016/j.ssci.2022.105914>
- Mohan, M., Richardson, G., Gopan, G., Aghai, M. M., Bajaj, S., Galgamuwa, G. A. P., Vastaranta, M., Arachchige, P. S. P., Amorós, L., Corte, A. P. D., de-Miguel, S., Leite, R. V., Kganyago, M., Broadbent, E. N., Doaemo, W., Shorab, M. A. B., & Cardil, A. (2021). UAV-supported forest regeneration: Current trends, challenges and implications. *Remote Sensing*, 13(13). <https://doi.org/10.3390/rs13132596>
- Mohapatra, A., & Trinh, T. (2022). Early wildfire detection technologies in practice; a review. *Sustainability*, 14(19). <https://www.mdpi.com/2071-1050/14/19/12270>

- Moinuddin, K., Khan, N., & Sutherland, D. (2021). Numerical study on effect of relative humidity (and fuel moisture) on modes of grassfire propagation. *Fire Safety Journal*, 125, 103422. <https://doi.org/https://doi.org/10.1016/j.firesaf.2021.103422>
- Moinuddin, K., Sutherland, D., & Mell, W. (2018). Simulation study of grass fire using a physics-based model: Striving towards numerical rigour and the effect of grass height on the rate of spread. *International Journal of Wildland Fire*, 27(12), 800–814. <https://doi.org/10.1071/WF17126>
- Morandini, F., Silvani, X., Dupuy, J.-l., & Susset, A. (2018). Fire spread across a sloping fuel bed: Flame dynamics and heat transfers. *Combustion and Flame*, 190, 158–170. <https://doi.org/https://doi.org/10.1016/j.combustflame.2017.11.025>
- Morvan, D. (2014). Wind effects, unsteady behaviors, and regimes of propagation of surface fires in open field. *Combustion Science and Technology*, 186(7), 869–888. <https://doi.org/10.1080/00102202.2014.885961>
- Morvan, D., & Frangieh, N. (2018). Wildland fires behaviour: Wind effect versus byram's convective number and consequences upon the regime of propagation. *International Journal of Wildland Fire*, 27, 636–641. <https://doi.org/10.1071/WF18014>
- Mueller, E. V., Campbell-Lochrie, Z., Walker-Ravena, C., & Hadden, R. M. (2023). Numerical simulations of flame spread in pine needle beds using simple thermal decomposition models. *Fire Safety Journal*, 141, 103886. <https://doi.org/https://doi.org/10.1016/j.firesaf.2023.103886>
- Mueller, E. V., Skowronski, N. S., Clark, K. L., Gallagher, M. R., Mell, W. E., Simeoni, A., & Hadden, R. M. (2021). Detailed physical modeling of wildland fire dynamics at field scale - an experimentally informed evaluation [Fire Safety Science: Proceedings of the 13th International Symposium]. *Fire Safety Journal*, 120, 103051. <https://doi.org/https://doi.org/10.1016/j.firesaf.2020.103051>
- Münzinger, M., Prechtel, N., & Behnisch, M. (2022). Mapping the urban forest in detail: From LiDAR point clouds to 3D tree models. *Urban Forestry & Urban Greening*, 74, 127637. <https://doi.org/10.1016/j.ufug.2022.127637>
- Murphy, R. R. (2004). Trial by fire [rescue robots]. *IEEE Robotics & Automation Magazine*, 11(3), 50–61. <https://doi.org/10.1109/MRA.2004.1337826>
- Myeong, W. C., Jung, K. Y., & Myung, H. (n.d.). Development of faros (fire-proof drone) using an aramid fiber armor and air buffer layer. *2017 14th International Conference on Ubiquitous Robots and Ambient Intelligence (URAI)*, 204–207. <https://doi.org/10.1109/URAI.2017.7992713>
- NASA. (2020, January). NASA Systems Engineering Handbook.
- NASA Earth Observatory. (2018). Camp fire adds another scar to 2018 fire season [Accessed on 13-Sep-2023]. <https://earthobservatory.nasa.gov/images/144300/camp-fire-adds-another-scar-to-2018-fire-season>
- National Aeronautics and Space Administration (NASA). (2021). What is unmanned aircraft systems traffic management? <https://www.nasa.gov/centers-and-facilities/ames/what-is-unmanned-aircraft-systems-traffic-management/>

- Nelson, R. M. (2015). Re-analysis of wind and slope effects on flame characteristics of mediterranean shrub fires. *International Journal of Wildland Fire*, 24, 1001–1007. <https://doi.org/10.1071/WF14155>
- Nelson Jr., R. M., & Adkins, C. W. (1986). Flame characteristics of wind-driven surface fires. *Canadian Journal of Forest Research*, 16(6), 1293–1300. <https://doi.org/10.1139/x86-229>
- Nguyen, V. (2019). Bayesian optimization for accelerating hyper-parameter tuning. *2019 IEEE Second International Conference on Artificial Intelligence and Knowledge Engineering (AIKE)*. <https://doi.org/10.1109/aike.2019.00060>
- Niu, Z., Zhong, G., & Yu, H. (2021). A review on the attention mechanism of deep learning. *Neurocomputing*, 452, 48–62. <https://doi.org/https://doi.org/10.1016/j.neucom.2021.03.091>
- Noble, I. R., Gill, A. M., & Bary, G. A. V. (1980). Mearthur's fire-danger meters expressed as equations. *Australian Journal of Ecology*, 5(2), 201–203. <https://doi.org/https://doi.org/10.1111/j.1442-9993.1980.tb01243.x>
- NWCG, N. W. C. G. -. (2021). Nwgc glossary of wildland fire, pms 205. <https://www.nwgc.gov/glossary/a-z>
- (NWCG), N. W. C. G. (n.d.). Atmospheric stability. Retrieved January 11, 2024, from <https://www.nwgc.gov/publications/pms425-1/atmospheric-stability>
- Office for National Statistics. (2015). Uk natural capital: Land cover in the uk. <https://www.ons.gov.uk/economy/environmentalaccounts/articles/uknaturalcapitalallandcoverintheuk/2015-03-17>
- Olaz, X., Alaez, D., Prieto, M., Villadangos, J., & Astrain, J. J. (2023). Quadcopter neural controller for take-off and landing in windy environments. *Expert Systems with Applications*, 225, 120146. <https://doi.org/https://doi.org/10.1016/j.eswa.2023.120146>
- O'Mara, F. P. (2012). The role of grasslands in food security and climate change. *Annals of Botany*, 110(6), 1263–1270. <https://doi.org/10.1093/aob/mcs209>
- Partheepan, S., Sanati, F., & Hassan, J. (2023). Autonomous unmanned aerial vehicles in bushfire management: Challenges and opportunities. *Drones*, 7(1). <https://doi.org/10.3390/drones7010047>
- Pedregosa, F., Varoquaux, G., Gramfort, A., Michel, V., Thirion, B., Grisel, O., Blondel, M., Prettenhofer, P., Weiss, R., Dubourg, V., Vanderplas, J., Passos, A., Cournapeau, D., Brucher, M., Perrot, M., & Duchesnay, E. (2011). Scikit-learn: Machine learning in Python. *Journal of Machine Learning Research*, 12, 2825–2830. <http://www.jmlr.org/papers/volume12/pedregosa11a/pedregosa11a.pdf>
- Peña, P. F., Ragab, A. R., Luna, M. A., Ale Isaac, M. S., & Campoy, P. (2022). WILD HOPPER: A heavy-duty UAV for day and night firefighting operations. *Heliyon*, 8(6), e09588. <https://doi.org/10.1016/j.heliyon.2022.e09588>
- Petersen, E. L., Mortensen, N. G., Landberg, L., Højstrup, J., & Frank, H. P. (1998). Wind power meteorology. part i: Climate and turbulence. *Wind Energy*, 1(S1), 25–45. [https://doi.org/https://doi.org/10.1002/\(SICI\)1099-1824\(199804\)1:1+25::AID-WE43.0.CO;2-D](https://doi.org/https://doi.org/10.1002/(SICI)1099-1824(199804)1:1+25::AID-WE43.0.CO;2-D)

- Plantinga, A. J., Walsh, R., & Wibbenmeyer, M. (2022). Priorities and effectiveness in wildfire management: Evidence from fire spread in the Western United States. *Journal of the Association of Environmental and Resource Economists*, 9(4), 603–639. <https://doi.org/10.1086/719426>
- Potter, B. E. (2012a). Atmospheric interactions with wildland fire behaviour - i. basic surface interactions, vertical profiles and synoptic structures. *International Journal of Wildland Fire*, 21(7), 779. <https://doi.org/10.1071/wf11128>
- Potter, B. E. (2012b). Atmospheric interactions with wildland fire behaviour-i. basic surface interactions, vertical profiles and synoptic structures. *International Journal of Wildland Fire*, 21, 779–801. <https://doi.org/10.1071/WF11128>
- Prestemon, J. P., Butry, D. T., Abt, K. L., & Sutphen, R. (2010). Net Benefits of Wildfire Prevention Education Efforts. *Forest Science*, 56(2), 181–192. <https://doi.org/10.1093/forestscience/56.2.181>
- Prokhorenkova, L., Gusev, G., Vorobev, A., Dorogush, A. V., & Gulin, A. (2018). Catboost: Unbiased boosting with categorical features. *Proceedings of the 32nd International Conference on Neural Information Processing Systems*, 6639–6649.
- Prudden, S., Fisher, A., Marino, M., Mohamed, A., Watkins, S., & Wild, G. (2018). Measuring wind with small unmanned aircraft systems. *Journal of Wind Engineering and Industrial Aerodynamics*, 176, 197–210. <https://doi.org/10.1016/j.jweia.2018.03.029>
- Public Safety Canada. (2017). *An emergency management framework for Canada (third edition)* (tech. rep.). Public Safety Canada, Ottawa, Ontario. Retrieved August 14, 2023, from <https://www.publicsafety.gc.ca/cnt/rsrscs/pblctns/2017-mrgnc-mngmnt-frmwrk/2017-mrgnc-mngmnt-frmwrk-en.pdf>
- Qurratulain, S., Zheng, Z., Xia, J., Ma, Y., & Zhou, F. (2023). Deep learning instance segmentation framework for burnt area instances characterization. *International Journal of Applied Earth Observation and Geoinformation*, 116, 103146. <https://doi.org/10.1016/j.jag.2022.103146>
- Ranquist E, S. M. Exploring the range of weather impacts on UAS operations. In: *Proceedings of the 18th conference on aviation, range, and aerospace meteorology*. American Meteorological Society. Seattle, WA, 2017.
- Rao, K., Williams, A. P., Flefil, J. F., & Konings, A. G. (2020). SAR-enhanced mapping of live fuel moisture content. *Remote Sensing of Environment*, 245, 111797. <https://doi.org/10.1016/j.rse.2020.111797>
- Raelison, O. D., Valenca, R., Lee, A., Karim, S., Webster, J. P., Poulin, B. A., & Mohanty, S. K. (2023). Wildfire impacts on surface water quality parameters: Cause of data variability and reporting needs. *Environmental Pollution*, 317, 120713. <https://doi.org/10.1016/j.envpol.2022.120713>
- Rehm, R. G., & Baum, H. R. (1978). The equations of motion for thermally driven, buoyant flows. *Journal of research of the National Bureau of Standards*, 83 3, 297–308. <https://api.semanticscholar.org/CorpusID:13971757>

- Rein, G. (2013). Smouldering fires and natural fuels. In *Fire phenomena and the earth system* (pp. 15–33). John Wiley & Sons, Ltd. <https://doi.org/https://doi.org/10.1002/9781118529539.ch2>
- Rein, G., & Huang, X. (2021). Smouldering wildfires in peatlands, forests and the arctic: Challenges and perspectives. *Current Opinion in Environmental Science & Health*, 24, 100296. <https://doi.org/https://doi.org/10.1016/j.coesh.2021.100296>
- Ribeiro, T. F., Silva, F., Moreira, J., & de C. Costa, R. L. (2023). Burned area semantic segmentation: A novel dataset and evaluation using convolutional networks. *ISPRS Journal of Photogrammetry and Remote Sensing*, 202, 565–580. <https://doi.org/10.1016/j.isprsjprs.2023.07.002>
- Rios, O., Jahn, W., Pastor, E., Valero, M. M., & Planas, E. (2018). Interpolation framework to speed up near-surface wind simulations for data-driven wildfire applications. *International Journal of Wildland Fire*, 27(4), 257–270. <https://doi.org/https://doi.org/10.1071/WF17027>
- Robinson, J. M., Harrison, P. A., Mavoa, S., & Breed, M. F. (2022). Existing and emerging uses of drones in restoration ecology. *Methods in Ecology and Evolution*, 13(9), 1899–1911. <https://doi.org/10.1111/2041-210X.13912>
- Rodriguez, B., Lareau, N. P., Kingsmill, D. E., & Clements, C. B. (2020). Extreme pyroconvective updrafts during a megafire [e2020GL089001 2020GL089001]. *Geophysical Research Letters*, 47(18), e2020GL089001. <https://doi.org/10.1029/2020GL089001>
- Ronchi, E., Wahlqvist, J., Ardinge, A., Rohaert, A., Gwynne, S. M. V., Rein, G., Mitchell, H., Kalogeropoulos, N., Kinateder, M., Bénichou, N., Kuligowski, E., & Kimball, A. (2023). The verification of wildland–urban interface fire evacuation models. *Natural Hazards*, 117, 1493–1519. <https://doi.org/10.1007/s11069-023-05913-2>
- Rossa, C. G., Davim, D. A., Sil, Â., & Fernandes, P. M. (2024). Field-based generic empirical flame length–fireline intensity relationships for wildland surface fires. *International Journal of Wildland Fire*, 33, WF23127. <https://doi.org/10.1071/WF23127>
- Rothermel, R. C. (1972). *A mathematical model for predicting fire spread in wildland fuels* (Research Paper). Rocky Mountain Research Station. Ogden, UT, U.S. Department of Agriculture, Intermountain Forest; Range Experiment Station.
- Rubí, J. N., de Carvalho, P. H., & Gondim, P. R. (2023). Application of machine learning models in the behavioral study of forest fires in the brazilian federal district region. *Engineering Applications of Artificial Intelligence*, 118, 105649. <https://doi.org/https://doi.org/10.1016/j.engappai.2022.105649>
- Sachindra, D. A., Huang, F., Barton, A., & Perera, B. J. C. (2014). Statistical downscaling of general circulation model outputs to precipitation—part 2: Bias-correction and future projections. *International Journal of Climatology*, 34(11), 3282–3303. <https://doi.org/https://doi.org/10.1002/joc.3915>

- Salamí, E., Barrado, C., & Pastor, E. (2014). UAV flight experiments applied to the remote sensing of vegetated areas. *Remote Sensing*, 6(11), 11051–11081. <https://doi.org/10.3390/rs6111051>
- Salinas, L. R., Tzoumas, G., Pitonakova, L., & Hauert, S. (2023). Digital twin technology for wildfire monitoring using UAV swarms. *2023 International Conference on Unmanned Aircraft Systems (ICUAS)*, 586–593. <https://doi.org/10.1109/ICUAS57906.2023.10155819>
- Sameer, M. M. A., Prasanth, T., & Anuradha, R. (2021). Rapid forest cover detection using ensemble learning. In *Lecture notes in electrical engineering* (pp. 181–190). Springer Singapore. <https://doi.org/10.1007/978-981-16-1244-2-15>
- Sánchez-Monroy, X., Mell, W., Torres-Arenas, J., & Butler, B. (2019). Fire spread upslope: Numerical simulation of laboratory experiments. *Fire Safety Journal*, 108, 102844. <https://doi.org/10.1016/j.firesaf.2019.102844>
- Santoso, M. A., Huang, X., Prat-Guitart, N., Christensen, E., Hu, Y., & Rein, G. (2019). Smouldering fires and soils. *Fire effects on soil properties*, 203–216.
- Sasaki, K., Inoue, M., Shimura, T., & Iguchi, M. (2021). In situ, rotor-based drone measurement of wind vector and aerosol concentration in volcanic areas. *Atmosphere*, 12(3). <https://doi.org/10.3390/atmos12030376>
- Schapire, R. E. (1999). A brief introduction to boosting. *Proceedings of the Sixteenth International Joint Conference on Artificial Intelligence*.
- Scheper, A. C., Verweij, P. A., & van Kuijk, M. (2021). Post-fire forest restoration in the humid tropics: A synthesis of available strategies and knowledge gaps for effective restoration. *Science of The Total Environment*, 771, 144647. <https://doi.org/10.1016/j.scitotenv.2020.144647>
- Schumann, R. L., Mockrin, M., Syphard, A. D., Whittaker, J., Price, O., Gaither, C. J., Emrich, C. T., & Butsic, V. (2020). Wildfire recovery as a “hot moment” for creating fire-adapted communities. *International Journal of Disaster Risk Reduction*, 42, 101354. <https://doi.org/10.1016/j.ijdr.2019.101354>
- Shadrin, D., Illarionova, S., Gubanov, F., et al. (2024). Wildfire spreading prediction using multimodal data and deep neural network approach. *Scientific Reports*, 14, 2606. <https://doi.org/10.1038/s41598-024-52821-x>
- Sharples, J., McRae, R., Weber, R., & Gill, A. (2009). A simple index for assessing fire danger rating. *Environmental Modelling & Software*, 24(6), 764–774. <https://doi.org/10.1016/j.envsoft.2008.11.004>
- Shono, K., Cadaweng, E. A., & Durst, P. B. (2007). Application of assisted natural regeneration to restore degraded tropical forestlands. *Restoration Ecology*, 15(4), 620–626. <https://doi.org/10.1111/j.1526-100X.2007.00274.x>
- Sierra-Escrigas, S. L., Peluffo, D. R., & García-Urueña, R. (2020). Shallow coral reef community mapping and update on its ecological units using aerial images at isla arena, colombian caribbean. *International Journal of Remote Sensing*, 41(21), 8198–8215. <https://doi.org/10.1080/01431161.2020.1763495>

- Sjöqvist, H., Långkvist, M., & Javed, F. (2020). An analysis of fast learning methods for classifying forest cover types. *Applied Artificial Intelligence*, 34(10), 691–709. <https://doi.org/10.1080/08839514.2020.1771523>
- Sjöström, J., & Granström, A. (2023). A phenology-driven fire danger index for northern grasslands. *International Journal of Wildland Fire*, 32, 1332–1346. <https://doi.org/10.1071/WF21124>
- Soliman, A. M. S., Cagan, S. C., & Buldum, B. B. (2019). The design of a rotary-wing unmanned aerial vehicles–payload drop mechanism for fire-fighting services using fire-extinguishing balls. *SN Applied Sciences*, 1. <https://doi.org/10.1007/s42452-019-1322-6>
- Stasiewicz, A. M., & Paveglio, T. B. (2021). Preparing for wildfire evacuation and alternatives: Exploring influences on residents’ intended evacuation behaviors and mitigations. *International Journal of Disaster Risk Reduction*, 58, 102177. <https://doi.org/10.1016/j.ijdrr.2021.102177>
- Stelzer, H. (2019). How to plant forest tree seedlings [Accessed: 05-Sep-2023]. <https://extension.missouri.edu/publications/g5008>
- Stengel, K., Glaws, A., Hettinger, D., & King, R. N. (2020). Adversarial super-resolution of climatological wind and solar data. *Proceedings of the National Academy of Sciences*, 117, 16805–16815.
- Sudhakar, S., Vijayakumar, V., Sathiya Kumar, C., Priya, V., Ravi, L., & Subramaniaswamy, V. (2020). Unmanned aerial vehicle (UAV) based forest fire detection and monitoring for reducing false alarms in forest-fires. *Computer Communications*, 149, 1–16. <https://doi.org/10.1016/j.comcom.2019.10.007>
- Sullivan, A. L. (2009a). Wildland surface fire spread modelling, 1990 - 2007. 1: Physical and quasi-physical models. *International Journal of Wildland Fire*, 18(4), 349. <https://doi.org/10.1071/wf06143>
- Sullivan, A. L. (2009b). Wildland surface fire spread modelling, 1990 - 2007. 2: Empirical and quasi-empirical models. *International Journal of Wildland Fire*, 18(4), 369. <https://doi.org/10.1071/wf06142>
- Sullivan, A. L. (2009c). Wildland surface fire spread modelling, 1990 - 2007. 3: Simulation and mathematical analogue models. *International Journal of Wildland Fire*, 18(4), 387. <https://doi.org/10.1071/wf06144>
- Sutherland, D., Sharples, J. J., Mell, W., & Moinuddin, K. A. M. (2021). A response to comments of cruz et al. on: ‘simulation study of grass fire using a physics-based model: Striving towards numerical rigour and the effect of grass height on the rate of spread’. *International Journal of Wildland Fire*, 30, 221–223. <https://doi.org/10.1071/WF20091>
- Tao, H., Habib, M., Aljarah, I., Faris, H., Afan, H. A., & Yaseen, Z. M. (2021). An intelligent evolutionary extreme gradient boosting algorithm development for modeling scour depths under submerged weir. *Information Sciences*, 570, 172–184. <https://doi.org/10.1016/j.ins.2021.04.063>

- Tavakol Sadrabadi, M., & Innocente, M. S. (2023). Vegetation cover type classification using cartographic data for prediction of wildfire behaviour. *Fire*, 6(2). <https://doi.org/10.3390/fire6020076>
- Tavakol Sadrabadi, M., & Innocente, M. S. (2024). Enhancing wildfire propagation model predictions using aerial swarm-based real-time wind measurements: A conceptual framework. *Applied Mathematical Modelling*, 130, 615–634. <https://doi.org/10.1016/j.apm.2024.03.012>
- Tavakol Sadrabadi, M., & Innocente, M. S. (2025). To cut or not to cut: Effect of vegetation height and bulk density on wildfire propagation under varied wind and slope conditions. *International Journal of Disaster Risk Reduction*, 105372. <https://doi.org/https://doi.org/10.1016/j.ijdr.2025.105372>
- Tavakol Sadrabadi, M., Innocente, M. S., Gkanas, E., & Papagiannis, I. (2022). Comparison of the effect of one-way and two-way fire-wind coupling on the modelling of wildland fire propagation dynamics. In *Advances in forest fire research 2022* (pp. 115–121). Imprensa da Universidade de Coimbra. https://doi.org/10.14195/978-989-26-2298-9_18
- Tavakol Sadrabadi, M., Peiro, J., Innocente, M. S., & Rein, G. (2024). *Conceptual design of a wildfire emergency response system empowered by swarms of unmanned aerial vehicles* [Preprint available at SSRN]. <https://doi.org/10.2139/ssrn.4942867>
- Teye, M., Azizpour, H., & Smith, K. (2018). Bayesian uncertainty estimation for batch normalized deep networks. <https://arxiv.org/abs/1802.06455>
- Thielicke, W., Hübert, W., Müller, U., Eggert, M., & Wilhelm, P. (2021). Towards accurate and practical drone-based wind measurements with an ultrasonic anemometer [AMT]. *Atmospheric Measurement Techniques*, 14(2), 1303–1318. <https://doi.org/https://doi.org/10.5194/amt-14-1303-2021>
- Thippeswamy, B. M., Ghouse, M., Deksiso, A., Prasad, B. M. P., Pramod, T. C., & Kumar, B. N. P. (2022). Pilot DroneUI: An user interface to control UAV using robot operating system. *2022 IEEE 3rd Global Conference for Advancement in Technology (GCAT)*, 1–6. <https://doi.org/10.1109/GCAT55367.2022.9971987>
- Thomas, P. (1963). The size of flames from natural fires. *Symposium (International) on Combustion*, 9(1), 844–859. [https://doi.org/https://doi.org/10.1016/S0082-0784\(63\)80091-0](https://doi.org/https://doi.org/10.1016/S0082-0784(63)80091-0)
- Torben P. Grumstrup, M. A. F., Sara S. McAllister. (2017). Qualitative flow visualization of flame attachment on slopes. *10th U. S. National Combustion Meeting*.
- Trianni, V., & Campo, A. (2015). Fundamental collective behaviors in swarm robotics. In J. Kacprzyk & W. Pedrycz (Eds.), *Springer handbook of computational intelligence* (pp. 1377–1394). Springer Berlin Heidelberg. https://doi.org/10.1007/978-3-662-43505-2_71
- Twidwell, D., Allen, C. R., Detweiler, C., Higgins, J., Laney, C., & Elbaum, S. (2016). Smokey comes of age: Unmanned aerial systems for fire management. *Frontiers in Ecology and the Environment*, 14(6), 333–339. <https://doi.org/10.1002/fee.1299>

- Tymstra, C., Stocks, B. J., Cai, X., & Flannigan, M. D. (2020). Wildfire management in Canada: Review, challenges and opportunities. *Progress in Disaster Science*, 5, 100045. <https://doi.org/10.1016/j.pdisas.2019.100045>
- Tzoumas, G., Pitonakova, L., Salinas, L., Scales, C., Richardson, T., & Hauert, S. (2023). Wildfire detection in large-scale environments using force-based control for swarms of UAVs. *Swarm Intelligence*, 17, 89–115. <https://doi.org/10.1007/s11721-022-00218-9>
- United Nations Environment Programme. (2022). *Spreading like wildfire: The rising threat of extraordinary landscape fires* (tech. rep.). United Nations Environment Programme. Retrieved August 14, 2023, from <https://www.unep.org/resources/report/spreading-wildfire-rising-threat-extraordinary-landscape-fires>
- USDA Forest Service. (2020). Burned area emergency response-baer. Retrieved August 2, 2023, from <https://www.fs.usda.gov/naturalresources/watershed/burnedareas-background.shtml>
- van Wagner, C. E. (1987). Development and structure of the Canadian forest fire weather index system. <https://cfs.nrcan.gc.ca/publications?id=19927>
- Vanella, M., McGrattan, K., McDermott, R., Forney, G., Mell, W., Gissi, E., & Fiorucci, P. (2021). A multi-fidelity framework for wildland fire behavior simulations over complex terrain. *Atmosphere*, 12(2). <https://doi.org/10.3390/atmos12020273>
- VanWagner, C. E. (1987). Forest fire research—hindsight and foresight. *Proceedings of the symposium on wildland fire*.
- Vasiljević, N., Harris, M., Tegtmeier Pedersen, A., Rolighed Thorsen, G., Pitter, M., Harris, J., Bajpai, K., & Courtney, M. (2020). Wind sensing with drone-mounted wind LiDARs: Proof of concept [AMT]. *Atmospheric Measurement Techniques*, 13(2), 521–536. <https://doi.org/https://doi.org/10.5194/amt-13-521-2020>
- Viegas, C., Chehreh, B., Andrade, J., & Lourenço, J. (2022). Tethered UAV with combined multi-rotor and water jet propulsion for forest fire fighting. *Journal of Intelligent & Robotic Systems*, 104. <https://doi.org/10.1007/s10846-021-01532-w>
- Viseras, A., Meissner, M., & Marchal, J. (2021). Wildfire front monitoring with multiple UAVs using Deep Q-learning. *IEEE Access*, 1–1. <https://doi.org/10.1109/ACCESS.2021.3055651>
- Vogwell, D. (2003). Stakeholder management. *PMI® Global Congress 2003—EMEA*.
- Volkova, L., Weiss Aparicio, A. G., & Weston, C. J. (2019). Fire intensity effects on post-fire fuel recovery in eucalyptus open forests of south-eastern australia. *Science of The Total Environment*, 670, 328–336. <https://doi.org/10.1016/j.scitotenv.2019.03.226>
- Vorster, A. G., Evangelista, P. H., Stovall, A. E. L., & Ex, S. (2020). Variability and uncertainty in forest biomass estimates from the tree to landscape scale: The role of allometric equations. *Carbon Balance and Management*, 15(1). <https://doi.org/10.1186/s13021-020-00143-6>
- Vrabič, R., Erkoyuncu, J. A., Butala, P., & Roy, R. (2018). Digital twins: Understanding the added value of integrated models for through-life engineering services

- [Proceedings of the 7th International Conference on Through-life Engineering Services]. *Procedia Manufacturing*, 16, 139–146. <https://doi.org/10.1016/j.promfg.2018.10.167>
- Wagenbrenner, N. S., Forthofer, J. M., Lamb, B. K., Shannon, K. S., & Butler, B. W. (2016). Downscaling surface wind predictions from numerical weather prediction models in complex terrain with windninja. *Atmospheric Chemistry and Physics*, 16(8), 5229–5241. <https://doi.org/10.5194/acp-16-5229-2016>
- Wahlqvist, J., Ronchi, E., Gwynne, S. M., Kinateder, M., Rein, G., Mitchell, H., Bénichou, N., Ma, C., Kimball, A., & Kuligowski, E. (2021). The simulation of wildland-urban interface fire evacuation: The WUI-NITY platform. *Safety Science*, 136, 105145. <https://doi.org/10.1016/j.ssci.2020.105145>
- Walsh, H. S., Spirakis, E., Andrade, S. R., Hulse, D. E., & Davies, M. D. (2020). *SMART-STEReO: Preliminary concept of operations* (tech. rep. No. NASA/TM—20205007665). National Aeronautics and Space Administration.
- Wang, H., & Raj, B. (2017). On the origin of deep learning. <https://arxiv.org/abs/1702.07800>
- Wang, L., Chen, M., Luo, Z., Zhang, B., Xu, J., Wang, Z., & Tan, A. C. (2024). Dynamic wake field reconstruction of wind turbine through physics-informed neural network and sparse lidar data. *Energy*, 291, 130401. <https://doi.org/10.1016/j.energy.2024.130401>
- Weibel, R., & Hansman, R. J. (2004). Safety considerations for operation of different classes of UAVs in the NAS. In *Aiaa 3rd "unmanned unlimited" technical conference, workshop and exhibit*. <https://doi.org/10.2514/6.2004-6421>
- Weise, D. R., & Biging, G. S. (1994). Effects of wind velocity and slope on fire behavior. In T. Kashiwagi (Ed.), *Fire safety science proceedings of the fourth international symposium* (pp. 1041–1051). <https://doi.org/10.3801/IAFSS.FSS.4-104>
- Weise, D. R., & Biging, G. S. (1996). Effects of wind velocity and slope on flame properties. *Canadian Journal of Forest Research*, 26(10), 1849–1858. <https://doi.org/10.1139/x26-210>
- Weise, D. R., Cobian-Iñiguez, J., & Princevac, M. (2018). Surface to crown transition. In S. L. Manzello (Ed.), *Encyclopedia of wildfires and wildland-urban interface (wui) fires* (pp. 1–5). Springer International Publishing. https://doi.org/10.1007/978-3-319-51727-8_24-1
- Weninger, T., Filipović, V., Mešić, M., Clothier, B., & Filipović, L. (2019). Estimating the extent of fire induced soil water repellency in mediterranean environment. *Geoderma*, 338, 187–196. <https://doi.org/10.1016/j.geoderma.2018.12.008>
- Westerling, A. L., Hidalgo, H. G., Cayan, D. R., & Swetnam, T. W. (2006). Warming and earlier spring increase western u.s. forest wildfire activity. *Science*, 313(5789), 940–943. <https://doi.org/10.1126/science.1128834>
- Wetz, T., Wildmann, N., & Beyrich, F. (2021). Distributed wind measurements with multiple quadrotor unmanned aerial vehicles in the atmospheric boundary layer [AMT]. *Atmospheric Measurement Techniques*, 14(5), 3795–3814. <https://doi.org/https://doi.org/10.5194/amt-14-3795-2021>

- Wollstein, K., O'Connor, C., Gear, J., & Hoagland, R. (2022). Minimize the bad days: Wildland fire response and suppression success. *Rangelands*, 44(3), 187–193. <https://doi.org/10.1016/j.rala.2021.12.006>
- Woo, S., Park, J., Lee, J.-Y., & Kweon, I. S. (2018). Cbam: Convolutional block attention module, 3–19. https://doi.org/10.1007/978-3-030-01234-2_1
- World Food Programme (WFP). (n.d.). Using drones to deliver critical humanitarian aid [Accessed on: 13-sep-2023]. <https://drones.wfp.org/updates/using-drones-deliver-critical-humanitarian-aid>
- World Meteorological Organization. (n.d.). Natural hazards and disaster risk reduction. Retrieved August 14, 2023, from <https://public.wmo.int/en/our-mandate/focus-areas/natural-hazards-and-disaster-risk-reduction>
- Wu, J., Chen, X.-Y., Zhang, H., Xiong, L.-D., Lei, H., & Deng, S.-H. (2019). Hyperparameter optimization for machine learning models based on bayesian optimizationb. *Journal of Electronic Science and Technology*, 17(1), 26–40. <https://doi.org/https://doi.org/10.11989/JEST.1674-862X.80904120>
- Wu, Y., Xing, H., & Atkinson, G. (2000). Interaction of fire plume with inclined surface. *Fire Safety Journal*, 35(4), 391–403. [https://doi.org/https://doi.org/10.1016/S0379-7112\(00\)00032-1](https://doi.org/https://doi.org/10.1016/S0379-7112(00)00032-1)
- Wu, Z., Pang, X., Han, Z., Yuan, K., Dai, S., Li, J., Chen, J., & Xing, B. (2022). Direct measuring particulate matters in smoke plumes from chimneys in a textile dyeing industrial park by a self-developed pm detector on an uav in yangtze river delta of china. *Sensors*, 22(12). <https://doi.org/10.3390/s22124330>
- Xanthopoulos, G., Delogu, G. M., Leone, V., Correia, F. J. M., & Magalhães, C. G. (2020). Chapter 6 - firefighting approaches and extreme wildfires. In F. Tedim, V. Leone, & T. K. McGee (Eds.), *Extreme wildfire events and disasters* (pp. 117–132). Elsevier. <https://doi.org/10.1016/B978-0-12-815721-3.00006-0>
- Xgboost project [Available at <https://github.com/dmlc/xgboost>]. (2022). <https://github.com/dmlc/xgboost>
- Yebra, M., Quan, X., Riaño, D., Larraondo, P. R., van Dijk, A. I., & Cary, G. J. (2018). A fuel moisture content and flammability monitoring methodology for continental australia based on optical remote sensing. *Remote Sensing of Environment*, 212, 260–272. <https://doi.org/10.1016/j.rse.2018.04.053>
- Yilmaz, O. S., Acar, U., Sanli, F. B., et al. (2023). Mapping burn severity and monitoring co content in türkiye's 2021 wildfires, using sentinel-2 and sentinel-5p satellite data on the gee platform. *Earth Science Informatics*, 16, 221–240. <https://doi.org/10.1007/s12145-023-00933-9>
- Yu, C., Bi, X., & Fan, Y. (2023). Deep learning for fluid velocity field estimation: A review. *Ocean Engineering*, 271, 113693. <https://doi.org/https://doi.org/10.1016/j.oceaneng.2023.113693>
- Zacharakis, I., & Tsihrintzis, V. A. (2023). Integrated wildfire danger models and factors: A review. *Science of The Total Environment*, 899, 165704. <https://doi.org/10.1016/j.scitotenv.2023.165704>

- Zhang, J., Hu, J., Lian, J., Fan, Z., Ouyang, X., & Ye, W. (2016). Seeing the forest from drones: Testing the potential of lightweight drones as a tool for long-term forest monitoring. *Biological Conservation*, 198, 60–69. <https://doi.org/10.1016/j.biocon.2016.03.027>
- Zhang, J., & Zhao, X. (2021). Spatiotemporal wind field prediction based on physics-informed deep learning and lidar measurements. *Applied Energy*, 288, 116641. <https://doi.org/https://doi.org/10.1016/j.apenergy.2021.116641>
- Zhang, J., Liu, J., & Huang, Z. (2023). Improved deep learning method for accurate flow field reconstruction from sparse data. *Ocean Engineering*, 280, 114902. <https://doi.org/https://doi.org/10.1016/j.oceaneng.2023.114902>
- Zhang, R., Wang, Z., Li, X., She, Z., & Wang, B. (2023). Water quality sampling and multi-parameter monitoring system based on multi-rotor UAV implementation. *Water*, 15(11). <https://doi.org/10.3390/w15112129>
- Zhao, X., Xu, Y., Lovreglio, R., Kuligowski, E., Nilsson, D., Cova, T. J., Wu, A., & Yan, X. (2022). Estimating wildfire evacuation decision and departure timing using large-scale gps data. *Transportation Research Part D: Transport and Environment*, 107, 103277. <https://doi.org/10.1016/j.trd.2022.103277>
- Zheng, Y., Jia, W., Wang, Q., & Huang, X. (2019). Deriving individual-tree biomass from effective crown data generated by terrestrial laser scanning. *Remote Sensing*, 11(23), 2793. <https://doi.org/10.3390/rs11232793>

Collaborator Agreement forms

Collaborator’s Agreement

Enhancing wildfire propagation model predictions using aerial swarm-based real-time wind measurements: A conceptual framework

This is a collaborator’s agreement for the published work

Enhancing wildfire propagation model predictions using aerial swarm-based real-time wind measurements: A conceptual framework

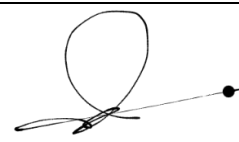

which was published in the year 2024 to

Mohammad Tavakol Sadrabadi and Mauro Sebastian Innocente. June 2024. Enhancing wildfire propagation model predictions using aerial swarm-based real-time wind measurements: A conceptual framework. Applied Mathematical Modelling, 130:615– 634. ISSN 0307-904X. doi: 10.1016/j.apm.2024.03.012

The following details each author’s contribution to the work:

- **Mohammad Tavakol Sadrabadi:** Conceptualization, Methodology, Software, Writing, Investigation, Visualization.
- **Mauro Sebastián Innocente:** Conceptualization, Methodology, Software, Writing, Supervision, Resources, Visualization.

Signatures:

M. Tavakol Sadrabadi	
Mauro Sebastián Innocente	

Collaborator’s Agreement

To cut or not to cut: Effect of vegetation height and bulk density on wildfire propagation under different wind and slope conditions

This is a collaborator’s agreement for the published work

To cut or not to cut: Effect of vegetation height and bulk density on wildfire propagation under different wind and slope conditions

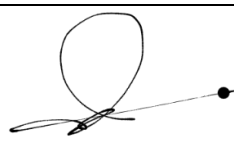

which was published in the year 2024 to

Mohammad Tavakol Sadrabadi and Mauro Sebastian Innocente (2024). To cut or not to cut: Effect of vegetation height and bulk density on wildfire propagation under different wind and slope conditions. Preprint available at EngRxiv: <https://doi.org/10.31224/4087>

The following details each author’s contribution to the work:

- **Mohammad Tavakol Sadrabadi:** Conceptualization, Methodology, Software, Writing, Investigation, Visualization.
- **Mauro Sebastián Innocente:** Conceptualization, Methodology, Software, Writing, Supervision, Resources, Visualization.

Signatures:

M. Tavakol Sadrabadi	
Mauro Sebastián Innocente	

Collaborator's Agreement

Vegetation cover type classification using cartographic data for prediction of wildfire behaviour

This is a collaborator's agreement for the published work


Vegetation cover type classification using cartographic data for prediction of wildfire behaviour

which was published in the year 2023 to

Mohammad Tavakol Sadrabadi and Mauro Sebastian Innocente., 2023, Vegetation cover type classification using cartographic data for prediction of wildfire behaviour. Fire, 6(2). ISSN 2571-6255. doi: 10.3390/fire6020076. URL: <https://www.mdpi.com/2571-6255/6/2/76>. The following details each author's contribution to the work:

- **Mohammad Tavakol Sadrabadi:** Conceptualization, Investigation, Methodology, Writing-original drafting, software, validation, data curation, visualisation, project administration
- **Mauro Sebastián Innocente:** Conceptualization, Investigation, Writing-review and editing, validation, resources, supervision, project administration

Signatures:

M. Tavakol Sadrabadi	
Mauro Sebastián Innocente	